ISAS - INTERNATIONAL SCHOOL
FOR ADVANCED STUDIES

The Manifold of Hot Galaxian Components

Thesis submitted to the
International School for Advanced Studies, Trieste, Italy
– Astrophysics Sector –
in partial fulfillment of the requirements for the degree of

Doctor Philosophiæ

Candidate:

Nicola Caon

Supervisors:

Prof. Dennis W. Sciama
Prof. Massimo Capaccioli

Academic Year 1992/93

TRIESTE

SISSA - SCUOLA
INTERNAZIONALE
SUPERIORE
DI STUDI AVANZATI
TRIESTE
Strada Costiera 11

Contents

Outline of this Thesis

Hot Galaxian Components (ellipticals, bulges and early–type dwarfs) populate a two dimensional manifold, named *Fundamental Plane* (FP), in the representative space of the global photometric and kinematical parameters. The FP provides direct information on the physical processes that determine the galaxy formation and evolution. On the observational side, however, its universality is still questioned on the issues of its zero-point, slope, thickness and possible dependence on the environment. Investigating the possible sources of such controversies, I realized that most of the FP properties are based upon data-sets which are affected by several problems: statistical incompleteness of the galaxy samples, incorrect methodology to derive global parameters, and poor accuracy of the measurements.

Prompted by these considerations, I constructed a new homogeneous and high-quality data-base of photometric and geometrical parameters for a large and deep luminosity sample of 80 early-type galaxies belonging to the Virgo and to the Fornax clusters. The photometry is based on a genuinely new methodology, named 'global mapping', which I developed in collaboration with Massimo Capaccioli. Based on the coupling of CCD images with PDS scans of large-field photographs, it provides a complete mapping of the galaxian light distribution from the center out to the very outskirts at state of the art accuracy.

The re-analysis of the relationships among global parameters, based on the above data-set, has led to the following results: 1) the discovery that there are two distinct families of galaxies, one being possibly an inbred variety, the other probably the product of evolution; 2) the falsification of the commonly accepted assumption of homology in early-type galaxies, in that the light distribution is directly correlated with the galaxian size and luminosity (hence the $r^{1/4}$ law must be no longer regarded as universal); 3) the finding that galaxies are located in different environments according to their isophotal shape, a property of which the well-known morphology-density relation is just a consequence.

This thesis contains 6 chapters and 2 appendixes assembled in logical order. Every chapter can be read as a separate entity. I have not included in the thesis those early works that have already been published in Journals or Conference Proceedings and also formed part of my 'Magister Philosophiæ' dissertation. A complete list of my publications related to the research project above outlined is provided at the end of this volume.

• Chapter 1 can be considered as the most informative, being devoted to the overview of my thesis project. After giving some introductory notes on the impressive growth of our knowledge about the properties of early-type galaxies in the last 20 years, it provides a con-

cise but exhaustive review on the Fundamental Plane of Hot Stellar Systems, which is the starting point of this study. Then, I present the motivations for this work, analysing the problems concerning the data-sets used by other authors and pointing out why there is the need for a new, homogeneous and very accurate data-set of photometric parameters for a statistically complete sample of galaxies. The choice of the sample, the observations and the data reduction, based on the 'global mapping' methodology, are then described. Finally, the main results achieved are illustrated, and the work in progress or planned for the immediate future is outlined.

- Chapter 2 presents the galaxy sample, the observations, the data reduction and analysis, and the determination of global photometric parameters for 47 early–type galaxies in the Virgo and in the Fornax clusters, to be added to the 33 Virgo galaxies I studied in my dissertation work. Particular emphasis has been given to those steps specific to the 'global mapping' methodology. This chapter, dealing with the technical aspects of this work, can be skipped at a first reading without losing any important information, as in all the following chapters the main properties of our data-set are shortly reported.
- Chapter 3 gives a preliminary account of the investigation of the relationships involving isophotal shapes and global properties. In particular the Luminosity Functions of the different isophotal classes are derived, and the correlations between ellipticity and position angle, and between ellipticity and luminosity, are analysed.
- Chapter 4 is dedicated to the study of correlations among global galaxy parameters. The existence of two distinct galaxian families populating the effective parameter plane is shown, first using only our own sample, then adding a much larger set of literature data. This dichotomy is further strengthened by the behavior of several global parameters with the galaxian half-light radius. The interpretation of this finding in terms of an inbred family opposed to a family whose members have experienced merging or accretion phenomena is also discussed.
- Chapter 5 is focused on the study of the projected light distribution of galaxies in our sample. It provides evidence that galaxian light profiles display a variety of shapes, which can be represented very well by a generalized de Vaucouleurs law (where the exponent $1/n$ is free rather than fixed to $1/4$), and are directly related to the galaxian size and luminosity.
- Chapter 6, the last one, illustrates the analysis of the environmental properties of the Virgo cluster galaxies, showing that there is a direct correlation between the isophote shape and the local environment.
- Appendix A contains a detailed report of the technique I devised to remove the column offsets in CCD images.
- Finally, Appendix B groups the tables and figures concerning the individual galaxies, and includes some notes about peculiar properties and characteristics of our galaxies.

I would like to acknowledge all the people who collaborated with me at different stages of this work. The 'global mapping' methodology was originally invented by Massimo Capaccioli, who guided me to further develop and improve this technique. The photometry of the

Virgo and Fornax galaxies (Chapter 2) was carried out together with Mauro D'Onofrio and Susanna Trevisani. M. Capaccioli and M. D'Onofrio co-author the works on the isophotal properties of our sample, on the two families in the $(\log R_e, \mu_e)$ plane, and on the shape of light profiles (Chapters 3, 4 and 5). The investigation of the environmental properties of our Virgo galaxies (Chapter 6) was done in collaboration with Maret Einasto (International Centre for Cosmology, Toravere, Estonia). Finnaly, Giampaolo Piotto and Carla Pellegrini contributed to refine the technique to remove column offsets in CCD frames (App. A).

It is a pleasure to thank the Director of the Astronomy Department of the University of Padova and the Director of the Padova Astronomical Observatory for the kind and generous hospitality during the many years of collaboration with the Padova group.

I also thank Paolo Salucci for a careful reading of this manuscript.

Chapter 1

Overview of my Thesis Project

1.1 The Early-type Galaxies

It is still a common practice to name *early-type* the heterogeneous collection of galaxy types comprising ellipticals, lenticulars, and (by an unwritten rule resting on some observational element), also bulges of spirals. Such a convention, originally instigated by morphological analogies and by the similarity of the surface brightness profiles, is now shaking under new photometric and kinematical evidences.

The common belief that ellipticals and bulges of lenticulars and spirals form a homogeneous and uninteresting family of oblate spheroids flattened by rotation about their polar axis, came suddenly to an end when Bertola & Capaccioli (1975), and later Illingworth (1977), found that bright ellipticals rotate too slowly to account for the observed flattening. Binney (1976) considered the anisotropy of the velocity dispersion tensor as a possible flattening mechanism: this opened the way to triaxial models, strongly invoked to explain the isophotal *twisting* observed in a fair fraction of objects (see Galletta 1980). More accurate and detailed investigations put into evidence the heterogeneity of kinematical behaviors of early-type galaxies, and showed that ellipticals comprise at least two families (high and low luminosity) with distinct kinematical behaviors. From the photometric point of view, the breakthrough took place when it was realized that both the presence of systematic deviations of the observed light profile from the $r^{1/4}$ law (i.e. the empirical fitting law proposed by de Vaucouleurs 1948), and the presence of systematic departures of the isophotes from the perfect elliptical shape, are the signatures of a faint underlying subcomponent (for instance weak discs; Capaccioli 1987). Furthermore, interactions and secondary evolution play an important role in determining the present observed structure of early-type galaxies: shell-like structures, counter-rotating cores, anomalous blue colors, counter-rotating dust lanes and gaseous discs, all clearly indicate that cannibalism and mergers are recent history at least for some ellipticals. A similar complexity and heterogeneity in properties has also been revealed by observations in the X-ray, radio, ultraviolet and far-infrared domains: for instance, galaxies of similar optical luminosity exhibit a wide range in X-ray emission, and the amount of cool gas does not show any correlation with the galaxy stellar content.

1.2 The Fundamental Plane of Hot Galaxian Components

Indeed, it seems that, as we enlarge the available parameters space and improve the quality of our data-sets, the complexity of early-type galaxies increases proportionally, so that we are still far from establishing a physical classification of galaxies based on their fundamental properties. This is not true. In fact, Hot Galaxian Components (ellipticals, bulges, early-type dwarfs, whose dynamics is dominated by random rather than ordered motions; hereinafter HGC) share some remarkable common properties, as shown by the existence of the so-called *Fundamental Plane* (FP), discovered independently by Djorgovski & Davis (1987) and by Dressler et al. (1987). In the parameter space defined by global parameters, such as luminosity, radius, surface brightness, velocity dispersion, colors, metallicity etc., early-type galaxies do not fill all of the available volume, but are confined to a two-dimensional surface, which becomes a plane after the proper mathematical transformations (*e.g* logarithms). The FP implicitely contains also important derived parameters, such as the mass and the mass-to-luminosity ratio, and provides powerful distance-indicators relations for early-type galaxies. On the other hand, the variables which describe the shape of the light distribution, such as ellipticity, isophotal twist, isophote shape descriptors etc., do not correlate with the FP, or even mutually.

We shall notice that the FP is not just a consequence of the Virial Theorem: the coefficients of the observed correlations depart significantly from those expected from the Virial Theorem, and must be telling something about the formation and evolutionary histories of ellipticals, involving, *e.g*, dissipative or dissipationless merging, infall processes, etc. The low dimensionality of the FP suggest self-regulation mechanisms in the processes which form and shape early-type galaxies, while details of their structure are likely determined by some stochastic processes which operate separately from the former.

An alternative version of the FP has been used by Burstein, Bender & Faber (1993), where all the important physical processes involved in the galaxy formation and evolution can be modelled. They define a new orthogonal coordinate system, called *k space*, by combining the three parameters that normally define the FP, that is central velocity dispersion, effective surface brightness and effective radius. If M is the mass of the galaxy within the luminous confines, L is the luminosity and I_e the effective surface brightness, then $k_1 \propto \log M$, $k_2 \propto \log(M/L)I_e^3$ and $k_3 \propto \log(M/L)$. The most important property of this transformation is that the k_1/k_2 projection is close to being a face-on view of the FP, while the k_1/k_3 projection gives an edge-on view of the plane. They found that all the types of HGC, with the exception of the extreme dwarf spheroidals, lie nearly in the same plane defined by giant ellipticals, and the thickness of this distribution is almost completely accounted for by measurements errors and the uncertainty on the galaxies distances. On the other hand, the object distribution within the FP separates itself into two apparent sequences. The first is populated by ellipticals, bulges and compact dwarfs, and is characterized by a decrease in surface brightness as the total luminosity increases; the second, which lies nearly perpendicular to the first one, is populated by dwarf ellipticals and dwarf spheroidals. The first sequence, named *Gas/Stellar Sequence*, is interpreted as one in which the gas versus stellar components of merging galaxies

compete in their evolutionary effects, with gas declining in influence in more massive systems; the second is explained by dwarf HGC being formed primarily from gas loss processes, including galactic winds and ram pressure stripping. Overall, the fundamental plane owes its basic existence to the homogeneity of the mass-to-luminosity ratio for old stellar populations, and a weak trend in M/L versus mass; most of the physical processes (except winds) tend to move galaxies into or within the FP, rather than move them away from it.

While the existence of such a basic uniformity of the global luminous and dynamical galaxy structures is no longer a matter of debate, there are some open questions about the dependence of the FP correlations on the environment. In fact, the FP correlations, being a product of galaxy formation and evolution, must reflect any possible variation in the formative and evolutive processes of galaxies in different environments, *e.g*, in the field, in small groups, in rich clusters. Indeed, de Carvalho and Djorgovski (1992) find that ellipticals in the field show a large scatter in their properties with respect to cluster ellipticals, and that they likely define two slightly different FPs. In particular, field ellipticals seem to contain an admixture of younger stellar populations, revealed by the population variables Mg_2 and colors. These results fits naturally into the picture where cluster HGC forms early, and in a more homogeneous way, while field HGC may have formed by relatively recent mergers. If these differences are real, the indiscriminate application to all ellipticals of the FP based distance indicator relations, such as the $\sigma - R_e - \mu_e$ or the $D_n - \sigma$ relations, may give spurious peculiar velocities, as also pointed out by Gregg (1992).

On the other hand, using a sample composed of essentially the same object used by de Carvalho and Djorgovski (1992), Burstein and collaborators have explored the sensitivity of the FP properties to cluster richness, galaxy absolute magnitude and stellar population, and found no systematic effects. Such a result has also been confirmed by Lucey et al. (1991), who detected no systematic dependence of the zero-point of the $D_n - \sigma$ relation over a factor of 150 in projected local galaxy density in the Coma cluster.

1.3 Motivations for the Thesis Work

It is clear that the goodness and the reliability of the astrophysical results that are drawn from such kinds of analyses rest not only on our ability to interpret the data we have, on our knowledge of the physical processes involved and our capability to construct theoretical models, but first of all, on the quality and accuracy of the data themselves. In principle, these should not be affected by any systematic errors or biases, and the measurement errors on the quantity of interest should be always smaller than that limit which allows to discriminate between two different hypotheses.

It is therefore surprising that such stringent requirements are often overlooked, and that in many case enlarging the available data-set to an ever increasing number of objects is considered much more important than improving its quality.

In fact, in investigating the problems connected to the Fundamental Plane, we have found that the galaxy samples used so far suffer from several problems.

- **Statistical completeness:** samples are generally magnitude-limited (that is only galaxies brighter than a given apparent luminosity and in a given sky area enter the sample), and therefore are biased toward intrinsically bright objects and are not representative of the global galaxy population. A clear example is Kormendy's (1977a) $\mu_e - R_e$ relation, which is just the projection of the FP onto a coordinate plane, and was considered valid for the whole class of ellipticals: μ_e is directly related to R_e, so that ellipticals form a uniparametric family. As I shall show in Chapter 4, this relation is an artefact of the strong bias of the sample used by Kormendy toward intrinsically luminous galaxies; actually, Kormendy's relation holds only for galaxy brighter than $M_B \simeq -19.3$, while fainter galaxies exhibit a completely different behavior in the effective parameters plane.

- **Methodology:** global parameters (effective radius and surface brightness, total luminosity) which, according to their original definition (de Vaucouleurs 1961), are model-independent, are often confused with the scale parameters of the best fitting $r^{1/4}$ law, in most cases applied to a limited portion (that inside the CCD frame) of the galaxy light profile. This, beyond being a methodological flaw, carries on the implicit assumption of *homology*, that is all ellipticals have the same luminous structure — notice that homology is a basic ingredient in the Virial Theorem in order to interpret the Fundamental Plane. On the contrary, as I shall shaw in Chapter 5, light profiles of early-type galaxies show a wide range of shapes, and are very well described by a generalized de Vaucouleurs law, with the exponent $1/n$ let free rather than fixed to 1/4. More importantly, the light profile shape is directly correlated with the galaxy luminosity and size.

- **Accuracy:** the photometric mapping is often limited by the small CCD field of view, and light profiles are therefore distorted by uncertain background subtraction. For instance, the brightest galaxies in the Virgo and in the Fornax clusters can reach effective diameters as large as 6–7 arcminute, which is comparable to the field of view of a typical CCD used at a medium-size telescope: this means that even 50% of the galaxy light may fall outside the CCD frame, and that there is no possibility to measure the blank-sky level directly on the galaxy image, while indirect methods to recover the night sky brightness are questionable (see Capaccioli & Caon 1989). Poor accuracy and incorrect methodology are responsible of the quite impressive disagreement on global parameters for a same object found into the literature: in Chapter 4 examples are shown of objects whose effective radii may vary by up to a factor of 5 from author to author, and whose effective surface brightness may differ even by 3 mag.

- **Parameter definition:** Some quantities are not defined in a unambiguous way. This is the case of the central velocity dispersion σ_c, one of the FP axes, which defines together with the maximum rotation velocity V_m the anisotropy parameter V_m/σ, used to gauge the degree of velocity anisotropy. Dressler (1984) measures central velocity dispersions within a $4'' \times 4''$ slit for Coma cluster galaxies and $16'' \times 16''$ for Virgo

galaxies; Davies et al. (1983) and Franx, Illingworth & Heckman (1989) define σ_c as the unweighted average within $1/2R_e$, while other authors simply do not mention the way they computed this quantity. We notice that these values may be influenced by the presence of a central mass concentration or of a kinematically decoupled inner subcomponent, or by velocity anisotropy. Also, many algorithms used so far do not account for possible systematic departures of the line profile from the gaussian shape, giving errors of 10% in the estimate of the velocity dispersion (van der Marel & Franx 1993).

1.4 Plan of the Thesis Work

1.4.1 A New Methodology

In order to circumvent the problems described above, we need a new and independent data-set of "model-free" photometric and geometric parameters, based on a methodology capable of mapping photometrically the galaxies over their whole extension. For this purpose, in collaboration with Massimo Capaccioli I developed, during my dissertation work, a genuinely new technique, named 'global mapping' methodology (Capaccioli & Caon 1989), further improved and refined during the following years. This methodology, coupling unsaturated CCD images of the inner galaxian regions with long exposure plates taken with large field (Schmidt) telescopes and having photometric quality, permits to perform, at state of the art accuracy, the complete photometric mapping from the center out to the very outskirts. The internal error is less than 0.1 mag out to $\mu_B \sim 26$ B–mag arcsec^{-2}, then it blows up reaching 100% uncertainty at $\mu_B \sim 28$, which is the ultimate limit to the photometry of extended objects, set by the statistical fluctuations in the distribution of subthreshold stars and galaxies. A block diagram illustrating the basic steps of the 'global mapping' technique is shown in Fig. 1.1 at the end of this Chapter.

1.4.2 Selection of the Galaxy Sample

I performed the 'global mapping' photometry on a large and deep luminosity-limited sample of 52 early-type galaxies belonging to the Virgo Cluster, and to a luminosity-limited sample of 28 early-type galaxies in the Fornax cluster. The main reason for selecting galaxies belonging to a cluster is that they are practically at the same distance from us. In fact, the depth of the Virgo cluster is ≤ 0.25 mag front to back (cf. Tonry, Ajhar & Luppino 1990), while the depth of the Fornax cluster is even smaller (Fornax is a more compact cluster than Virgo). This ensures that errors on distance-dependent quantities are greatly reduced. Moreover, galaxies belonging to a same cluster forms a quite homogeneous sample as far as stellar populations, hence formative and evolutive histories, are concerned (de Carvalho & Djorgovski 1992). Notice also that luminosity-limited samples are formed by simply imposing an apparent magnitude cut-off. The fact that the Virgo and the Fornax cluster are placed nearly at the same distance (cf. Jacoby et al. 1992) allows to form a unique luminosity-limited 'Virgo+Fornax' sample.

1.4.3 Observations and Data Reduction

The collection of CCD and plate material, and their reduction and analysis has been the most time consuming and somewhat tedious part of my work. CCD observations have been carried out personally in the course of several runs, using the major telescopes at ESO-La Silla (2.2m ESO-MPI, 1.5m Danish, 1.5m ESO) and at Kitt Peak (2.3m Steward Observatory), all equipped with high-quality CCD detectors. Photographic material was taken at the ESO and at the UK Schmidt telescopes; the plates were scanned with the PDS machines both in Padova and at the ESO Headquarters in Garching. The reduction of all this material was performed by means of the most complete and powerful packages available for the reduction and analysis of astronomical data, such as MIDAS (the Munich Image Data Analysis System) and IRAF (Image Reduction and Analysis Facility); I also wrote some original software (MIDAS and IRAF procedures, SuperMongo macros as well as Fortran codes) to cope with some specific tasks involved in the 'global mapping' methodology. I benefitted very much from the 'Adaptive Filtering', a technique (developed at the Astrophysical Institute of Potsdam) capable of smoothing the images without broadening sharp features such as galaxy centers, stars, etc. Also, I had to devise an original technique in order to remove the column offset pattern present in one set of images taken with a RCA High-Resolution chip. This technique has proven to be very effective: applied to a set of exposures on crowded stellar fields (for which this problem is particularly relevant), it has allowed to obtain reliable measurements of magnitudes and colors even for stars close to the limiting magnitude.

The efforts made in this stage were rewarded by the construction of an accurate and homogeneous data-set of global parameters for 19 galaxies in the Virgo cluster and 28 galaxies in the Fornax cluster, which adds to the data-set already available for the 33 Virgo galaxies I studied in my Laurea dissertation. These data were also supplemented by the photometric parameters of the bulge components of 35 spiral galaxies belonging to the Virgo cluster studied by D'Onofrio (1991).

A further step has been the collection of literature data for as many as 1500 galaxies, the analysis of the methodologies used by other authors to derive global photometric parameters, and the homogenization of the different data-sets.

1.5 Results

1.5.1 The Two Families of Hot Galaxian Components

With our data-set at handle, we have re-analysed the $\mu_e - R_e$ correlation proposed by Kormendy, in order to establish its reality and to verify to what extent it could be affected by the selection of the sample and by the confusion of effective parameters with the scale parameters of the best fitting $r^{1/4}$ law. We discovered, by using only our own galaxies, that two distinct families populate the $(\log R_e, \mu_e)$ plane.

The first one, that we name '*ordinary*', consists of ellipticals and bulges fainter than $M_B \simeq -19.3$ mag, with effective parameters ranging over a wide interval: $\Delta \log R_e \sim 0.7$dex, $\Delta\mu_e \sim 3.5$ mag. The interval spanned by the effective radius, as well as the sharp boundary

at $R_e \simeq 3$ kpc, appears to be independent of the total luminosity. The second family, named '*bright*', consists of the 12 brightest galaxies of our sample, well isolated from the '*ordinary*' galaxies. This group, together with the most luminous members of the '*ordinary*' family, fits the uniparametric Kormendy's relation: $\mu_e \simeq 3.0 \log R_e + \text{const.}$.

In order to strengthen this result, we have collected literature values of the effective parameters for about 1400 galaxies, spanning an as wide as possible range in luminosity and morphological type. However, the notable increase of the size of the sample is somewhat counterbalanced by its heterogeneity and its lower quality. In fact, the gap between the two family disappears, which may be due to measurement errors which tend to fill the gap. Our results about the distinct properties of the two galaxian families is fully confirmed by literature data. Remarkably, all bright galaxies places in a narrow strip following the Kormendy relation. As far as the '*ordinary*' family is concerned, galaxies with luminosities differing by as much as 3 dex share the same range of r_e, and, whatever their luminosity is (down to $M_B \simeq -12$), do not grow larger than $R_e \simeq 3$ kpc.

The dichotomy between the two galaxy families is shown also in the Luminosity Function. At variance with previous results, showing that the LF of E and S0 galaxies, both in cluster and in the field, is bell-shaped (see Binggeli, Sandage & Tammann 1988), our sample show a bimodal distribution, with a secondary bump at very high luminosities, populated by the '*bright*' galaxies.

Prompted by this finding, we have investigate whether the dichotomy in the effective parameters plane and in the Luminosity Function manifests itself also in other physical properties. For this purpose we collected from the literature all the available observables for galaxies of our sample. Indeed, the dependence on R_e of parameters such as the metallicity index Mg_2, the color gradient, the hot and cold gas content, the radio emission, is quite different in the two families. Also, there are indications for the existence of two distinct galaxy families in the mass–metallicity gradient plane (Danziger et al. 1993).

We suggest that the '*ordinary*' family is an inbred variety, while the '*bright*' family is the result of some sort of environmental evolution.

1.5.2 Luminosity Structure of Hot Galaxian Components

At this point, we may argue that, if Hot Galaxian Components exhibit this heterogeneity in the various physical properties, the common belief that they share on the whole the same luminosity structure — which implies that their light profiles should have the same shape — is at least questionable. Indeed, as already mentioned, the assumption of homology seems justified by the fact that luminosity profiles of elliptical galaxies and bulges are well described by the classical $r^{1/4}$ de Vaucouleurs law. In this context, deviations from the $r^{1/4}$ behavior are explained in terms of the presence of subcomponents or as the result of interactions with the environment. Motivated by this skepticism, we have analysed the light profiles along the main axes and the equivalent profiles of all the galaxies in our sample, aiming at testing whether their shapes are related to the luminosity or size of the galaxies. We found that a very good and useful parameterization of the shapes of luminosity profiles is provided by the

parameter n of the generalized de Vaucouleurs law, where the exponent $1/n$ is let free rather than fixed to 1/4. It turns out that n ranges over a wide interval, from 1 (i.e. the exponential law) to 17, and correlates quite well with R_e, in the sense that profiles becomes shallower with increasing galaxian size. While the scatter in n may hide a possible discontinuity between the two families in the $\log R_e$-$\log n$ plane, it is remarkable that all galaxies in the '*bright*' family have $n > 4$, while almost the totality of galaxies in the '*ordinary*' group have $n < 4$. This result has consequences for the claimed independence of the shape of light profiles with respect to the Fundamental Plane parameters, and casts some doubts on the validity of the disc-bulge decomposition technique based on the $r^{1/4}$ + exponential models. We also put into evidence that the indiscriminate use of the $r^{1/4}$ law to compute effective parameters and total luminosities gives results strongly dependent on which part of the light profile is fitted, and it is largely responsible for the large discrepancies among the values of global parameters found by different authors for a same object. Also, the adoption of standard growth curves to extrapolate photoelectric measurements is proved to be methodologically wrong.

1.5.3 Environmental Properties

In collaboration with Maret Einasto, I studied the environmental properties of galaxies in our Virgo sample. The aim was that of testing whether galaxies belonging to the '*bright*' and to the '*ordinary*' family inhabit different environments inside the cluster, and whether there exists any correlation between isophotal properties and the local environment. Analysing the local projected densities around our Virgo galaxies, we found that boxy galaxies are located in denser environments than discy galaxies. This is not the mere reflection of the well-known morphology-density relation, as the segregation according to the isophotal classification is shown independently by the E and by the S0 groups; furthermore, there seems to be no relation between the disc-to-bulge ratio and the local environment. A weaker segregation is detected between '*bright*' and '*ordinary*' galaxies, the former being located in higher density regions.

1.6 Future Work

Apart from the results mentioned above, this work has led to new questions, and to suggestions about how to improve our knowledge on the Hot Galaxian Components.

In order to enlarge the parameter space, in collaboration with S. Zaggia (Astr. Dept., Padova) I am presently studying the major axis kinematics of 15 early-type galaxies belonging to the Fornax Cluster, using the long exposure spectra I took at the 1.5m ESO telescope.

Our first aim is to see how differences in the photometric global properties and in the luminosity structure reflect into the dynamical behavior, and to test whether they are related to the presence of kinematically decoupled subcomponents or nuclear mass concentrations, found in a fair fraction of luminous galaxies.

The other topic we are interested in is connected to the use of the σ_c-D_n relation as a distance indicator. A first look at the velocity dispersion profiles and at the radial velocity

curves we have obtained shows a large heterogeneity of behaviors: for instance, some velocity dispersion curves are centrally peaked, while other are much more shallow; some other likely reveals the presence of two distinct stellar components. This implies that the σ_c-D_n relation is affected by the uncertainties on the definition of 'central velocity dispersion' and on the way it is measured (just the central value, the average inside $1/2\ R_e$, etc.), as already mentioned. We plan to test whether $\langle\sigma\rangle_{D_n}$, the luminosity-averaged value of the velocity dispersion within D_n, provides a tighter correlation with D_n itself. Furthermore, we shall explore a range of alternative values of the mean surface brightness entering the definition of D_n (the standard value is 20.75 B–mag arcsec^{-2}), searching for the one giving the best correlation. Also, combining the rotational speed with the velocity dispersion to account for both forms of the kinetic energy, random and ordered motion, is expected to improve correlations with photometric parameters.

The study of the global parameters relationships, in particular the μ_e-r_e relation, is being extended to a wider range of environments. I have recently secured B- and R-band CCD observations (1.5m ESO-Danish telescope) for about 60 early-type galaxies belonging to southern clouds and groups, while Schmidt plates are already at our disposal. The addition of the R-band images (available also for the Fornax galaxies; their reduction is in progress) will allow to investigate, using a larger and more homogeneous data-base than that built with literature data, the behavior of mean color indexes and color gradients with the galaxian luminosity or size, and to increase our information about the the properties of the two galaxian families.

We are also re-analysing the well-known correlations between the isophotal shape parameter A_4/a and several global photometric (optical luminosity, radio and X emission) and kinematical (V_m/σ) parameters (Bender et al. 1989a). We are motivated by the criticism of Governato, Reduzzi and Rampazzo (1993), who notice that these correlations become weaker or even disappear when new recent measurements are added and when a more careful analysis of the data is made. Our large, accurate and homogeneous photometric data-set for our luminosity-limited sample of Virgo and Fornax galaxies, complemented by the most recent literature data on the other relevant quantities, will be of great help in clarifying this matter.

The investigation of the detailed structure of elliptical galaxies in more detail is also the aim of a Key Programme at the European Southern Observatory (Bender et al. 1989), started about 3 years ago, of which I am an active member: I conducted an observing run in August 1990 at the 1.5m ESO-Danish telescope, and I performed the isophotal analysis both on the CCD images I took and on the CCD images coming from another observing run at the 2.2m ESO-MPI telescope.

The project is divided into 3 parts:
1) A complete census of isophotal shapes of early–type galaxies brighter than $B_T = 13.5$ and with Type $T < -3$ in either the RC2 or Lauberts–Valentijn catalogue, which will allow a thorough analysis of the distribution of isophotal shapes with respect to luminosity, ellipticity and other photometric parameters. Also, radio and X measurements are already available for a large fraction of these objects.

2) The mapping of the warm interstellar medium of a subset of these galaxies, through narrow-band imaging, in order to study its physical state and its possible connection with the hot X-ray gas.
3) A detailed spectroscopic investigation of a subset of discy galaxies. The comparison between the angular momentum vector of the bulge and of the disc will allows to test whether disc stem form late accretion events (in which case no correlation between the angular momenta is expected)

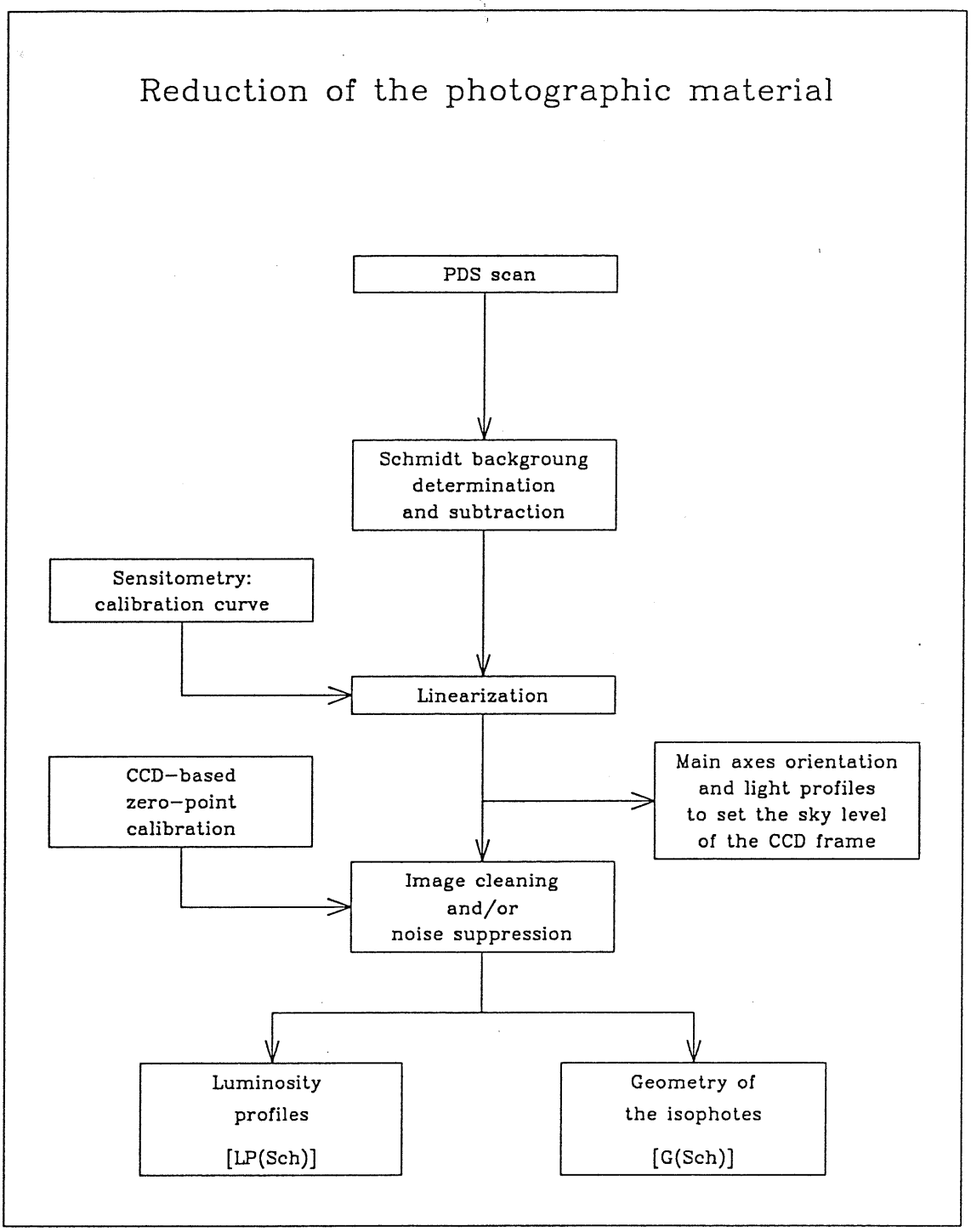

Figure 1.1: Block diagrams displaying the main steps in the reduction of the Schmidt and the CCD material, and in the subsequent astrophysical analysis of the combined data.

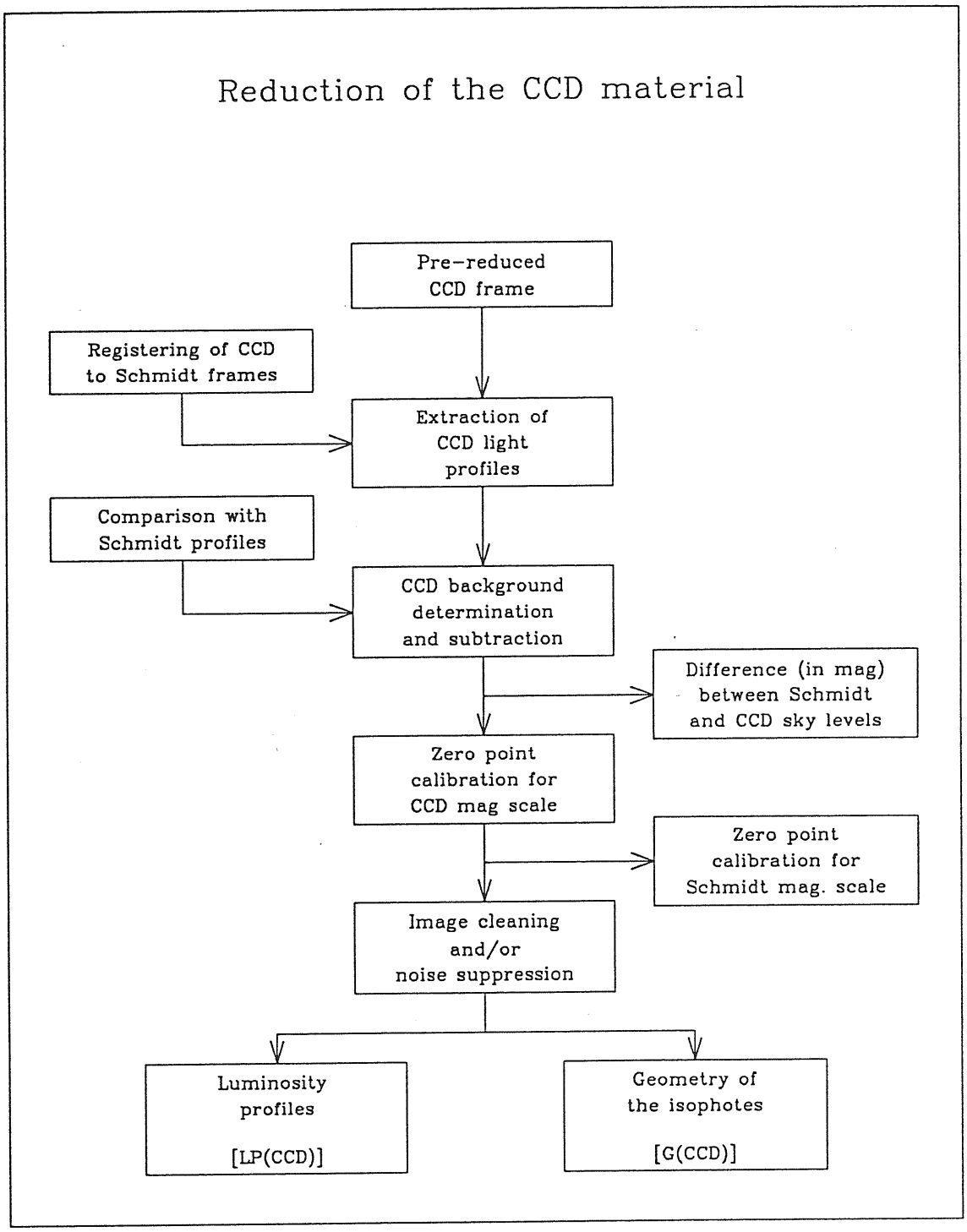

Figure 1.1: *Continued*

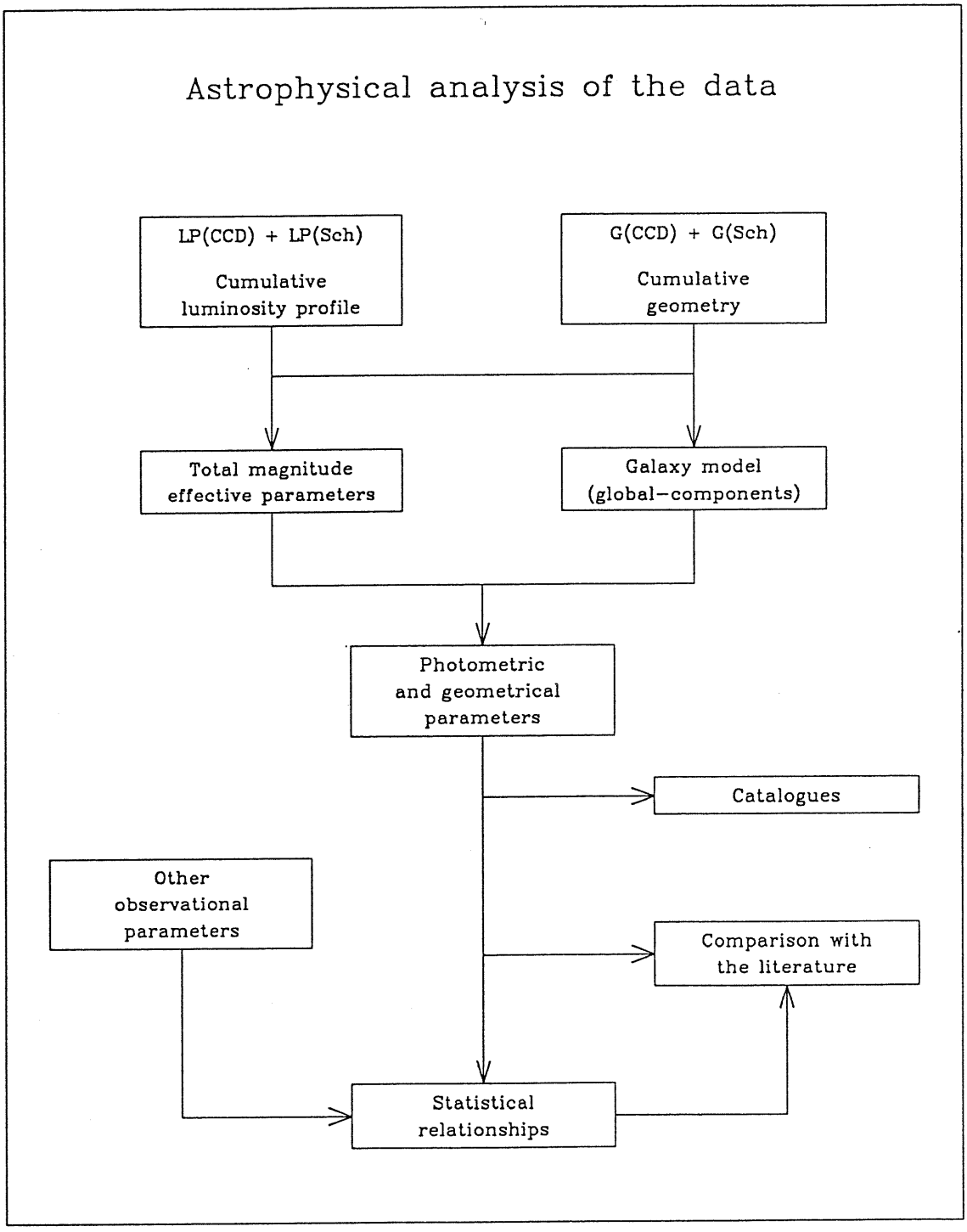

Figure 1.1: *Continued*

Chapter 2

B-band 'Global Mapping' Photometry of 47 Virgo and Fornax Galaxies

2.1 Introduction

The study of global properties of early-type galaxies has seen an impressive growth in recent years after the discovery that these systems populate a two dimensional manifold, named *Fundamental Plane* (FP), in the representative space of the global photometric and kinematical parameters (Dressler et al. 1987, Faber et al. 1987, Kormendy & Djorgovski 1989). In other words, among the observed or derived quantities for hot stellar systems, such as characteristic radius and corresponding surface brightness, luminosity, mass, mass-to-light ratio, velocity dispersion and metallicity, only two variables are independent, while all the other parameters can be expressed as a combination of these two.

However, on the observational side, the universality of the FP is still questioned with regard to zero-point, slope, thickness, and possible dependence on the environment.

In investigating the possible sources of such controversies, we realized that the galaxy samples used so far suffer from three main problems: 1) statistical completeness: samples are generally magnitude-limited, therefore biased toward intrinsically bright objects and not representative of the global galaxy population; 2) methodology: global parameters (such as luminosity, effective radius and surface brightness) are those obtained by fitting a $r^{1/4}$ law to a limited portion (that inside the CCD frame) of the galaxy light profile; 3) accuracy: light profiles are possibly distorted by uncertain background subtraction (a common problem in CCD photometry).

In order to bypass these problems, we have constructed a new database of *model-free* photometric parameters (including isophote shape descriptors) for a large and deep luminosity-limited sample of 80 early-type galaxies belonging to the Virgo and to the Fornax clusters. The photometry is based on the *global mapping* methodology (Capaccioli & Caon 1989): combining CCD images and large-field deep Schmidt plates, it provides a mapping at state of the art accuracy of the light distribution from the center down to $\mu_B = 28$ mag arcsec^{-2},

internal errors being less than 0.1 mag out to $\mu_B \sim 26$.

In this Chapter we present the results for 19 E and non-barred S0 galaxies belonging to the Virgo cluster, and for 28 E and non-barred S0 galaxies belonging to the Fornax cluster. They add to the data-set for the 33 galaxies studied with the same methodology by Caon, Capaccioli & Rampazzo (1990; hereinafter CCR). This Chapter is structured as follows. In Section 2.2, the galaxy sample, and the photographic and CCD material used in this work are presented. In Section 2.3, I describe the reduction and the analysis of the material, illustrating in details how CCD and photographic images are combined together. The original technique I devised in order to remove the column offset pattern present in one of the CCDs used is detailed in Appendix A. In Section 2.4, I perform the isophote shape analysis, and obtain the "model-independent" global photometric parameters of our galaxies. They are then compared with literature data, discussing the possible sources of the significant disagreement found for the brightest galaxies.

Final ellipticity, position angle and main axes light profiles of each galaxy are presented both in tabular and graphical form in Appendix B. There we also display the radial run of the main isophote shape descriptors, both for the galaxies of the present sample and for the 33 galaxies of CCR, who followed a different approach to derive the geometrical properties of their objects.

2.2 Observations

2.2.1 The Sample

The Fornax sample consists of all the E and non-barred S0 belonging to the Fornax Cluster galaxies and brighter than $B_T = 15.0$. Position, classification and photometric data were taken from the Fornax Cluster Catalogue (FCC; Ferguson 1989). The sample, 28 galaxies in total, does not include IC 1919 (for which the CCD presents an odd marked gradient) and FCC 338 (which has a very irregular aspect). Scanning the literature on the cosmic distance scale, we found that the Fornax cluster is placed from about 0.1 mag nearer to 0.1 mag farther than Virgo, depending on the particular distance indicator used (see the review by Jacoby et al. 1992). Here we adopt for Fornax the same distance modulus as Virgo: $(m - M) = 31.3$ (18.3 Mpc), after Capaccioli et al. (1990a).

The Virgo sample consists of 19 early–type galaxies mostly placed in the southern part of the Virgo cluster. The membership to the Virgo cluster is well established for 7 of them, for 11 is uncertain, while one galaxy (NGC 4360) is probably a background object. Data about these galaxies were taken from the Virgo Cluster Catalogue (Binggeli, Sandage & Tammann 1985). These galaxies, together with the 33 Virgo galaxies already studied by CCR, are all the E and non barred S0 galaxies brighter than $M_B \simeq -17.3$ placed in the Virgo area covered by our Schmidt plates. We notice that this sample is 80% complete if we consider the whole cluster; the missing objects are situated in the outskirts of the cluster, for which we do not have CCD and photographic material.

Table 2.1 lists all the relevant information on the present galaxies.

2.2.2 Photographic Material

The photographic material for the Fornax cluster consists of a sky-limited plate taken at the UK Schmidt telescope, plus a sky-limited plate taken at the ESO Schmidt telescope for mapping those galaxies placed near one edge of the UK plate. For the Virgo cluster, 6 sky-limited ESO Schmidt plates were utilized. The relevant data on the plates are listed in Table 2.2

The plates were digitized with the PDS 1010A microdensitometer of the Padova Astronomy Department. The area of each scan was chosen large enough to ensure a reliable modelling of the blank-sky surrounding each galaxy therein contained. The slit size was fixed to 50 x 50 μm (3.35 arcsec), while the stepping size was set to 35 μm (2.35 arcsec). The PDS frames were aligned with the plate edges, taken as indicative of the absolute astronomical orientation.

The digital scans were reduced by means of the 'Interactive Numerical Mapping Package' (Barbon, Benacchio & Capaccioli 1976; Capaccioli 1989a), adapted to work on our VAX-VMS system by Fasano (1990). Usually a plane or a second degree surface was sufficient to model the sky background surrounding relatively isolated galaxies, while higher degree polynomials were used in case of galaxies close to other objects of comparable luminosity or size.

We tested the reliability of the background subtraction by means of simulations. We created artificial images containing an $r^{1/4}$ galaxy plus several stars and smaller galaxies superposed on a background represented as a 2-D polynomial with degree varying from 1 to 5; noise was then added to the resulting image to reproduce the typical signal-to-noise ratio of our plates. The images were then reduced as described before, and the fitted polynomial was compared to the input one. We found that the maximum difference inside the region occupied by the galaxy of interest was always less than 0.2% density units: such a difference produces an error on the measured galaxian intensity which is less than 0.1 mag down to 4 mag below the sky level.

The calibration curves were built as the logarithm of the opacitance $\omega = 10^{D-D_{fog}} - 1$ (de Vaucouleurs 1968) versus the logarithm of the relative intensity of the sensitometric spots. The curves were fitted by a 3rd degree polynomial. The density frames were then linearized by the formula:

$$J(x,y) = \frac{I_{gal}(x,y)}{I_{sky}(x,y)} = \frac{\mathrm{dex}\,\{P\,[\log\omega(x,y)]\}}{\mathrm{dex}\,\{P\,[\log\omega_{sky}(x,y)]\}} - 1$$

where $P\,[\log\omega]$ is the calibration curve, ω_{sky} is the background opacitance provided by the polynomial model, and J is the specific intensity in the galaxy normalized to the intensity of the night sky.

We also tested how the uncertainty on the fitting of the calibration curve turns into errors in the measured galaxian light distribution. We performed several fits of the calibration curve, varying the fog value, using a different degree of the polynomial, or attaching a different weight to the datapoints. We found that, for all the fits that we judged acceptable, the relative errors

Table 2.1: The sample

Ident.	R.A. (1950)	DEC	Type	B_T	Code
		Virgo cluster			
NGC 4215	12 13 21.6	06 40 48	S0(9)	13.12	?
NGC 4255	12 16 23.4	05 03 48	S0(6)	13.61	?
NGC 4261	12 16 50.4	06 06 12	E2	11.31	?
NGC 4268	12 17 14.4	05 33 42	S0(6)	13.73	?
NGC 4269	12 17 15.6	06 17 48	S0(2)	13.69	?
NGC 4270	12 17 16.8	05 44 30	S0(6)	13.11	?
NGC 4281	12 17 48.6	05 39 54	S0(6)	12.27	?
NGC 4339	12 21 01.8	06 21 36	S0(0)	12.32	?
NGC 4342	12 21 06.6	07 19 54	S0(7)	13.54	?
NGC 4360	12 21 49.8	09 34 12	E2	13.47	B
NGC 4365	12 21 55.8	07 35 42	E3	10.51	M
NGC 4370	12 22 22.8	07 43 18	S0(6)	13.69	M
NGC 4377	12 22 40.8	15 02 24	S0(3)	12.67	M
NGC 4472	12 27 14.4	08 16 42	E2/S0(2)	9.31	M
NGC 4526	12 31 30.6	07 58 30	S0(6)	10.61	M
NGC 4570	12 34 21.0	07 31 24	S0(7)/E7	11.82	M
NGC 4600	12 37 49.8	03 23 30	S0(6),N	13.47	?
NGC 4623	12 39 38.4	07 57 06	E7	13.22	M
NGC 4636	12 40 17.4	02 57 42	E1/S0(1)	10.48	?
		Fornax cluster			
FCC 019*	03 20 28.5	−37 34 25	dS0(8),N	15.2	
FCC 021 = NGC 1316	03 20 47.6	−37 23 10	S0 pec	9.4	
FCC 047 = NGC 1336	03 24 35.9	−35 53 10	E4	13.3	
FCC 055*	03 25 20.3	−34 41 52	S0(9),N	13.9	
FCC 063 = NGC 1339	03 26 06.1	−32 27 26	E4	12.7	
FCC 083 = NGC 1351	03 28 38.3	−35 01 26	E5	12.3	
FCC 090*	03 29 13.4	−36 27 29	E4 pec	15.0	
FCC 119*	03 31 35.6	−33 44 19	S0 pec	15.0	
FCC 136*	03 32 34.1	−35 42 39	dE2,N	14.8	
FCC 143 = NGC 1373*	03 33 03.3	−35 20 06	E3	14.3	
FCC 147 = NGC 1374	03 33 21.1	−35 23 29	E0	11.9	
FCC 148 = NGC 1375	03 33 21.2	−35 25 51	S0	13.6	
FCC 152	03 33 33.7	−32 37 39	S0/a pec	14.1	
FCC 161 = NGC 1379	03 34 08.7	−35 36 22	E0	11.7	
FCC 167 = NGC 1380	03 34 31.6	−35 08 22	S0/a	11.3	
FCC 170 = NGC 1381	03 34 36.2	−35 27 34	S0(9)	13.0	
FCC 177 = NGC 1380A	03 34 51.2	−34 54 07	S0(9)	13.2	
FCC 202 = NGC 1396*	03 36 11.4	−35 36 03	d:E6,N	15.3	
FCC 204*	03 36 15.4	−33 17 16	dS0(8),N	14.9	

Table 2.1: *continued*

Ident	R.A. (1950)	DEC	Type	B_T	Code
FCC 213 = NGC 1399	03 36 34.2	−35 36 46	E0	10.6	
FCC 219 = NGC 1404	03 36 57.4	−35 45 20	E2	10.9	
FCC 249 = NGC 1419	03 38 50.3	−37 40 09	E0	13.6	
FCC 255	03 39 06.4	−33 56 13	S0(6),N	13.7	
FCC 276 = NGC 1427	03 40 24.6	−35 33 06	E4	11.8	
FCC 277 = NGC 1428	03 40 27.7	−35 18 40	E5	13.8	
FCC 301*	03 43 10.1	−36 07 37	E4	14.2	
FCC 324*	03 46 00.3	−36 37 23	dS0(8)	15.3	
FCC 335*	03 48 43.8	−36 03 29	E	14.2	

Notes to the Table:
Column 1: the asterisk marks the galaxies for which only CCD images were used;
columns 4 and 5: morphological type and total apparent blue magnitude from Binggeli et al. (1985) for the Virgo galaxies; from Ferguson (1989) for the Fornax galaxies;
column 6: membership to the Virgo Cluster, from Binggeli et al. (1985): M=member, ?=uncertain, B=background.

Table 2.2: The Schmidt plates

Plate	emulsion + filter	Center		exp. time
		R.A.	DEC.	
UK J14646	IIIa-J + GG 395	03 36	−25 32	80 min
ESO 8780A	IIaO + GG 385	03 28	−36 50	90 min
ESO 7949A	IIaO + GG 385	12 23	11 30	75 min
ESO 8049A	IIaO + GG 385	12 23	13 05	75 min
ESO 8450A	IIaO + GG 385	12 38	3 31	60 min
ESO 8461A	IIaO + GG 385	12 39	7 57	60 min
ESO 8464A	IIaO + GG 385	12 28	8 18	60 min
ESO 8014A	IIaO + GG 385	12 20	6 25	75 min

Notes to the Table:
The scale of the UK Schmidt plate plate is 67.1 arcsec/mm, the scale of the ESO plates 67.5 arcsec/mm.

in I_{gal}/I_{sky} were lower than 0.05 mag for $\mu_{gal} - \mu_{sky} > 0$. Notice that, while the errors on the measured galaxian signal due to an inaccurate background subtraction increase as the galaxy intensity decreases, errors coming from the fit of the calibration curve follow the opposite trend, becoming smaller as I_{gal}/I_{sky} decreases.

We did not scan the photographic images of the smallest and faintest objects in the Fornax cluster. In fact, in these cases the CCD field of view is relatively large enough to allow a reliable measure of the sky background level on the borders of the frame.

2.2.3 CCD Material

Most of the Virgo and Fornax galaxies were observed at the Cassegrain focus of the ESO 1.5m Danish telescope (scale 15.″43 mm^{-1}, pixel size 0.″463, field 2.′4 × 3.′95) during two different runs, in October 1990 and in February 1991. Six of the Virgo galaxies were observed at the 2.3m telescope of the Steward Observatory, at Kitt Peak, Arizona (pixel size 0.″3, field 1.′9 × 2.′0), in January 1991. Exposure times ranged from a few minutes for the brightest galaxies up to 25 minutes for the faintest ones. Most of the night were photometric, with seeing varying between 1.1 and 2.2 arcsec (see Table 2.3). Pre-reduction (bias and dark current subtraction, field-flatting) was performed using IRAF, the Image Reduction and Analysis Facility developed at the National Optical Astronomy Observatories. One of the CCD used (CCD #15 at the ESO 1.5 Danish telescope) was affected by rather strong column offsets. A special treatment had to be devised in order to remove effectively this pattern; a detailed description of all the steps involved in this task can be found in Appendix A.

No attempt has been made to improve the resolution of our CCD images. The reason is that none of the global parameters that we aim to measure depend on the actual resolution of our images: in fact, the main redistribution of the energy, due to instrumental and seeing convolution, takes place within galactocentric distances which are significantly smaller than the effective sizes of our objects. In Table 2.3 we list the full width half maximum (FWHM) of the single gaussian functions best-fitting the profiles of stars present in our CCD frames, and the major axis radii r_L and corresponding surface brightness values μ_L at which the effects of the seeing convolution on the light profiles become < 5%. These figures were computed with our data using numerical simulations by Peletier et al. (1990; see their Fig. 3). We shall notice that for all of our galaxies, r_L is much smaller than the effective radius (Table 2.5).

2.3 Data Reduction and Analysis

2.3.1 Coupling CCD and Photographic Images

Light profiles along the principal axes and along the two directions at 45° from them, of both CCD frames and photographic scans, were computed by averaging with a *k-clipping* algorithm 21 centered cross-sections spanning an opening angle of 5 degrees. For the most flattened galaxies, the opening angle for the major axis was reduced in order to keep the differences between the 0° cross-section and each of those tilted within a given limit (0.01 mag at 3 effective radii).

Table 2.3: The seeing convolution

Ident.	FWHM	r_L	μ_L	Ident.	FWHM	r_L	μ_L
NGC 4215	1″.70	2″.3	18.8	NGC 4255	1″.10	1″.5	18.5
NGC 4261	1″.12	1″.8	18.0	NGC 4268	1″.29	1″.6	18.9
NGC 4269	1″.25	2″.5	19.7	NGC 4270	1″.20	1″.6	18.7
NGC 4281	1″.22	1″.5	18.5	NGC 4339	1″.18	2″.4	19.2
NGC 4342	1″.27	1″.6	17.6	NGC 4360	1″.29	1″.9	19.4
NGC 4365	1″.34	1″.7	17.8	NGC 4370	1″.82	2″.6	21.5
NGC 4377	1″.71	4″.0	19.4	NGC 4472	1″.34	2″.5	17.7
NGC 4526	1″.92	2″.4	18.0	NGC 4570	1″.90	2″.3	17.9
NGC 4600	1″.87	2″.4	20.3	NGC 4623	1″.62	2″.0	19.5
NGC 4636	1″.09	2″.2	18.5				
FCC 019	1″.54	2″.0	22.1	FCC 055	1″.57	2″.0	20.4
FCC 090	1″.29	3″.3	21.1	FCC 119	1″.31	2″.9	21.8
FCC 136	1″.24	2″.4	21.7	FCC 152	1″.61	2″.3	20.6
FCC 204	1″.62	1″.8	21.3	FCC 255	1″.77	2″.2	20.2
FCC 301	1″.43	1″.8	19.4	FCC 324	1″.25	1″.9	22.8
FCC 335	1″.38	1″.7	21.1	NGC 1316	1″.66	3″.3	17.5
NGC 1336	1″.68	2″.3	20.0	NGC 1339	2″.14	3″.6	19.3
NGC 1351	2″.05	3″.2	19.1	NGC 1373	1″.55	1″.7	19.4
NGC 1374	1″.70	3″.2	18.9	NGC 1375	1″.78	2″.2	19.3
NGC 1379	1″.62	3″.5	19.4	NGC 1380	2″.06	2″.6	18.4
NGC 1380A	1″.84	2″.3	20.0	NGC 1381	1″.35	1″.8	18.1
NGC 1396	1″.10	1″.4	21.3	NGC 1399	1″.84	2″.7	17.9
NGC 1404	2″.20	4″.0	18.1	NGC 1419	1″.74	4″.4	20.3
NGC 1427	1″.65	2″.6	18.6	NGC 1428	1″.58	2″.4	19.9

Notes to the Table:

r_L and μ_L are the major axis radius and surface brightness where seeing effects on light profile become smaller that 5%.

In order to improve the signal-to-noise ratio (S/N) in the outskirts of our galaxies, we have smoothed both CCD and photographic images by the 'adaptive filter' described in Richter et al. (1993). Its most important characteristic is the capability of smoothing significantly the low S/N outer regions without altering the light distribution in the higher-gradient inner ones and without smearing the stellar-like images. Having verified that the filtered light profiles (in both CCD and photographic images) are identical to the unfiltered ones in their inner part, we retained only the filtered profiles.

The major axis position angle P.A. has been computed as follows: if the position angle profile has a regular behavior, the average value of the P.A. measurements is taken, excluding the inner few arcsec (affected by seeing convolution) and the very outer isophotes (where spurious values can be produced by a non-perfect field-flatting and by the poor S/N); if the P.A. profile shows two distinct components, the P.A. corresponding to the outer one is chosen.

CCD and photographic images were reduced to the same orientation using common stars, whenever possible, or the position angle profiles; usually, an accuracy of a few tenths of degree

is achieved.

The determination of the background level in CCD images, I_{sky}^{CCD}, is chosen as the one which provides the best matching of the narrow field CCD photometry to the wide field photographic photometry in the interval $22.5 \lesssim \mu_B \lesssim 24.5$, where the deep photographs are not saturated (as they are inwards), and the CCD images still have a good enough S/N ratio. We assume that I_{sky} is constant over both the whole CCD frame and the photographic scan; since in the CCD and photographic images the normalized galaxy signal must differ only for a multiplicative factor (related to the different sky brightness and atmospheric extinction in the two images), it is

$$\frac{I_{rel}^{CCD}(r)}{I_{rel}^{SCH}(r)} = \frac{I_{sky}^{SCH}}{I_{gal}^{SCH}(r)} \times \frac{I_{gal}^{CCD}(r)}{I_{sky}^{CCD}} = \frac{I_{sky}^{SCH}}{I_{sky}^{CCD}} = const, \tag{2.1}$$

where $I_{rel}(r)$ is the galaxian light profile normalized to the sky background. The above formula can be rewritten in logarithmic scale, to obtain:

$$-2.5\left(\log I_{sky}^{CCD}(r) - \log I_{sky}^{SCH}(r)\right) = \Delta m_{sky} = \mu_{sky}^{SCH} - \mu_{sky}^{CCD} = const, \tag{2.2}$$

The matching is then performed by searching for the I_{sky}^{CCD} for which the slope a of the linear fit of the residuals:

$$\log I_{rel}^{CCD}(r) - \log I_{rel}^{SCH}(r) = A\,r + B \tag{2.3}$$

is zero.

The final value for the CCD sky level and for the difference of the sky level between CCD and photographic images was taken as the mean of the determinations for each of the eight cross-sections. In a few cases, one of the cross-sections gave discrepant results and was disregarded. The 1-σ uncertainty about the mean value is typically less than 1% for I_{sky}^{CCD}, and less than 0.07 mag for Δm_{sky}. We wish to remark here that the uncertainty on I_{sky}^{CCD} is not significantly better than that achieved by other common methods of measuring the sky-background directly on CCD images (at least for objects not completely filling the frame; see for instance Peletier et al. 1990). What the 'global mapping' technique provides is the possibility of using the photographic profiles from where the uncertainty on the CCD blank-sky level begins to affect heavily the CCD light profiles.

2.3.2 Photometric Zero Point

As in CCR, the zero point of the photometric scale was established by matching the CCD centered growth-curves (i.e. the total luminosity $L(< R)$ within centered circular apertures as a function of the radius) to the photoelectric integrated magnitudes. The data from the compilations of Longo & de Vaucouleurs (1983, 1985) were supplemented with the measurements by Poulain (1988) and Poulain & Nieto (1993). No color correction was applied to CCD data. This fact has a negligible consequence on the zero point determination (less than 0.02 mag), as integrated (B-V) colors do not vary by more than 0.1 mag in the range of interest: ($R \lesssim 50''$), and the coefficient c_B in the color equation $B = b + c_B \times (B - V)$ for the

Table 2.4: Corrections to aperture photometry

Source	Corrections (mag)
Tif-69	$\delta m = 0.150\ (\log R - 1.00)$
Las-70	$\delta m = 0.060$
Svi-78	$\delta m = 0.036\ (\log R - 1.06)$
PFA-79	$\delta m = 0.064\ (\log R - 2.06)$
Mic-82	$\delta m = 0.260\ (\log R - 1.72)$
Pou-88	$\delta m = 0.078\ (\log R - 1.65)$
PoN-93	$\delta m = 0.093\ (\log R - 1.25)$

Notes to the Table:
Corrected values are obtained by adding the correction term to the original measurements.
Column 1: codes as in Longo & de Vaucouleurs (1983,1985), except PoN-93: Poulain & Nieto (1993)
Column 2: R is the aperture radius in arcsec.

combination filter-detector we used is lower than 0.15, as estimated in other observing runs with the same setup (see Saviane et al. 1993, in preparation).

As extensively discussed in Capaccioli & de Vaucouleurs (1983), photoelectric photometry is frequently subjected to systematic errors. We investigated the presence of such errors in our photoelectric data sources by analysing, for each source in turn, the residual differences between the photoelectric magnitudes and the corresponding quantities from the zero point adjusted growth curves. We found that in 7 cases the photoelectric data show a significant trend with the aperture radius, approximately linear in $\log R$ (Table 2.4, and example in Fig. 2.1). Photoelectric magnitudes have been corrected accordingly, and used for a second and final determination of zero points of our CCD images. Notice that all these data consistently indicate an increase of the residuals inwards, likely produced by the aperture off-centering bias (Capaccioli & de Vaucouleurs 1983).

The zero point of the photographic plate was determined by the formula: $\mu_{sky}^{SCH} = \mu_{sky}^{CCD} + \Delta m_{sky}$ (Equation 2.2). The mean values for the photographic sky background were then computed: $\langle \mu_{sky}^{SCH} \rangle = 22.08$ for the Fornax UK plate, 22.60 for the Fornax ESO plate, while the sky background for the ESO Virgo plates ranges from 22.04 to 22.25. The individual values of μ_{sky}^{SCH} for the objects of a same plate are found to vary within a remarkably small interval: in fact, for all of the plates containing more than 3 galaxies the 1-σ uncertainty on the mean sky level is lower than 0.04 mag. This figure indicates that likely no other sources of error affect our data, beyond the uncertainties associated to the photoelectric calibrators and to the determination of Δm_{sky}. For consistency reasons, and given the small difference with the individual determinations of μ_{sky}, we adopted the mean value $\langle \mu_{sky}^{SCH} \rangle$ for all galaxies in the UK plate and in the 8014A ESO plate.

In order to compute the zero point of CCD frames of galaxies lacking aperture photometry,

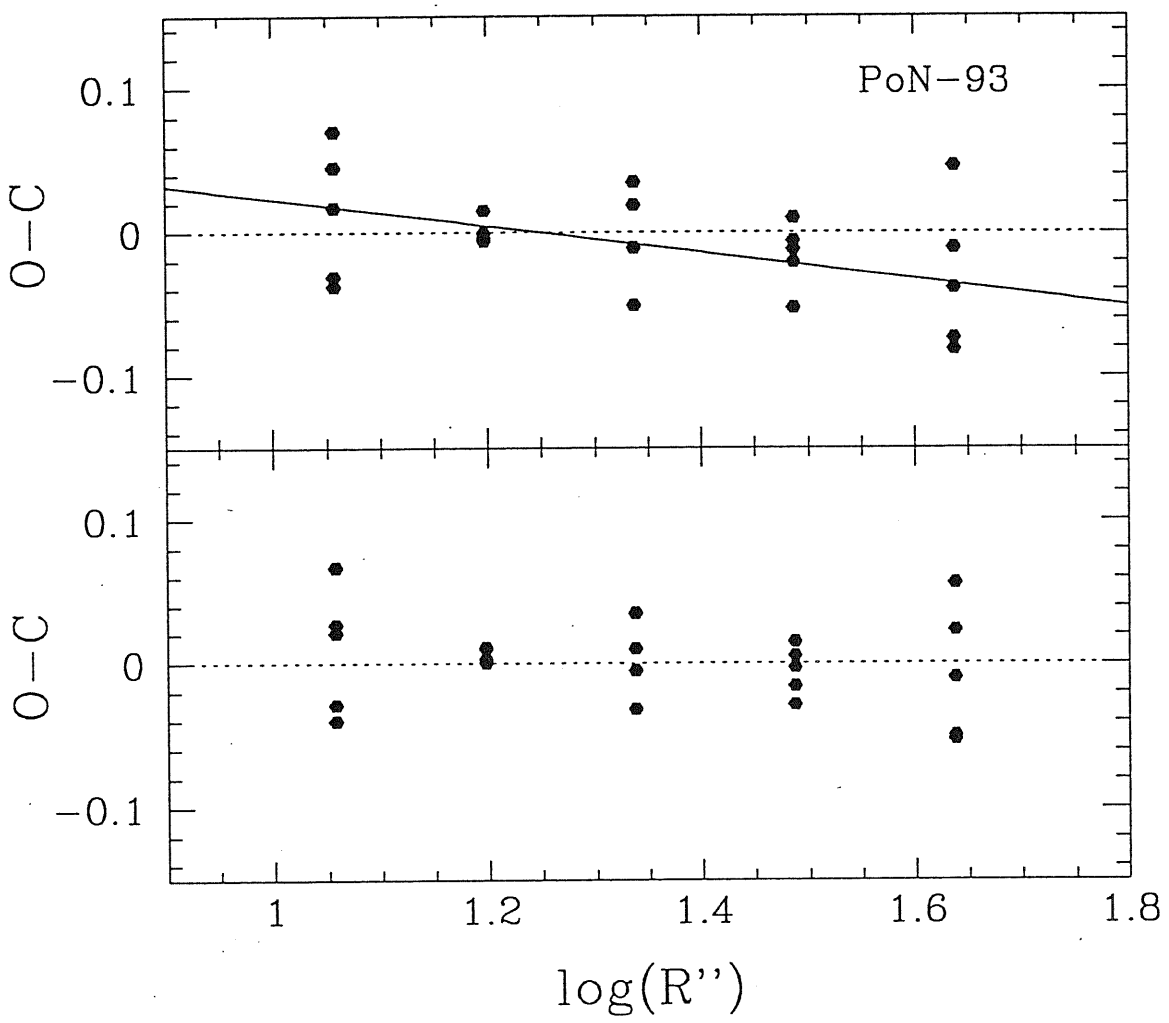

Figure 2.1: *Top*: The residuals between photoelectric magnitudes published by Poulain & Nieto and our calibrated CCD growth curves are plotted versus $\log R''$; the best-fit straight line is shown as a solid line. *Bottom*: The residuals after the correction of the photoelectric measurements.

we have used galaxies with zero point from photoelectric photometry as standard stars. We plotted μ_{sky}^{CCD} versus $-2.5 \log I_{sky}^{CCD}$, and fitted a straight line of slope 1 to the datapoints. This relation then allowed us to transform the sky counts measured on a given frames into the corresponding sky surface brightness, with an accuracy of about 0.05 mag (estimated as the rms of the above fit).

2.4 Results

2.4.1 Isophotal Analysis

The isophotal analysis has been performed on CCD frames, in order to measure the departures of the isophote from the elliptical shape. We also considered the sample of 33 early-type galaxies studied by CCR, for which the geometrical analysis was performed using a different approach, the 'bulge fitting' technique (see CCR). We remark here that isophotal analysis carried out on photographic scans can not provide, because of their intrinsic characteristic (undersampling in the intermediate regions, low signal-to-noise ratio in the outer ones), a detailed parameterization of the isophotal properties. For this reason, we performed the isophotal analysis on photographic images with the only purpose of extending farther out ellipticity and position angles profiles.

We used the algorithm described in Bender & Möllenhoff(1987), and kindly provided us by R. Bender. It uses a least-square ellipse fit, and measures the systematic deviations of the isophotes from pure ellipses by a Fourier expansion of the radial deviation, $\Delta r(E) = r_{isoph}(E) - r_{ell}$. Here r_{isoph} and r_{ell} are the radial coordinates of the actual isophote and of the best interpolating ellipse respectively, and E is the eccentric anomaly. The coefficients A_k and B_k of the Fourier expansion:

$$\Delta r(E) = \sum_{k=1}^{N} [A_k cos(kE) + B_k sin(kE)]$$

are usually normalized dividing them by the semimajor axis length. For each frame, interfering objects and defects were masked; the fitting program replaces these regions with their symmetric counterparts with respect to the galaxian center. Generally, 100 isophotes per galaxy are fitted, spaced in surface brightness by 0.1 mag. The output consists of surface brightness, ellipticity, position angle, and Fourier coefficients up to the 19th, as a function of the galactocentric radius. For sake of clarity, I will use the terms $\cos k$ and $\sin k$ to indicate the normalized Fourier coefficients A_k/a and B_k/a respectively (a is the semimajor axis length).

In order to improve the determination of the isophotal parameters in the outer regions, we carried out the isophotal analysis also on the 'adaptive filtered' images. Having verified that, similarly to the case of light profiles, the filter does not introduce any distortion in shape of the inner isophotes of our galaxies, (see example in Fig. 2.2), we decided to retain the results of the filtered images only.

We disregarded the data corresponding to isophotes for which the applied masking left less than 80% of the isophote contour: according to the simulations by Sparks et al. (1991), an incompleteness of 20% produces an uncertainty in the Fourier coefficient $\cos 4$ as large as 1% of the isophotal radius.

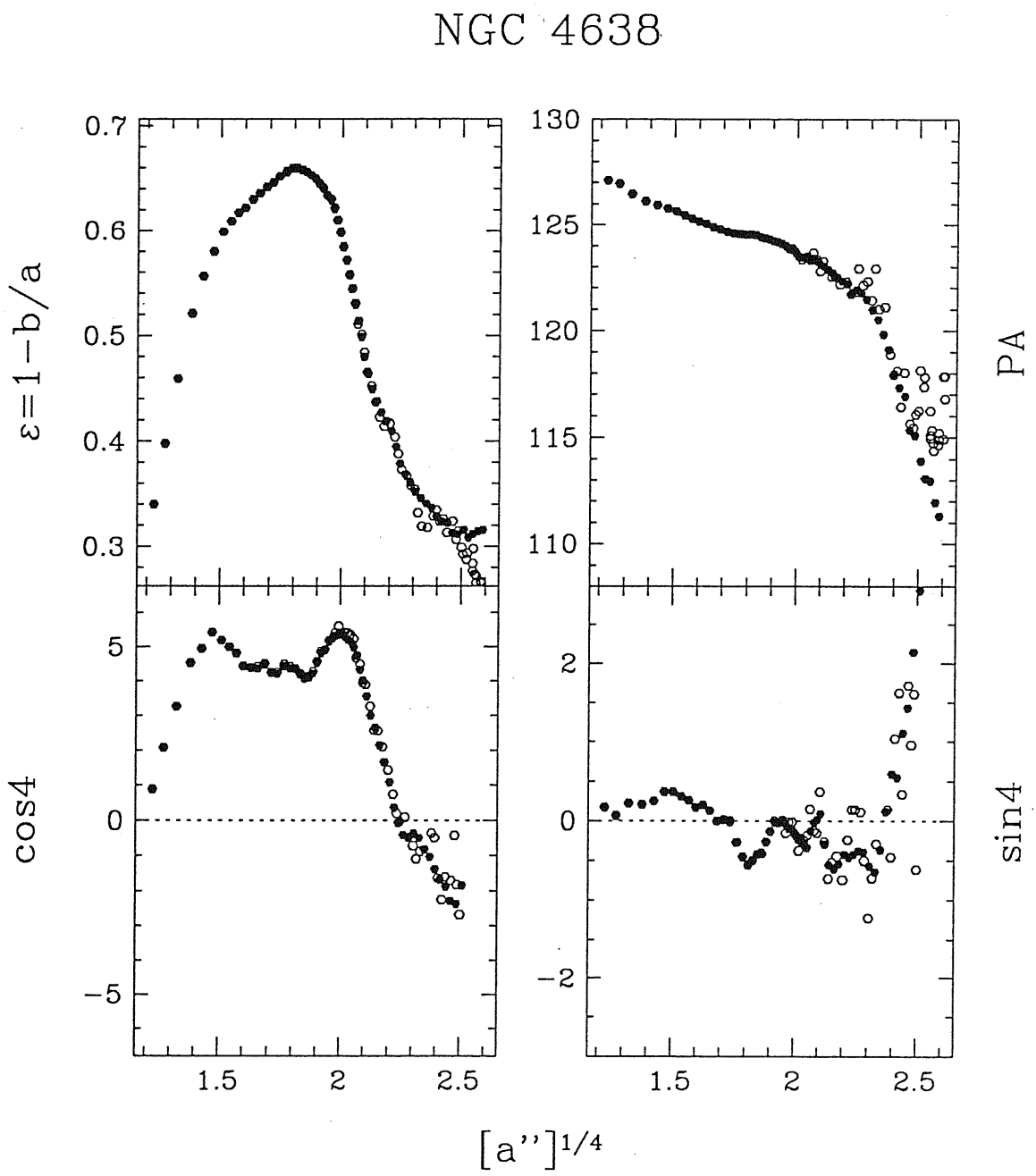

Figure 2.2: Comparison of the ellipticity, position angle, cos 4 and sin 4 (multiplied by 100) profiles computed on the unfiltered (*open dots*) and filtered (*filled dots*) images of NGC 4638. Notice that the two sets of points are coincident in the inner and intermediate regions, while in the outer regions the filtered image provides a more regular and stable behavior of the isophotal parameters.

2.4.2 Composite Profiles

Final ellipticity, orientation and light profiles were constructed by combining the inner CCD and the outer photographic data, leaving the maximum overlap allowed by the characteristics of the data.

No correction for scattered light of the nucleus into the outskirts is applied to the surface brightness values. According to Capaccioli (1987), the contamination of the galaxy light profile by light coming from the inner region of the galaxy increases systematically with radius until the latter becomes the dominant signal. The correction for such effect requires some *a priori* model of the true light distribution of the galaxy, and the accurate measure of the complete PSF profile. The latter task is impossible in the case of Schmidt plate, because stars have saturated cores and are heavily undersampled. Notice however that, when applied to the galaxy of our sample, the model by Capaccioli (1987) shows that the scattered light becomes important at light levels well below the limiting magnitude of our light profiles; furthermore, part of the scattered light is removed by the background subtraction in the Schmidt images.

A simple test on the uncertainty of our final measures of the galaxian light distribution can be performed by computing the absolute difference $|\Delta m_B|$ between the two opposite sides of the final light profiles. This quantity provides an upper limit of the cumulative accidental error, since it incorporates also the intrinsic differences between the two opposite sides of the galaxy. Fig. 2.3 shows that accidental errors in our set of data are likely lower than 0.1 mag out to $\mu_B \simeq 26$ B–mag arcsec^{-2}.

2.4.3 Global Parameters

Total magnitudes, as well as effective radii R_e and corresponding effective surface brightnesses $\mu_e = \mu(R_e)$, were computed from elliptical growth curves $G_e(a)$. Luminosity profiles along the main axes, and ellipticity and position angle profiles were used to built up a two dimensional model of each galaxy, which was integrated out to a fixed level $\mu_B = 32$ on the $r^{1/4}$ extrapolation of the outer luminosity profile, assuming that geometrical profiles stay constant outside the last measured isophote. The extrapolation term, that is the fraction of the galaxy luminosity outside the last surface brightness measurement, is generally lower than 0.15%.

We also computed, integrating the galaxy model within circular rather than elliptical annuli, the effective aperture A_e, that is the diameter of the circular region containing half the total luminosity, and R_n, the photometric parameter introduced by Dressler et al. (1987), defined as the radius of the circular region within which the mean surface brightness is $\langle \mu(< r) \rangle = 20.75$ B–mag arcsec^{-2}. The main source of errors on μ_e, R_e and A_e is the uncertainty δB_T on the computed total luminosity: in fact, a overestimation of the total galaxy luminosity turns into an effective isophote larger and fainter than the right one, while the contrary happens if L_T is underestimated. From an $r^{1/4}$ model with circular isophotes

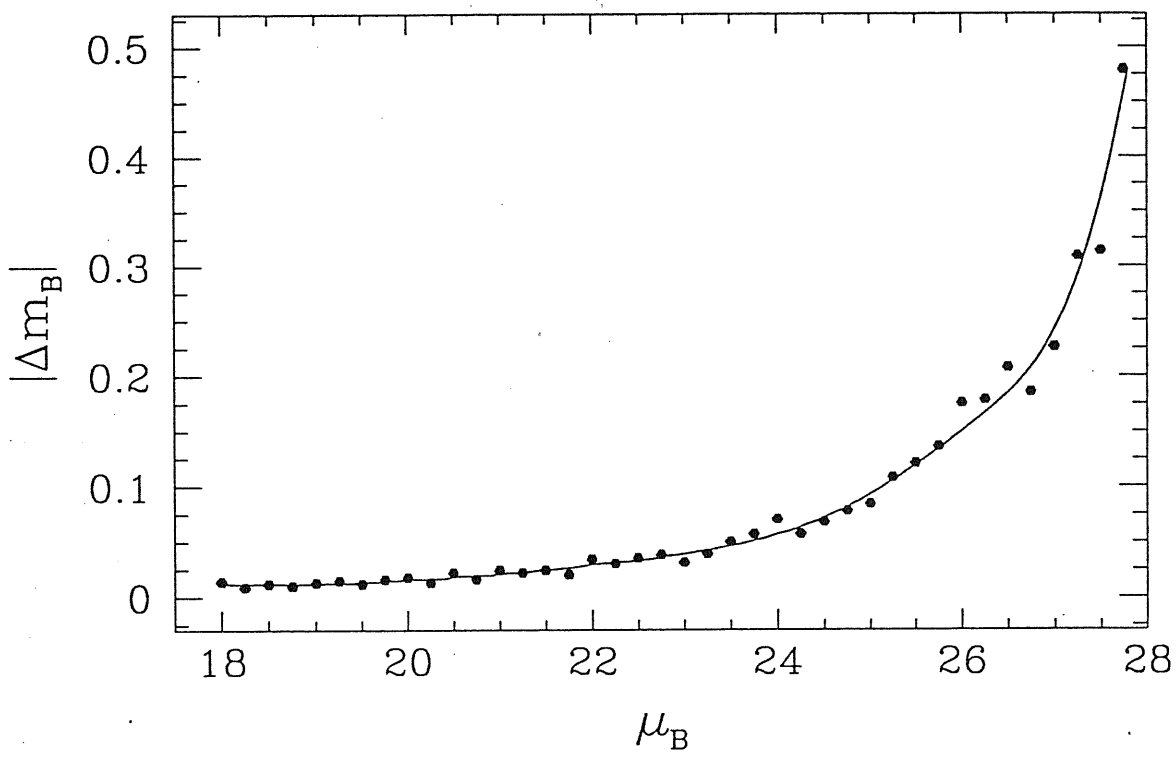

Figure 2.3: Median of the absolute difference between opposite cross-sections of the 47 Virgo and Fornax galaxies, plotted versus the corresponding surface brightness. The solid lines is the spline interpolation to the datapoints. The trend of $|\Delta m_B|$ is in close agreement with that presented in CCR, and recalls the trend of the internal (accidental) errors in surface photometry discussed by Capaccioli, Held & Nieto (1987) (see their Fig. 2).

we have computed the following relations:

$$\delta\mu_e = -3.8\delta B_T \qquad \delta \log R_e = 0.8\delta B_T \tag{2.4}$$

On the other hand, the error on R_n is due essentially to the uncertainty on the zero point calibration. Finally, the semimajor axis a_{25} and the semiminor axis b_{25} at the $\mu_B = 25$ standard isophote, and their ratio $R_{25} = a_{25}/b_{25}$ have been calculated in order to compare them with the literature data.

All these global parameters are listed in Table 2.5

2.4.4 External Comparisons

Our measurements of B_T, R_e, a_{25}, and R_{25} have been compared with the values published in the *Third Reference Catalogue of Bright Galaxies* (de Vaucouleurs et al. 1991; hereinafter RC3). Fig. 2.4 shows no systematic trend with the luminosity for the total magnitude residuals ΔB_T of galaxies fainter than $B_T = 11.0$: the mean difference is -0.003 with a dispersion

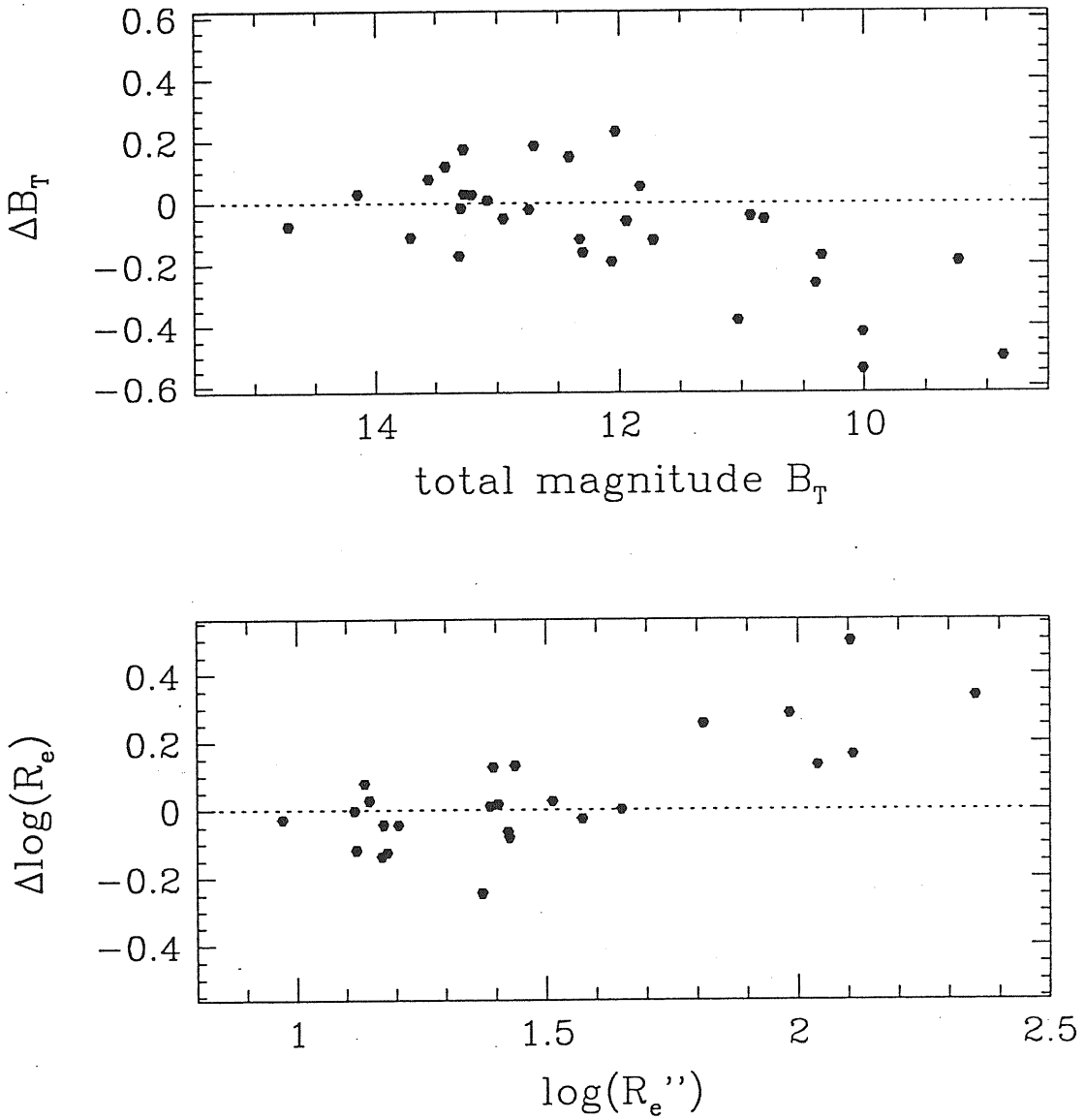

Figure 2.4: Comparison of our determinations of the total magnitude B_T (*top*) and effective radii R_e (*bottom*) with the RC3 values.

$\sigma_B = 0.11$. On the contrary, for object brighter than $B_T = 10.5$ our magnitudes are systematically and largely brighter than the RC3 values. Correspondingly, for the latter galaxies we measure significantly larger values of the effective radius, while the agreement is quite good for the other galaxies: the mean difference in $\log R_e$ is -0.02, with a dispersion $\sigma_{\log R_e} = 0.09$.

This large discrepancy for the most luminous galaxies has already been found by Capaccioli, Piotto & Rampazzo (1988) in a completely different set of objects, and in the 33 Virgo

early-type galaxies of CCR.

We notice that the excess in our measurement of total luminosity and effective radii can not be due to zero point errors, given the very good agreement among the individual values of the zero points of photographic images of galaxies belonging to the same plate, neither to a scale error, in that the photometric scale is the same for bright and faint galaxies and for the latter we do not have any problems in the comparison with the RC3 values. This conclusion is supported by the comparison between our data and RC3 values of the semimajor axis length and of the flattening at the $\mu_B = 25$ isophote (Fig. 2.5). Here no trend in the residuals is present, and the agreement with the RC3 values is quite satisfactory for both luminous and faint galaxies: $\langle \Delta \log a_{25} \rangle = 0.02$ with $\sigma_{\log a_{25}} = 0.06$, while $\langle \Delta \log R_{25} \rangle = 0.02$ with $\sigma_{\log R_{25}} = 0.07$.

We attribute the origin of the above discrepancy to the common practice of applying standard growth curves or fitting laws (*e.g* the $r^{1/4}$ function) to obtain integrated magnitudes of galaxies whose outer light distribution remain unknown (as in most CCD photometry and in photoelectric measurements of bright galaxies). A very deep photometric study, such as that provided by the 'global mapping' methodology, is necessary for such objects.

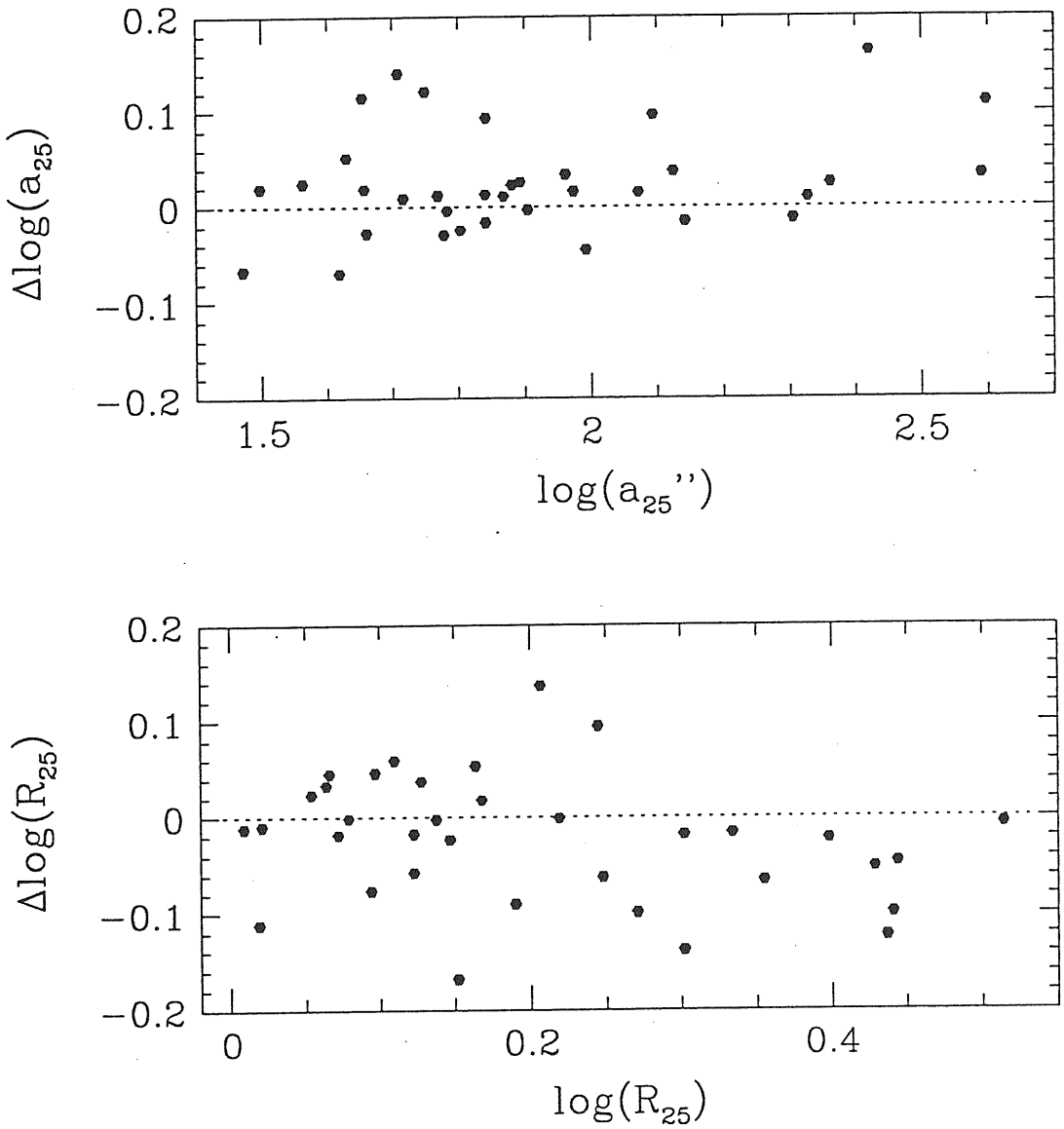

Figure 2.5: Logarithmic differences between our measurements and RC3 values for the semi-major axis length a_{25} (*top*) and flattening $R_{25} = a/b$ (*bottom*) of the standard isophote.

Table 2.5: Global parameters

Ident.	Type	B_T	ΔB_T	a_e	b_e	μ_e	ϵ_e	a_{25}	b_{25}	ϵ_{25}	R_n
NGC 4215	S0(9)	12.95	0.02	21.2	8.0	21.55	0.62	69.3	27.7	0.60	14.4
NGC 4255	S0(6)	13.60	0.06	13.4	7.5	21.79	0.44	42.5	22.8	0.46	11.5
NGC 4261	E2	11.03	0.21	70.8	59.8	23.45	0.16	133.2	106.5	0.20	27.5
NGC 4268	S0(6)	13.71	0.01	14.2	7.2	21.67	0.49	45.7	22.8	0.50	10.4
NGC 4269	S0(2)	13.32	0.29	30.5	25.0	24.01	0.18	45.0	36.3	0.19	10.0
NGC 4270	S0(6)	13.08	0.05	20.6	9.5	21.84	0.54	60.7	28.1	0.54	13.5
NGC 4281	S0(6)	12.06	0.09	36.7	16.7	22.22	0.54	94.0	53.1	0.43	19.9
NGC 4339	S0(0)	12.41	0.08	27.7	25.8	22.82	0.07	73.8	63.4	0.14	15.8
NGC 4342	S0(7)	13.07	0.04	8.1	3.0	19.59	0.63	37.4	20.4	0.45	17.3
NGC 4360	E2	13.42	0.08	23.1	19.2	23.49	0.17	45.3	37.8	0.17	8.7
NGC 4365	E3	10.35	0.12	109.9	84.1	23.73	0.23	201.8	146.7	0.27	36.2
NGC 4370	S0(6)	13.31	0.26	27.0	14.6	22.83	0.46	56.1	36.2	0.35	—
NGC 4377	S0(3)	12.74	0.02	14.0	12.2	21.61	0.13	52.0	44.1	0.15	17.7
NGC 4472	E2/S0(2)	8.87	0.20	256.9	197.5	24.07	0.23	396.6	295.2	0.26	65.9
NGC 4526	S0(6)	10.40	0.04	68.9	29.0	21.91	0.58	230.2	85.8	0.63	43.5
NGC 4570	S0(7)/E7	11.72	0.05	27.7	9.3	20.81	0.67	118.0	36.1	0.69	27.5
NGC 4600	S0(6),N	13.29	0.09	25.4	14.5	22.68	0.43	51.1	38.4	0.25	6.9
NGC 4623	E7	13.27	0.06	26.3	8.4	22.03	0.68	69.2	24.9	0.64	9.7
NGC 4636	E1/S0(1)	10.01	0.20	147.6	112.7	23.85	0.24	263.7	180.6	0.31	34.6
FCC 019	dS0(8),N	15.49	0.17	19.7	9.6	24.08	0.51	26.3	15.4	0.41	—
FCC 055	S0(9)	14.02	0.15	18.7	8.0	22.38	0.57	41.4	22.4	0.46	4.8
FCC 090	E4 pec	14.77	0.15	11.4	9.7	23.37	0.15	30.3	18.3	0.39	4.7
FCC 119	S0 pec	15.05	0.11	19.0	16.3	24.36	0.14	25.2	22.2	0.12	—
FCC 136	dE2,N	14.69	0.21	26.4	20.6	24.67	0.22	30.1	24.0	0.20	—
FCC 152	S0/a pec	14.08	0.20	20.5	11.8	23.09	0.42	43.9	25.8	0.41	4.8
FCC 204	dS0(8),N	15.00	0.16	22.5	8.4	23.58	0.63	33.1	14.9	0.55	—
FCC 255	S0(6),N	13.81	0.03	20.9	9.3	22.57	0.56	43.8	28.2	0.35	6.1
FCC 301	E4	14.13	0.02	13.3	8.1	22.60	0.39	31.3	26.9	0.14	7.6
FCC 324	dS0(8)	15.47	0.28	30.6	13.8	24.98	0.55	30.5	13.8	0.55	—
FCC 335	E	14.40	0.18	19.8	12.3	23.49	0.38	35.8	23.1	0.35	—
NGC 1316	S0 pec	9.23	0.10	132.2	90.5	22.91	0.31	390.1	222.0	0.43	70.1
NGC 1336	E4	13.27	0.07	30.8	22.9	23.62	0.26	60.0	40.8	0.32	8.0
NGC 1339	E4	12.70	0.02	15.7	11.1	21.49	0.29	58.7	44.3	0.25	17.8
NGC 1351	E5	12.30	0.04	33.7	22.3	22.92	0.34	91.4	55.1	0.40	16.9
NGC 1373	E3	14.15	0.06	11.1	8.5	22.38	0.23	29.6	28.3	0.04	7.7
NGC 1374	E0	11.94	0.02	26.6	24.2	22.30	0.09	78.2	74.5	0.05	22.1
NGC 1375	S0	13.21	0.06	24.0	9.3	22.08	0.61	63.5	28.1	0.56	11.0
NGC 1379	E0	12.03	0.02	23.9	23.3	22.01	0.03	75.9	74.3	0.02	21.3
NGC 1380	S0/a	10.82	0.08	52.4	26.6	21.90	0.49	138.6	97.6	0.30	38.1
NGC 1380A	S0(9)	13.29	0.02	32.4	7.1	21.96	0.78	69.4	25.1	0.64	7.4
NGC 1381	S0(9)	12.32	0.03	23.5	8.0	20.92	0.66	80.2	29.3	0.63	21.2
NGC 1396	d:E6,N	14.73	0.37	32.0	19.9	25.04	0.38	31.4	19.5	0.38	8.1
NGC 1399	E0	10.01	0.04	134.1	120.8	24.15	0.10	212.2	183.1	0.14	42.2
NGC 1404	E2	10.93	0.25	26.0	23.0	21.24	0.11	124.1	96.3	0.22	41.8
NGC 1419	E0	13.56	0.10	9.4	9.3	21.71	0.00	36.5	32.2	0.12	11.4
NGC 1427	E4	11.82	0.09	39.2	27.1	22.75	0.31	98.2	69.9	0.29	21.1
NGC 1428	E5	13.91	0.07	12.4	7.8	21.85	0.37	41.5	20.7	0.50	8.5

Chapter 3

Isophote Shapes and Galaxy Structure

3.1 Introduction

In the last years increasing evidence of a non trivial link between isophote shape and global or structural parameters of early-type galaxies has emerged. Bender et al. (1989a) were first to look systematically at the correlations between the deviation of isophotes from the perfect elliptical shape (either disc-like or *boxy*) and the global properties of E galaxies. They showed that the $\cos 4$ parameter, which is the most significant Fourier coefficient in the expansion of the isophote shape deviations, correlates quite well with the kinematical behavior, the optical luminosity, the X-ray and radio emission of the parent galaxies. On this empirical ground, isophotal properties, rather than just mere details of the galaxian structure, appear to be related to the processes of formation and evolution. They add to the information contained in the global-properties correlations, such as the Fundamental Plane and its variants (e.g. Djorgovski & Davis 1987; Bender, Burstein & Faber 1992), and the $(\log R_e, \mu_e)$ plane (Chapter 4). On the same empirical line goes the recent finding that the shape of the luminosity profile of early-type galaxies depends on the total luminosity L_B (or on the scale length R_e): the exponent n of a generalized de Vaucouleurs-like fitting-formula: $\mu = a + b * R^{1/n}$, correlates positively with L_B and with R_e as well (Chapter 5)

On the other hand, computer simulations of dissipationless collapse (Stiavelli, Londrillo & Messina 1991) and of merging processes (Governato, Reduzzi & Rampazzo 1993) have recently cast some doubts on the significance of the isophote shape descriptors: the final product do appear discy or boxy according to the viewing angle. Furthermore, Ryden (1991) has shown that a single galaxy model may exhibit different ellipticity and twisting profiles according to the angle of view.

In conclusion, the issue of the significance of the isophote shape descriptors is unclear. Governato et al. (1993) claim that the correlations found by Bender et al. (1989a) become significantly weaker (or even disappear) when new recent data are added and a more careful statistical analysis of the available data-sets is made.

For a clarification of all this matter, much can be done from the observational point of

view, in particular enlarging the sample of galaxies for which all the relevant measurements are available. Here, we analyse the isophotal data for our luminosity-limited sample of 80 early-type galaxies in the Virgo and Fornax clusters, for which the relevant global photometric quantities (such as total luminosity and model-independent effective parameters), together with the isophote shape descriptors, have been measured in Chapter 2. Having observed practically all E and non-barred S0 galaxies of the two clusters with $B_T \lesssim 14.0$ mag, there is a subset of our sample (65 objects) which is luminosity-limited with cutoff at $M_B \simeq -17.3$.

A more comprehensive investigation will be provided by the Key-Programme (KP) which is being carried out at the European Southern Observatory (Bender et al. 1989b). The KP data-set will consist in the detailed description of isophote shapes of about 300 early-type galaxies brighter than $B_T = 13.5$, complemented by the study of the interstellar medium for a subset of objects and of the detailed internal kinematics of selected discy galaxies.

This Chapter is organized as follows. In Section 3.2 I comment briefly on our sample and, after summarizing the isophote fitting procedure, I describe the parameterization of the isophote properties. Section 3.3 is devoted to the presentation and discussion of some relationships between the various geometrical and photometric parameters.

The present Chapter should be intended as a preliminary account of the results so far obtained; a more detailed and thorough analysis of the isophotal data and of their relationships with global properties, with the aim of investigating whether isophote shapes are really linked to the physical structure of galaxies or are instead mere morphological details, is in progress.

3.2 The Data

The Virgo cluster sample consists of the 33 E and S0 galaxies in the Virgo cluster studied by CCR, and of 19 early-type galaxies belonging to the Southern part of the cluster (Chapter 2). Together, they form a volume and luminosity-limited sample, with a cutoff at $B_T = 14$, or $M_B = -17.3$ assuming a Virgo distance modulus $(m - M) = 31.3$, after Capaccioli et al. (1990a). The Fornax cluster sample consists of the 28 non-barred early-type galaxies belonging to the Fornax cluster and brighter than $B_T = 15$ (Chapter 2).

Assuming for Fornax the same distance as for Virgo (which could be in error by at most 5-10%; see Jacoby et al. 1992), we selected all the Virgo and Fornax galaxies brighter than $M_B = -17.3$, thus forming a final homogeneous luminosity-limited 'Virgo+Fornax' sample of 65 galaxies.

The isophote analysis has been performed only on the CCD frames of our images. We used the fitting program described in Bender & Möllenhoff(1987). Systematic deviations of the isophotes from pure ellipses are measured by the Fourier expansion of the radial deviation, $\Delta r(E) = r_{isoph}(E) - r_{ell}$, where r_{isoph} and r_{ell} are the radial coordinates of the actual isophote and the best interpolating ellipse respectively, and E is the eccentric anomaly. The output consists of surface brightness, ellipticity, position angle, and of the normalized Fourier coefficients (up to the 20th), as a function of the galactocentric radius (see Chapter 2 for details).

In order to improve the determination of the isophotal parameters in the outer regions, we have smoothed the CCD images by the adaptive filter described in Richter et al. (1993). Since the filter does not introduce any distortion in shape of the inner isophotes of our galaxies, we retained the results of the filtered images only.

Isophotes with threefold symmetry have non-zero sin 3 and cos 3 terms. The sin 4 and cos 4 coefficients describe shapes with fourfold symmetry. The presence of a stellar disc along the major axis, i.e. excess light on this axis, is indicated by a positive cos 4 term; on the contrary, 'boxy' isophotes with their corners at 45° to the major and minor axis give negative cos 4 terms. The most important coefficient is then cos 4, which discriminate between boxy and discy isophotes, and seems to be intimately related to the physical structure of the galaxy. It should be added here that the radial run of the cos 4 coefficient can not be used alone to measure the importance of the disc relative to the spheroidal component, as it is insufficient to disentangle the effect of the inclination from that of the disc-to-bulge ratio. In other words, the same cos 4 profile can be obtained from a faint disc seen edge-on as well as from a substantially brighter disc but seen more face-on (Rix & White 1990). Scorza (1993) shows that central surface brightness and scale length of the disc influence mainly the amplitude and the profile of cos 4 while the inclination predominantly affects the cos 6 coefficient, and partly cos 4. Both coefficients must be used to determine the disc parameters.

For each galaxy we have extracted, from the plots presented in Appendix B, the relevant global isophotal parameters, as detailed below. Looking at the galaxy images helped in case of doubts or suspects of the presence of some substructure. Also, in handling our data, we have taken into account the fact that the measurements in the very inner region are affected both by the seeing convolution (and possibly inaccurate guiding) and by the inadequacy of the Fourier fitting program to cope with the small number of pixels on which isophotes are sampled, while measurements in the outer regions where the signal is a fraction of the sky background can be affected by small errors in the field-flatting and by the poor signal-to-noise ratio. The isophotal parameters are listed in Table 3.1

- *Isophotal classification.* Galaxies have been grouped into seven classes, according to the radial behavior of the cos 4 coefficient:

  1. discy (Discy): $\cos 4 > 0.005$ over a significant radial range;
  2. pure elliptical (Ell): cos 4 stays close to 0 (that is within ± 0.005) over the entire radial range;
  3. boxy (Boxy): $\cos 4 < -0.005$ over a significant radial range;
  4. inner boxy, outer discy (B→D): cos 4 increases from negative to positive;
  5. inner discy, outer boxy (D→B): cos 4 decreases from positive to negative;
  6. boxy, discy, boxy (BDB), or discy, boxy, discy (DBD): cos 4 changes sign twice;
  7. irregulars (Irr), if the radial run of cos 4 is too noisy to allow a reliable classification, or if cos 4 as well as the other Fourier coefficients display an irregular behavior.

Table 3.1: Isophotal parameters of Virgo and Fornax galaxies

Ident.	Type	B_T	ε_{max}	$F(\varepsilon)$	cos 4 max	cos 4 min	cos 6 peak	Class	Twist
IC 3468	E1,N	13.63	0.26	Dec	1.0	–	–	Disky	18
IC 3540	S0(2)	14.69	0.18	Irr	–	–	–	Ell	25
IC 3653	E3	14.43	0.14	Dec	–	–	–	Ell	5
IC 3773	d:S0(9)	13.84	0.62	Inc	2.4	–	1.2	Disky	2
NGC 4168	E2	12.22	0.16	Max	2.0	–	–	Disky	2
NGC 4200	S0(4)	13.96	0.42	Inc	–	–	–	Irr	2
NGC 4215	S0(9)	13.12	0.72	Max	14.0	–	10.0	Disky	1
NGC 4255	S0(6)	13.61	0.53	Max	2.2	–	–	Disky	11
NGC 4261	E2	11.31	0.27	Dec	–	−1.8	0.5	Boxy	4
NGC 4268	S0(6)	13.73	0.58	Max	2.2	−1.6	0.8	B→D	10
NGC 4269	S0(2)	13.69	0.23	Max	–	–	–	Ell	15
NGC 4270	S0(6)	13.11	0.61	Max	1.0	−4.0	−1.2	DBD	10
NGC 4281	S0(6)	12.27	0.55	Max	2.0	–	–	Disky	2
NGC 4339	S0(0)	12.32	0.11	Irr	–	–	–	Ell	22
NGC 4342	S0(7)	13.54	0.66	Max	3.6	–	−1.0	Disky	3
NGC 4352	S0(8)	13.43	0.64	Max	2.7	–	1.1	Disky	4
NGC 4360	E2	13.47	0.18	Max	0.8	−0.4	0.6	DBD	17
NGC 4365	E3	10.51	0.26	Irr	–	−1.2	0.7	Boxy	6
NGC 4370	S0(6)	13.69	0.39	Irr	–	–	–	Ell	5
NGC 4374	E1	9.71	0.25	Dec	–	−0.5	0.5	Boxy	3
NGC 4377	S0(3)	12.67	0.21	Irr	1.5	–	−0.6	Disky	25
NGC 4387	E5	13.08	0.42	Max	–	−1.7	–	Boxy	4
NGC 4406	S0(3)/E3	9.63	0.25	Inc	–	−1.0	–	Boxy	11
NGC 4415	d:E1,N	13.58	0.15	Irr	–	–	–	Ell	11
NGC 4417	S0(7)	11.78	0.71	Inc	5.5	−1.1	2.4	Disky	3
NGC 4431	dS0(5),N	13.86	0.51	Max	1.0	−1.0	–	BDB	14
NGC 4434	E0/S0(0)	13.07	0.09	Irr	–	–	–	Ell	32
NGC 4436	dE6/dS0,N	14.01	0.60	Max	1.5	–	1.0	Disky	1
NGC 4452	S0(9)	12.22	0.90	Max	12.5	–	4.5	Disky	4
NGC 4458	E1	12.93	0.15	Dec	–	–	–	Ell	24
NGC 4459	S0(2)	11.26	0.21	Inc	–	–	–	Ell	15
NGC 4464	E3	13.46	0.27	Max	1.1	–	–	Disky	6
NGC 4472	E2/S0(2)	9.31	0.18	Inc	–	−0.5	–	Boxy	6
NGC 4473	E5	11.02	0.47	Inc	1.0	–	–	Disky	1
NGC 4474	S0(8)	12.33	0.60	Max	9.0	–	4.0	Disky	1
NGC 4476	S0(5)	13.01	0.45	Dec	1.0	−1.1	–	D→B	4
NGC 4478	E2	12.36	0.19	Irr	–	−1.2	–	Boxy	20
NGC 4486	E0	9.47	0.09	Inc	–	–	–	Ell	40
NGC 4526	S0(6)	10.61	0.52	Inc	2.3	−3.0	2.2	B→D	5
NGC 4550	E7/S0(7)	12.64	0.70	Inc	2.5	–	0.9	Disky	4
NGC 4551	E2	13.06	0.29	Max	–	−1.0	–	Boxy	7
NGC 4552	S0(0)	10.38	0.11	Inc	–	−1.0	–	Boxy	10
NGC 4564	E6	12.02	0.59	Max	2.4	–	–	Disky	2
NGC 4570	S0(7)/E7	11.82	0.75	Inc	5.0	–	1.2	Disky	3
NGC 4578	S0(4)	12.48	0.32	Inc	–	–	–	Ell	2

Table 3.1: *continued*

Ident.	Type	B_T	ε_{max}	$F(\varepsilon)$	cos 4 max	cos 4 min	cos 6 peak	Class	Twist
NGC 4600	S0(6),N	13.47	0.44	Max	2.0	–	1.3	Disky	14
NGC 4621	E4	10.30	0.38	Inc	2.2	–	0.7	Disky	1
NGC 4623	E7	13.22	0.69	Inc	3.4	–	1.0	Disky	2
NGC 4636	E1/S0(1)	10.48	0.24	Inc	–	–	–	Ell	24
NGC 4638	S0(7)	11.99	0.66	Max	5.5	−2.0	2.3	Disky	16
NGC 4649	S0(2)	9.56	0.21	Inc	–	−0.7	–	Boxy	8
NGC 4660	E3/S0(3)	12.03	0.46	Max	3.5	–	−1.0	Disky	9
FCC 019	dS0(8),N	15.49	0.68	Max	2.9	−2.2	–	D→B	22
FCC 055	S0(9),N	14.02	0.63	Max	6.9	–	2.4	Disky	2
FCC 090	E4 pec	14.77	0.44	Min	2.6	−3.0	–	Irr	55
FCC 119	S0 pec	15.05	0.15	Irr	2.5	–	1.3	Disky	18
FCC 136	dE2,N	14.69	0.26	Max	1.9	–	–	Disky	10
FCC 152	S0/a pec	14.08	0.44	Max	–	−1.0	–	Boxy	13
FCC 204	dS0(8),N	15.00	0.65	Max	3.0	–	–	Disky	3
FCC 255	S0(6)N	13.81	0.63	Max	2.6	–	1.1	Disky	4
FCC 301	E4	14.13	0.49	Dec	1.0	−1.7	–	D→B	15
FCC 324	dS0(8)	15.47	0.60	Max	–	−2.2	−1.2	Boxy	6
FCC 335	E	14.40	0.62	Dec	1.2	–	–	Disky	12
NGC 1316	S0 pec	9.23	0.43	Max	1.0	−3.7	2.0	D→B	19
NGC 1336	E4	13.27	0.36	Inc	1.7	−1.4	1.1	D→B	12
NGC 1339	E4	12.70	0.31	Max	1.1	–	–	Disky	6
NGC 1351	E5	12.30	0.38	Inc	1.1	–	–	Disky	2
NGC 1373	E3	14.15	0.26	Irr	2.1	–	–	Disky	55
NGC 1374	E0	11.94	0.12	Irr	–	–	−0.8	Ell	7
NGC 1375	S0	13.21	0.61	Inc	–	−4.0	2.1	Boxy	4
NGC 1379	E0	12.03	0.04	Irr	–	–	–	Ell	50
NGC 1380	S0/a	10.82	0.57	Max	5.7	–	2.2	Disky	4
NGC 1380A	S0(9)	13.29	0.83	Max	17.5	–	8.8	Disky	2
NGC 1381	S0(9)	12.32	0.76	Max	15.5	–	8.2	Disky	2
NGC 1396	dE6,N	14.73	0.39	Inc	–	−1.4	−2.7	Boxy	4
NGC 1399	E0	10.01	0.13	Max	1.0	–	0.9	Disky	17
NGC 1404	E2	10.93	0.15	Irr	–	–	−0.8	Ell	15
NGC 1419	E0	13.56	0.18	Min	–	–	–	Ell	110
NGC 1427	E4	11.82	0.34	Inc	–	−0.9	–	Boxy	5
NGC 1428	E5	13.91	0.51	Max	1.1	−2.1	1.3	BDB	3

Notes to the Table:

Type: morphological classification from the Virgo Fornax Catalogue (Binggeli et al. 1985) and from Ferguson (1989) for the Fornax galaxies;
B_T: blue total magnitudes from CCR and from Chapter 2;
F(ε): shape of the ellipticity curve, coded as explained in the text;
Class: isophote shape classification, coded as in the text;
cos 4 and cos 6: their values have been multiplied by 100;
Twist: maximum excursion of the position angle of the major axis.

- *Peak values of* $\cos 4$. It is defined only for pure discy (positive value) and pure boxy (negative value) galaxies.
- *Maximum ellipticity.* It has been measured from the ellipticity curve, taking care of excluding those regions where ellipticity variations are likely to be produced by either seeing or the poor signal-to-noise ratio.
- *Shape of the ellipticity curve.* The radial run of ε has been classified into five groups:

  Inc: flattening increases monotonically with radius out to the last measured isophote;

  Max: flattening increases to a maximum, then decreases outwards;

  Irr: flattening is roughly constant or displays an irregular behavior;

  Dec: flattening decreases steadily with radius;

  Min: flattening presents a minimum at intermediate radii.

  In the following Section, we shall include the two galaxies belonging to the last group inside the class of monotonically increasing ellipticities.
- *Twist angle.* It is computed as the maximum excursion in the position angle of the major axis, excluding the inner few arcsec and also the very outer isophotes in those cases where the PA measurements are suspected to be affected by inaccurate field-flatting or by the poor S/N ratio.

3.3 Results and Discussion

Fig. 3.1 shows the Luminosity Functions of the four isophotal classes. Here we have grouped together in the 'irregular' class galaxies showing irregular trends of the Fourier coefficients and galaxies in which both discy and boxy isophotes coexist.

Boxy galaxies are preferably found in the bright end of the LF, while there is a small percentage at low luminosity. As pointed out by Nieto & Bender (1989), boxiness in luminous ellipticals has a different physical interpretation than that in faint ones: while the former probably due their appearance to merging processes, the latter are thought to be the result of strong tidal torques of a nearby massive galaxy. On the contrary, discy galaxies, which are the most numerous group, populate the faint end of the LF. A similar characteristic is shown by galaxies with a more complex or irregular isophote shape behavior. Galaxies with negligible deviations of the isophotes from perfect ellipses exhibit a LF slightly but steadily increasing towards fainter magnitudes. In total, we have 45% discy galaxies, 18% boxy, 20% ellipticals and 17% with other types of isophote behaviors.

At variance with previous studies, showing that E and S0 galaxies both in the field and in the Virgo cluster have bell-shaped LFs (see Fig. 1 in Binggeli, Sandage & Tammann 1988), the cumulative Luminosity Function of our luminosity-limited 'Virgo+Fornax' sample exhibits a bimodal distribution, with a secondary bump at very high luminosities, centered at $M_B \simeq -21.2$. This reflects the fact that the total luminosities of our brightest objects are

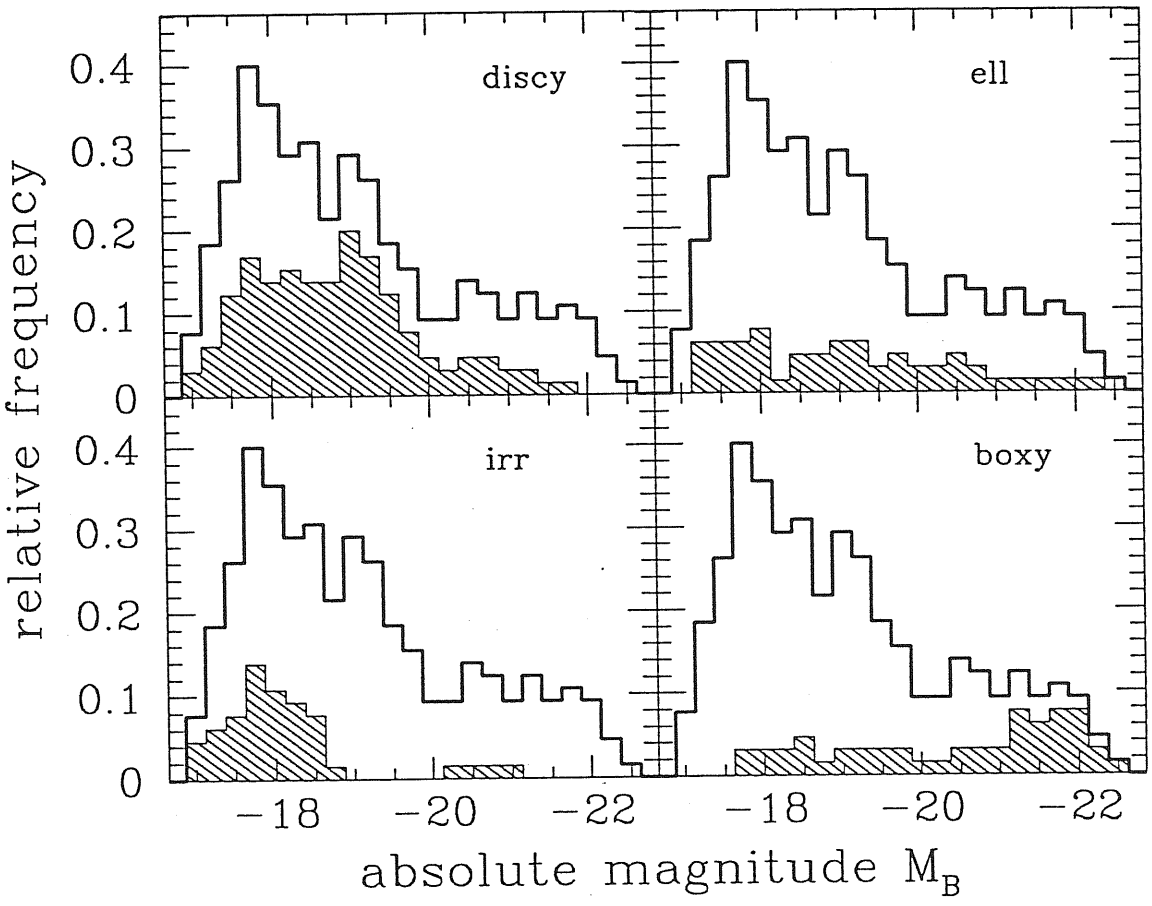

Figure 3.1: The Luminosity Functions of the four isophotal classes. The solid line is the global LF of our sample. Data are smoothed by a running window 1.0-mag wide, moved in steps of 0.25 mag. The 'irr' class comprises galaxies showing irregular behaviors of the isophotal parameters and galaxies in which both boxy and discy isopothes coexist.

systematically in excess (up to 0.5 mag) over the literature values, as discussed in Chapter 2. Notice also that the secondary bump in our LF is formed mostly by boxy galaxies.

Fig. 3.2 displays the maximum ellipticity of galaxies divided according to their isophote classification. We note that all galaxies flatter than $\varepsilon_{max} = 0.45$ are either discy or belong to the 'irregular' group; pure elliptical and pure boxy galaxies are only found for $\varepsilon_{max} < 0.45$. As the detectability of isophotal distortions depends strongly on the inclination of the galaxies, both for discy (Rix & White 1990) and boxy (Ryden 1992) shapes, it is suggested that galaxies with elliptical isophotes are boxy or discy objects where the isophotal distortions remain undetected because of an unfavourable angle of view. The lack of boxy galaxies flatter than $\varepsilon_{max} = 0.45$ may indicate that boxy objects are intrinsically rounder than discy ones. Notice also that, within the discy class, object rounder than $\varepsilon_{max} = 0.5$ are mostly classified E or intermediate type, while those flatter than this value are mostly S0s, as is

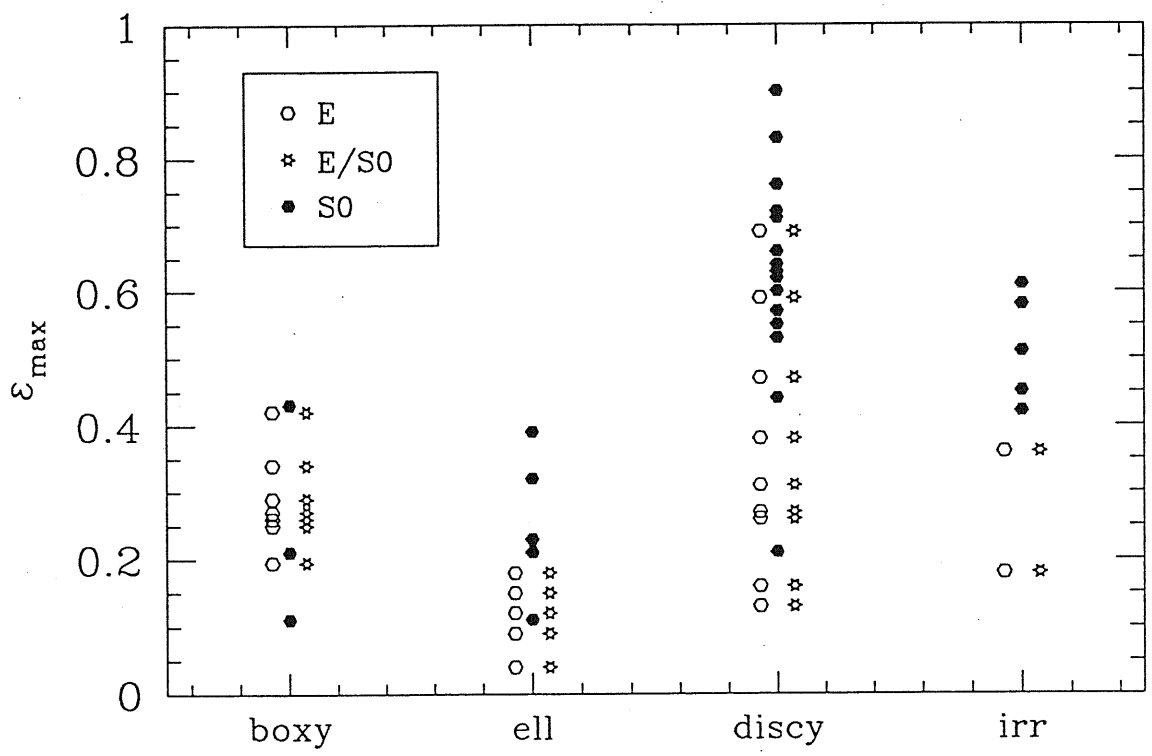

Figure 3.2: The peak value of the ellipticity curve is plotted versus the isophotal classification. The morphological classification is marked by using different symbols.

expected from the considerations on the detectability of discs as a function of the galaxy inclination (cf. Capaccioli, Caon & Rampazzo 1990).

About 75% of the galaxies in our sample have an ellipticity profile that increases with radius until either it reaches a maximum or until the last measured isophote. These behaviors are not limited to flattened objects, but also to nearly round ones, and indicate that the luminosity distribution is intrinsically more flattened at intermediate radii. A more informative plot is that of $\cos 4$ as a function of the shape of the ellipticity profile (Fig. 3.3). We can see that discy galaxies with $\cos 4 > 2$ all present a maximum at intermediate radii or have steadily increasing ellipticity curves; they are also among the most flattened objects. This figure can be interpreted in terms of the local projected disc-to-bulge ratio: in the inner and outer regions the bulge light dominates over the disc, while at intermediate radii the opposite holds. The maximum is reached at the location of the maximum value of the local projected disc-to-bulge ratio. In some cases, the disc is so bright or so large that its light dominates over the bulge light at least out to the last measured isophote, producing the observed increasing flattening over the whole radial range.

Fig. 3.4 shows the maximum ellipticity as a function of the total absolute magnitude. It

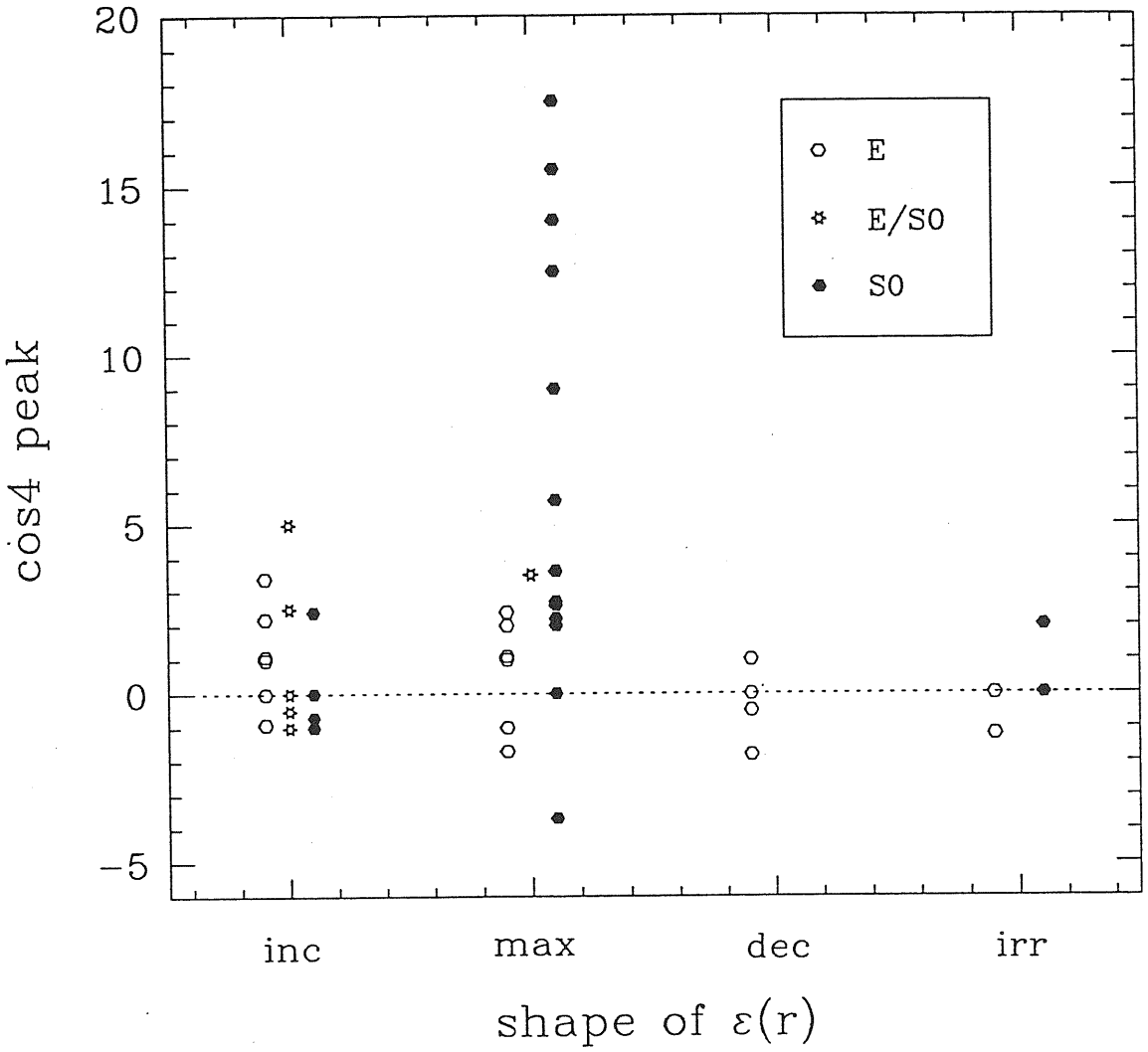

Figure 3.3: The peak value of the cos 4 Fourier coefficient is plotted for the four ellipticity curve classes.

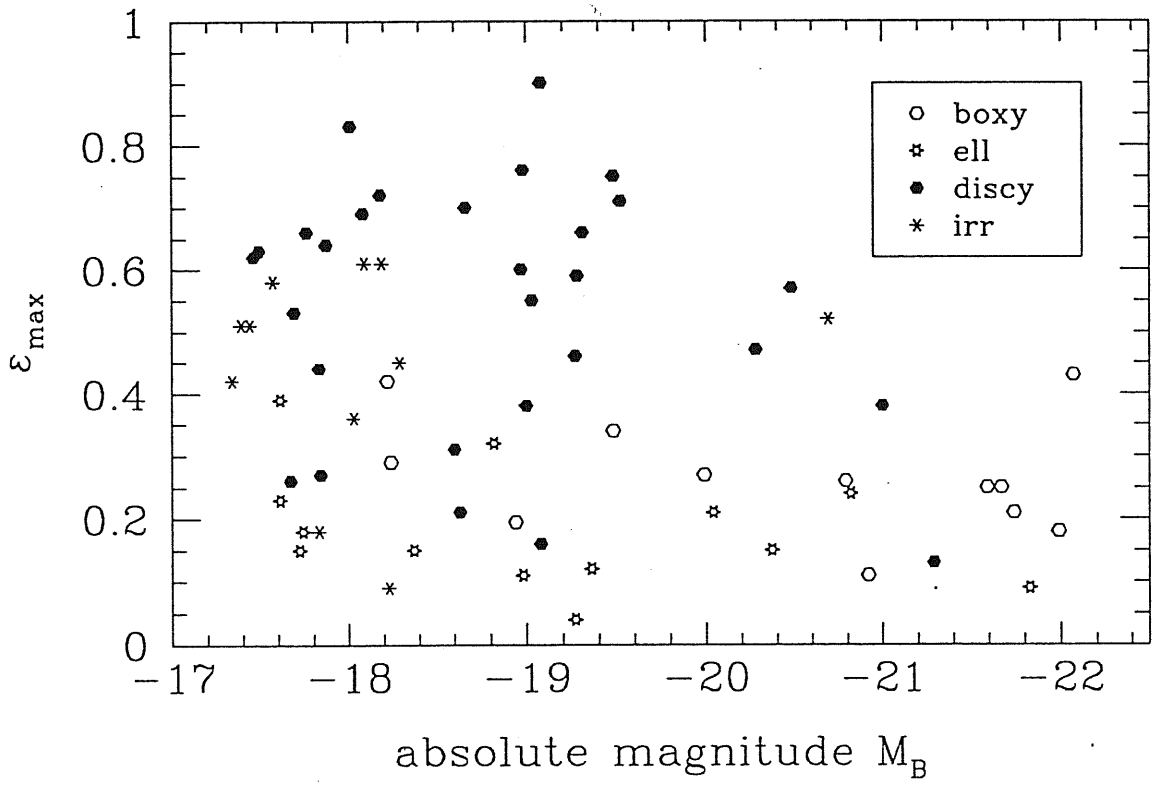

Figure 3.4: The maximum value of the ellipticity curve plotted versus the total absolute magnitude.

is remarkable that in the luminosity interval $-22.0 \lesssim M_B \lesssim -19.0$ the upper envelope of the ε_{max} distribution is roughly a straight line, with a flattening which increases towards fainter luminosities. This holds true even considering only disc galaxies or only boxy and elliptical galaxies, although with a weaker trend. This suggests that the maximum intrinsic flattening of galaxies is a decreasing function of the luminosity. Notice also that in the faint part of the diagram, $M_B \gtrsim -19.5$, the number of discy object overwhelms that of the other types for $\varepsilon_{max} > 0.4$, while the opposite happens for $\varepsilon_{max} < 0.4$.

In Fig. 3.5 the variation in position angle is plotted versus the maximum ellipticity. In analysing this figure, we should exclude those points at $\varepsilon_{max} < 0.05$ (dotted line), where the position angle measurements are affected by large uncertainties due to the roundness of the isophotes. It is evident that the range of the values of Δ P.A. increases with decreasing ε_{max}; this trend is more marked for galaxies with boxy or elliptical isophotes than for discy galaxies. The geometrical structures commonly invoked to explain isophote twists in galaxies without stellar discs are essentially two: those having isodensity surface which are rotationally symmetric figures tilted with respect to one another, and those in which isodensity structures are triaxial with common principal axes and ellipticities varying with radius (see for instance

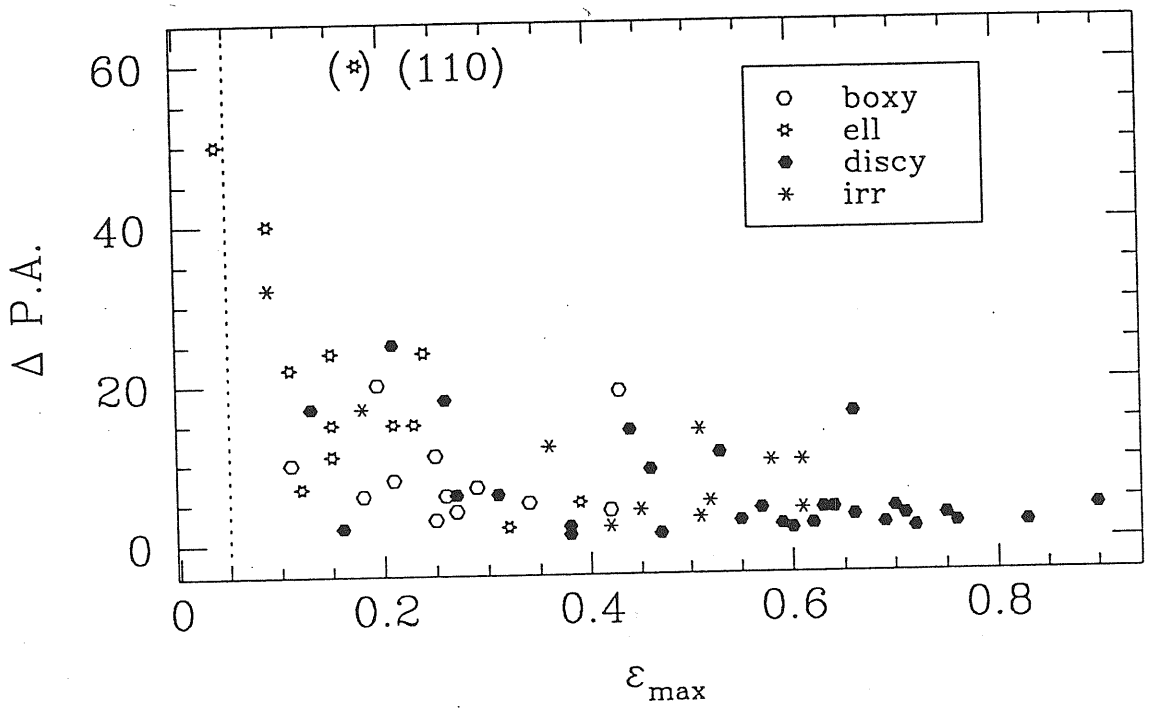

Figure 3.5: The twisting angle plotted against the peak of the ellipticity curve. Different isophotal classifications are coded by using different symbols. For more clarity, the upper limit on Δ P.A. has been set to 65: the point at $PA = 110$ is shown in brackets. The vertical dotted line is drawn at $\varepsilon_{max} = 0.05$.

Capaccioli et al. 1990c). Whatever is the cause of the variation in position angle in early-type galaxies, we expect that the prominent but structureless stellar discs of discy galaxies stabilize the position angle, that is keep Δ P.A. small.

However, we shall notice that some discy objects in the range $0.4 < \varepsilon_{max} < 0.7$ have a non negligible flattening. This can be explained as due to the presence of a small bar not recognized in the image of the galaxy, or as due to the combination of two axisymmetric components having slightly different principal planes, as suggested by Michard & Marchal (1990; see also Bertola, Vietri & Zeilinger 1990); alternatively, the twist can be produced by a stellar disc which is mildly warped, similarly to the well-known warps of gaseous discs.

Chapter 4

The $(\log R_e, \mu_e)$ plane of Hot Galaxian Components

4.1 Introduction

The long debated question of how many physical parameters are necessary to describe elliptical galaxies (Brosche 1973) has found an answer in the last years only. At first, observations seemed to indicate that E galaxies and spheroidal components (bulges) form a uniparametric family, i.e. all global parameters are correlated among themselves. For instance, the fact that the central velocity dispersions, σ_c, were found to depend on the total luminosities, L_T, was translated into a law, named after Faber & Jackson (1976): $L_T \propto {\sigma_c}^{\alpha}$. Also, the photometric scale parameters, such as the effective radius R_e and the corresponding surface brightness μ_e, were found to be mutually dependent (Kormendy 1977a).

These results were questioned by several authors. Terlevich et al. (1981) showed that the residuals from the Faber-Jackson relation correlate with the metallicity indicator Mg_2, while de Vaucouleurs & Olson (1982) stated that the same residuals depend on the mean surface brightness. Both studies brought up the case of the existence of a second (hidden) parameter. Along this line, benefiting from a large sample of early-type galaxies with photometric and kinematical data, Djorgovski & Davis (1987 = DD87) showed that galaxies populate a thin plane in the 3-D space, named 'Fundamental Plane' (FP). Among the observed or derived quantities for such systems, such as characteristic radius and corresponding surface brightness, luminosity, mass, mass-to-light ratio, velocity dispersion, and metallicity, there are only two independent variables which support most of the variance. All the other parameters can be expressed as a combination of these two (Dressler et al. 1987, Faber et al. 1987, Kormendy & Djorgovski 1989), which are, for instance, the effective (equivalent) radius R_e and surface brightness $\mu_e = \mu(R_e)$, i.e. the parameters pertaining to the isophote encompassing half the total luminosity.

The thickness of the plane is fully accounted for by observational errors, and the position of each galaxy above or below the plane is independent of any of the shape parameters such as flattening profile, isophote twisting, velocity anisotropy and detailed radial run of the light profiles. In this view, the Faber-Jackson and μ_e-R_e relations are projections of the FP onto

coordinate planes.

The above results are of importance in what the existence of a FP shows that the structural properties of galaxies span a narrower range than expected from models, indicating that some regulating mechanisms must be at work. The value of the exponents in the equations defining the FP, and the distribution on the FP of the various types of galaxies which populate systematically different regions, provide basic information and physical constraints on galaxy formation and evolution processes (Djorgovski, de Carvalho & Han 1989; Burstein, Bender & Faber 1993 = BBF).

In spite of the vast popularity gained by the FP, its universality has been nonetheless questioned with regard to zero-point, slope, and thickness, and a controversy exists concerning the differences between field and cluster ellipticals (de Carvalho & Djorgovski 1992). A surprising fact and a matter of concern is also that opposite conclusions about the properties of the FP are drawn from approximately the same data-set. This is a further indication that some basic issues still call for a clarification: two of them are the statistical completeness of the adopted galaxy samples, and the definition of a unique methodology and of standard procedures for data analysis. In fact large differences can be found among total magnitudes and effective parameters for the same galaxies studied by various authors (cf. Capaccioli, Piotto & Rampazzo 1988, and CCR). They depend mostly on the uncertainty in setting the sky-background level — which plagues CCD images of large galaxies —, on the calibration of the photometric scale, and on the adopted extrapolation to infinity of the growth curves, often assumed to be universal. Moreover, much anarchy is present in the definition of the structural parameters μ_e and R_e; they are often given as the scaling parameters of an empirical formula fitting some light profile (e.g. the $r^{1/4}$ law) rather than the parameters of the isophote encircling half the total luminosity.

Prompted by these considerations, we decided to construct a new database of "model-free" photometric parameters for a large and deep luminosity-limited sample of early-type galaxies (CCR, Chapter 2) and bulges of spirals (D'Onofrio 1991) belonging to the Virgo cluster, and use it to re-analyse the relation between μ_e and R_e. For now we must abstain from commenting on the FP, since central velocity dispersion measurements are available only for 40% of our sample galaxies.

With literature data added to ours in order to extend the sample toward both brighter and fainter luminosities, we show here that spheroids (E galaxies and bulges of all luminosity classes) populate two different regions of the $(\log R_e, \mu_e)$ plane, and we argue that this segregation likely corresponds to the existence of two physically distinct families of objects.

The first family consists of ellipticals and of hot galaxy components (bulges) fainter than $M_B \simeq -19.3$ mag, with effective parameters ranging over a large interval for the same total luminosity: $R_e$varies by $\sim$ 0.7 dex and μ_e by $\sim$ 3.5 mag. The interval spanned by R_e is the same at any luminosity (down to $M_B \simeq -12$, by adding literature data for dE and dS0 galaxies), with a sharp upper boundary at $R_e \simeq 3$ kpc.

The second is a one parameter family (μ_e depends on R_e; Kormendy 1977a), consisting of galaxies with $M_B < -19.3$ and $R_e > 3$ kpc, populating a very narrow strip in the $(\log R_e, \mu_e)$

plane, which extends over more than 1 dex in R_e, with slope $d\mu_e/d\log R_e \simeq 3$. Typically they have boxy isophotes and populate cluster condensations (brightest cluster members); this family also includes objects hosting QSO's and Seyfert nuclei. There are indications that this distribution is related to merging processes. Here we also look deeper into the properties of the two families by searching for correlations of the structural parameters with other observables compiled from the literature.

This Chapter is organized as follows. In Section 4.2, we introduce our Virgo-Fornax sample, discuss its characteristics and completeness, and briefly comment on the data reduction. The relation between μ_e and R_e with our Virgo-Fornax data-set is shown in Section 4.3. In Section 4.4, we discuss the large set of literature data, and in Section 4.5, we use it to build the *broad–sample* $(\log R_e, \mu_e)$ plane. The correlations of the structural parameters with the other observables are examined in Section 4.6 and discussed in Section 4.7.

4.2 The Virgo-Fornax Sample

Our photometric sample of Virgo galaxies consists of 52 Es and non-barred S0s (CCR, Chapter 2), and of 54 spirals of morphological types from Sa to Sc (D'Onofrio 1991). According to the membership list of Binggeli et al. (1985), the early-type sample is 80% complete to the total apparent magnitude $B_T = 14$, i.e. to the absolute magnitude $M_B = -17.3$, if a distance modulus of $(m - M)_0 = 31.3$ is adopted after Capaccioli et al. (1990a). The spiral sample is also 80% complete to $B_T = 13.5$. In both cases the missing objects lie mostly at the cluster outskirts, not covered by our large-field plates. As for the Fornax cluster, CCD and plate material has been collected for 28 E and non-barred S0 galaxies (Chapter 2). With respect to the membership list of Ferguson (1989), this sample is 95% complete to $B_T = 15$.

Since our strategy requires an accurate surface photometry covering the largest possible range in surface brightness, we have adopted the so-called 'global mapping' technique (Capaccioli & Caon 1989). Combining unsaturated CCD images with large-field (Schmidt) deep photographs, it allows a mapping of the light distribution of galaxies from the center down to $\mu_B = 28$ B–mag arcsec^{-2}, with a relative accuracy better than 0.1 mag from outside the seeing-convolved core out to $\mu_B \sim 26$. A key feature of this technique is the sky-background subtraction in the CCD images. The CCD blank-sky level μ_s is determined by requiring that the sky subtracted CCD light profile matches, in the unsaturated range, the corresponding profile extracted from the photographic image (where μ_s can be measured with a precision better than 0.5%). Although the error on $\mu_s(CCD)$, usually $< 2\%$, is not better than for other common methods of measuring the sky-background directly on the CCD frame (at least for objects not completely filling the frame), the 'global mapping' technique provides the possibility of using the photographic profile from where the CCD light profile becomes unreliable because of the uncertainty on the blank-sky level.

The geometric and photometric parameters for the set of E and S0 galaxies were extracted from two-dimensional models built coupling the luminosity profiles along the main axes with the ellipticity and position angle profiles (see CCR and Chapter 2 for details). In particular, we calculated total magnitudes B_T by integrating the galaxy flux out to the last observed

isophote (typically 1/100 of the night-sky luminosity) and by adding an extrapolation correction, rarely not exceeding 15%, based on the $r^{1/4}$ extension of the light profiles out to $\mu_B \sim 32$ As a consequence we were able to compute the parameters a_e, b_e, and μ_e of the effective isophote, which encircles half the total luminosity. They are not the scale parameters of the $r^{1/4}$ or any other fitting law.

For the spirals a straightforward approach has been followed, justified by the composite nature of the objects: the main axis light profiles were decomposed into the sum of a $r^{1/4}$ law (de Vaucouleurs 1948) for the bulge and an exponential law (Freeman 1970) for the disc respectively, rejecting solutions which did not appear plausible (for a review of decomposition techniques see Capaccioli & Caon 1992). We used an interactive procedure similar to that described by Kormendy (1977b), obtaining meaningful results for 35 objects (D'Onofrio 1991).

For both samples, no corrections were applied for galactic and internal extinction. The former is small because the Virgo and the Fornax clusters are close to the Galactic Poles; the latter is negligible even for spirals, as proven by the independence of the computed face-on central surface brightness of the disc upon inclination (D'Onofrio 1991).

Since all early-type galaxies of Virgo and Fornax can be considered at the same distance from us — the depth of the Virgo clusters is at most 10% (rms scatter) of its distance (see Tonry, Ajhar & Luppino 1990), and Fornax is nearly at the same distance and even more compact —, their scale parameters do not suffer from the uncertainties affecting sparse and/or distance-unconstrained samples. Larger systematic effects may plague the group of NGC 4472, which is possibly $\sim 20\%$ more distant than the rest of the Virgo cluster (Binggeli, Tammann & Sandage 1987), and the spiral sample (Tully & Shaya 1984). Here, given the present uncertainty on the distance of the Fornax cluster (cf. Jacoby et al. 1992), we have assumed the same distance modulus as Virgo.

The errors on the effective parameters for the early-type galaxies are essentially related to the uncertainty on B_T (cf. Chapter 2). From the comparison with published total magnitudes, we estimate $|\Delta B_T| \leq 0.1$ mag, which translates into R_e and μ_e as $|\Delta \log R_e| < 0.08$, and $|\Delta \mu_e| < 0.4$. For bulges of spirals it is more difficult to give a quantitative estimate of the errors on the effective parameters. They are mostly related to the uncertainty of the decomposition and to the inadequacy of our simplified photometric model to reproduce the actual luminosity behavior of the galaxian subcomponents. As for spheroids, errors in μ_e and R_e are inversely correlated, conserving the bulge luminosity (see also Schombert & Bothun 1987).

4.3 The $(\log R_e, \mu_e)$ Plane for the Virgo-Fornax Sample

Figure 4.1 shows the distribution of the representative points for our 87 Virgo and 28 Fornax ellipticals and bulges in the $(\log R_e, \mu_e)$ plane. We can easily identify two groups. The first one, that we call '*ordinary*' family, appears confined within a strip bounded by lines which are of constant luminosity for galaxies with homologous light-distributions:

$$L_T = sI_eR_e^2 \tag{4.1}$$

s is a 'structural parameter' whose value depends on the shape of the galaxy light profiles; for a generalized de Vaucouleurs law (Sersic 1968)

$$I(r) = I_0 \, \mathrm{dex}\Big(- r^{1/n} \Big) \tag{4.2}$$

numerical calculations show that, in the range $0.5 < n < 16.5$, the structural parameter is very accurately approximated by the relation (see Chapter 5):

$$\log s = 0.030 \, [\log n]^2 + 0.441 \log n + 1.079 \tag{4.3}$$

The '*bright*' family consists of 12 galaxies, the brightest of the sample. Well isolated from the others, they are characterized by large effective radii ($\langle R_e \rangle = 10$ kpc) and relatively low surface brightness ($\langle \mu_e \rangle = 23.7$ B–mag arcsec^{-2}). This group, together with the brightest members of the '*ordinary*' group, fits the uniparametric relation reported by Hamabe & Kormendy (1987 = HK): $\mu_e = 2.94 \log R_e + 20.75$, with zero point tuned to our Virgo cluster distance.

A least-square fit for the early-type members of the '*ordinary*' family (E and S0 galaxies of both Virgo and Fornax with $M_B > -19.3$) yields:

$$M_B = -5.66(\pm 0.07) \log R_e + 1.02(\pm 0.01) \mu_e - 40.2(\pm 0.3) \tag{4.4}$$

From the Virial Theorem:

$$\frac{L}{R} \left(\frac{M}{L} \right) \propto \sigma^2 \tag{4.5}$$

and from our data:

$$L \propto I_e^{1.02 \pm 0.01} \, R^{2.26 \pm 0.03} \tag{4.6}$$

By combining eqsuations 4.5 and 4.6:

$$L \propto I_e^{-0.81 \pm 0.11} \, \sigma^{3.58 \pm 0.13} \left(\frac{M}{L} \right)^{-1.79 \pm 0.05} \tag{4.7}$$

which compares quite well with Djorgovski & Davis' (1987) FP:

$$L \propto \langle I \rangle_e^{-0.86} \sigma^{3.45} \tag{4.8}$$

if the mass-to-light ratio M/L is marginally dependent on L. ($\langle I \rangle_e$ is the mean surface brightness within the effective isophote). Equation 4.4 changes into:

$$M_B = -5.40(\pm 0.04) \log R_e + 1.00(\pm 0.01) \mu_e - 39.8(\pm 0.3) \tag{4.9}$$

if the '*bright*' family is added to the '*ordinary*' one, with which equation 4.7 becomes:

$$L \propto I_e^{-0.86 \pm 0.06} \, \sigma^{3.72 \pm 0.08} \left(\frac{M}{L} \right)^{-1.86 \pm 0.03} \tag{4.10}$$

The coefficient of $\log R_e$ in equation 4.9 differs from the expectation for an homologous family (eq. 4.1 with $s = $ const.). Assuming that the structural parameter s depends on the effective

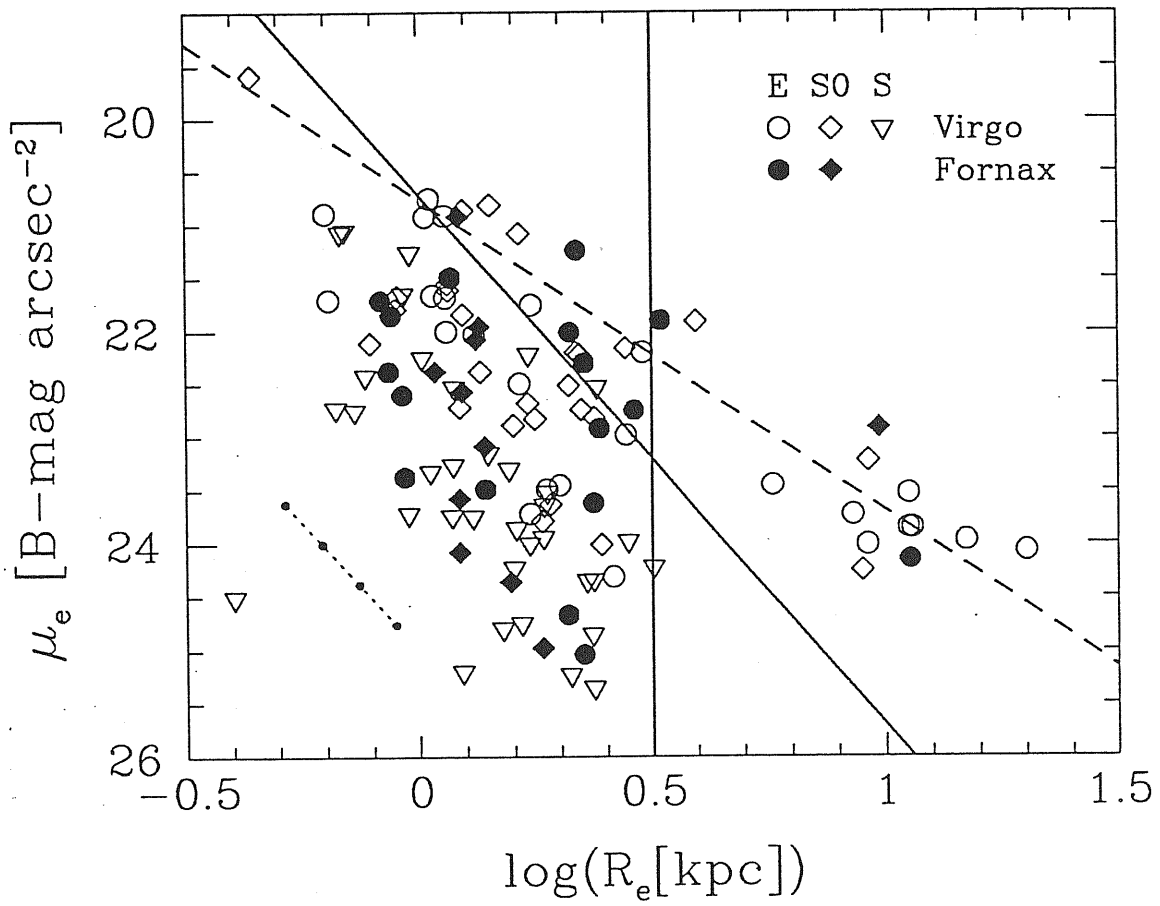

Figure 4.1: Sample of 87 Virgo galaxies (ellipticals and bulges of S0s and spirals) and of 28 Fornax (Es and S0s), showing some sort of bimodal distribution in the ($\log R_e, \mu_e$) plane. The adopted distance modulus is 31.3 mag both for Virgo and Fornax clusters. The upright solid line $\log R_e = 0.5$ is an estimate of the upper boundary to the effective radius for the so-called '*ordinary*' family (see text). The diagonal solid line marks the locus of constant luminosity $M_B = -19.3$ for homologous galaxies. The dashed line is the HK relation, holding for the brightest group. The drift caused by an error on the total magnitude B_T is indicated by the dotted line (distance between two ticks corresponds to $\delta B_T = 0.1$ mag). Note that the discontinuity in $\log R_e$ between the two families might not be real, but just a spurious consequence of the poor statistics or a peculiarity of the local environment.

radius: $s = u \times R_e^\gamma$, where u is now a universal constant, we obtain $\gamma = 0.16$, which means that s increases, though slowly, with R_e. This corresponds to a progressive shallowing of the light profile as R_e stretches, which is indeed observed (Chapter 5).

From Fig. 4.1 we see that objects of equal luminosity span the ranges $\Delta\mu_e \sim 3.5$ mag and $\Delta \log R_e \sim 0.7$. This spread is unlikely due to projection effects. For instance, the surface brightness of an oblate spheroid at face-on view is $2.5 \log(b/a)$ fainter than at the view angle

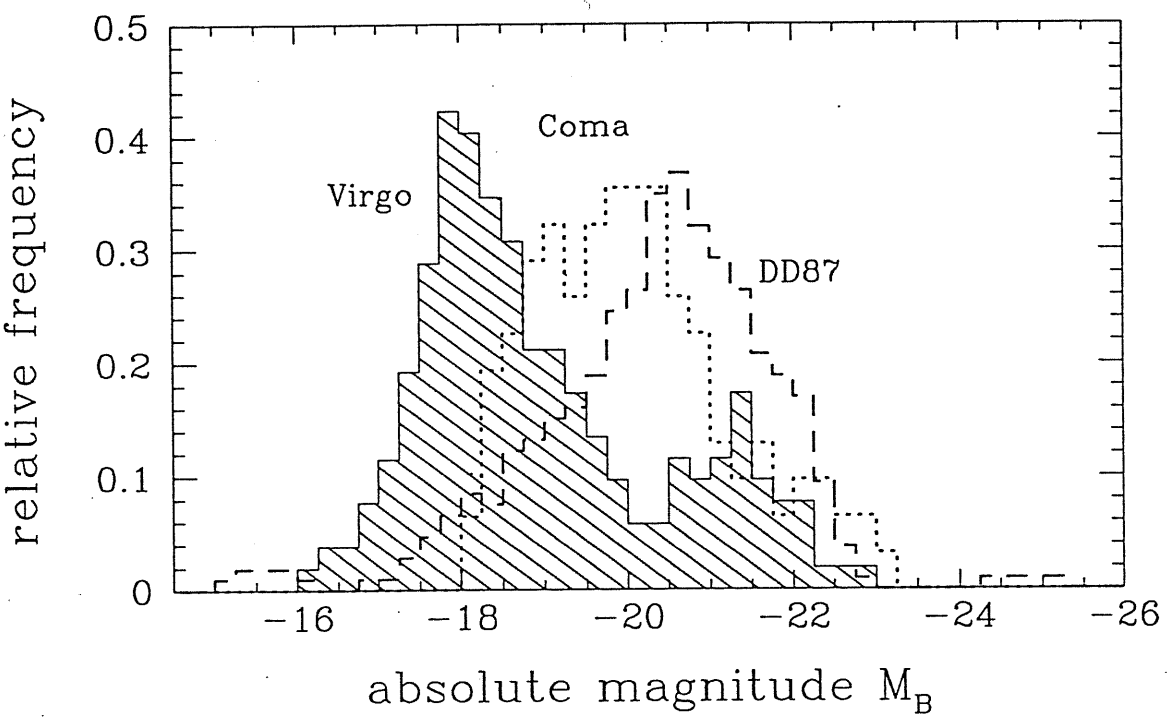

Figure 4.2: The Luminosity Function for the 52 early-types of our Virgo sample (shaded histogram) is compared with the LF for the 33 Coma galaxies studied by Jørgensen et al. (1992; dotted line) and with the LF for the sample of DD87 (dashed line). Data have been registered to the same distance scale and photometric band, and smoothed by a running window 1.0-mag wide, moved in steps of 0.25 mag.

inducing the apparent axis ratio b/a of the isophotes; therefore, going from $\varepsilon = 1 - b/a = 0$ to $\varepsilon = 0.6$, μ_e varies at most by 1 mag. Since photometric errors are estimated to be $\delta \log R_e \simeq 0.08$ and $\delta \mu_e \simeq 0.4$ (Capaccioli & Caon 1991), this implies that most of the dispersion in μ_e at the same luminosity is intrinsic, in spite of the fact that galaxies with equal M_B tend to have the same structural parameter s (or the same shape descriptor n). This explains why intrinsic shape tests for E galaxies based on photometry should fail to provide any definite answer (as they actually do; cf. Bertola 1985), even when the dependence of μ_e on total luminosity is accounted.

4.4 Literature Data

In order to extend the luminosity range and morphological types toward both brighter (BCG, QSO) and fainter (dwarf early-type) galaxies, we have compiled a catalogue of structural parameters from the literature, aiming also at cross-comparing different sources. Tables 4.1 and 4.2, and the accompanying notes, contain the basic information on the literature data

Table 4.1: Sources for the μ_e-R_e relation

Source	Code	Telescope	Detector	Type	N. gal.	Band	Method	Notes
This work		INT 2.5 m	CCD	Spiral	35	B, V	B/D dec.	
		ESO-Dan. 1.5 m	CCD	E/S0	80	B	flux int.	
		Steward Obs. 2.3 m						
		UK Schmidt	ph. plate	E/S0	80	B		
		ESO Schmidt						
Kormendy 1977	Kor77	M. Wilson 1.5 m	ph. plate	E	34	B	$r^{1/4}$ fit	1
		Palomar Schmidt						
Boroson 1981	Bor81	KPNO 1.0 m	ph. plate	Spiral	16	B	B/D dec.	2
Schneider et al. 1983	SGH83	Palomar 1.5 m	CCD	BCG	249	r, g	$r^{1/4} + PSF$ fit	3
Thomsen & Frandsen 1983	TF83	Wise 1.0 m	Elec. pl.	BCG	31	B, V	$r^{1/4} + PSF$ fit	4
		ESO-Dan. 1.5 m	Elec. pl.					
Malkan et al. 1984	Mal84	Palomar 1.5 m	SIT	Quasar	39	r	$r^{1/4} + PSF$ fit	5
Malumuth & Kirshner 1985	MK85	KPNO 0.9 m	CCD	BCG	34	V	$r^{1/4}$ fit	6
Michard 1985	Mic85	OHP 1.2 m	ph. plate	E/S0	35	B	flux int.	7
Lauer 1985	Lau85	Lick 1.0 m	CCD	E	42	r	$r^{1/4}$ fit	8
Kent 1985	Ken85	Whipple 0.61 m	CCD	Spiral	78	r	B/D dec.	9
Hoessel & Schneider 1985	HS85	Palomar 1.5 m	CCD	BCG	174	r	$r^{1/4} + PSF$ fit	10
Kodaira et al. 1986	KWO86	Kiso Schmidt	ph. plate	Spiral	138	V	B/D dec.	11
Schombert 1987	Sch87	Palomar Schmidt	ph. plate	BCG	342	V	$r^{1/4}$ fit	12
		Palomar 1.5 m	CCD					
Djorgovski & Davis 1987	DD87	Nickel 1 m	CCD	E, S0	262	R	$r^{1/4}$ fit	13
Capaccioli et al. 1988	CPR88	ESO-MPI 2.2 m	CCD	E	9	B	flux int.	14
		ESO Schmidt	ph. plate					
Bender et al. 1988	BDM88	Calar Alto 1.23 m	CCD	E, S0	74	V, R, I	$r^{1/4}$ fit	15
Davies et al. 1988	DPCDK	UK Schmidt	ph. plate	dwarf	187	B	$r^{1/n}$ fit	16
Peletier et al. 1990	PDIDC	KPNO 2.1 m, 0.9 m	CCD	E	30	B	flux int.	17
Irwin et al. 1990	IDDP	UK Schmidt	ph. plate	dwarf	134	B	exp. fit	18
Jørgensen et al. 1992	JFK92	ESO-Dan. 1.5 m	CCD	E, S0	44	B	flux $r^{1/4}$ int.	19
Binggeli & Cameron 1992	BC92	2.5 Du Pont	ph. plate	dwarf	220	B	flux int.	20

Notes to Table 4.1:
columns 1 and 2: Reference to the source and adopted code; columns 3 and 4: Telescope and detector; columns 5 and 6: Morphological type and number of galaxies; column 7: Photometric band; column 8: Method to derive the effective parameters, coded as: *B/D dec.* = bulge-disk decomposition; *exp. fit* = fit of light profiles with an exponential law; $r^{1/n}$ *fit* = fit of light profiles with a generalized de Vaucouleurs law; $r^{1/4}(+PSF)$ *fit* = fit of light profiles with a $r^{1/4}$ law (convolved with the PSF); *flux int.* = direct integration of the galaxy flux; *flux* $r^{1/4}$ *int.* = fit of a $r^{1/4}$ model to the growth curve.

Comments on Table 4.1

1) Kormendy (1977, Kor77). Poor agreement for the 10 galaxies in common. Kor77 data are more sparse than ours and show brighter μ_e. The discrepancy is likely due to the different way of calculating effective parameters (see text).

2) Boroson (1981, Bor81) and *Schombert and Bothun* (1987, SB87). No galaxies in common with us. Using the same material of Bor81, SB87 showed that different bulge-disk decomposition techniques give results differing up to $\Delta \log R_e \simeq 0.5$.

3) Schneider, Gunn & Hoessel (1983, SGH83). Sample of BCG's in 84 Abell clusters of moderate redshift ($0.04 \leq z \leq 0.30$). The μ_e–R_e relation has approximately the HK slope and extends to $\mu_e \simeq 27$ and $R_e \simeq 150$ kpc.

4) Thomsen & Frandsen (1983, TF83). BCG's in two nearby groups and three clusters with $0.06 \leq z \leq 0.15$. Estimated accuracy for R_e is 10%. The μ_e–R_e relation is that typical of the '*bright*' family.

5) Malkan (1984), *Malkan* et al. (1984; Mal84). Sample of 33 host galaxies of QSO's and 6 objects classified as Seyfert. The $r^{1/4}$ and the exponential formulae give equally good fits to the light profiles. These objects are all in the region of the '*bright*' family.

6) Malumuth & Kirshner (1985, MK85). Sample consisting of BCG's from rich and poor clusters. Data form a narrow strip in the $(\log R_e, \mu_e)$ plane with the same slope of the HK relation.

7) Michard (1985, Mic85). Mic85 gives effective apertures A_e (see RC2) and corresponding mean surface brightnesses m'_e. We take $\mu_e = m'_e + 1.393$ and compute R_e from A_e (cf. Nieto 1982). Results are in good agreement with ours (Fig. 4.3).

8) Lauer (1985, Lau85). Poor agreement with our measurements: Lau85 has brighter μ_e and smaller R_e. This is likely due to the small field of Lau85 CCD and to the use of a $r^{1/4}$ fit of just the inner light profiles (see text).

9) Kent (1985, Ken85). No spirals in common with us. Points in the $(\log R_e, \mu_e)$ plane overlap with ours. The only difference is the presence of galaxies in the range $\log R_e = 0.5$–0.9.

10) Hoessel & Schneider (1985, HS85). BCG's of Abell clusters. Half of the objects have multiple nuclei. Azimuthally averaged radial surface brightness profiles measured out to 25 kpc; $r^{1/4}$ models fitted out to 16 kpc. Points in the $(\log R_e, \mu_e)$ plane define a very narrow strip with the HK slope.

11) Kodaira, Watanabe & Okamura (1986, KWO86). Large sample of E and S galaxies of Virgo and Ursa Major clusters, studied on photographic plates of the Kiso Schmidt telescope. The agreement with our data is poor (Fig. 4.3), very likely because of the quality of the material preventing accurate photometry.

12) Schombert (1987, Sch87). The sample contains E, S0, D, and cD galaxies, with parameters corrected for cosmological effects. In the $(\log R_e, \mu_e)$ plane, D, cD, and gE galaxies are in the '*bright*' part, while ellipticals are superposed both to our '*bright*' and '*ordinary*' objects.

13) Djorgovski & Davis (1987, DD87). For the 18 ellipticals in common the agreement with us is poor (Fig. 4.3). DD87 data follow approximately the '*bright*' distribution but with systematically brighter μ_e. The trend of the HK relation is not clearly evident.

14) Capaccioli, Piotto & Rampazzo (1988, CPR88). Photometry of 9 early-type galaxies, performed by the same 'global mapping' technique applied to our Virgo and Fornax samples.

15) Bender et al. (1988, BDM88). Study focused on the isophotal shape analysis; it provides values of R_e but not of μ_e. We have calculated them assuming $r^{1/4}$ models with B_T's from the Revised Shapley-Ames Catalog (Sandage & Tammann 1981). The agreement is quite poor.

16) Davies et al. (1988, DPCDK). Dwarfs belonging to the Fornax cluster. Light profiles are fitted by a generalized de Vaucouleurs profile $\mu = \mu_0 + 1.086(r/A)^N$. Part of these data are flawed by insufficient angular resolution, and some galaxies are probably background objects.

17) Peletier et al. (1990, PDIDC). Quite good agreement for objects in the domain of the '*ordinary*' family, poor for the most luminous galaxies, with μ_e brighter by 1 mag. This may be related to the small size of the CCD field.

18) Irwin et al. (1990, IDDP). Dwarfs belonging to the Fornax cluster. Parameters derived from the exponential fit to light profiles have been transformed into effective parameters by the equations: $\mu_e = \mu_0 + 1.82$ and $R_e = 1.68h$ holding for the exponential model.

19) Jørgensen et al. (1992, JFK92). 44 E and S0 galaxies, 33 of which belonging to the Coma cluster. We have adopted a Coma-Virgo differential distance modulus of 3.75 mag after Capaccioli et al. (1990), and redshift distances for the other 11 objects. Points in the $(\log R_e, \mu_e)$ plane follow the HK relation and are mainly in the '*bright*' family domain.

20) Binggeli & Cameron (1992, BC92). Surface brightness profiles (azimuthally averaged) have been studied by BC92 for 174 dE, 20 dS0, 24 E/S0, and 7 Sa galaxies. The dwarf galaxy sample is essentially complete to $B_T \sim 18$. The errors in the parameters are estimated $\leq 20\%$. Effective parameters have been derived according to the definition (i.e. not through profile fitting). The agreement among the 13 objects in common with us is very good (Fig. 4.3).

Table 4.2: Analysis of the literature data for the μ_e–R_e relation

Source	N_c	μ_B^{lim}	median(M_B)	Range(M_B)	$\langle \Delta \log R_e \rangle$	$\langle \Delta \mu_e \rangle$
This work (E,S0)		~ 28.0	-18.24	-15.81, -22.43		
This work (S)		~ 28.0	-18.60	-17.60, -20.80		
Kor77	10	~ 27.0	-20.46	-18.40, -21.37	-0.336 ± 0.185	-1.653 ± 0.868
Bor81		~ 26.0	-20.98	-18.35, -22.19		
SGH83		~ 24.5	-20.73	-17.95, -22.24		
TF83		~ 28.0	-20.55	-19.18, -22.14		
Mal84		~ 27.0	-21.60	-19.00, -23.60		
MK85	1	~ 28.0	-22.61	-20.90, -23.77		
Mic85	22	~ 28.0	-19.36	-17.60, -21.96	-0.048 ± 0.136	-0.084 ± 0.703
Lau85	9	~ 23.0	-20.76	-18.98, -22.25	-0.138 ± 0.261	-1.681 ± 0.874
Ken85		~ 25.5	-19.02	-14.97, -21.76		
HS85		~ 27.0	-21.43	-20.43, -22.25		
KWO86	56	~ 27.5	-18.03	-15.27, -21.52	-0.144 ± 0.436	-0.170 ± 2.233
Sch87		~ 26.5	-21.22	-16.95, -23.04		
DD87	18	~ 24.0	-20.48	-15.53, -24.74	-0.089 ± 0.321	-0.966 ± 1.394
CPR88		~ 28.0	-20.32	-19.19, -21.80		
BDM88	19	~ 25.0	-20.41	-17.73, -22.34	-0.335 ± 0.308	-1.122 ± 1.499
DPCDK		~ 27.0	-13.80	-11.70, -17.20		
PDIDC	10	~ 24.5	-20.73	-17.61, -22.86	-0.114 ± 0.205	-0.537 ± 0.789
IDDP		~ 27.0	-12.60	-10.60, -15.10		
JFK92		~ 24.0	-20.43	-18.51, -22.73		
BC92	13	~ 28.0	-14.78	-11.78, -19.15	-0.056 ± 0.048	-0.175 ± 0.305

Notes to the Table:
Column 1: reference code;
column 2: number of objects in common with our sample;
column 3: mean limit to the surface brightness;
columns 4 and 5: median value and range in absolute magnitude;
columns 6 and 7: mean difference ($\pm 1\sigma$) of R_e and μ_e values with our sample.

(reduced to a common system), as well as the codes adopted for the various sources.

A number of steps has been required to homogenize the different data sets; also, an analysis has been made of the methodologies applied to derive the effective parameters.

a) Photometric band. Surface brightnesses and magnitudes have been transformed into the B-band adopting the following mean color indexes: $\langle B - r \rangle = 1.2$ and $\langle B - V \rangle = 0.9$. Observations of the same objects in different colors show that the effective radius does not change significantly with the photometric band.

b) Distance. Effective radii and luminosities have been re-scaled adopting a Hubble constant $H_0 = 70$ km sec^{-1} Mpc^{-1} and $q_0 = 0.5$ for redshift distances, or, directly, a Virgo distance of 18.3 Mpc.

c) Photometric methodology. In the literature there is a variety of different methods to compute the effective parameters. Usually a $r^{1/4}$ law (sometimes convolved with the Point Spread Function) is fitted to the luminosity profiles; in other cases the growth curve is fitted by a $r^{1/4}$ model. In four studies only (Mic85, CPR88, PDIDC, and BC93), besides ours, the effective parameters are derived by applying *directly* the definition (see §2), i.e. without critical model assumptions. When the mean surface brightness is given, we adopt the transformation equation: $\mu_e = \langle \mu \rangle_e + 1.39$, holding for a $r^{1/4}$ law.

d) Galaxy sample. In order to be statistically complete, the sample shall consist of all galaxies within a well defined luminosity range which are contained in a well defined volume of space. Very few samples satisfy such conditions: BCG samples are formed by the few brightest galaxies in some clusters, but generally without a homogeneous luminosity cutoff; other samples consist of cluster and field galaxies chosen according to their apparent magnitudes or their proximity. All such samples are therefore biased toward intrinsically bright galaxies: an example is shown in Fig. 4.2, where the LF of E and S0 galaxies for our sample is compared to that used by DD87 to investigate the Fundamental Plane.

The main source of disagreement among the various authors is in the method used to derive the effective parameters. In fact, the representation of light profiles by empirical models provides parameters which depend upon the fitting procedure or the fitted surface brightness range.

An emblematic example is displayed in Fig. 4.4: the observed luminosity profile of the elliptical galaxy NGC 4621 is compared with $r^{1/4}$ models making use of our 'global mapping' effective parameters and of those given by Kormendy (1977a). It is evident that, while Kormendy's interpolation describes quite well the inner part of the luminosity profile, out to $r \sim 80''$, where $L/L_T = 0.45$, it fails in modelling the outer region where the profile turns shallower; the $r^{1/4}$ model with our parameters is indeed more representative of the global photometric behavior (here we anticipate that the best fit of a generalized $r^{1/n}$ law to the light profile of NGC 4621 gives $n = 6.14$; see Chapter 5)

This is further illustrated in Fig. 4.5, where for nine of our brightest galaxies we compare our model-free effective parameters with those we derived by a plain $r^{1/4}$ fit to the inner part of the light profile. The effect of using $r^{1/4}$ parameters instead of the model-free ones is of spreading the points along the HK relation.

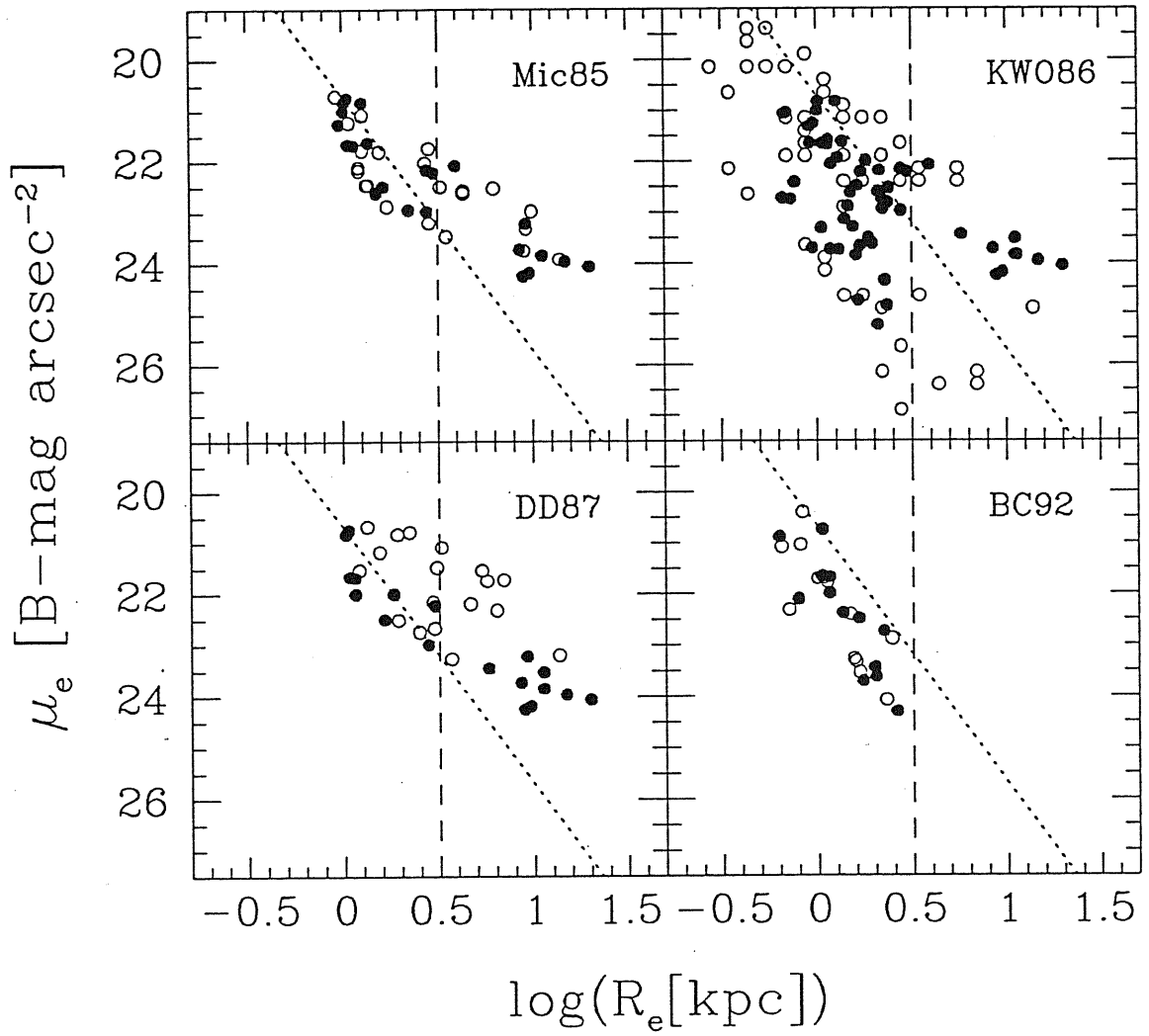

Figure 4.3: In each panel, for the subset of galaxies in common, our values of the effective parameters (*filled circles*) are compared with those published in the sources indicated (*open circles*); coding as in Table 4.1. The dotted line marks the locus of constant luminosity $M_B = -19.3$; the dashed line is placed at $R_e = 3$ kpc.

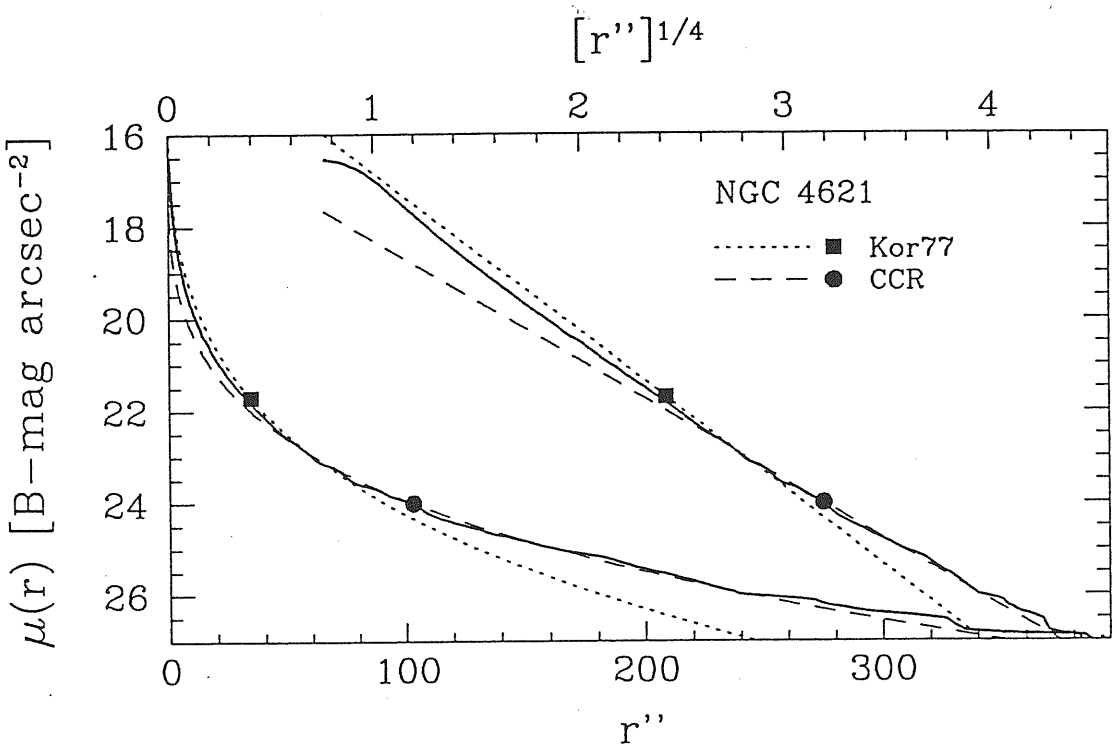

Figure 4.4: The observed equivalent light profile of NGC 4621 (from CCR) is compared with $r^{1/4}$ models drawn using *1)* our model-free effective parameters (dashed line) and *2)* those adopted by Kormendy (dotted line), after re-scaling to a common distance. The same light profile and the $r^{1/4}$ models are plotted both in linear units (left curves, bottom scale) and in $r^{1/4}$ units (right curves, upper scale). Dots mark the values of the effective parameters for the two models.

Lastly, in Fig. 4.6, values of R_e and μ_e for the same galaxies from various sources are compared; differences in R_e up to 0.5 dex and in μ_e up to 3 mag are easily found.

4.5 The $(\log R_e, \mu_e)$ Plane for the Broad-Sample

The existence of two distinct families of galaxies in the $(\log R_e, \mu_e)$ plane is further supported once literature data are added to ours, in spite of their heterogeneity as for quality and characteristics of the environment.

The *broad–sample* is plotted in Fig. 4.7. The solid lines mark the boundaries for the region of the '*ordinary*' family: $R_e < 3$ kpc, $M_B > -19.3$ mag. The short-dashed line represents the HK relation for the '*bright*' family. The long-dashed line in the figure reproduces the fit by Binggeli & Cameron (1993 = BC) to their data-set of early-type dwarf galaxies (see below).

BCGs all place in a quite narrow strip (slightly curled), which follows approximately the uniparametric HK relation, with slope of $\simeq 3$ (computed for $\log R_e > 1$), and a rms scatter

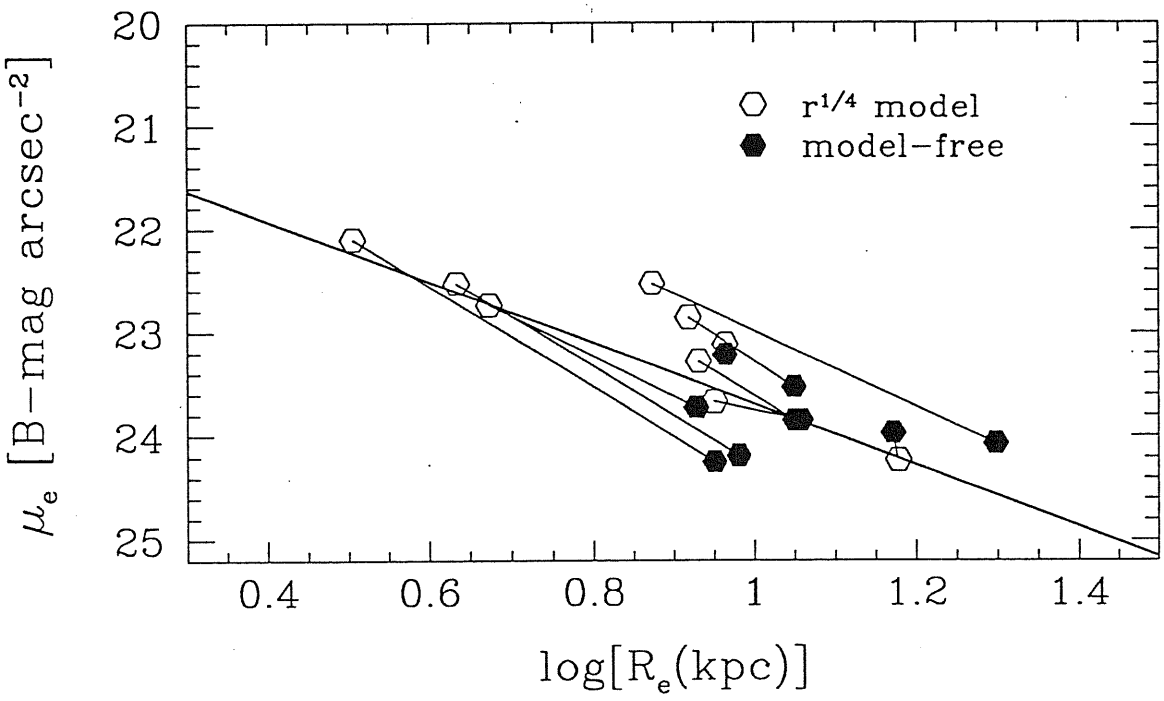

Figure 4.5: For nine of the 10 brightest Virgo E and S0's, model-free effective parameters are compared with those derived through $r^{1/4}$ fits to the inner parts of the equivalent light profiles. One galaxy (NGC 4526) was excluded because its light profile is affected by a strong dust-lane. The solid line represents the HK relation.

of about 0.5 mag in μ_e at fixed R_e. The strip extends to $R_e \simeq 300$ kpc. This behavior is characteristic of each single BCG sample. Interesting enough, the representative points of host galaxies of QSO's (Mal84) overlap to those of BCGs in the $(\log R_e, \mu_e)$ plane, suggesting a possible peculiarity of the '*bright*' family. For these objects, however, the accuracy of the effective parameters is rather poor, as noted by the authors themselves, and therefore the above indication must be taken *cum grano salis*.

The brightest Virgo ellipticals are superposed on this sequence, but they span a quite small range in effective parameters, as already noted. The marked gap between the two families, which was present in our data (Fig. 4.1), has now disappeared. At the moment we are unable to establish whether this gap is real (and therefore it is wiped out, in Fig. 4.7, by the heterogeneity of the *broad-sample* data) or whether it is a consequence of the poor statistics of our Virgo-Fornax sample. We shall note that the first hypothesis rests on the circumstance that the error vector is roughly aligned with the HK relation (cf. Capaccioli & Caon 1991); thus, large errors tend to fill the gap, if any.

We note here that the LFs of BCG samples (Fig. 4.8) are peaked at the same absolute magnitude of the secondary bright bump found in our Virgo sample. On the other hand, the LF of the Coma sample (JFK92; see Fig. 4.2) is peaked at $M_B \simeq -20.0$, just where the Virgo

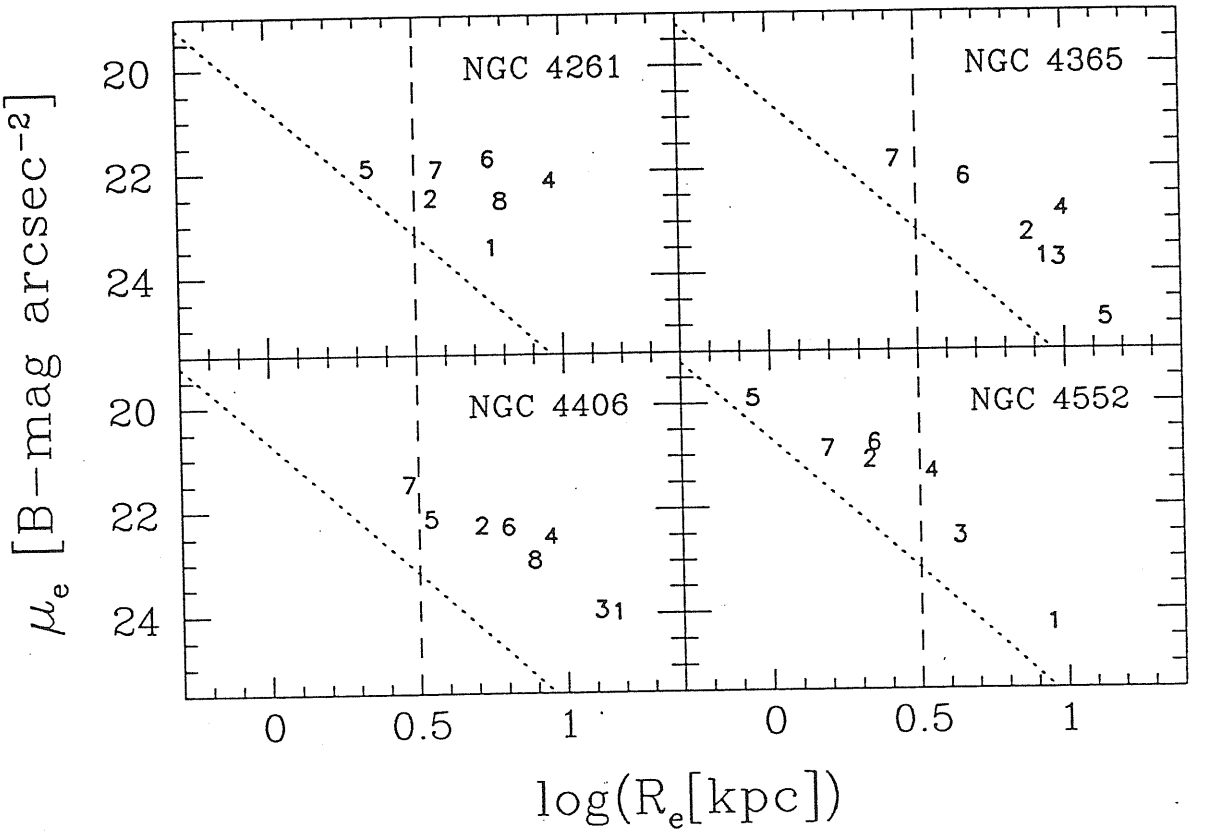

Figure 4.6: For 4 Virgo elliptical galaxies, values of the effective parameters R_e and μ_e taken from the literature are compared with ours. Codes are: 1 = this work; 2 = Kormendy (1977a); 3 = Michard (1985); 4 = Lauer (1985); 5 = Kodaira et al. (1986); 6 = Djorgovski & Davis (1987); 7 = Bender et al. (1988); 8 = Peletier et al. (1990); 9 = Binggeli & Cameron (1993).

LF presents the minimum in between the two peaks. Although the 33 E's studied by JFK92 do not form a complete sample of the Coma cluster, the marked difference between the two LFs, if confirmed, suggests that even the *type-specific* LF may actually be a function of the environment (see also Jerjen, Tammann & Binggeli 1990).

The representative points of dwarf galaxies (BC93, Davies et al. 1988 = DPCDK, Irwin et al. 1990) place just below our '*ordinary*' group, within the same boundary in R_e. Dwarfs seem thus the natural extension of such group toward fainter luminosities and fainter effective surface brightnesses.

The *broad–sample* has also been plotted in the (M_B, μ_e) plane of Fig. 4.7b in order to discuss the results of BC91 and DPCDK. BC91 suggest that dwarf and faint ellipticals and S0s (our '*ordinary*' family) follow the surface brightness-luminosity relation (reduced to our

Virgo distance):

$$\langle\mu\rangle_e \simeq 0.75 M_B + 34.98 \tag{4.11}$$

with a considerable scatter (0.8 mag at 1 sigma level), most of which is cosmic. Here $\langle\mu\rangle_e = -2.5 \log \langle I\rangle_e + \text{const.}$; for an homologous family $\langle\mu\rangle_e = \mu_e - k$, where $k = 1.15 \log n + 0.70$ for the generalized de Vaucouleurs formula. The slope of equation 4.11 is not far from unity, that is from the condition $R_e = \text{const.}$, and indeed, the line at $R_e = 3$ kpc corresponds almost perfectly to the lower envelope of the dwarf distribution.

We fully agree with BC91 that the low-luminosity Es ($M_B > -19.3$) do not share the M_B-$\langle\mu\rangle_e$ relation defined by the giants. Fig. 4.7b suggests that low-luminosity Es simply extend the dwarf distribution toward brighter M_B and $\langle\mu\rangle_e$. Similarly, we are not in the position of establishing whether the compact dwarf ellipticals (prototype M32), which populate the upper left part of $(\log R_e, \mu_e)$ plane (see Fig. 4.7a), are a third family or — less likely, though — an extension of the distribution of the '*ordinary*' family to very small objects which, due to their compactness and proximity to giant galaxies, are still observable/observed.

In this context we shall comment on the claim by DPCDK that the representative points of their Fornax cluster dwarfs are spread in the effective parameters plane (open squares in Figs. 4.7). Part of these data are likely flawed by insufficient angular resolution (cf. Ferguson & Sandage 1988), so that the exponential fitting of luminosity profiles can give unreliable results. Moreover, some of the DPCDK galaxies are suspected to be background objects which pollute the (M_B, μ_e) distribution.

4.6 Correlations between Structural and Physical Parameters

Does the the existence of two families in the $(\log R_e, \mu_e)$ plane bear any physical meaning? In an attempt to answer this basic question, we have compiled from the literature a catalogue of observables for the early-type galaxies of our Virgo-Fornax sample. We aim at testing whether the line $R_e = 3$ kpc dividing the two families in the effective parameters plane is also a 'watershed' for other physical properties.

In particular we have looked at the 21 cm line emission, the radio continuum flux at 6 cm, the CO mappings at 2.6 mm, the IRAS fluxes from 12 to 100 μm, the UV luminosities, the X-ray data in the 0.2–4 keV band, and the masses for the interstellar medium components. We also considered other photometric and spectroscopic quantities such as color gradient, metallicity index, isophote shape parameters, maximum ellipticity, central velocity dispersion, and anisotropy parameter.

In Table 4.3 we list those parameters which show some sort of dependence on the effective radius R_e (Figs. 4.9). The sources of the data and the numbers of galaxies used are in columns 2 and 3 respectively. Unfortunately the intersections of our Virgo-Fornax photometric data-base with the lists of UV magnitudes (Longo, Capaccioli & Ceriello 1991), CO abundances (Roberts et al. 1991), and SNe events (Barbon, Cappellaro & Turatto 1989) are almost empty. No significant correlations exist with dustiness alone (data from van der Bergh

& Pierce 1990), with HI flux alone (from Roberts et al. 1991), with IRAS fluxes at 12, 25, 60 and 100 μm (from Knapp et al. 1989), with L_{IR}/L_B (from Bally & Thronson 1989), and with the residuals from the Faber-Jackson relation. Positive correlations are shown in the panels from *a*) to *j*) of Fig. 4.9

Fig. 4.9*a*: galaxies with a large R_e tend to have boxy-shaped or elliptical isophotes. Note that this correlation is degraded by the projection effects which influence both cos 4 and R_e.

Fig. 4.9*b*: strong ellipticities are found only in the '*ordinary*' family. Should this result be confirmed by a larger sample, it would imply that the light distribution in '*bright*' galaxies is close to spherically symmetric (cf. Capaccioli, Caon & Rampazzo 1990).

Fig. 4.9*c*: the Mg_2 index is more dispersed for the '*ordinary*' galaxies. This is expected in view of the result of Fig. 3*a* and of the finding by Longo et al. (1989) of some dependence of the Mg_2 index on cos 4.

Fig. 4.9*d*: '*bright*' galaxies have a larger dispersion of the anisotropy parameter $(V/\sigma)^*$ (Davies et al. 1983). According to BBF this parameter is a crude measure of the ratio of baryonic mass in (cold) gas to mass in stars at the time when the last major merger occurred.

Fig. 4.9*e*: '*bright*' galaxies seem to possess a low HI-mass per unit of B-light. Note however that the HI data are just upper limits.

Fig. 4.9*f*: The mass of cold dust, computed by Roberts et al. (1991) from the 60 and 100 μm IRAS fluxes, is related here to the total luminosity in the B-band. In this sample of early-type galaxies the M_{dust}/L_B ratio is very low for the '*bright*' objects.

Figs 4.9*g* and *h*: Radio and X-ray fluxes correlate with R_e (as they do with cos 4; cf. Bender et al. 1989a). Bright E and S0 galaxies are known to be dominated by the emission from a hot interstellar medium and to be powerful X-ray emitters. The radio luminosity is also large for these objects.

Fig.4.9*i*: The color gradients of '*bright*' galaxies present a very small dispersion. Vader et al. (1988) found a dependence of color gradient on absolute magnitude and on rotational velocity, a fact which led them suspect the existence of two families of early-type galaxies. Color gradients provide useful hints to galaxy formation theories, since dissipation and merging produce different effects on galaxy colors (cf. White 1979, and Carlberg 1984).

Fig. 4.9*j*: The luminosity density, now plotted versus M_B to help comparison with Djorgovski (1992), shows opposite trends for the two families. (Here the vertical line is at $M_B = -19.3$ mag, the luminosity boundary between '*ordinary*' and '*bright*' galaxies). This behavior is in marked contrast to that claimed by Djorgovski (1992); his straight-line fitting to the distribution ($\rho_L \propto L^{-0.9}$; dotted line) is due to a lack of data for fainter galaxies. Several processes could in principle modify the densities of proto-ellipticals: dissipative collapse increases the density at a fixed mass, dissipationless merging increases the mass, but decreases the density, dissipative merging increases both the mass and density, and galactic winds by SNe decrease both. A non-trivial mechanism should regulate the maximum density achievable by the stellar systems (~ 1 L$_\odot$ pc^{-3}) and the maximum effective radius ($R_e = 3$ kpc).

4.7 Discussion

The existence of two families of galaxies in the $(\log R_e, \mu_e)$ plane is clearly seen in Figs. 4.1 and 4.7*a*,*b*, in spite of the heterogeneity of the literature data. Remarkable features are that galaxies with luminosities differing by as much as 3 dex nonetheless share the same range of R_e, and that, whatever the luminosity is, the '*ordinary*' galaxies do not grow larger in size than $R_e \simeq 3$ kpc. The break in the distribution of the structural parameters calling for the existence of two main families of galaxies occurs at $M_B \simeq -19.3$.

We have studied here the correlations of the effective radius R_e with different physical observables, keeping in mind that R_e is not affected by the same problems as the cos 4 parameter proposed by Bender et al. (1989a). (The limits of cos 4 have been analysed by Rix & White (1990), and Stiavelli et al. (1991), who pointed out that it depends strongly on the inclination and on the intrinsic shape of the galaxy as well as on the specific view angle.) A clear separation in the properties of the two families is evident for the many physical parameters presented in the panels of Fig. 4.9. The results of Figs. 4.9 should not be interpreted in a strictly statistical sense, because the completeness of the data sample is poor and we have not applied any test to determine the confidence level of the observed correlations, or to establish if the data can be drawn from two different populations.

If, as many pieces of evidence indicate, the boxy appearance in luminous galaxies is the result of merging events, we may wonder how merging bears the position of the merger product in the $(\log R_e, \mu_e)$ plane. Following Hoessel (1980), the evolution in size as a function of mass is governed by equation $\delta R_e/R_e = k\,\delta M/M$, where M is the total mass, and k is a parameter in the interval $1 < k < 2$, depending on the mechanism of the merging process. Entering the definition for the scale parameters, $L \propto I_e {R_e}^2$, and assuming that the mass-to-light ratio is a power law of the mass, $M/L \propto M^\gamma$, the representative points of merger products are found to move along lines of slope:

$$\frac{\delta \mu_e}{\delta \log R_e} = 2.5 \left(2 - \frac{1-\gamma}{k}\right). \tag{4.12}$$

For typical values of k and γ ($0 \leq \gamma \leq 0.2$), $\delta\mu_e/\delta\log R_e$ ranges from 2.5 to 4.0. This interval is almost centered at the slope of HK relation, a fact which gives further support to the merging scenario for the '*bright*' family. Also the high frequency of multiple nuclei among BCGs goes in this direction.

We notice the interesting position of the galaxies hosting an active nucleus (Malkan 1984; Malkan, Margon & Chanan 1984). Although for these objects significant errors can be present due to seeing effects and strong selection effects may exist, the association of host galaxies of QSO's with the line of mergers is remarkable.

In summary, the results presented here all seem to support the view that the '*ordinary*' family is an inbred variety while the '*bright*' family is the result of some sort of environmental evolution. If this is true, we suggest that the $(\log R_e, \mu_e)$ plane for E galaxies and bulges may be viewed as the 'logical equivalent' to the HR diagram for stars: it marks the locus occupied by galaxies at the end of the dissipative collapse ('*ordinary*' family) and traces the evolutionary track of objects which have experienced significant merging ('*bright*' family).

An interesting fact to note is that, while ordinary Es ($M_B < -18.0$) and bulges form a discontinuous sequence with respect to dwarfs in the core-parameters diagram (M_B, μ_0) (see Kormendy 1985, and BC91), such behavior is not present in the ($\log R_e, \mu_e$) plane. Here these objects populate a continuous distribution, interrupted at $M_B \simeq -19.3$, i.e. at the breakpoint between our two families. Why global parameters provide a different behavior than core parameters is still unclear.

Table 4.3: Data from the literature

Parameter	Data Source	No. of detections (No. of upper limits)
cos 4 peak	Chapter 2	77
ϵ_{max}	Chapter 2	77
Mg_2 index	Davies et al. (1987)	30
$(V/\sigma)^*$	Bender et al. (1993)	18
HI mass	Knapp et al. (1985) and Wardle & Knapp (1986)	(40)
Dust mass	Roberts et al. (1991)	18 (23)
L_X	Fabbiano et al. (1992)	16 (10)
$L_{6\,cm}$	Roberts et al. (1991)	15 (23)
Color gradients	Vader et al. (1988)	16
	Peletier et al. (1990)	10

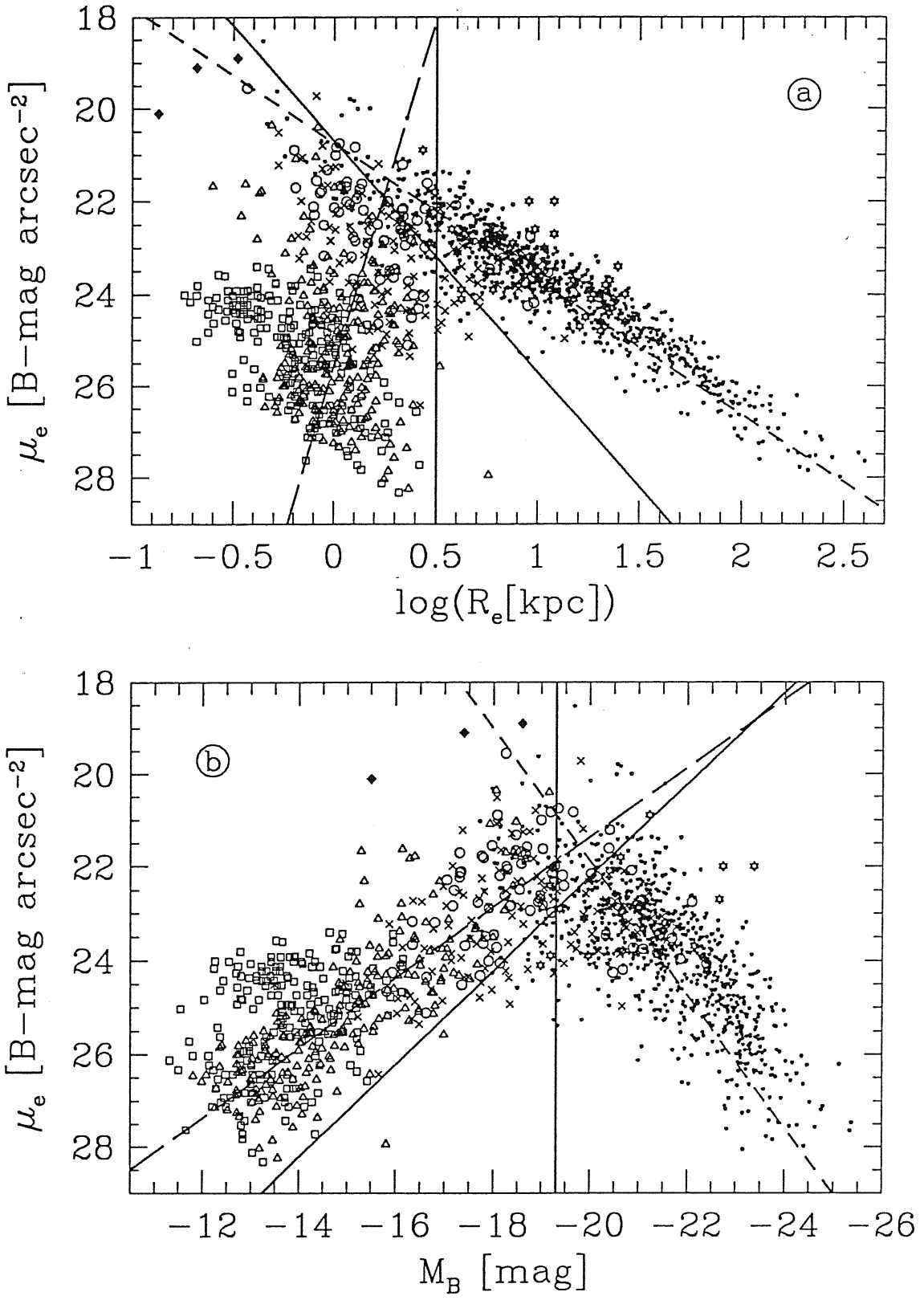
a
18
20
22
24
26
28
μ_e [B−mag arcsec^{-2}]
−1
−0.5
0
0.5
1
1.5
2
2.5
log(R$_e$[kpc])
b
18
20
22
24
26
28
μ_e [B−mag arcsec^{-2}]
−12
−14
−16
−18
−20
−22
−24
−26
M$_B$ [mag]

Figure 4.7: *Panel a)* The $(\log R_e, \mu_e)$ plane for the *broad-sample* of more than 1500 galaxies. Open circles are E and S0 galaxies of the Virgo-Fornax sample measured by the 'global mapping' technique. Crosses represent the bulges of spirals from Kent (1985) and D'Onofrio (1991). The small filled dots are data from Schneider et al. (1983), Thomsen & Frandsen (1983), Malumuth & Kirshner (1985), Hoessel & Schneider (1985), Michard (1985), Schombert (1987), Capaccioli et al. (1988), and Jørgensen et al. (1992). Starred symbols are galaxies hosting a QSO and Seyferts from Malkan (1984) and Malkan et al. (1984). Open triangles are BC93 data. Open squares are galaxies from the Fornax survey by DPCDK and Irwin et al. (1990); uncertain data have been disregarded. Compact dwarf ellipticals (Bender & Nieto 1990) are indicated as filled diamonds. The heavy solid lines correspond to $R_e = 3$ kpc and to $M_B = -19.3$ mag. The long-dashed line is the Binggeli & Cameron (1991 = BC91) relation (eq. 4.11). The dashed line is the HK relation.
Panel b) The same data as in panel *a)*, plotted in the (M_B, μ_e) plane with the same coding for symbols of representative points and for lines. The latter have been derived from those in panel *a)* under the assumption of homology.

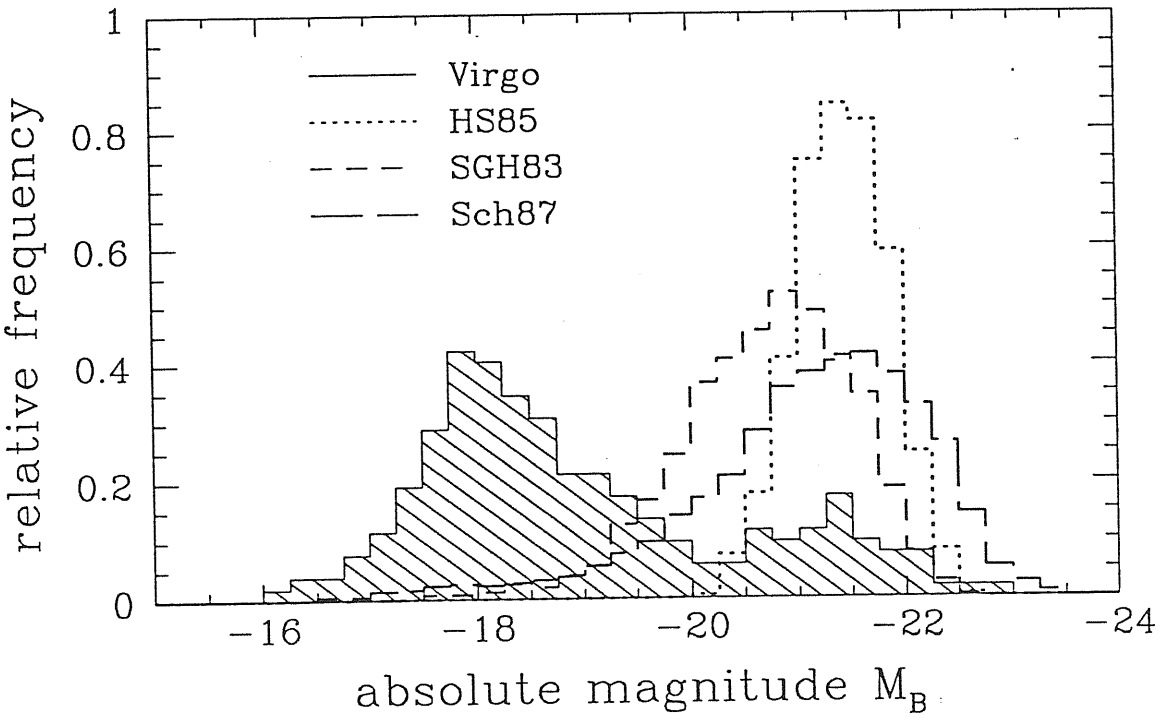

Figure 4.8: The LFs of the BCG samples used to populate the $(\log R_e, \mu_e)$ plane: SGH83 (short-dashed line), HS85 (dotted) and Sch87 (long-dashed). Magnitudes have been adjusted as explained in the text. The LF of the Virgo E and S0 galaxies (dashed histogram) is plotted for comparison.

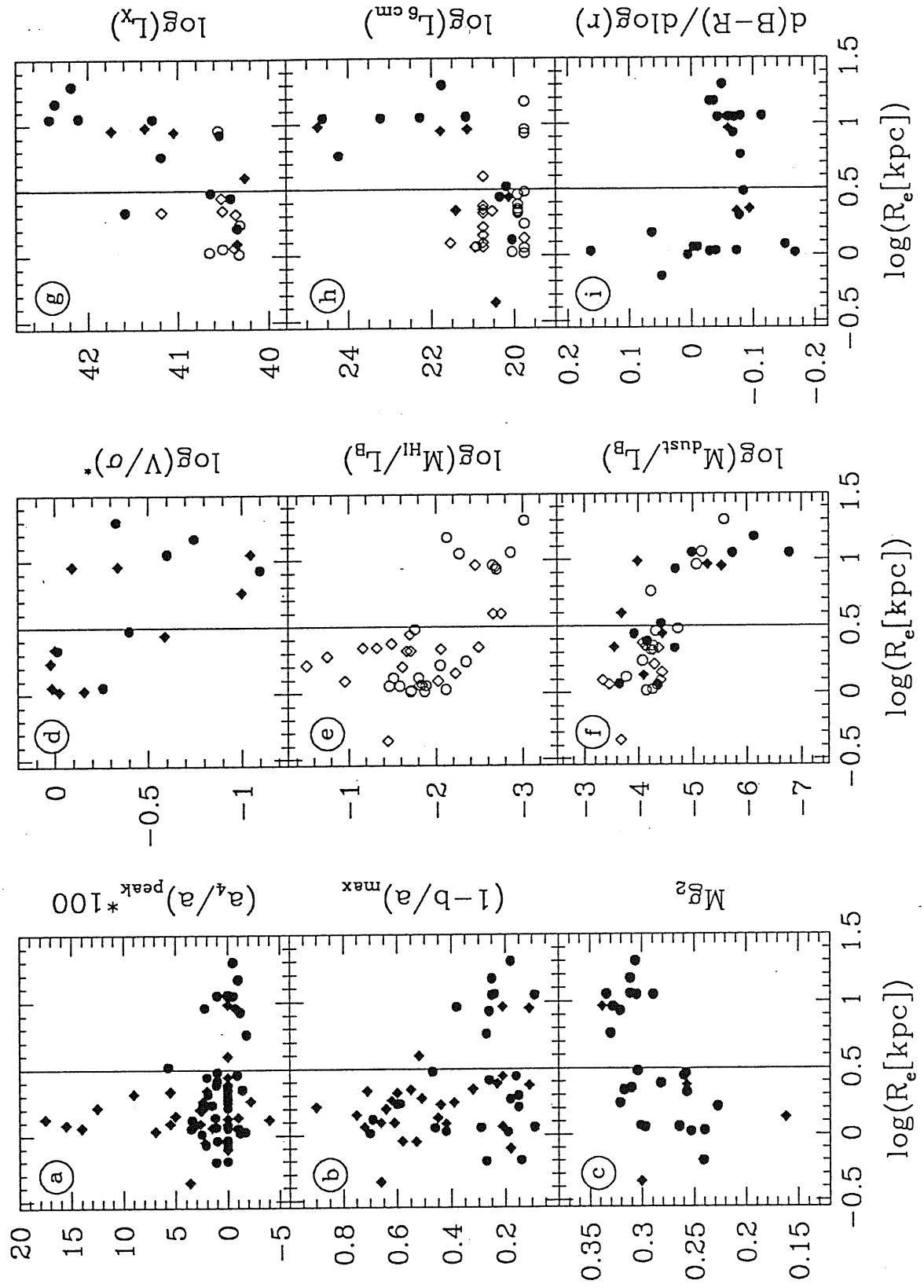
(a) $(a_4/a)_{peak}*100$
(b) $(1-b/a)_{max}$
(c) M_{g_2}
(d) $\log(V/\sigma)^*$
(e) $\log(M_{HI}/L_B)$
(f) $\log(M_{dust}/L_B)$
(g) $\log(L_X)$
(h) $\log(L_{6\,cm})$
(i) $d(B-R)/d\log(r)$
$\log(R_e[kpc])$

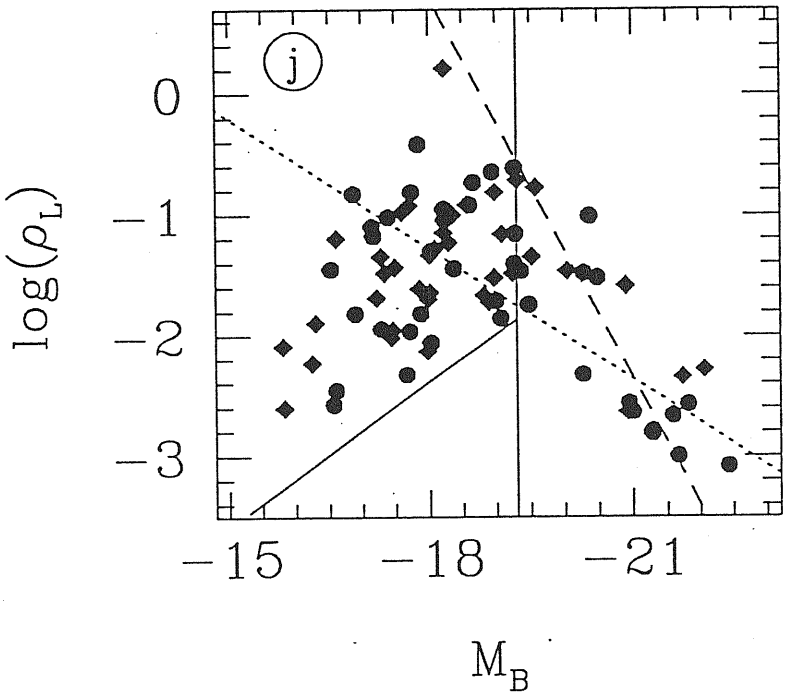

Figure 4.9: *Symbols:* from panel *a*) to *j*) filled circles represent E and dE galaxies from our Virgo-Fornax sample; filled squares are S0 and dS0 galaxies. Open symbols are upper limits. The solid vertical line shows the $R_e = 3$ kpc boundary between the '*ordinary*' and '*bright*' families.
Panel a) cos 4 is the relative value of the fourth cosine coefficient which measures the deviation of the isophote shape from a perfect ellipse (cf. Bender & Möllenhoff 1987). The parameter used here is the maximum positive value for discy objects and the minimum negative value for boxy galaxies. *Panel b*) ε_{max} is the maximum observed ellipticity. *Panel c*) The Mg_2 index is the deficit of flux expressed in magnitudes at the Mg *b* line, compared with a nominal continuum determined by interpolation from neighboring regions. *Panel d*) $(V/\sigma)^*$ is the ratio of observed V/σ to that expected for an oblate isotropic rotator of equal ellipticity. V is the maximum rotational velocity, and σ is the central velocity dispersion. *Panel e*) M_{HI}/L_B in $M_\odot/L_\odot$ is the ratio of the total HI gas content to the absolute B-luminosity. *Panel f*) M_{dust}/L_B in $M_\odot/L_\odot$ is the ratio of the dust mass derived from IRAS fluxes to the absolute B-luminosity. *Panel g*) L_X is the X-ray luminosity for the Einstein data, in erg s^{-1}. *Panel h*) L_{6cm} is the radio luminosity at 6 cm continuum, in Watt Hz^{-1}. *Panel i*) $d(B-R)/d\log(r)$ is the logarithmic color gradient. *Panel j*) ρ_L is the luminosity density within the volume containing half the total emitted light in $L_\odot$ pc^{-3}. The diagonal solid line marks the locus of the constant effective radius $R_e = 3$ kpc; the vertical solid line is at $M_B = -19.3$, and marks the breakpoint luminosity for the two families of galaxies. The dotted line represents the scaling law proposed by Djorgovski (1992); the dashed line corresponds to the HK relation.

Chapter 5

On the Shape of the Light Profiles of Early–type Galaxies

5.1 Introduction

Several attempts have been made in the past to find 'good' empirical representations of the light profiles of galaxies, to be used as tools for quantitative classification and parameterization, for the identification of components and/or signatures of interactions, and as tests for models and predictions of numerical simulations (cf. the review by Capaccioli 1989b).

Among the formulae proposed so far, the $r^{1/4}$ law, introduced by de Vaucouleurs (1948) to represent the light profiles of ellipticals and of the spheroidal components of disc galaxies, has justifiably gained a popularity which has often been confused with 'universality'.

The $r^{1/4}$ formula

$$I(r) = I_e \exp\left\{-k\left[\left(\frac{r}{r_e}\right)^{1/4} - 1\right]\right\} \tag{5.1}$$

has 'scale' parameters only: a characteristic radius r_e, and the corresponding surface brightness I_e. The constant k is usually chosen in such a way that r_e is the radius of the isophote containing half of the total luminosity; then $k = 7.6692$, and r_e and I_e are named effective radius and effective surface brightness. Useful formulae and tables related to the $r^{1/4}$ law may be found in Poveda, Iturriaga & Orozoco (1960), de Vaucouleurs (1961), Young (1976), and Mellier & Mathez (1987).

The $r^{1/4}$ formula has succeeded in reproducing, with a remarkable accuracy, the luminosity profiles of quite a few E galaxies. For instance, according to de Vaucouleurs & Capaccioli (1979) and Capaccioli et al. (1990b), the $r^{1/4}$ fit of the surface brightness distribution of the standard E1 NGC 3379 gives observed–calculated (O–C) residuals smaller than 0.08 mag over a 10-mag range. Also, the $r^{1/4}$ law has been often used as a reference for the class of E galaxies in testing and interpreting the results of numerical models of violent relaxation (van Albada 1982), merging of galaxies (Barnes 1988) and tidal stripping of ellipticals (Aguilar & White 1986). While these models produce $r^{1/4}$-like density profiles, a physical basis for this law is still lacking.

Moreover, the analysis of the systematic deviations from the $r^{1/4}$ behavior has proven an effective tool for the discovery of secondary components (such as stellar discs), substructures (lenses, shells, ripples, etc.), and tidal effects (seen as a shallowing or a steepening of the light profiles in the outer parts; cf. Kormendy 1980, Prugniel, Nieto & Simien 1987). And even the very first identification of the two fundamental photometric components of disc galaxies (de Vaucouleurs 1958, 1959) originated from the intuition that bulges of spirals might have $r^{1/4}$ light profiles.

Modern photometry of galaxies has shown, however, that, for a large fraction of elliptical galaxies and of spheroids, the $r^{1/4}$ law is only a first-order approximation: often it fits well only a limited interval of the luminosity profile.

For instance, Michard (1985) noted that systematic deviations from the $r^{1/4}$ fit are similar for galaxies of similar luminosities. The best match seems to occur for objects with $M_B = -21$, with typical deviations of the order of 0.1–0.2 mag arcsec^{-2} (Capaccioli 1985).

Schombert (1986) found that, for a large fraction of the brightest cluster galaxies, the $r^{1/4}$ interpolation is applicable to the middle part of the light profile only (between 21 and 25 B–mag arcsec^{-2}). More importantly, he pointed out that the shape of the light profiles is a unique function of the total luminosity: they become shallower in an ($r^{1/4}$, μ) diagram as the luminosity increases (see his Fig. 14).

Binggeli & Cameron (1991) have shown that, at the faint end of the galaxy luminosity function, dwarf ellipticals are better described by exponential or by King model profiles. By examining a wider range of luminosities, the same authors conclude that "profile type is strongly correlated with the total magnitude of the galaxy".

As for bulges of S0s, it has been noted (e.g. Capaccioli 1987, 1989b) that the minor-axis light-profiles of edge-on objects deviate systematically from the $r^{1/4}$ trend [an upward concavity in the ($r^{1/4}, \mu$) representation].

All of the above evidence casts some doubts on the universality of the $r^{1/4}$ law, and in particular on its reliability for deriving accurate effective parameters for early–type galaxies, as the results are too dependent on the portion of the light profile that is fitted[1]. This fact, and the uncertainty on the sky–background subtraction, is the main reason for the large discrepancies in the values of the effective parameters of early-type galaxies reported by different authors (see Chapter 4).

Prompted by these considerations, we decided to study the behavior of a generalized de Vaucouleurs formula (Sersic 1968), i.e. of a power law in which the exponent is a free parameter $1/n$. Let us say explicitly that the emphasis of this work is not in showing that the $r^{1/n}$ law provides better fits than the simple de Vaucouleurs formula; improved representations of light profiles are just expected as an obvious consequence of the introduction of a free parameter. Our aim is instead to investigate whether the parameter n has any physical justification by searching for correlations with global photometric parameters (effective radius and total luminosity).

[1] We remark here that in principle r_e is a model–independent parameter, being simply the radius of the isophote encircling half of the total luminosity. Therefore its identification with the scale-radius of the $r^{1/4}$ law is justified only for those galaxies that are perfectly fitted by the $r^{1/4}$ law over the whole light profile.

In Section 2 we give a brief account of the properties of the $r^{1/n}$ law. A more complete description (luminosity density, dynamical characteristics and phase-space distribution function) was given by Ciotti (1991). In Section 3 we present the application of the $r^{1/n}$ law to the light profiles of a volume–limited sample of early–type galaxies in the Virgo and in the Fornax clusters. Finally, in Section 4 we discuss the implications of the correlation between n and R_e, also in relation to the dichotomy between the '*ordinary*' and the '*bright*' galaxy families, claimed in Chapter 4.

5.2 Photometric Properties of the $r^{1/n}$ Law

In its simplest form the $r^{1/n}$ law, originally proposed by Sersic (1968), is given by the formula

$$I(r) = I_0 \, \mathrm{dex}(-r^{1/n}) \tag{5.2}$$

Introducing the scale-radius r_e, it can be rewritten

$$I(r) = I_e \, \mathrm{dex}\left\{-b_n\left[\left(\frac{r}{r_e}\right)^{1/n} - 1\right]\right\} \tag{5.3}$$

and, in logarithmic form, as

$$\mu(r) = \mu_e + c_n\left[\left(\frac{r}{r_e}\right)^{1/n} - 1\right] \tag{5.4}$$

with $c_n = 2.5\, b_n$. The coefficient b_n can be chosen in such a way that the scale-radius r_e is the radius encircling half of the total luminosity L_T. The latter can be expressed as a function of r_e and I_e:

$$L_T = K_n \, I_e \, r_e^2 \tag{5.5}$$

We have computed the coefficients b_n and K_n by numerical integration of a $r^{1/n}$ galaxy model. In the range explored, $0.5 \leq n \leq 16.5$, they are very well approximated by the relations

$$b_n = 0.868\, n - 0.142 \tag{5.6}$$

and

$$\log(K_n) = 0.030[\log(n)]^2 + 0.441 \log(n) + 1.079 \tag{5.7}$$

both with a rms scatter of 0.014.

For fitting purposes we will use the relation

$$\mu(r) = A + B\, r^{1/n} \tag{5.8}$$

where, according to equation 5.4, the effective parameters of the $r^{1/n}$ model are

$$\begin{aligned} \mu_e^\star &= A + c_n \\ r_e^\star &= (c_n/B)^n \end{aligned} \tag{5.9}$$

We have added a superscript $\star$ to the scale parameters of the $r^{1/n}$ formula to prevent confusion with their model-independent analogues.

5.3 An Application of the $r^{1/n}$ Law

The $r^{1/n}$ law has been fitted to the major and minor axis light-profiles and to the equivalent profiles of 80 early–type galaxies belonging to a sample of Virgo cluster and of Fornax cluster members. The B–band photometry that we use here is the result of the coupling of CCD images with deep Schmidt plates. This 'global mapping' technique (Capaccioli & Caon 1989) provides accurate light profiles spanning wide surface brightness ranges. Details about the properties of the sample and the data reduction can be found in CCR and in Chapter 2.

The radial range of the light profiles over which the best fit with relation (5.8) has been computed goes from outside the region dominated by the seeing (typically a few arcsec, and $\mu_B > 19.6 \pm 1.1$) out to where the uncertainty in the sky subtraction and some possible contamination from nearby objects render the light profiles unreliable. In other words, we fit the formula to the entire range of surface brightness covered by state of the art photometric observations, removing only what is not measurable or just not directly measured. More specifically, convolution experiments (see below and CCR) have been used to determine the boundary of the region where the surface brightness is changed by more than 5 % because of seeing convolution. As for the outer boundary of our fitting range, we have adopted the standard value of $\mu_B = 27$ mag arcsec^{-2}, where the average photometric error is not larger than 0.25 mag according to fig. 2.3. This limit has been moderately varied to account for the properties intrinsic to each galaxian image.

For some objects with peculiar inner light-profiles, the fit has been restricted to a smaller radial range. In a few cases, especially for very flattened discy galaxies, the fit of the $r^{1/n}$ law was simply impossible. Eleven galaxies out of 80 could not be fitted at all because of the presence of prominent disc components, dust lanes, tidal distortions, or simply because of the irregular shape of the light profiles (see Table 5.1). For the remaining 69 galaxies, 20 major axis light profiles, 12 equivalent profiles and 2 minor axis light profiles could not be fitted by the $r^{1/n}$ law. In some cases the fit required an additional (exponential?) component, while in others the profiles are intrinsically distorted.

In order to minimize the possible repercussions of seeing blurring for results, we have repeated the fitting procedure with light profiles deconvolved according to the technique of Bendinelli (1991), and using in all cases a single Gaussian point spread function (PSF) with the stellar full width at half maximum (FWHM) measured by CCR, and those listed in Chapter 2.

In practice, for each galaxy profile we have scanned a fine grid of values of n, and computed the rms scatter of the (O−C) residuals. We have then chosen as the best value for the exponent the one giving the smallest scatter σ_n. Note that for many objects the residuals are due to noise and do not reflect systematic departures from the $r^{1/n}$ law. The resulting values of n range from 1 to 17. Two examples of the quality of the fits are shown in Fig. 5.1, for a high and a low value of n.

In order to estimate the uncertainty associated to the determination of n, for the light profiles of each galaxy we computed the values $n_1 < n$ and $n_2 > n$ at which the rms scatter σ of the (O−C) residuals exceeds by 25% the value of the best fit. For $n \lesssim 10$ we obtain

Table 5.1: List of rejected objects

Ident.	Type	M_B [mag]	$\log(R_e)$ [kpc]	μ_e B-mag arcsec^{-2}	Notes on light profiles
IC 3773	dS0(9)	−17.46	0.26	23.79	irregular; stretched
NGC 4200	S0(4)	−17.34	0.09	22.72	dominant disc; rapid fall off
NGC 4269	S0(2)	−17.98	0.39	24.01	irregular
NGC 4377	S0(3)	−18.56	0.06	21.61	dominant disc; irregular
NGC 4417	S0(7)	−19.52	0.33	22.20	dominant disc; irregular; stretched
NGC 4526	S0(6)	−20.90	0.60	21.91	dominant disc; irregular
NGC 4578	S0(4)	−18.82	0.35	22.74	irregular
FCC 301	E4	−17.17	−0.04	22.60	irregular; stretched
NGC 1316	S0 pec	−22.07	0.99	22.91	irregular; dust lanes
NGC 1381	S0(9)	−18.98	0.09	20.92	dominant disc; stretched
NGC 1396	d:E6,N	−16.57	0.35	25.04	irregular

typically:

$$\Delta n = n - n_1 \simeq n_2 - n \simeq 0.25\, n \tag{5.10}$$

For $n > 10$, the above relation still holds for n_1, while $n_2 - n$ can reach values as large as n itself. For example, if a light profile is best fitted by an $r^{1/4}$ law (typical scatter $\sigma_n \simeq 0.05$), the use of an $r^{1/3}$ or an $r^{1/5}$ law would cause σ to increase by 25%. On the other hand, when $n > 8$ is the best-fitting result, the same increment of σ is achieved by using an $r^{1/(8\pm2)}$ law.

For each galaxy of our sample, Table 5.2 provides the identification (column 1), the morphological type according to Binggeli et al. (1985) for the Virgo galaxies, and according to Ferguson (1989) for the Fornax galaxies (column 2), the total luminosity in the B–band, the logarithm of the (model-independent) effective radius R_e (in kpc), and the corresponding surface brightness I_e (columns 3 to 5) from CCR and from Chapter 2, the borders, μ_{start} and μ_{end}, of the surface brightness range of the fit (columns 7 and 8), the values of n for the major and minor axes (n_{maj} and n_{min}) and for the equivalent light-profile (n_{eq}) (column 8), the rms scatter σ_n of the fit (column 9), the coefficients A and B of the fitting formula (5.8), where μ is in BSS units (B-mag arcsec^{-2}) and r in arcsec (columns 10 and 11), and a code for the quality of the fit (column 12), G=good, F=fair, P=poor, which gives an indication of the occurrence of systematic deviations of the model from the data both inside and outside the fitting range.

The largest deviations occur in the inner few arcsec, i.e. in the region dominated by seeing and where nuclear subcomponents distinct from the main body of the galaxy may be present (cf. Nieto 1992). Our experiments of deconvolution of the light profiles with the Gaussian expansion method devised by Bendinelli (1991) show that in some cases the deconvolved profiles follow the $r^{1/n}$ law up to the center, but for most of the galaxies the $r^{1/n}$ formula

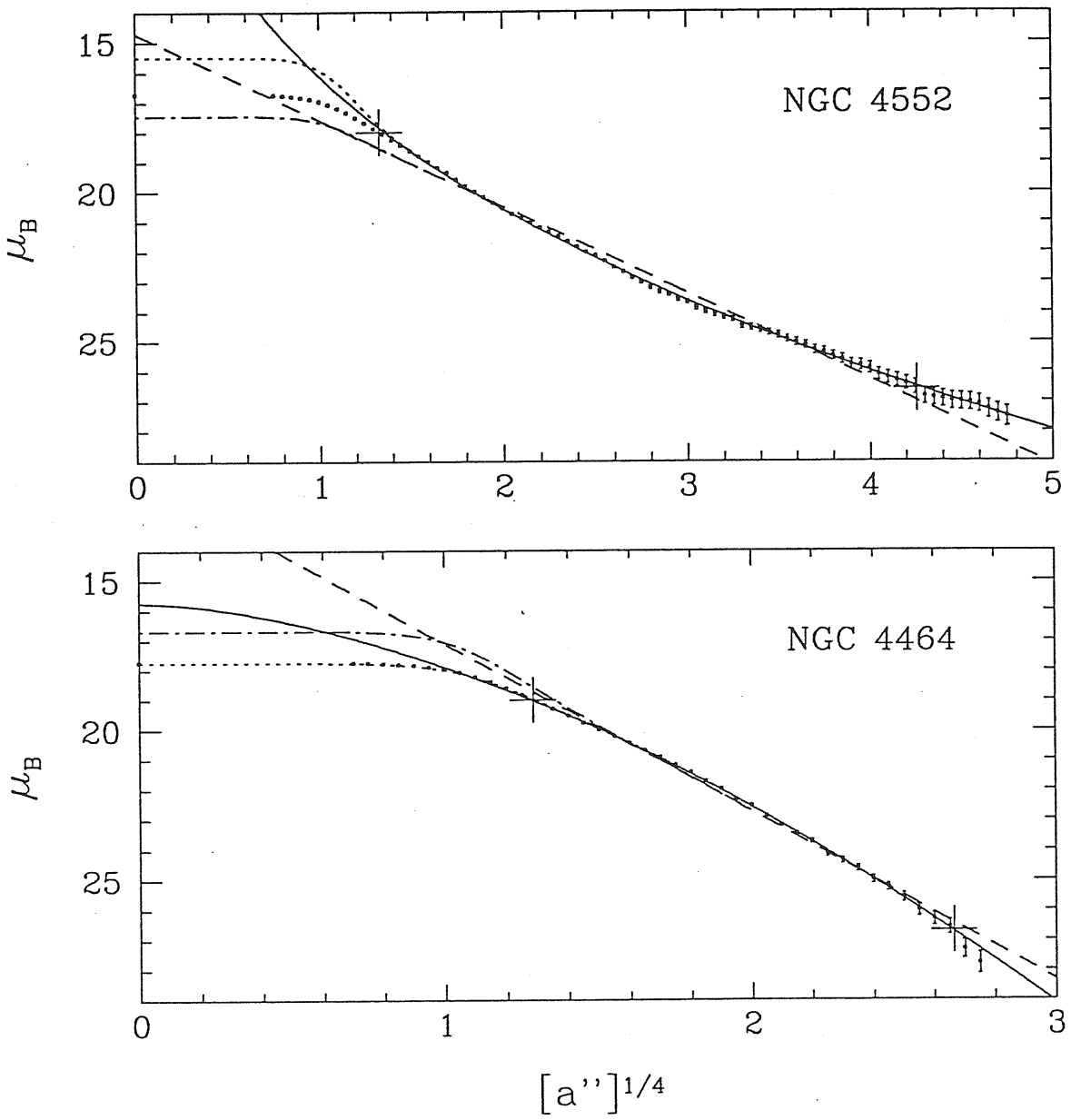

Figure 5.1: Observed major axis B-band light profiles of the S0 galaxy NGC 4552 and of the E3 NGC 4464 (*filled circles*), fitted by an $r^{1/n}$ law (solid line) with $n = 13.9$ and $n = 2.4$ respectively. Crosses mark the borders of the fitting interval. The relative uncertainty of the data is indicated by the error bars, barely visible everywhere but in the outer parts. The dotted lines show the $r^{1/n}$ models convolved with a single Gaussian PSF and the proper FWHM (2 arcsec for both galaxies, according to CCR). The dashed lines reproduce the $r^{1/4}$ laws best fitting the data within the same intervals.

fails to model light profiles inside $\sim$ 1 arcsec (or $\sim$ 0.1 kpc, adopting for the both the Virgo and the Fornax clusters a distance of 18.3 Mpc after Capaccioli et al. 1990a). This is not at all surprising in view of the variety of behaviors exhibited by the nuclei of early-type galaxies (cf. Møller, Stiavelli & Zeilinger 1993).

The extrapolation of the $r^{1/n}$ best fit to the outer parts of the light profiles (typically for $\mu > 26.5 \pm 0.9$ B–mag arcsec^{-2}) is also often inadequate, mainly because of the large uncertainty in the photometry at these very faint light levels. However, we cannot exclude the presence of systematic deviations caused by environmental effects.

The empirical parameters A and B are found to present an approximately linear correlation with n. A least-squares fit for the values pertaining to the major axis fit gives $A = 21.09 - 1.60\,n$ (rms= 1.15), and $B = -1.743 + 1.330\,n$ (rms= 0.860). Analogous relations are valid for the minor axis and equivalent light profiles. However, none of these relations bears any physical significance, all being artifacts of the formulation of the $r^{1/n}$ law. In fact:

$$A = \mu_e^\star - 2.5\,b_n = \mu_e^\star - 2.17\,n + 0.355 \tag{5.11}$$

Therefore A depends on n alone, with $\mu_e^\star$ contributing just to the scatter; at fixed n, μ_e varies at most by 3 mag. Similarly, we have $B = \left[c_n/(r_e^\star)^{1/n}\right]$, or, in logarithmic form

$$\log B = \log c_n - \frac{1}{n}\log r_e^\star \simeq \log n - \frac{1}{n}\log r_e^\star + \text{constant} \tag{5.12}$$

As $r_e^\star$ is coupled with n, B turns out to be a function of n alone, while the contribution to the scatter at fixed n due to $r_e^\star$ is cut down by the coefficient $(1/n)$.

5.4 Results

Fig. 5.2 gives a quick impression of the dramatic improvement in the fit of the major axis light profiles of the sample galaxies using the $r^{1/n}$ formula rather than just the $r^{1/4}$ law.
As stated in Section 1, this result is not at all surprising in view of the introduction of an additional free parameter, which, however, might carry no physical meaning. We shall show now that in fact n correlates with the global galaxian parameters.

A plot of n_{maj} versus R_e for the galaxies of our sample (Table 5.2) shows that n increases steadily with R_e (Fig. 5.2). The same property applies to n_{min} and n_{eq}, but with a larger scatter for n_{min} and a slightly smaller scatter for n_{eq}. We also note that the trend of n with R_e does not seem to be different for the two families of hot stellar systems introduced in Chapter 4, namely the '*ordinary*' ($R_e < 3$ kpc) and the '*bright*' ($R_e > 3$ kpc) galaxies. However, a possible discontinuity between the two families may be hidden by the large dispersion of the values of n. A least square fit gives:

$$\log(n) = 0.28 + 0.52\log(R_e) \tag{5.13}$$

with a rms= 0.18. A similar correlation is obtained if we plot n versus the total luminosity M_B of the galaxies.

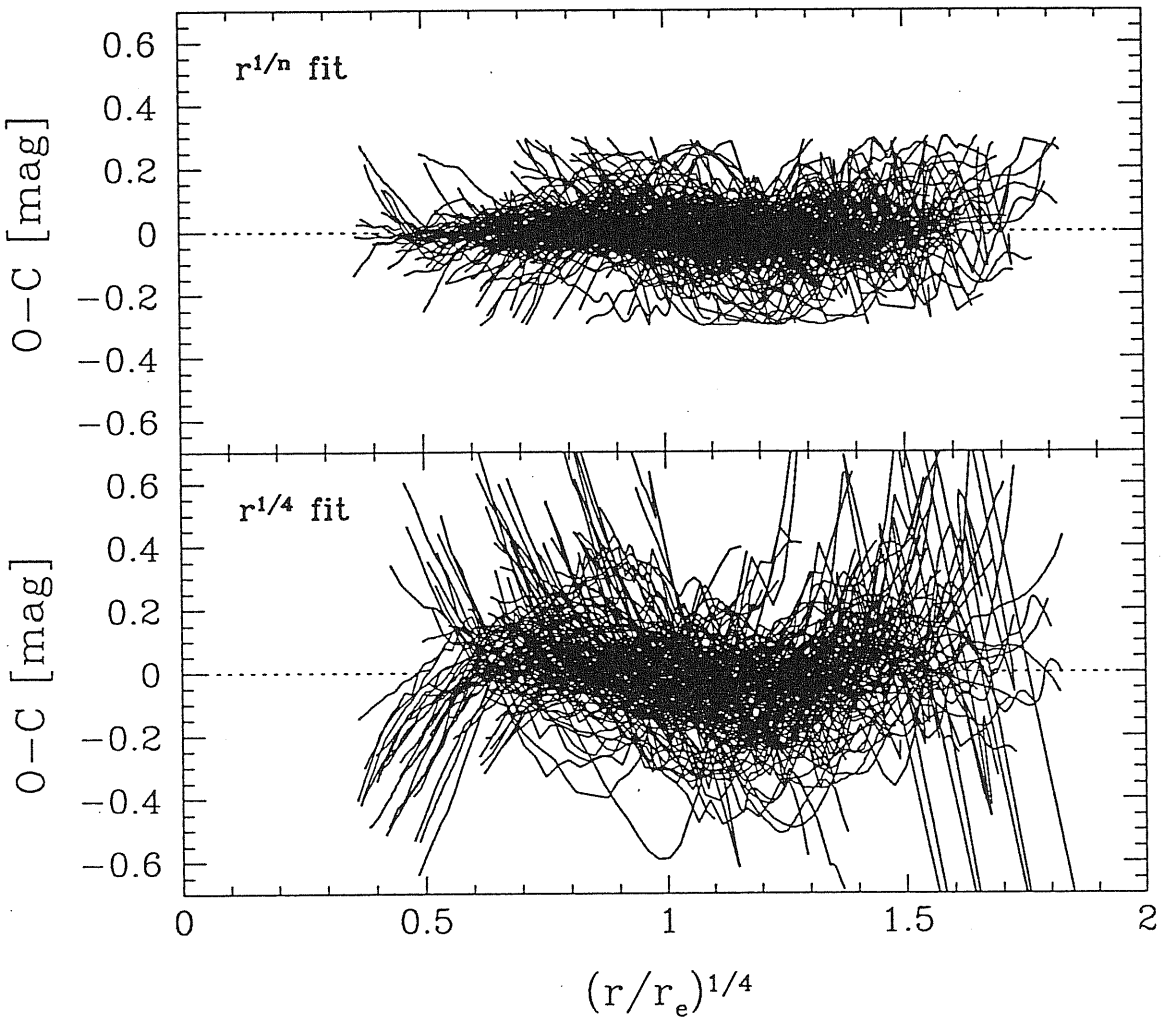

Figure 5.2: Radial run of the (O−C) residuals (in magnitudes) for the fit of the B-light profiles of our galaxies with the $r^{1/n}$ law (upper panel) and with the de Vaucouleurs law (lower panel); the abscissa is the reduced galactocentric distance r/r_e.

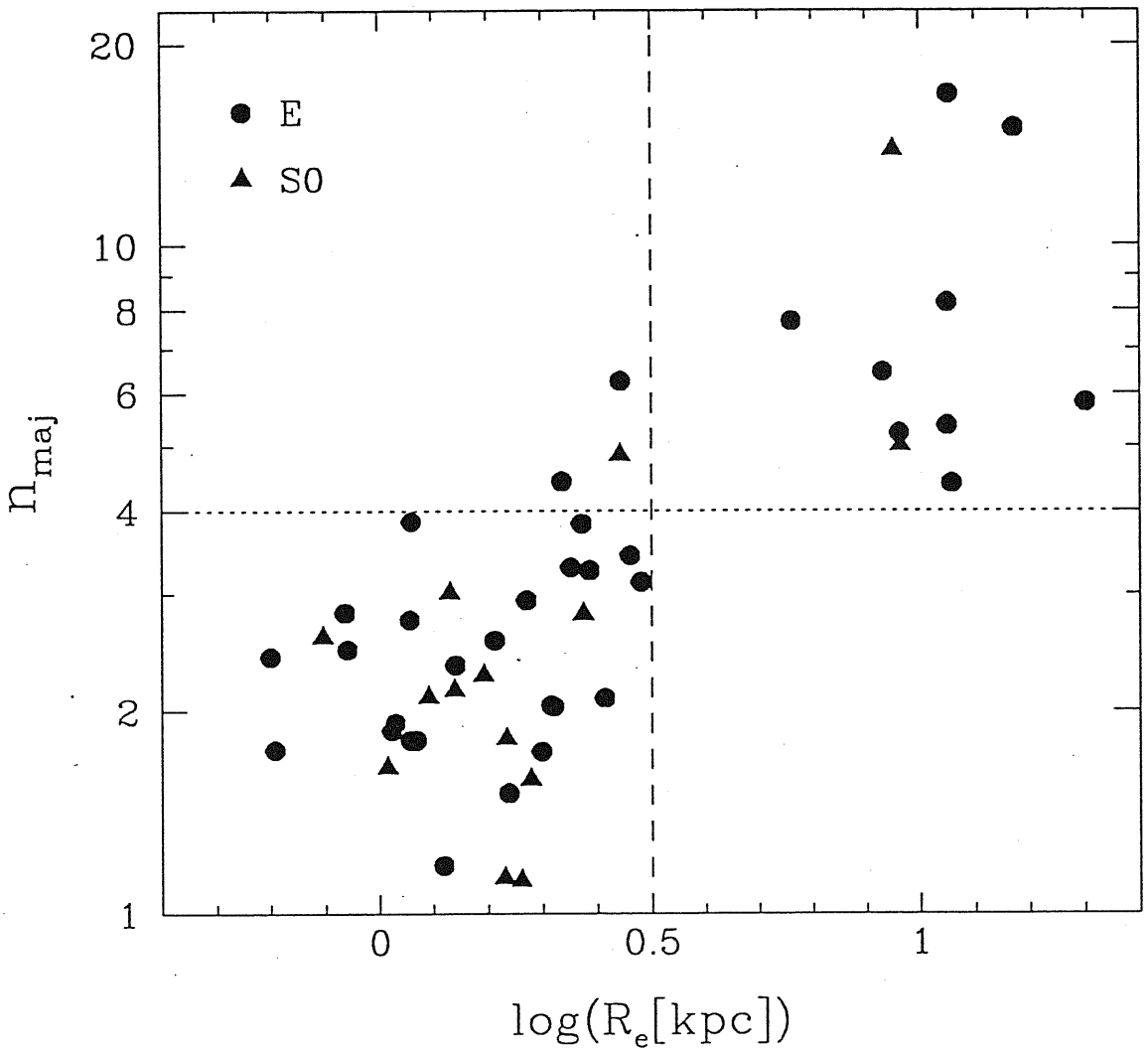

Figure 5.3: Plot of n_{maj} versus the effective radius R_e [kpc] for the galaxies of our sample. Circles are for ellipticals and triangles are for S0s. The dotted line marks the value $n = 4$, corresponding to the de Vaucouleurs law; the dashed line ($R_e = 3$ kpc) marks the separation between the '*ordinary*' and '*bright*' galaxy families.

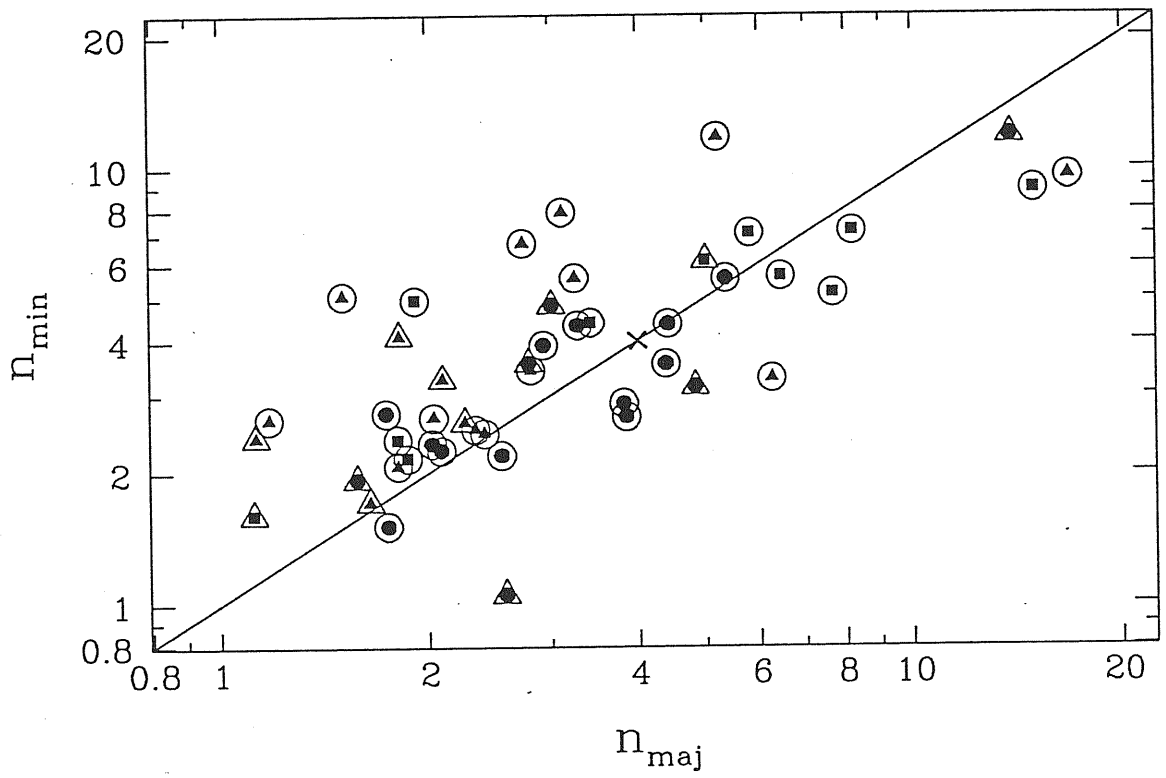

Figure 5.4: Plot of n_{min} versus n_{maj}. Elliptical and S0 galaxies are marked as open circles and open triangles respectively. The inner filled symbols refer to the geometrical properties of the isophotes: discy (*triangles*), boxy (*squares*), and all other (*circles*) objects. The cross at the center is the value $n = 4$ of the $r^{1/4}$ law. The solid line is where $n_{maj} = n_{min}$.

Fig. 5.4 correlates n_{maj} with n_{min}. Different open symbols are used for E and S0 galaxies (circles and triangles respectively). The sample is further subdivided according to the isophote shape classification introduced by Bender, Döbereiner & Möllenhoff (1988): discy objects ($\cos 4 > 0$) are indicated by solid triangles, boxy objects ($\cos 4 < 0$) by solid squares, and all other galaxies by solid circles. We note that most of the objects with discy signatures have minor axis profiles significantly steeper than the major axis ones. This effect is probably due to the presence of a real flat component (disc), more prominent along the major than along the minor axis.

In order to verify if the correlation observed in Fig. 5.2 extends to fainter galaxies, we have made use of the data from Davies et al. (1988). These authors fitted the B-band light-profiles of a low-surface-brightness galaxy sample of the Fornax cluster with a generalized de Vaucouleurs law in the form $I = I_0 \exp\left[-(r/A)^N\right]$. By transforming their exponent N into our n, and by computing the values of R_e (which are not fully consistent with the model-independent values used for our galaxies), we were able to add Davies et al. data to

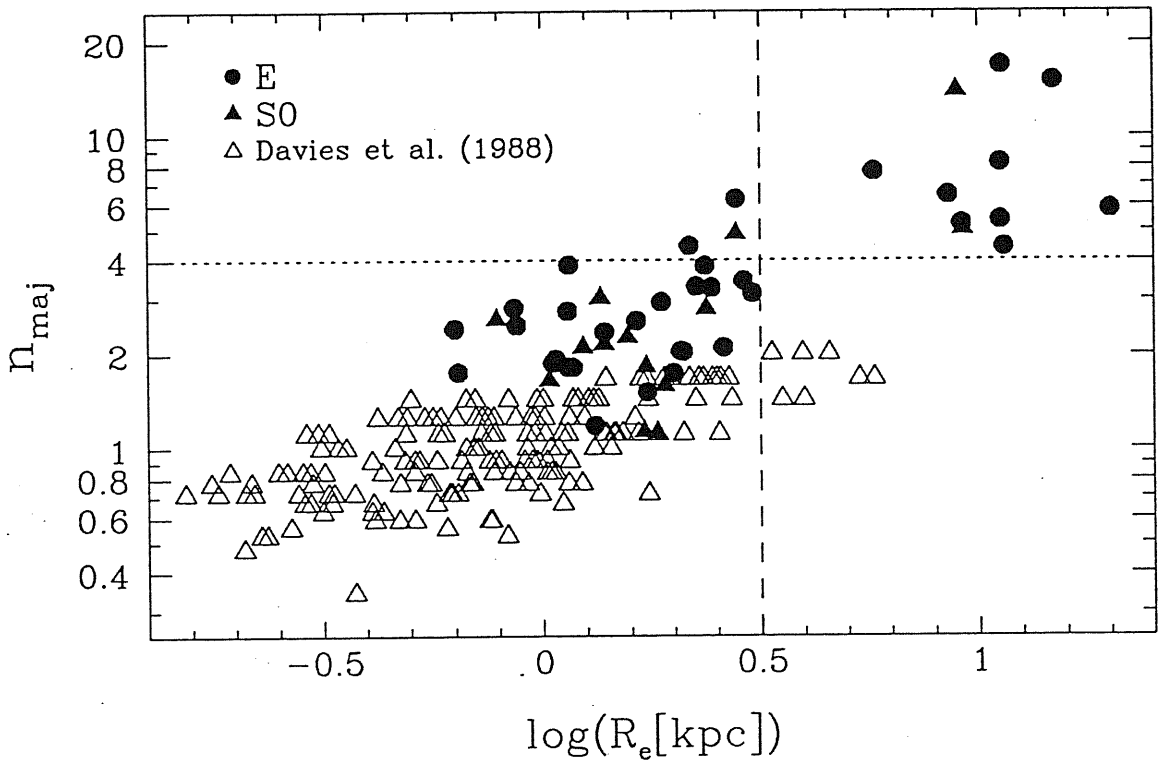

Figure 5.5: Plot of n_{maj} versus R_e [kpc], obtained by adding to our Virgo and Fornax clusters data (*filled symbols*) those of Davies et al. (1988) (*open triangles*). For our objects we retain the distinction between Es and S0s.

the present ones (Fig. 5.5). It is now evident that the correlation between n and R_e holds, although with a large scatter, from $n = 0.3$ and $R_e = 0.1$ kpc out to $n = 12.6$ and $R_e = 32$ kpc. Here the value $n = 4$ seems to divide the '*ordinary*' and the '*bright*' families. Galaxies with $n > 4$ belong to the class of galaxies that have possibly grown in size and luminosity by merging processes (Chapter 4).

5.5 Discussion

The results obtained in this work can be summarized as follows.

1. Elliptical and S0 galaxies are fitted by a generalized de Vaucouleurs law (with exponent n from 1 to 17) over most of their light profiles ($\Delta\mu \simeq 7$ mag) with very small scatter ($\langle \mathrm{rms} rangle \simeq 0.05$ mag).

2. A good correlation exists between the exponent n and the global galaxian parameters R_e and M_B: galaxies with larger values of n are generally more luminous.

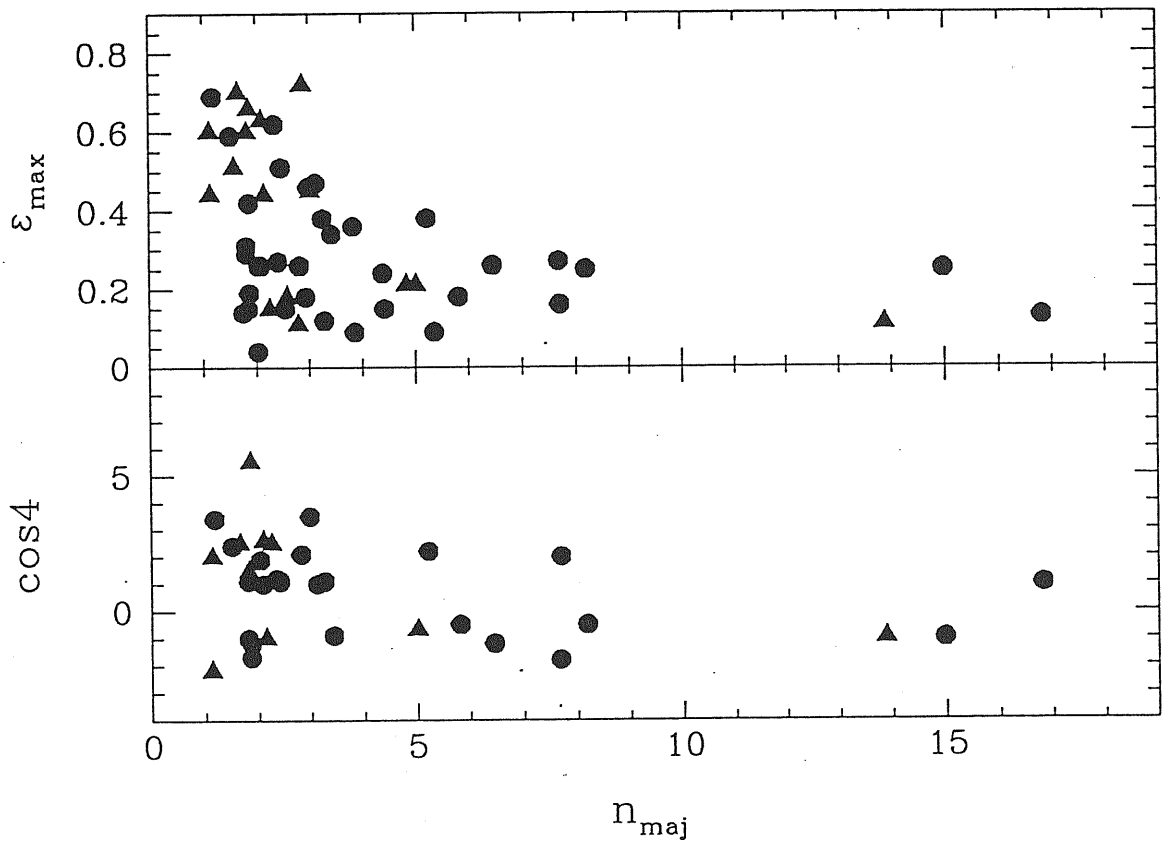

Figure 5.6: Plot of the maximum ellipticity ε_{max} and of the cos 4 isophote shape descriptor versus n_{maj}. Symbols as in Fig. 5.3.

3. The exponent n roughly correlates with the isophote shape parameter cos 4: boxy galaxies have larger n than discy galaxies (Fig. 5.6). This is an expected property in view of the primary correlation between cos 4 and the effective parameters. In contrast, n does not correlate with the angle of maximum twist of the isophotes.

4. A trend is visible in the diagram of n_{maj} versus the maximum ellipticity ε_{max}, with more elongated galaxies having lower values of n (Fig. 5.6). This trend disappears when n_{min} is considered instead of n_{maj}; such a minor correlation of ε_{max} with the residual of n with respect to the line that best fit the $\log R_e - \log n$ correlation is therefore probably the result of the presence of a disc structure.

5. The exponent n is not systematically larger for Es than for S0s, as one might suspect in view of the effects of the disc.

The most interesting fact here is that the light profile shape parameter n correlates with the global parameters of the Fundamental Plane (either R_e or, alternatively, M_B). Although the scatter in the correlations is large, the above result is at variance with the claim (e.g. Djorgovski & Davis 1987) that the variables describing the shape of the light distribution are independent of the Fundamental Plane parameters. Moreover, it provides evidence that the segmentation of the light profiles of early-type galaxies into tidal classes (Kormendy 1980) is unreal. In fact, stretching or truncation of light profiles (i.e. large or small value of n) is directly correlated with structural parameters rather than with the environmental conditions, as also indicated by the lack of correlation between n and the local projected galaxian density (Chapter 6). Also, while Kormendy's observation of a change of slope applies to the outer light profile only, our parameter n is 'global' in the sense that it applies to the entire light profile.

Recently Makino, Akiyama & Sugimoto (1990), looking for a physical explanation of the de Vaucouleurs law using dynamical arguments, pointed out that any $r^{1/n}$-law model is practically indistinguishable from the de Vaucouleurs law for $3 < n < 10$. They argued against the 'universality' of the $r^{1/4}$ law, which is merely a good function to adopt for the description of light profiles. Here, using real data, we have shown that the $r^{1/4}$ law is only a particular case of a more general $r^{1/n}$ law, where n is a function of total luminosity. The de Vaucouleurs law therefore loses its universality but, possibly, for assuming another important property: it flags the transition between the '*ordinary*' and the '*bright*' families or, in other words, it forms the boundary between the inbred variety of hot stellar systems and the category of objects that developed by accretion.

Table 5.2: Results of the fit for the sampled galaxies

Ident.	Type	M_B	$\log(R_e)$	μ_e	μ_{start}	μ_{end}	n_{maj} n_{eq} n_{min}	σ_n	A	B	Q
		[mag]	[kpc]	B-mag arcsec^{-2}				[mag]			
IC 3468	E1,n	−17.67	0.41	24.31	20.75	26.40	2.09	0.037	19.20	0.976	G
					20.75	25.60	2.21	0.026	19.12	1.118	G
					21.00	25.50	2.25	0.039	19.18	0.278	G
IC 3540	S0(2)	−16.61	−0.10	22.11	21.50	27.25	2.58	0.077	15.61	2.747	F
					22.00	26.75	1.30	0.066	19.50	0.504	F
					21.50	26.75	1.05	0.092	20.12	0.278	G
IC 3653	E3	−16.87	−0.19	21.70	20.00	27.25	1.75	0.138	17.99	1.182	F
					20.00	26.80	1.82	0.106	17.87	1.316	F
					20.50	26.00	1.51	0.033	18.71	0.839	G
NGC 4168	E2	−19.07	0.44	22.98	20.00	26.20	6.25	0.048	11.24	6.689	F
					19.50	26.80	2.53	0.040	16.37	1.659	G
					20.00	26.00	3.27	0.035	16.22	2.406	G
NGC 4215	S0(9)	−18.35	0.06	21.55	–	–	–	–	–	–	–
					19.20	27.00	2.63	0.060	16.38	2.064	F
					20.00	27.50	3.34	0.048	14.05	4.041	F
NGC 4255	S0(6)	−17.70	−0.05	21.79	–	–	–	–	–	–	–
					–	–	–	–	–	–	–
					19.00	26.50	3.36	0.056	13.60	4.459	G
NGC 4261	E2	−20.27	0.76	23.45	18.50	26.00	7.68	0.038	8.17	8.852	G
					19.00	24.30	7.65	0.034	8.64	8.648	G
					19.00	26.50	5.14	0.075	13.05	4.760	F
NGC 4268	S0(6)	−17.59	−0.04	21.67	–	–	–	–	–	–	–
					–	–	–	–	–	–	–
					20.00	27.00	1.95	0.044	17.44	1.547	F
NGC 4270	S0(6)	−18.22	0.09	21.84	–	–	–	–	–	–	–
					–	–	–	–	–	–	–
					20.00	26.00	2.35	0.044	16.66	1.997	G
NGC 4281	S0(6)	−19.24	0.34	22.22	–	–	–	–	–	–	–
					21.00	24.70	2.37	0.029	17.25	1.289	P
					20.50	27.00	4.42	0.039	12.96	4.934	F
NGC 4339	S0(0)	−18.89	0.37	22.82	19.50	27.00	2.79	0.103	16.96	1.772	F
					19.50	26.00	3.50	0.061	15.67	2.807	G
					19.50	26.00	3.55	0.061	15.49	2.950	G
NGC 4342	S0(7)	−18.23	−0.36	19.59	–	–	–	–	–	–	–
					18.00	25.00	2.32	0.037	14.98	2.403	F
					19.00	25.50	7.35	0.036	1.61	15.480	G
NGC 4352	S0(8)	−17.86	0.20	22.89	–	–	–	–	–	–	–
					20.70	26.00	2.30	0.076	18.11	1.353	P
					20.00	26.00	13.43	0.071	−5.03	23.312	P
NGC 4360	E2	−17.88	0.27	23.49	20.50	27.50	2.93	0.028	17.10	2.190	G
					20.50	27.50	3.33	0.033	16.34	2.842	G
					21.00	27.00	3.91	0.052	15.21	3.850	G

Table 5.2: *continued*

Ident.	Type	M_B	$\log(R_e)$	μ_e	μ_{start}	μ_{end}	n_{maj} n_{eq} n_{min}	σ_n	A	B	Q
		[mag]	[kpc]	B-mag arcsec^{-2}				[mag]			
NGC 4365	E3	−20.95	0.93	23.73	18.50	26.50	6.45	0.033	10.84	6.215	G
					18.50	26.50	6.08	0.034	11.35	5.863	G
					18.50	26.50	5.62	0.053	12.05	5.349	G
NGC 4370	S0(6)	−17.99	0.27	22.83	–	–	–	–	–	–	–
					–	–	–	–	–	–	–
					21.00	25.00	3.23	0.028	15.97	2.997	G
NGC 4374	E1	−21.59	1.05	23.85	18.50	26.50	8.19	0.032	7.60	8.682	G
					18.50	26.50	8.47	0.027	6.67	9.698	G
					19.00	27.00	7.14	0.043	9.48	7.299	G
NGC 4387	E5	−18.22	0.03	21.66	19.00	26.50	1.92	0.064	17.55	0.983	G
					19.00	24.50	2.12	0.021	17.04	1.418	F
					19.80	26.50	4.97	0.074	10.39	7.191	G
NGC 4406	E3	−21.67	1.17	23.97	18.50	24.50	14.98	0.036	0.44	16.495	G
					18.50	24.50	11.03	0.019	5.43	11.666	G
					18.50	24.50	8.89	0.020	8.08	9.159	G
NGC 4415	dE1,N	−17.72	0.30	23.45	20.00	25.00	1.74	0.057	19.55	0.640	F
					20.50	25.80	1.85	0.068	19.45	0.754	G
					21.30	27.00	2.73	0.070	17.69	1.921	G
NGC 4431	dS0,N	−17.44	0.28	23.63	20.50	27.00	1.58	0.084	20.14	0.418	G
					20.50	27.00	1.78	0.060	19.89	0.662	G
					21.50	27.00	1.93	0.049	19.79	0.894	G
NGC 4434	E0	−18.23	0.06	22.00	19.00	25.50	3.85	0.043	14.00	4.053	G
					19.00	24.80	4.17	0.044	13.42	4.620	G
					19.80	26.50	2.68	0.075	16.46	2.111	F
NGC 4436	dS0,N	−17.29	0.23	23.72	20.50	27.00	1.82	0.082	19.48	0.643	G
					21.00	28.00	2.40	0.063	18.38	1.526	G
					20.70	27.50	4.10	0.078	15.13	4.595	G
NGC 4452	S0(9)	−19.08	0.21	21.08	–	–	–	–	–	–	–
					–	–	–	–	–	–	–
					20.50	26.30	8.21	0.069	5.77	12.713	F
NGC 4458	E1	−18.37	0.21	22.49	20.00	25.60	2.55	0.044	17.28	1.635	G
					20.00	24.70	2.84	0.028	16.86	2.022	P
					20.50	26.50	2.19	0.063	18.17	1.168	P
NGC 4459	S0(2)	−20.04	0.44	22.16	20.00	24.75	4.84	0.036	12.55	4.589	F
					20.00	24.70	5.14	0.027	11.73	5.315	P
					20.50	28.00	3.13	0.070	15.70	2.198	F
NGC 4464	E3	−17.84	−0.20	20.89	19.00	26.70	2.41	0.037	15.73	2.163	G
					19.00	26.00	2.61	0.024	15.42	2.589	G
					20.30	26.00	2.46	0.023	16.14	2.287	F
NGC 4472	E2	−22.43	1.30	24.07	18.50	26.50	5.81	0.030	12.07	4.680	G
					18.50	26.50	6.27	0.023	11.20	5.479	G
					18.50	27.00	7.06	0.030	9.75	6.814	G

Table 5.2: *continued*

Ident.	Type	M_B	$\log(R_e)$	μ_e	μ_{start}	μ_{end}	n_{maj} n_{eq} n_{min}	σ_n	A	B	Q
		[mag]	[kpc]	B-mag arcsec^{-2}				[mag]			
NGC 4473	E5	−20.28	0.48	22.20	20.80	26.70	3.12	0.044	15.73	1.897	F
					19.00	26.70	5.29	0.038	10.84	5.839	G
					18.50	26.90	7.89	0.041	5.27	11.238	G
NGC 4474	S0(8)	−18.97	0.32	22.51	–	–	–	–	–	–	–
					19.50	26.30	2.62	0.067	16.69	1.755	G
					20.00	27.00	10.75	0.068	0.08	17.391	F
NGC 4476	S0(5)	−18.29	0.13	22.38	20.50	28.00	3.01	0.045	15.81	2.446	G
					20.20	28.00	3.70	0.061	14.55	3.714	G
					19.50	25.80	4.83	0.048	12.64	5.759	G
NGC 4478	E2	−18.94	0.02	20.75	18.50	27.00	1.87	0.049	16.99	0.954	G
					18.50	27.00	1.98	0.030	16.80	1.139	G
					19.50	26.90	2.16	0.048	16.35	1.474	G
NGC 4486	E0	−21.82	1.05	23.53	19.00	24.50	5.36	0.017	12.57	4.346	F
					19.00	26.50	6.51	0.051	10.31	6.253	F
					20.00	26.80	5.56	0.055	11.25	5.215	F
NGC 4550	S0(7)	−18.66	0.02	20.92	20.00	28.00	1.65	0.143	18.07	0.468	F
					19.50	24.50	1.82	0.034	17.28	0.934	F
					19.00	26.50	1.71	0.050	17.30	1.149	G
NGC 4551	E2	−18.24	0.06	21.68	19.00	28.00	1.81	0.065	17.97	0.816	G
					19.50	28.00	1.89	0.074	17.86	0.976	G
					19.50	25.50	2.38	0.036	16.87	1.754	G
NGC 4552	S0(0)	−20.92	0.95	24.25	18.00	26.50	13.87	0.065	−3.97	20.087	F
					18.00	26.50	12.81	0.064	−2.42	18.552	G
					17.50	27.00	11.81	0.082	−0.61	16.850	G
NGC 4564	E6	−19.28	0.24	21.75	20.50	26.40	1.51	0.053	18.57	0.329	F
					19.50	26.20	2.42	0.031	16.61	1.501	F
					18.00	26.50	5.08	0.053	10.48	6.819	G
NGC 4570	S0(7)	−19.58	0.15	20.81	–	–	–	–	–	–	–
					19.70	26.00	1.49	0.020	18.09	0.426	P
					18.00	26.00	3.09	0.058	13.24	3.728	F
NGC 4600	S0(6)	−18.01	0.23	22.68	20.50	27.50	1.13	0.053	20.10	0.163	F
					20.20	26.30	1.64	0.035	19.35	0.573	G
					20.50	26.00	2.40	0.034	18.16	1.484	G
NGC 4621	E4	−21.00	0.96	24.01	17.50	24.00	5.22	0.029	12.17	4.714	G
					17.50	25.00	6.14	0.031	10.63	6.316	G
					17.50	26.50	11.75	0.077	1.52	15.363	G
NGC 4623	E7	−18.03	0.12	22.03	20.70	26.50	1.18	0.022	19.98	0.130	F
					20.50	26.50	1.66	0.012	19.03	0.596	G
					20.50	26.50	2.64	0.047	16.89	2.302	G
NGC 4636	E1	−21.29	1.06	23.85	20.00	27.00	4.39	0.036	15.69	2.608	G
					21.00	26.30	2.86	0.037	18.07	1.046	F
					19.50	26.50	3.54	0.096	16.13	2.069	F

Table 5.2: *continued*

Ident.	Type	M_B	$\log(R_e)$	μ_e	μ_{start}	μ_{end}	n_{maj} n_{eq} n_{min}	σ_n	A	B	Q
		[mag]	[kpc]	B-mag arcsec^{-2}				[mag]			
NGC 4638	S0(7)	−19.31	0.09	20.86	–	–	–	–	–	–	–
					20.00	27.00	3.39	0.069	13.59	3.441	F
					18.00	27.00	5.06	0.094	10.97	6.506	F
NGC 4649	S0(2)	−21.74	0.96	23.22	18.50	26.00	5.01	0.056	12.70	4.038	G
					19.00	25.00	5.84	0.040	11.10	5.447	G
					19.00	27.50	6.11	0.055	10.34	6.122	G
NGC 4660	E3	−19.27	0.06	20.91	18.00	27.50	2.74	0.143	14.98	2.140	P
					18.00	27.00	3.87	0.074	12.63	4.315	G
					18.00	27.00	6.70	0.056	6.55	10.251	G
FCC 019	dS0(8),N	−15.81	0.09	24.08	–	–	–	–	–	–	–
					–	–	–	–	–	–	–
					22.50	27.00	1.74	0.027	21.19	0.799	G
FCC 055	S0(9)	−17.28	0.03	22.38	–	–	–	–	–	–	–
					–	–	–	–	–	–	–
					20.70	25.20	2.00	0.062	18.54	1.353	F
FCC 090	E4 pec	−16.53	−0.03	23.37	–	–	–	–	–	–	–
					20.70	26.80	6.45	0.028	9.49	9.617	F
					20.70	28.00	4.24	0.040	13.12	5.973	F
FCC 119	S0 pec	−16.25	0.19	24.36	22.00	27.00	2.26	0.067	19.75	1.262	P
					22.00	27.00	2.59	0.032	19.13	1.731	F
					22.00	27.00	2.60	0.041	19.22	1.750	G
FCC 136	dE2,N	−16.61	0.32	24.67	21.50	27.00	2.04	0.031	20.36	0.861	G
					21.50	26.80	2.22	0.019	20.02	1.124	G
					22.00	26.70	2.67	0.017	19.14	1.789	G
FCC 152	S0/a pec	−17.22	0.14	23.09	22.00	27.50	2.15	0.054	18.47	1.134	P
					22.00	27.30	4.57	0.031	12.92	5.581	F
					–	–	–	–	–	–	–
FCC 204	dS0(8),N	−16.30	0.09	23.58	–	–	–	–	–	–	–
					–	–	–	–	–	–	–
					22.00	26.80	1.80	0.020	19.84	1.142	G
FCC 255	S0(6),N	−17.49	0.09	22.57	21.00	27.50	2.10	0.056	17.25	1.260	F
					21.00	27.00	2.67	0.026	16.82	2.154	F
					20.80	27.00	3.26	0.027	16.52	3.063	F
FCC 324	dS0(8)	−15.83	0.26	24.98	23.00	27.00	1.12	0.050	22.31	0.126	F
					23.20	27.00	1.49	0.030	21.78	0.428	G
					23.00	26.50	1.60	0.021	21.79	0.634	G
FCC 335	E	−16.90	0.14	23.49	21.50	26.50	2.34	0.054	18.25	1.454	F
					21.50	26.00	2.58	0.027	17.87	1.938	F
					21.50	26.00	2.51	0.020	18.18	1.962	P
NGC 1336	E4	−18.03	0.37	23.62	21.00	26.50	3.82	0.048	16.74	2.830	F
					20.50	27.00	3.24	0.053	17.20	2.345	G
					20.50	27.00	2.87	0.030	17.47	2.080	G

Table 5.2: *continued*

Ident.	Type	M_B	$\log(R_e)$	μ_e	μ_{start}	μ_{end}	n_{maj} n_{eq} n_{min}	σ_n	A	B	Q
		[mag]	[kpc]	B-mag arcsec^{-2}				[mag]			
NGC 1339	E4	−18.60	0.07	21.49	20.00	26.80	1.81	0.042	18.20	0.709	F
					20.00	26.80	1.98	0.045	17.80	0.991	G
					20.00	27.20	2.07	0.067	17.57	1.208	F
NGC 1351	E5	−19.00	0.39	22.92	19.50	28.00	3.25	0.110	16.02	2.302	P
					19.50	28.00	4.20	0.083	14.16	3.963	F
					19.50	28.00	5.58	0.070	11.35	6.650	F
NGC 1373	E3	−17.15	−0.06	22.38	20.00	27.50	2.81	0.036	16.41	2.548	G
					20.00	27.50	3.22	0.030	15.72	3.278	G
					20.50	27.50	3.42	0.054	15.63	3.585	F
NGC 1374	E0	−19.36	0.35	22.30	19.00	28.00	3.28	0.042	15.46	2.514	G
					19.00	27.50	3.74	0.043	14.63	3.237	G
					19.50	27.50	4.34	0.056	13.54	4.227	G
NGC 1375	S0	−18.09	0.12	22.08	–	–	–	–	–	–	–
					–	–	–	–	–	–	–
					20.00	27.70	4.09	0.070	13.74	4.913	G
NGC 1379	E0	−19.27	0.32	22.01	19.50	27.70	2.03	0.046	17.95	0.845	G
					19.50	27.20	2.19	0.031	17.67	1.026	G
					19.50	27.20	2.33	0.033	17.45	1.175	F
NGC 1380	S0/a	−20.48	0.52	21.90	–	–	–	–	–	–	–
					–	–	–	–	–	–	–
					19.00	27.30	4.24	0.041	12.90	4.122	G
NGC 1380a	S0(9)	−18.01	0.13	21.96	–	–	–	–	–	–	–
					–	–	–	–	–	–	–
					20.50	27.50	3.20	0.059	15.09	4.072	F
NGC 1399	E0	−21.29	1.05	24.15	19.00	27.50	16.81	0.090	−8.17	24.140	F
					19.00	27.50	12.24	0.078	0.11	16.159	P
					19.00	27.50	9.52	0.078	5.14	11.455	F
NGC 1404	E2	−20.37	0.34	21.24	17.70	24.60	4.42	0.054	12.02	4.406	G
					18.00	24.50	4.60	0.031	11.55	4.848	G
					18.00	25.20	4.37	0.032	12.03	4.506	G
NGC 1419	E0	−17.74	−0.08	21.71	–	–	–	–	–	–	–
					19.00	28.00	5.04	0.060	10.96	6.953	P
					19.00	28.00	4.12	0.048	12.63	5.315	F
NGC 1427	E4	−19.48	0.46	22.75	19.50	28.00	3.42	0.058	15.60	2.464	G
					19.50	27.00	3.82	0.040	14.82	3.196	G
					20.00	26.50	4.40	0.044	13.68	4.298	G
NGC 1428	E5	−17.39	−0.06	21.85	20.20	27.80	2.47	0.064	17.20	1.711	F
					–	–	–	–	–	–	–
					–	–	–	–	–	–	–

Chapter 6

Morphological Segregation of Early-type Galaxies in the Virgo Cluster

6.1 Introduction

The well-known morphological segregation of galaxies can be described as a continuous change in clustering properties of galaxies along the Hubble sequence. Elliptical galaxies are located preferentially in high-density regions: groups and clusters of galaxies; spirals lie in lower density environments (Hubble and Humason 1931, Dressler 1980). There are also evidences for luminosity segregation: both early- and late-type galaxies brighter than $M \approx -19.5$ are more strongly clustered (Hamilton 1988, Einasto 1991).

During the last decade it has become clear that elliptical galaxies split into at least two physically distinct families (Bertola & Capaccioli 1978, Bender et al. 1989b, Nieto and Bender 1989)

About 30% of elliptical galaxies show boxy isophotes. These galaxies are, in general, bright, have low specific angular momentum and are supported by anisotropic pressure; they usually are strong radio, UV and X-ray emitters. Many of them show peculiarities such as counter-rotating cores, shells, dust-lanes and small gaseous discs, which are interpreted as merging signatures. Faint boxy ellipticals are generally low-mass companions of massive galaxies.

About 70% of the remaining elliptical galaxies show pointed isophotes. These objects are generally radio-quiet and do not have strong X-ray emission; their dynamics is consistent with isotropic oblate models. These galaxies are usually fainter than boxy galaxies. The strong similarity of their properties with those of S0 galaxies suggests that they host a faint stellar disc, populating an end of the disc-to-bulge ratio sequence, that toward vanishing small discs (Capaccioli 1987, Bender et al. 1989b, Capaccioli & Caon 1992).

A small fraction of galaxies have nearly perfect elliptical isophotes; however, it is likely that in these cases the presence of boxy or discy features remain undetected because of an unfavourable viewing angle (cf. Chapter 3).

Two families of galaxies are also found in the μ_e–R_e plane, where R_e is the effective radius and μ_e is the corresponding effective surface brightness (Chapter 4). The '*bright*' family is formed by galaxies brighter than $M_B \simeq -19.3$. Their effective radii extend from 3 kpc up to 300 kpc, and are directly related to the effective surface brightness: $\mu_e \simeq 3 \log R_e +$ const. The '*ordinary*' family is composed by all galaxies fainter than $M_B \simeq -19.3$. Effective parameters range over a wide interval for galaxies with a same total luminosity ($\Delta R_e \sim 0.7$ dex and $\Delta \mu_e \sim 3.5$ mag), a property that is largely intrinsic, that is, not due to measurement errors or projection effects. The interval spanned by R_e is the same at any luminosity, with a sharp upper boundary $R_e \simeq 3$ kpc. It is found that the '*bright*' family is composed mainly of boxy galaxies and galaxies with elliptical isophotes; discy galaxies preferably belong to the '*ordinary*' family.

In this Chapter we will investigate whether different classes of early-type galaxies segregate in space according to morphology and to luminosity. For this purpose we analyse the location of early-type galaxies in the Virgo cluster relative to the groups which form the Virgo cluster complex, comparing local projected densities around galaxies. We find that all boxy galaxies are located in local density enhancements inside groups, while discy galaxies are located both in groups and in the field between groups, lying, in general, in regions of lower local densities. The different environmental properties of discy and boxy galaxies is not just due to the normal morphology-density relation (S0 galaxies tend to be discy, while boxy galaxies mostly belong to the class of ellipticals). In fact, the same results are found when the analysis is performed separately on the elliptical and on the lenticular galaxies.

A similar segregation, although weaker, is detected also between galaxies from the '*bright*' and the '*ordinary*' family, the former being located in higher density regions.

6.2 The Data

The basic sample (Table 6.1) is composed of 52 elliptical and non-barred S0 galaxies in the Virgo cluster, studied in CCR and in the present thesis (Chapter 2). With respect to the membership list by Binggeli et al. (1985) the sample is 80% complete to the total apparent magnitude $B_T \simeq 14.0$ (it does not include some galaxies in the cluster outskirts). The present sample of early-type galaxies is the first providing a fair number of galaxies with both accurate global photometric parameters and isophote shape descriptors. One galaxy, NGC 4360, has been excluded by the sample because it is likely a background object (its redshift is $\simeq 7000$ km/s).

The boundaries of the Virgo cluster area adopted in the present study are given in Table 6.2. In order to include all the galaxies belonging to the Virgo cluster we selected a region which is slightly larger than that considered by Binggeli et al. (1985). Data about the other members of the Virgo cluster were taken from a compilation of all known galaxy redshifts kindly made available to us by J. Huchra (1991, private communication). Only galaxies having redshifts in the appropriate interval (513 galaxies) were retained, in order not to contaminate the sample with background objects. The Virgo cluster contains several groups: the M87 group (the main group in the Virgo cluster area), the M49 and NGC 4649

groups, and the W and M clouds. Data about these groups (centers, boundaries, and numbers of members) are given in Table 6.2. Membership for each galaxy of our sample is listed in Table 6.1.

Looking at Table 6.1, we see that 10 out of 51 galaxies in our Virgo cluster sample do not belong to any group: 8 of them are discy galaxies, 2 are galaxies with nearly elliptical isophotes. On the contrary, all boxy galaxies belong to a group. This fact is already an evidence of the differences in spatial distribution between boxy and discy galaxies: the former are located inside groups, the latter may be found both in groups and in the field regions between and around groups. The projected distribution of galaxies in the Virgo cluster is shown in Figure 6.1.

6.3 Local Density around Virgo Early-type Galaxies

Projected local densities around galaxies have been calculated as follows:

$$D2(N) = N/(\pi S_N^2)$$

where S_N is the angular distance to the Nth nearest neighbour of a given galaxy. Since we do not know *a priori* what is more important, the presence of a close companion or the presence of a small group (if any), we calculated local densities around each galaxy of our sample of galaxies up to the 8th nearest neighbour ($1 \leq N \leq 8$).

We could not calculate also spatial local densities, since we do not have any information about the location of each galaxy along the line of sight. Radial velocities cannot be used to estimate distances, as they are just the product of the internal dynamics of the cluster.

6.3.1 Local Densities around Boxy and Discy Early-type Galaxies

Mean and median local projected densities for galaxies belonging to the different isophotal classes are plotted in Fig. 6.2.

Differences in local densities of boxy and discy galaxies are largest when 5–6 neighbours are considered, then they become smaller; thus, what is important is not just the presence of one close neighbour but of a small subgroup. The Kolmogorov-Smirnov test shows that the differences between density distributions are statistically significant at 95% confidence level.

These differences are not only due to the fact that some discy early-type galaxies lie in the field between groups: discy galaxies tend to have lower local densities even inside the groups. Galaxies with elliptical isophotes have a local density distribution similar to that of discy galaxies.

Our sample contain both elliptical and lenticular galaxies (galaxies classified as E/S0 are included into the S0 group). Therefore the results above may be simply the reflection of the well-known morphology-density relation. The fact that there are 6 boxy and 7 discy galaxies among elliptical galaxies, and 16 discy and only 4 boxy galaxies among lenticular galaxies, seems to favour this interpretation. Prompted by this consideration, we performed the calculations of local densities separately for elliptical galaxies and lenticular galaxies. The

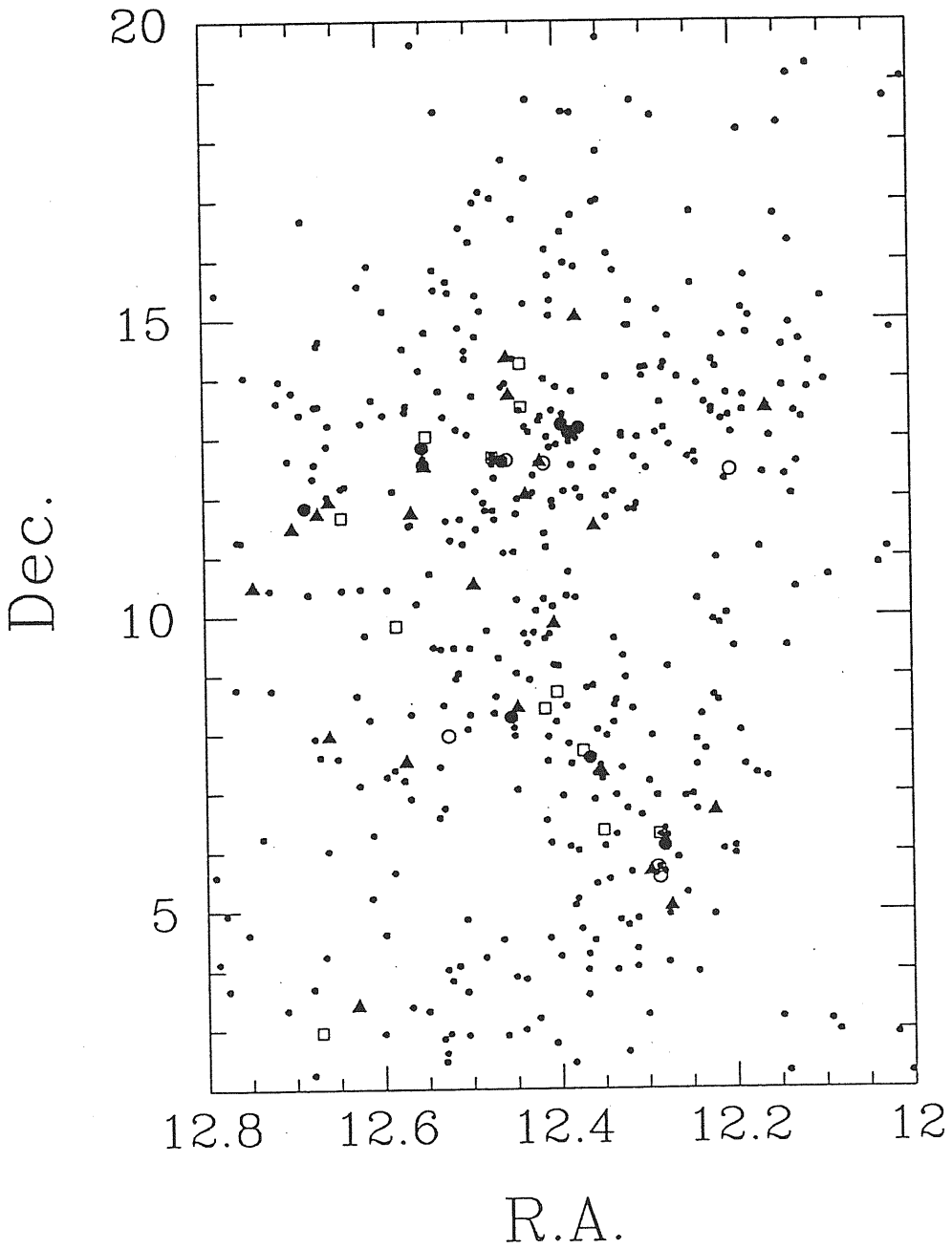

Figure 6.1: Distribution of galaxies in the Virgo cluster area. *Filled circles*: boxy galaxies; *filled triangles*: discy galaxies; *empty circles*: galaxies with irregular or complex isophotal behavior; *empty squares*: galaxies having isophotes with no significant deviations from the elliptical shape; *small dots*: all other galaxies belonging to the Virgo cluster.

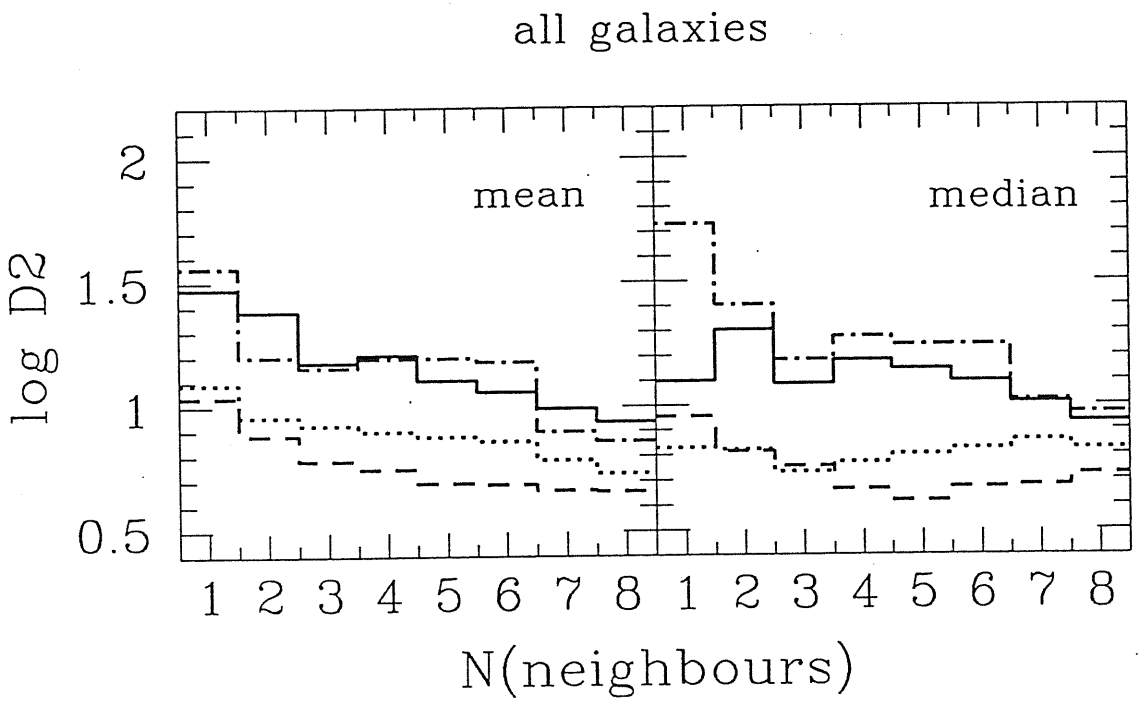

Figure 6.2: Mean and median values of the local projected densities, measured in galaxies per squared degree, for all the galaxies of our sample, grouped according their isophotal classification: boxy galaxies (solid line); discy galaxies (dashed line); galaxies with nearly perfectly elliptical isophotes (dotted line); galaxies with irregular isophotes or with boxy and discy isophotes coexisting (dot-dashed line). N is the number of the nearest neighbour out to which densities are calculated ($1 \leq N \leq 8$).

results are presented in Figs. 6.3 for elliptical galaxies, and in Fig. 6.4 for lenticular ones. Among the S0 galaxies, we have grouped together boxy galaxies and those galaxies in which boxy and discy isophotes coexist. In fact, both classes belong to the family of discy objects, except that their bulge is boxy instead of spheroidal (Nieto & Bender 1989): we here assume that pure boxy S0s owe their morphological classification to the fact that the presence of a disc is revealed by the surface brightness distribution, but escapes detection in the isophotal analysis because of the unfavourable angle of view (all boxy S0s in our sample have quite small flattenings).

Fig. 6.3 shows that local projected densities around boxy elliptical galaxies are considerably higher than around discy galaxies, while galaxies with elliptical isophotes have intermediate densities. The discrepancy between median and mean values for the latter isophotal class is explained by the poor statistics (4 objects), and by the fact that it includes NGC 4486, which has a much higher projected density than the other galaxies of this class.

The same result is found in the S0 sample. Discy galaxies with boxy signatures present significantly higher densities than pure discy galaxies or galaxies with elliptical isophotes. Comparing Fig. 6.3 with Fig. 6.4, we can see that densities around boxy ellipticals are higher

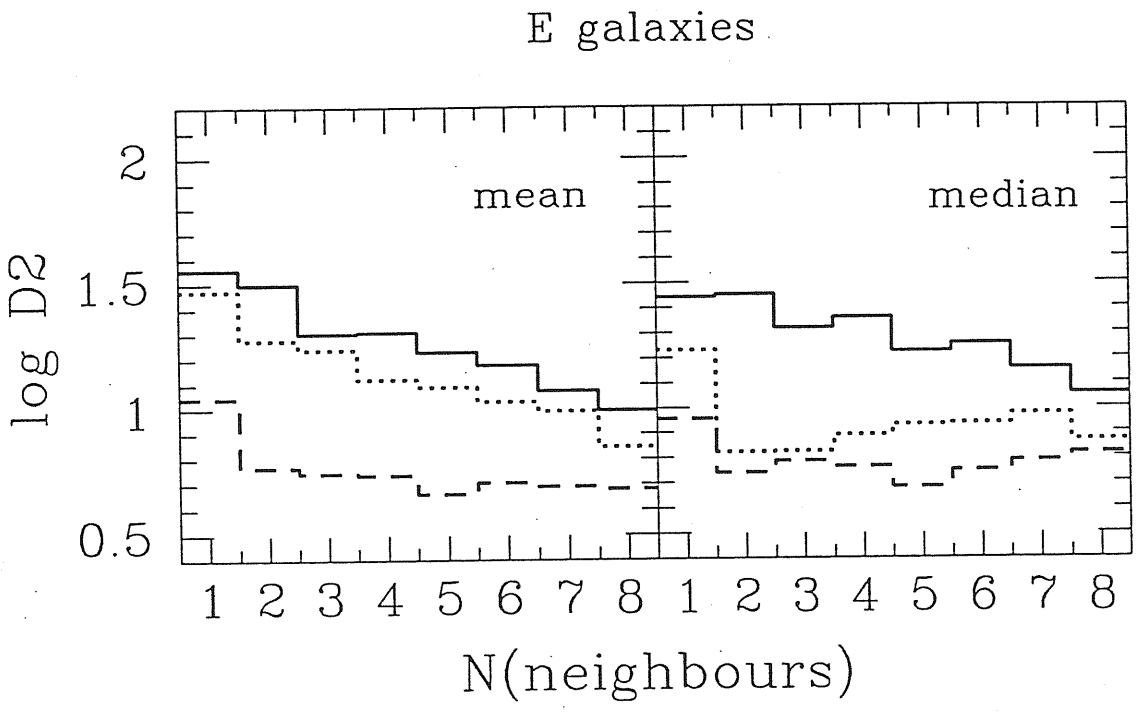

Figure 6.3: Local projected densities, measured in galaxies per squared degree, are plotted for only galaxies classified as ellipticals, divided according their isophotal classification: boxy (solid line), discy (dashed line), and galaxies with elliptical isophotes (dotted line). N is the number of the nearest neighbour up to which densities are calculated ($1 \leq N \leq 8$).

than those around boxy S0s, while discy Es and pure discy S0s display much lower, nearly equal densities. Taking into account that the disc-to-bulge ratio D/B of discy Es are confined in a very small range ($D/B < 0.15$), while those of S0s cover a wider interval ($0.1 < D/B < 2.0$), as showed by Scorza (1993), this would suggest that there is no dependence of the disc-to-bulge ratio on the environment.

To establish whether the differences in local densities are due the presence of to substructures inside groups, or to the location of galaxies relative to group centers, we performed the following test. We gave the coordinates of each galaxy a random shift within a certain interval. If differences disappear for shifts as small as those which destroy substructures but preserve the global structure of the group, then differences are related to substructures. Our experiments show that, in order to wash out differences, shifts as large as those required to destroy substructures are needed. Therefore differences in the case of real distributions are related to the presence of substructure in groups.

6.3.2 Local Densities around '*Bright*' and '*Ordinary*' Galaxies

Mean and median local densities for galaxies from '*bright*' and '*ordinary*' families are plotted in Fig. 6.5.

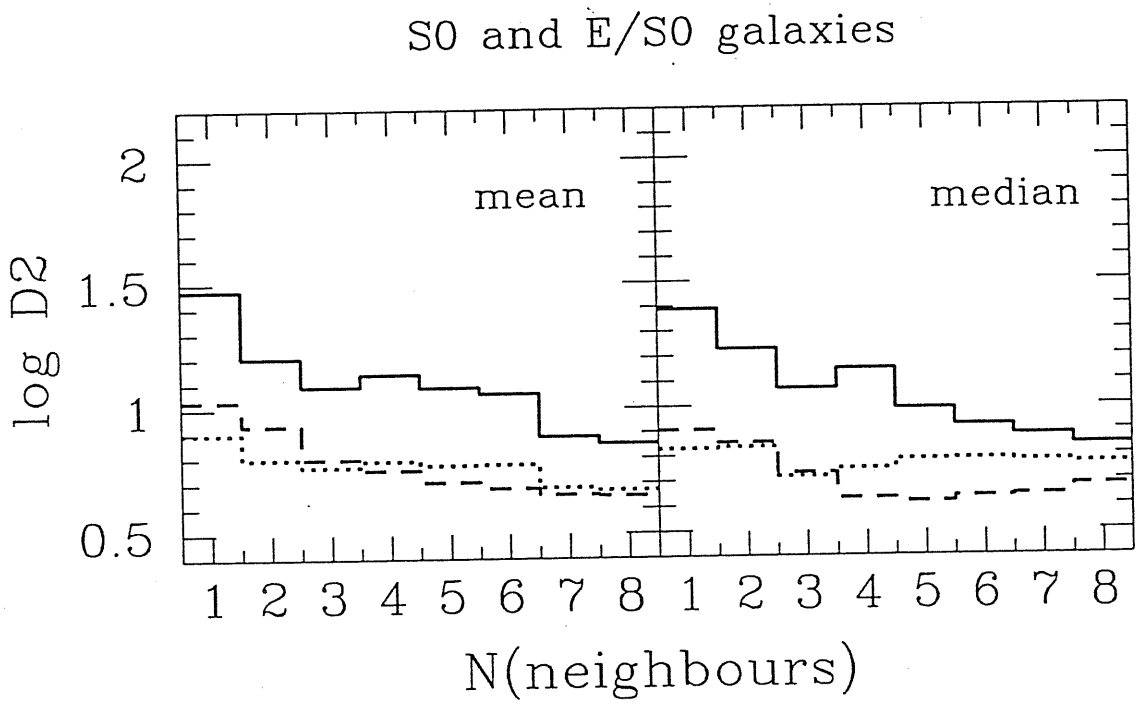

Figure 6.4: Local projected densities around S0 and E/S0 galaxies are plotted, dividing galaxies according to their isophotal classification: boxy galaxies and galaxies with coexisting discy and boxy isophotes (solid line), discy galaxies (dashed line), and galaxies with elliptical isophotes (dotted line). N is the number of the nearest neighbour up to which densities are calculated ($1 \leq N \leq 8$).

It evidences that galaxies belonging to the '*bright*' family are located, in general, in higher density environment than galaxies belonging to the '*ordinary*' family. The statistical significance of this effect is, however, much lower than in the previous case (K-S test shows that differences between distance and density distributions are statistically significant at 70% confidence level). Since '*bright*' galaxies have mainly boxy or elliptical isophotes, the higher local densities may partly be a reflection of the isophote shape–density relation.

6.4 Conclusions

We have shown that there exists a remarkable morphological segregation between boxy and discy early-type galaxies: boxy galaxies are all located in local density enhancements in the inner regions of groups; discy galaxies are located, in general, in lower density environment both in groups and in the field. This finding is not just the reflection of ordinary morphology-density relation between elliptical and lenticular galaxies. In fact, the segregation according to the isophotal classification is shown independently by the E and by the S0 groups. The fact that disky E and S0 galaxies have equal local densities suggests that the galaxian property that appears to be more sensitive to the environment is just the presence or not of a stellar

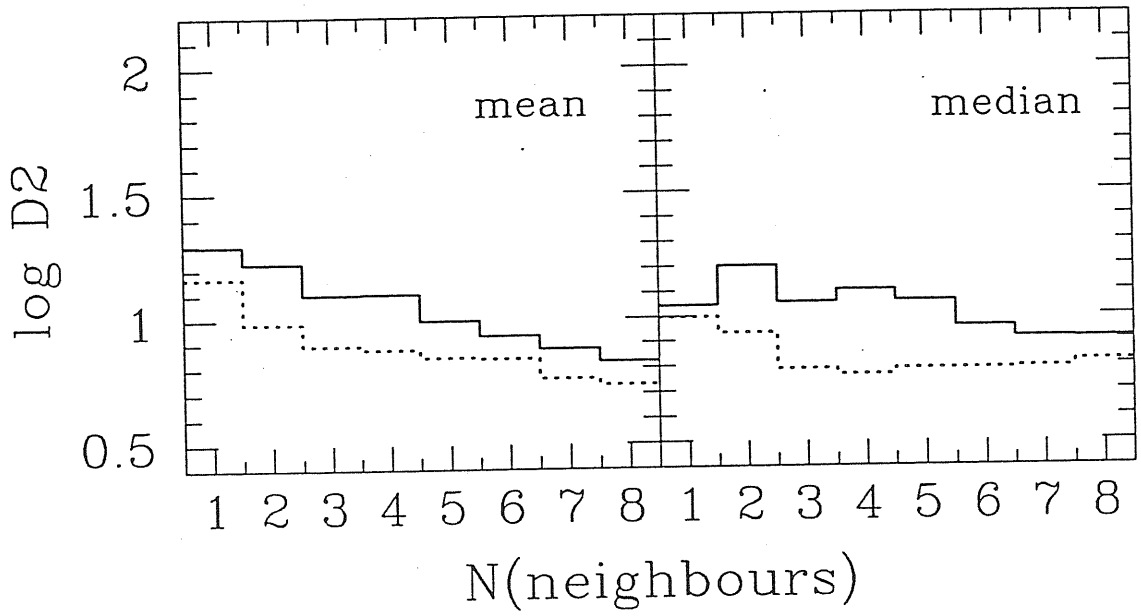

Figure 6.5: Local projected densities of galaxies belonging to the '*bright*' family (solid line) are compared with those of galaxies belonging to the '*ordinary*' family (dotted line). N is the number of the nearest neighbour up to which densities are calculated, $1 \leq N \leq 8$.

disc, rather than the bulge-to-disc ratio (and therefore the classification as an E or a S0 galaxy). Also, a weak luminosity segregation is detected between galaxies belonging to the '*bright*' and to the '*ordinary*' family, the former being located in higher density regions. This result is likely the consequence of the fact that '*bright*' galaxies tend to have boxy or elliptical isophotes, while discy galaxies are preferably found in the '*ordinary*' family.

The present results are in agreement with recent studies by Whitmore (1991) and Einasto (1992), which showed that the morphology-density relation reflects the fact that early-type galaxies are located in small groups which belong to clusters or to filaments. The presence of morphological segregation between boxy and discy galaxies is in line with the speculations considering boxy and discy galaxies as the final product of different processes of formation and evolution of galaxies: boxy galaxies formed (by merging during early epochs of galaxy formation?) in high density regions in clusters and groups; discy early-type galaxies, belonging to the end of the sequence of galaxies harboring a stellar disc, typically lie in the lower density environment.

This result is obtained using a complete but still small sample of early-type galaxies in one cluster. A deeper and more statistically significant analysis requires larger samples of early-type galaxies with comparable accuracy of photometric and isophotal parameters, and spanning a wider range of environments (from small groups to big clusters). On this line,

some indications have been found that in compact groups the fraction of boxy galaxies is low while there is a large fraction of galaxies with asymmetric distortions (Bettoni and Fasano 1993; Zepf & Whitmore 1993). This may support the idea that boxy galaxies formed during early epoch of galaxy formation, while galaxies in compact groups show features which are characteristic of recent interactions and accretion events.

Table 6.1: Basic data on early-type galaxies in the Virgo cluster

Name	Morph. type	M_B	$\log(R_e)$	μ_e	Isoph. class	Group	Comments
IC 3468	E1,N	−17.67	0.414	24.31	Discy	V1? V4?	
IC 3540	S0(2)	−16.61	−0.104	22.11	Ell	V4	
IC 3653	E3	−16.87	−0.192	21.70	Ell	V4	
IC 3773	d:S0(9)	−17.46	0.261	23.79	Discy	V4?	
NGC 4168	E2	−19.07	0.444	22.98	Discy	V3	
NGC 4200	S0(4)	−17.34	0.088	22.72	Irr	V3	
NGC 4215	S0(9)	−18.35	0.063	21.55	Discy	V5	
NGC 4255	S0(6)	−17.70	−0.049	21.79	Discy	V5?	foreground?
NGC 4261	E2	−20.27	0.761	23.45	Boxy	V5	
NGC 4268	S0(6)	−17.59	−0.046	21.67	B→D	V5	
NGC 4269	S0(2)	−17.98	0.389	24.01	Ell	V5	
NGC 4270	S0(6)	−18.22	0.094	21.84	DBD	V5	
NGC 4281	S0(6)	−19.24	0.343	22.22	Discy	V5	
NGC 4339	S0(0)	−18.89	0.375	22.82	Ell	V2	
NGC 4342	S0(7)	−18.23	−0.357	19.59	Discy	V2	
NGC 4352	S0(8)	−17.86	0.200	22.89	Discy	V1?	background?
NGC 4360	E2	−17.88	0.271	23.49	DBD	V2?	background
NGC 4365	E3	−20.95	0.931	23.73	Boxy	V2	
NGC 4370	S0(6)	−17.99	0.246	22.83	Ell	V2	
NGC 4374	E1	−21.59	1.050	23.85	Boxy	V1	
NGC 4377	S0(3)	−18.56	0.064	21.61	Discy	V1?	(north)
NGC 4387	E5	−18.22	0.030	21.66	Boxy	V1	
NGC 4406	S0(3)/E3	−21.67	1.172	23.97	Boxy	V1	
NGC 4415	d:E1,N	−17.72	0.299	23.45	Ell	V2	
NGC 4417	S0(7)	−19.52	0.335	22.20	Discy	V2	
NGC 4431	dS0(5),N	−17.44	0.279	23.63	BDB	V1	
NGC 4434	E0/S0(0)	−18.23	0.060	22.00	Ell	V2	
NGC 4436	dE6/dS0,N	−17.29	0.235	23.72	Discy	V1	
NGC 4452	S0(9)	−19.08	0.213	21.08	Discy	V1	
NGC 4458	E1	−18.37	0.213	22.49	Ell	V1	
NGC 4459	S0(2)	−20.04	0.443	22.16	Ell	V1	
NGC 4464	E3	−17.84	−0.200	20.89	Discy	V2	
NGC 4472	E2/S0(2)	−22.43	1.301	24.07	Boxy	V2	
NGC 4473	E5	−20.28	0.481	22.20	Discy	V1?	background?
NGC 4474	S0(8)	−18.97	0.319	22.51	Discy	V1	
NGC 4476	S0(5)	−18.29	0.131	22.38	D→B	V1	
NGC 4478	E2	−18.94	0.024	20.75	Boxy	V1	
NGC 4486	E0	−21.82	1.050	23.53	Ell	V1	
NGC 4526	S0(6)	−20.90	0.598	21.91	B→D	V2	
NGC 4550	E7/S0(7)	−18.66	0.016	20.92	Discy	V1, V4	
NGC 4551	E2	−18.24	0.058	21.68	Boxy	V1, V4	
NGC 4552	S0(0)	−20.92	0.951	24.25	Boxy	V1, V4	
NGC 4564	E6	−19.28	0.239	21.75	Discy	V1, V4	
NGC 4570	S0(7)/E7	−19.58	0.153	20.81	Discy	V2	
NGC 4578	S0(4)	−18.82	0.346	22.74	Ell	V4?	background?
NGC 4600	S0(6),N	−18.01	0.231	22.68	Discy	?	
NGC 4621	E4	−21.00	0.962	24.01	Discy	V4, H	

Table 6.1: *continued*

Name	Morph. type	M_B	$\log(R_e)$	μ_e	Isoph. class	Group	Comments
NGC 4623	E7	−18.03	0.120	22.03	Discy	V4?	south
NGC 4636	E1/S0(1)	−21.29	1.058	23.85	Ell	?	
NGC 4638	S0(7)	−19.31	0.096	20.86	Discy	V4, H	
NGC 4649	S0(2)	−21.74	0.964	23.22	Boxy	V4, H	
NGC 4660	E3/S0(3)	−19.27	0.057	20.91	Discy	V4, H	

Notes to the Table:

Morphological type: from Binggeli et al. (1985)

B_T, R_e and μ_e: total blue apparent magnitude, effective radius and effective surface brightness respectively, from CCR and from Chapter 2

Isophotal class: B→D – inner boxy, outer discy;
D→B – inner boxy, outer discy;
Irr – irregular isophote shapes
Ell – nearly perfectly elliptical
DBD (BDB) – discy (boxy) in the inner region, then changes to boxy (discy) and returnes to discy (boxy) again outward

V1 – V5: groups in the Virgo Cluster; H: Hickson group (Mamon 1989)

Table 6.2: Data about groups and clusters in the Virgo cluster area

Cluster/ Group	Center R.A.	Center Dec.	V_0	No. of galaxies	Limits R.A.	Limits Dec.	range of V_{rad}
Virgo (M87)	12^h28^m	$12°40'$	1292	635	$12^h.1 \div 12^h.9$	$2°.0 \div 20°.0$	$-600 \div 3000$
V1 (M87)	12^h28^m	$12°40'$	1292	91	$12^h.3 \div 12^h.6$	$11°.0 \div 15°.0$	$-600 \div 2000$
V2 (M49)	12^h27^m	$8°16'$	997	83	$12^h.3 \div 12^h.6$	$6°.0 \div 11°.0$	$-600 \div 2000$
V3 (M-cloud)	12^h12^m	$12°27'$	2376	16	$12^h.1 \div 12^h.3$	$11°.5 \div 15°.5$	$2000 \div 3000$
V4 (M59)	12^h39^m	$11°55'$	444	32	$12^h.5 \div 12^h.8$	$10°.5 \div 14°.5$	$300 \div 2100$
V5 (W-cloud)	12^h13^m	$6°41'$	2067	30	$12^h.1 \div 12^h.3$	$4°.0 \div 9°.0$	$2000 \div 3000$

Appendix A

A New Method to Remove Column Offsets in CCD Images

A.1 Introduction

RCA high resolution CCDs are known to show a vertical structure (column pattern) produced by a different column by column sensitivity. This causes some columns to have an excess or a deficiency of signal with respect to the mean local background; the effect, in relative terms, increases as the background level decreases. The problem is relevant for most of the astrophysical observations, particularly in the cases in which spectroscopy or stellar photometry of faint stars is involved. If not properly corrected, even small offsets can cause large photometric errors in measuring stars close to the magnitude limit of the image.

Above a certain background level (depending on the set-up of the particular chip) it is common practice to treat the effect as a simple column by column offset, i.e. as if the difference ΔS_{ADU} between the mean ADU level of a column and that it would have in absence of the offset (the latter can be estimated as the average value of the surrounding columns), were constant (independent of the signal itself). However, this is only a first, crude approximation, and it is not at all true for some 'wild' columns. Moreover, the dependence of the column offset on the mean local background value is different for different columns, i.e.it is impossible to fit the trend with a single analytical function, equal for all the columns. This is clearly visible in Fig. A.1, where the column offsets for 5 different columns are plotted against the mean local background (this example, as in the following figures, is taken from images collected at the ESO/MPI 2.2m telescope, using the RCA high resolution ESO#8 CCD in direct imaging) Each curve represent the fit by a spline (see Sect. A.2) to the background dependent offsets of a single column; the *full dots* represent the offsets calculated on flat-field images having different mean count levels. (For sake of simplicity, hereinafter we shall speak of 'column offset', even if this is not the correct definitions). It is important to note that, within a given column, ΔS_{ADU} is constant, i.e. does not depend on the position along the column itself. Moreover, the column offset is only a function of the ADU level, hence it is independent of the color pass-band: this has been verified by comparing four series of flats, in the B-, V-, R- and I-bands. Instead, the column offset pattern may change if the CCD setup is even slightly

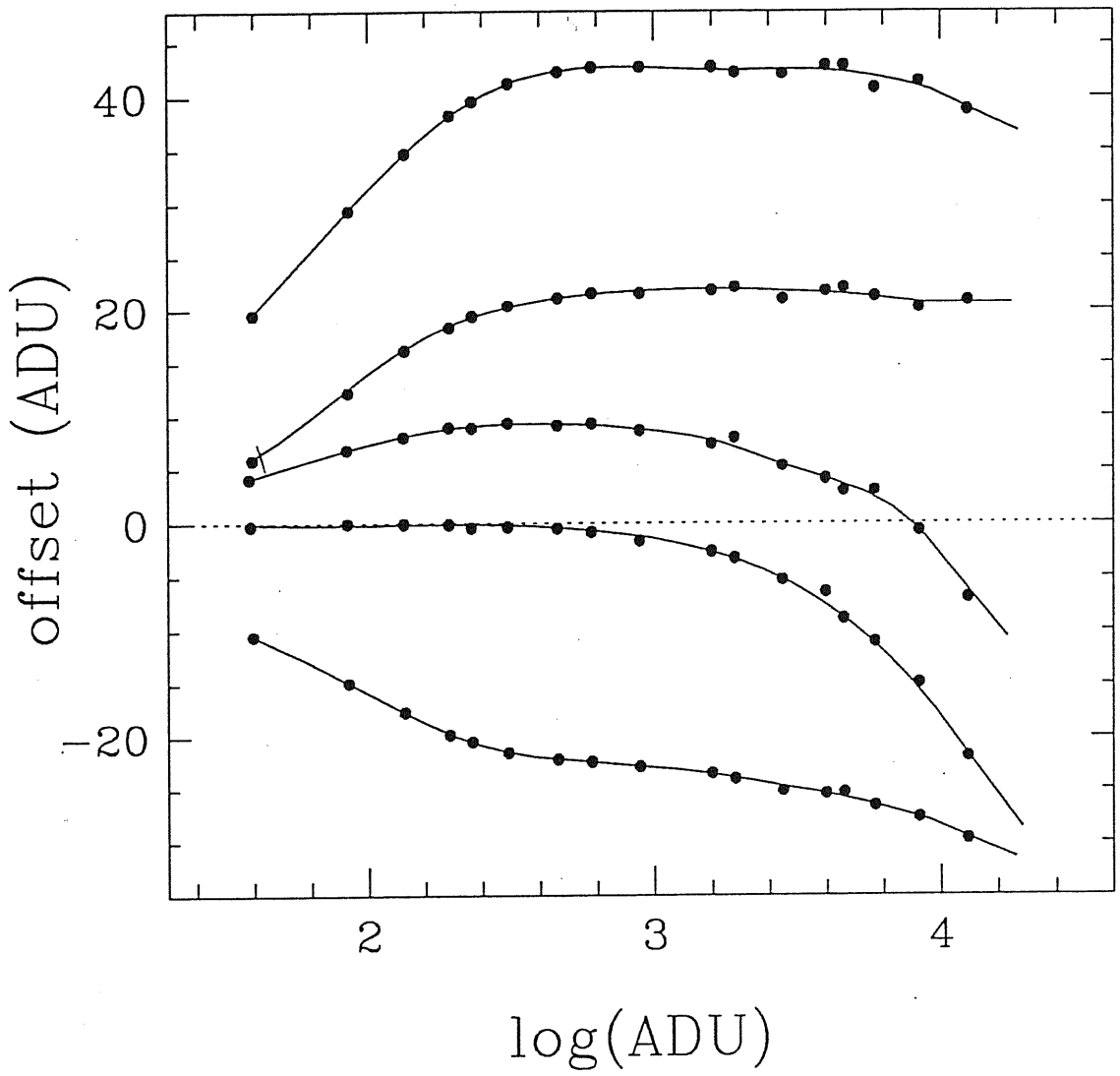

Figure A.1: The trend of the column offsets with the background level (in ADU) is shown for five different columns. The *full dots* are the offsets measured as described in the text, while the solid line is a spline interpolation to the datapoints. Different columns can have completely different offsets and functional trends. The relative effect is much stronger at low background levels.

modified, as shown in Fig.A.2: not only the values of the offsets are modified, but even their dependence of the offset on the background level is altered significantly.

A.2 The Solution

The method we have devised in order to correct for the column offset can be summarized in the following steps:

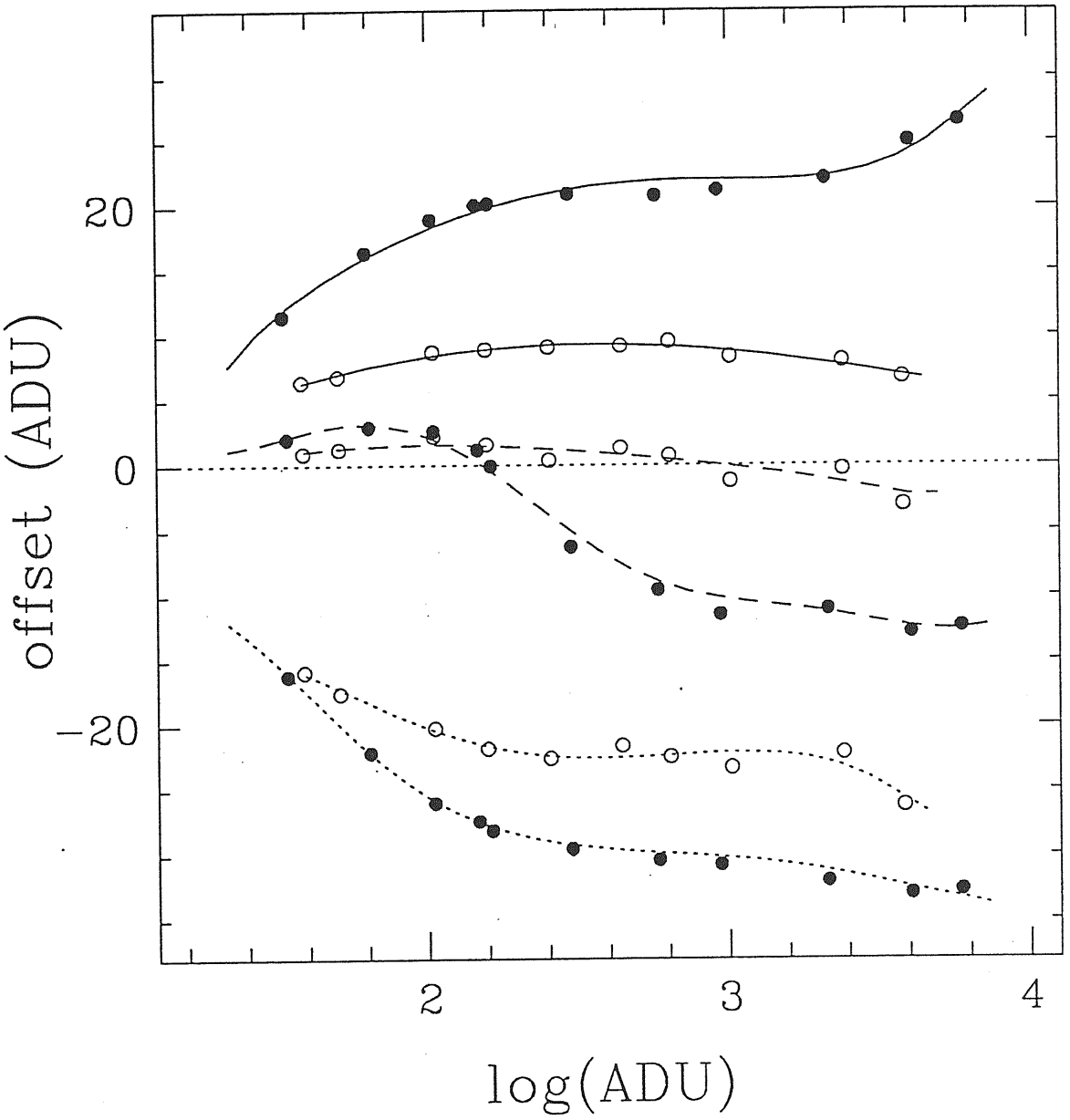

Figure A.2: The column offset as a function of the average local background for three columns measured in two flat-field series taken with two different CCD set-up. A same line type identifies the same column, while *empty dots* and *filled dots* refer to the two different set-ups. Unfortunately, we do not have any record of the detailed set-up changes: the two sets of flat-fields have been taken with the same filter and procedure in two observing runs at the ESO/MPI 2.2m telescope in March 1-3 and March 7-9 1990, respectively. The conversion factor and the RON were the same.

- During the observing run, in day-time, a series of dome flat-fields, with an as wide as possible range of levels should be secured; ideally, the faintest flats should have a count level equal or less than the background level of the less exposed scientific frame, while the brightest flat should have an average background equal to — or higher than — the maximum count level reached in the scientific exposures. Multiple flat-fields with the same background are necessary in order to increase the S/N ratio, particularly at low count levels. The more the exposures, the better the correction. Table A.1 lists the mean background (in ADU, after bias subtraction) for the series of flat-fields used for the application we present in this paper. Since the column offset is only a function of the ADU level, flat-fields can be taken in a single band, possibly that for which the detector has the most uniform response. As the offsets depend strongly on the CCD setup, even a small variation in the setup requires a new series of flat-fields (cf. Figure A.2)

- After the flats have been acquired, a median filtering on each flat-field should be performed in order to remove the cosmics. In order not to alter the column offset pattern, the filtering window must be one dimensional, aligned with the column axis.

- If the frame contains overscan regions, or bad columns or rows at its edges, they should be trimmed out. Of course, the same treatment must be applied to all the calibration and scientific frames. The flat-fields must also be bias subtracted (and dark subtracted if it is necessary). The flat-fields with the same count-level can be averaged.

- For each flat-field (or average flat-field) one must compute the "average row" summing up all the rows and dividing by the number of rows. In the case that there are significant variations of sensitivity at the edges of the frame, the sum must be performed excluding the corresponding rows. Again, it is important to acquire flat-fields at the wavelength at which the CCD has the most uniform response.

- In a plot of the "average line" (Fig. A.3) the columns affected by the offsets are clearly visible, superimposed on a more regular trend (i.e. with variations on a scale of few tens of pixels), which reflects the sensitivity variations across the frame. The background must be interpolated with some adequate function. Typically this function is a a cubic or higher degree spline, or a Legendre polynomial. Care should be taken in order to render the interpolation insensitive to the column offset, for instance with an iterative, k-clipping algorithm. Some trials are usually necessary to finely tune the fitting parameters (a fast and very effective way of performing this task is provided in IRAF by the command CURFIT). The difference between the original data and the interpolated ones gives the column offsets.

- Now, for each column we can plot the offsets *vs.* the original local background counts or their logarithm. The offsets can be interpolated with an appropriate function (as in Fig. A.1), in order to account for the noise present in the data. We used the spline fitting algorithm of P. Dierckk — Algorithms for smoothing data with periodic and parametric

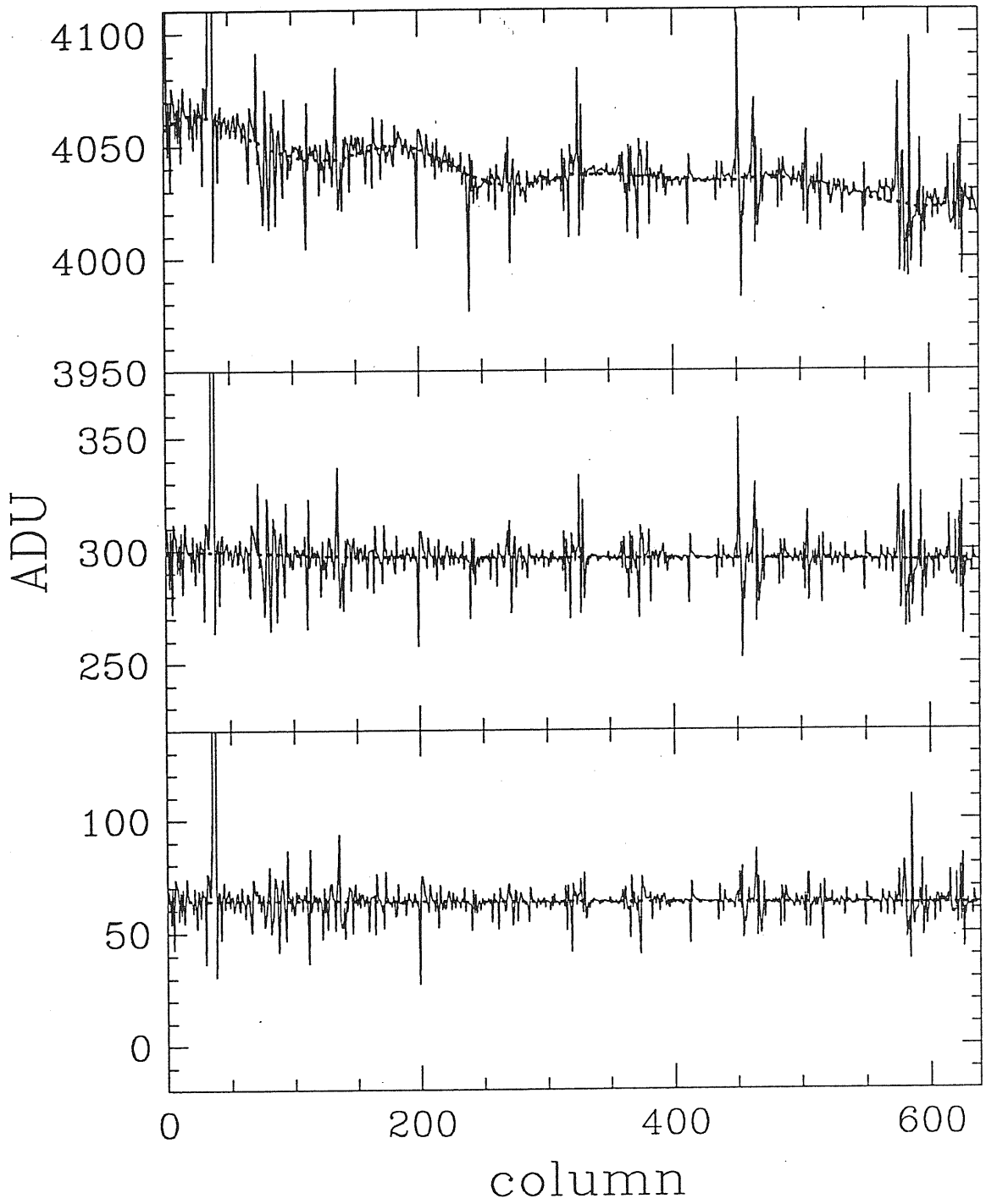

Figure A.3: The average rows from three flat-field images having different mean count levels are shown in solid line. The dashed line is our best estimated of the "true" average row, *i.e.* the one we would measure if there were no column offsets. In all the three panels the limits on the Y axis span the same interval in order to facilitate the comparison.

splines. Computer Graphics and Image Processing, 20, 171 (1982) —, which we implemented inside the SuperMongo graphic package. At this point, for each column we have a function which describes the dependence of the offset on the count level. This function is then used to correct all the scientific frames (already bias and dark subtracted), including the twilight flat-fields. For each pixel in the image, the corresponding offset is evaluated, as a function of the corresponding column and count level, and subtracted out.

A.3 Conclusions

The technique we have described seems somewhat sophisticated and time consuming, as it must be executed interactively. A proper interpolation of the average count row of a flat-field requires, in our experience, about 5-10 minutes, while the spline interpolation of the column offsets versus the background level requires about two or three minutes per column. The code for subtracting out the offsets takes a couple of minutes per image in a VAXstation 4000-60. Therefore, we estimate that about four or five days may be necessary for correcting the column pattern in a High Resolution RCA CCD (640 $\times$ 1040). Actually, this time is compensated by the much better correction of the column offsets than that usually achieved with more standard techniques (see Meurs 1987).

Even in case of faint objects and/or backgrounds, where the effect is the most relevant, the correction is still quite satisfactory: column offsets are reduced down to 1-2% of their original values, so that the residual pattern is far below the shot + read-out noise of the frame, as can be seen in Fig. A.4.

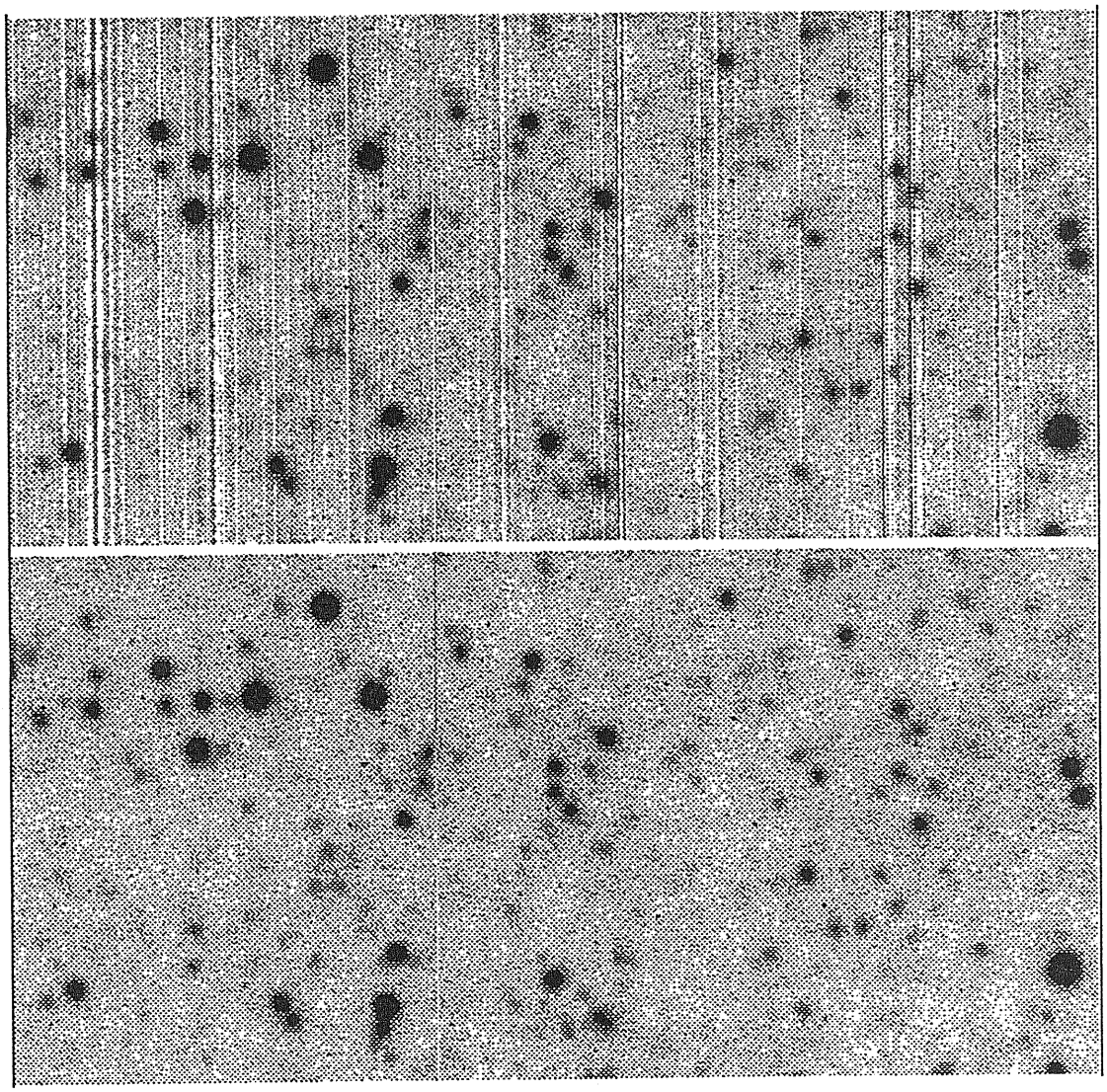

Figure A.4: A subregion of a B-band 40 min exposure (seeing 1".1 FWHM) on a stellar field in the irregular galaxy Sextans A is shown before (*top*) and after (*bottom*) the column offsets correction.

Table A.1: B-band flat-fields

Number of frames	Counts [ADU]
3	22
3	29
3	38
3	50
3	74
3	100
3	123
3	160
3	190
3	310
3	572
3	800
3	1000
3	1500
5	2000
5	4000
5	6000

Appendix B

Tables and Figures for Individual Galaxies

B.1 Tables

Tables B–1 to B–47 list the data on the final flattening, orientation and the folded light profiles along the principal axes of each galaxy of our sample. Column 1 gives the galactocentric distance in arcsec$^{1/4}$, columns 2 and 3 the luminosity profiles along the major and the minor axes respectively, columns 4 and 5 the ellipticity and the major axis position angle (measured in degrees from N through E) profiles respectively. For four galaxies (NGC 4281, NGC 4370, NGC 4526, NGC 1316), severely affected by strong dust lanes, we have tabulated separately the surface brightness along the two opposite sides of the major and of the minor axes.

B.2 Figures

The following figures display, for the 52 galaxies studied in this work:
in the *left panel*, the main axes folded light profiles, the major axis position angle profile (measured in degrees from N through E) and the ellipticity curve;
in the *right panel*, the radial run of the main isophotal shape descriptors: cos 3, sin 3, cos 4, sin 4, cos 6, sin 6, all multiplied by 100. All these quantities are plotted as a function of the galactocentric distance in arcsec$^{1/4}$.

In order to facilitate the comparison among the various objects, we have adopted the following scheme:

The interval in position angles is chosen among the values: Δ P.A. = 30°, 60°, 90°, 120°, 150°, 180°.
The interval in ellipticity varies from 0 to a maximum chosen among the four following values: $\varepsilon = 0.3, 0.6, 0.9, 1.0$
Light profiles are plotted in a fixed range of surface brightness: 15.5–31.0. The minor axis is shifted by +2 mag to avoid overlapping with the major axis.
The interval in the Fourier coefficients: cos 3, sin 3, sin 4, sin 6, which parametrize non-

axysimmetric distortions of the isophote shape, is fixed to -3.0 – 3.0; the intervals in $\cos 4$ and $\cos 6$ are symmetric about 0 and varies according to the peak value of each coefficient.

The dotted line in the inner part of the light profiles marks the region where the seeing convolution changes the true surface brightness by more than 0.05 mag. For the four objects hosting strong dust lanes, we have displayed separately the light profile along the two opposite sides (solid and dashed lines) of the major and of the minor axes.

We also plot the ellipticity curve, the position angle profile and the radial run of the main Fourier coefficients of the 33 galaxies already studied by CCR, using the same scheme as above.

B.3 Notes on the Individual Galaxies

NGC 4215. The major axis light profiles show a distinct component at $r \sim 25''$, likely an equatorial ring seen edge-on, as also suggested by the isophotal map.

NGC 4261. It is a well-known radio source in the Virgo cluster. It apparent rotation axis forms an angle of 5° with the photometric major axis, suggesting a close to prolate shape (Davies & Birkinshow 1986).

NGC 4269. The presence of a nearby galaxy (IC 3155) of comparable luminosity 1′ SW, and of a bright star 1′ N, makes the measurement of isophotal parameters and of light profiles somewhat more uncertain, which also reflects on the determination of global parameters.

NGC 4281. It shows a inner dust lane parallel to the major axis; even if it has been masked out for the isophotes analysis, isophotal parameters are uncertain in the inner 20 arcsec.

NGC 4360. According to Binggeli et al. 1985, this galaxy is likely a background object projecting in the Virgo cluster. The light contamination from a bright star, 1.5 NW, probably affects isophotal shape measurements for $r \gtrsim 50''$.

NGC 4365. This galaxy is surrounded by a luminous X-ray halo (Forman, Jones & Tucker 1985).

NGC 4370. It hosts a rather prominent dust lane placed along the equatorial plane of the galaxy and extending out to $\sim 40''$ from the center.

NGC 4472. It is the brightest object in the Virgo cluster (even brighter than NGC 4486). It is a strong radio and X-ray emitter, and its kinematics is characterized by a counter rotating stellar core (Saglia et al. 1993).

NGC 4526. It hosts an inner dust lane parallel to the major axis, extending out to $\simeq 20''$ from the nucleus.

NGC 4636. Deviations of isophotes shape from the elliptical shape are very small. This galaxy exhibits a radio jet, and possesses a large and luminous X-ray halo.

NGC 1316. It is the well-known radio source Fornax A. It displays tails and filaments in the outer parts, 'ripples', dust and gas in the inner parts. These characteristics, the velocity dispersion significantly lower than that of galaxies of similar luminosity, and the peculiar structure of the radio emission, all suggest that NGC 1316 is a merger remnant.

NGC 1373. The imperfect removal of a superposed small edge-on galaxy on the north side may be the cause of the irregularity in the Fourier coefficients behavior seen at $r \simeq 15''$.
NGC 1399. It is the central galaxy in the Fornax cluster. Outside about $30''$ it shows a marked isophote twist and a positive value of the A_4/a Fourier coefficient. Recently, new evidences for the presence of a central dark mass concentrations have been reported by Stiavelli, Møller & Zeilinger (1993).
NGC 1404. This galaxy is superposed on the outskirt of the very luminous NGC 1399. In order to avoid the contamination from the light of NGC 1399, light profiles have been cut at about $100''$.

NGC 4215

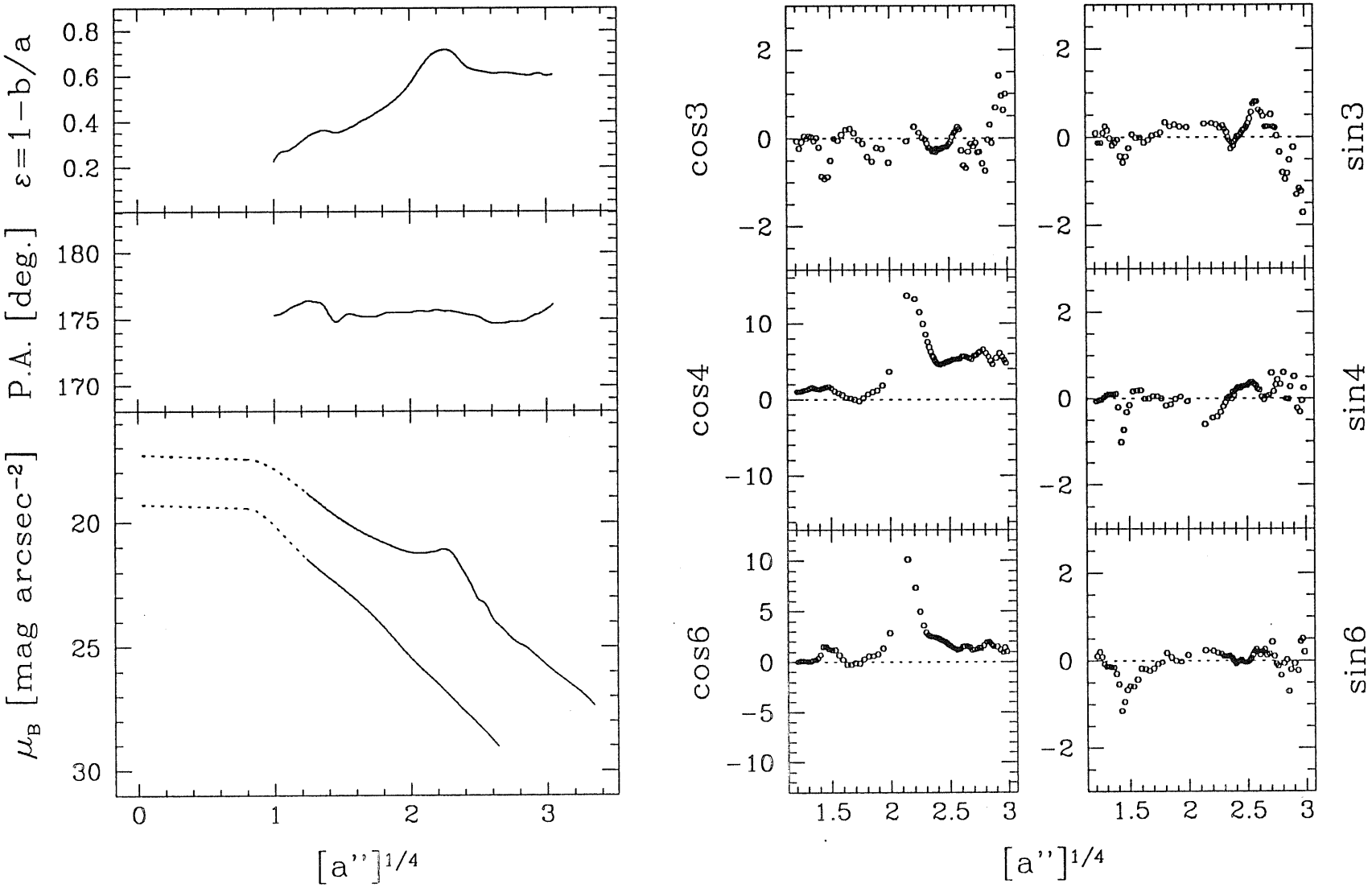
ε=1−b/a
P.A. [deg.]
μB [mag arcsec-2]
[a'']1/4
cos3
cos4
cos6
sin3
sin4
sin6
[a'']1/4

NGC 4255

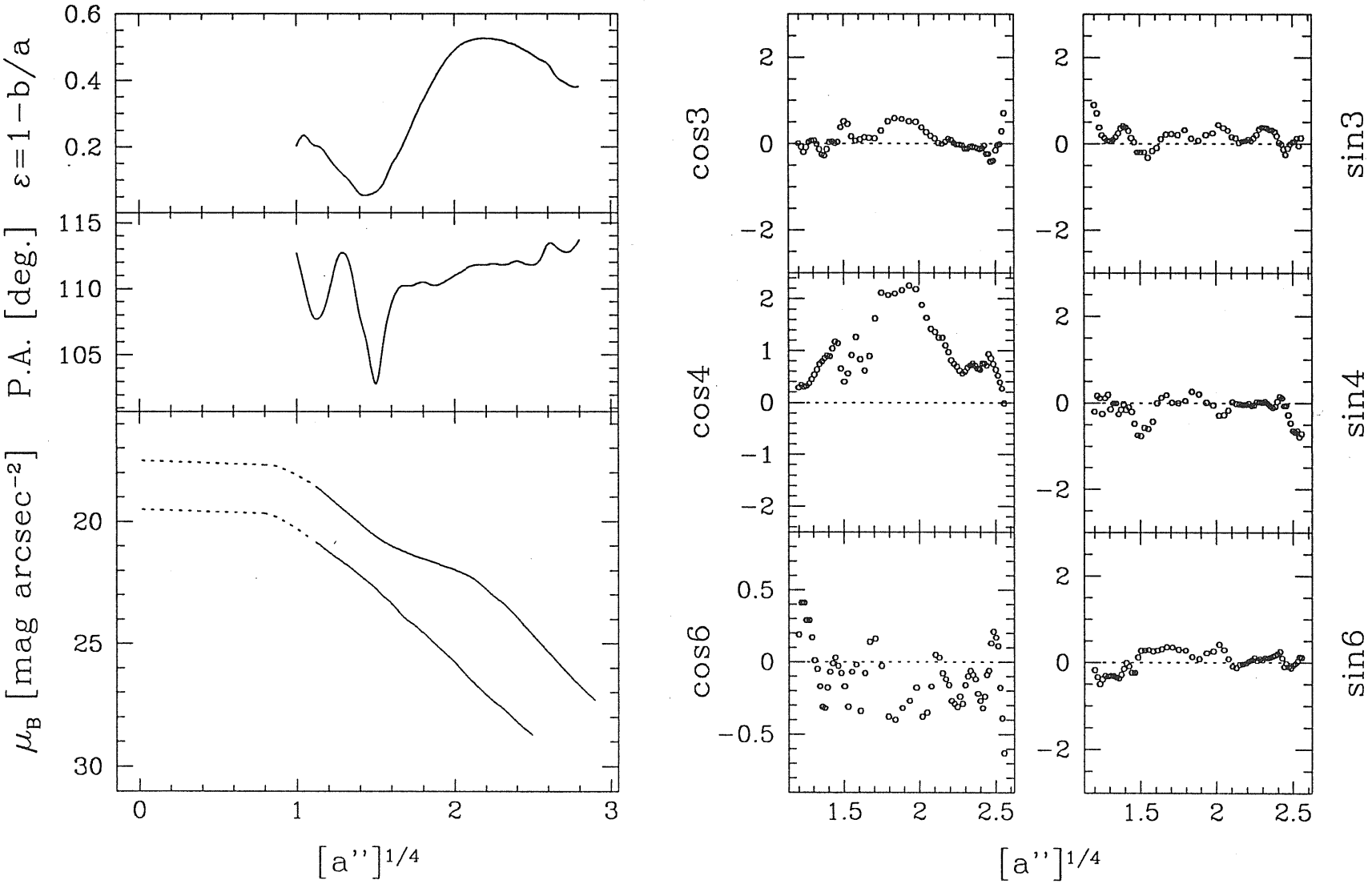
ε=1−b/a
P.A. [deg.]
μB [mag arcsec−2]
[a'']1/4
cos3
cos4
cos6
sin3
sin4
sin6
[a'']1/4

NGC 4261

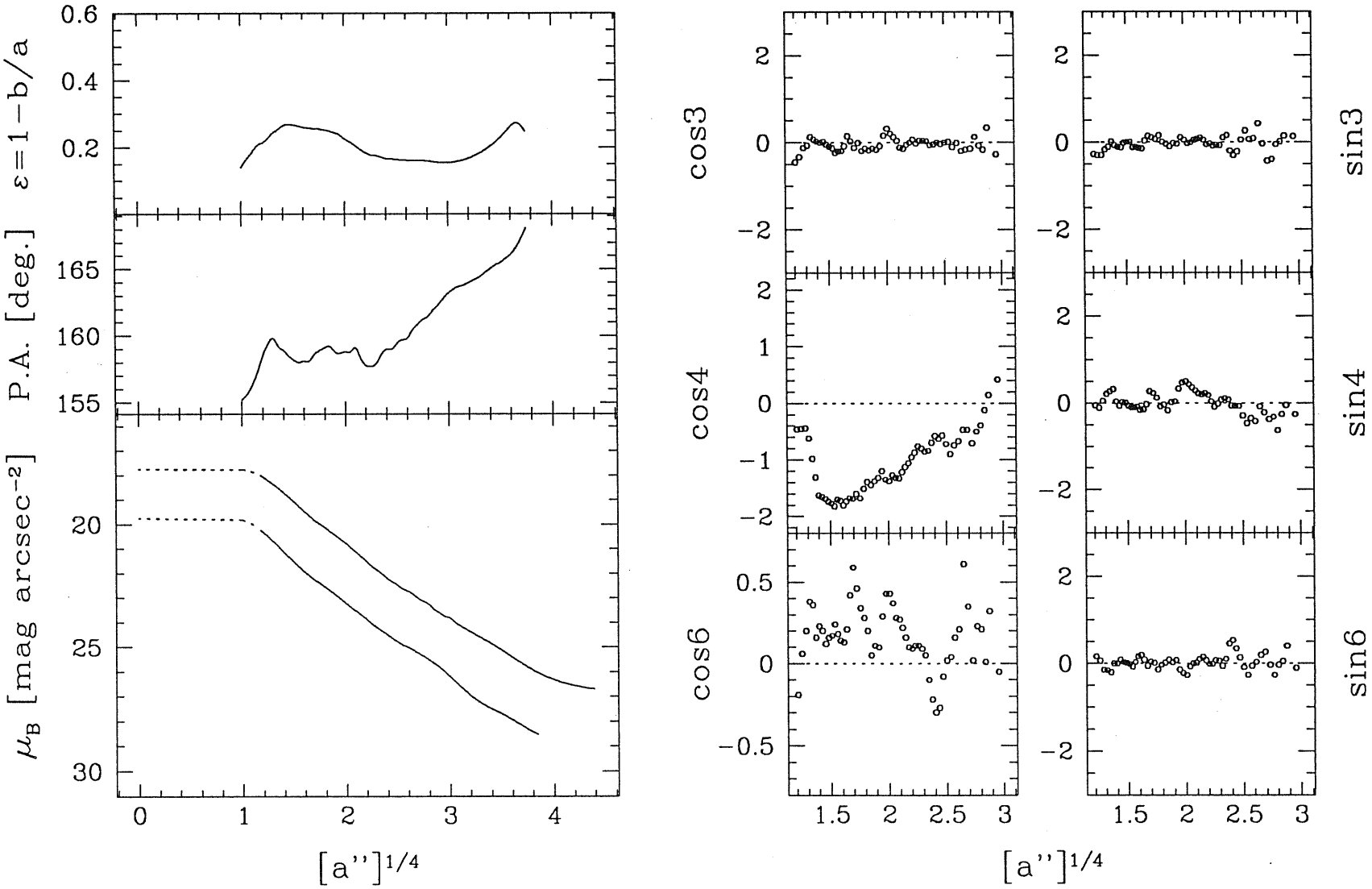
ε=1−b/a
P.A. [deg.]
μB [mag arcsec-2]
[a'']1/4
cos3
sin3
cos4
sin4
cos6
sin6
[a'']1/4

NGC 4268

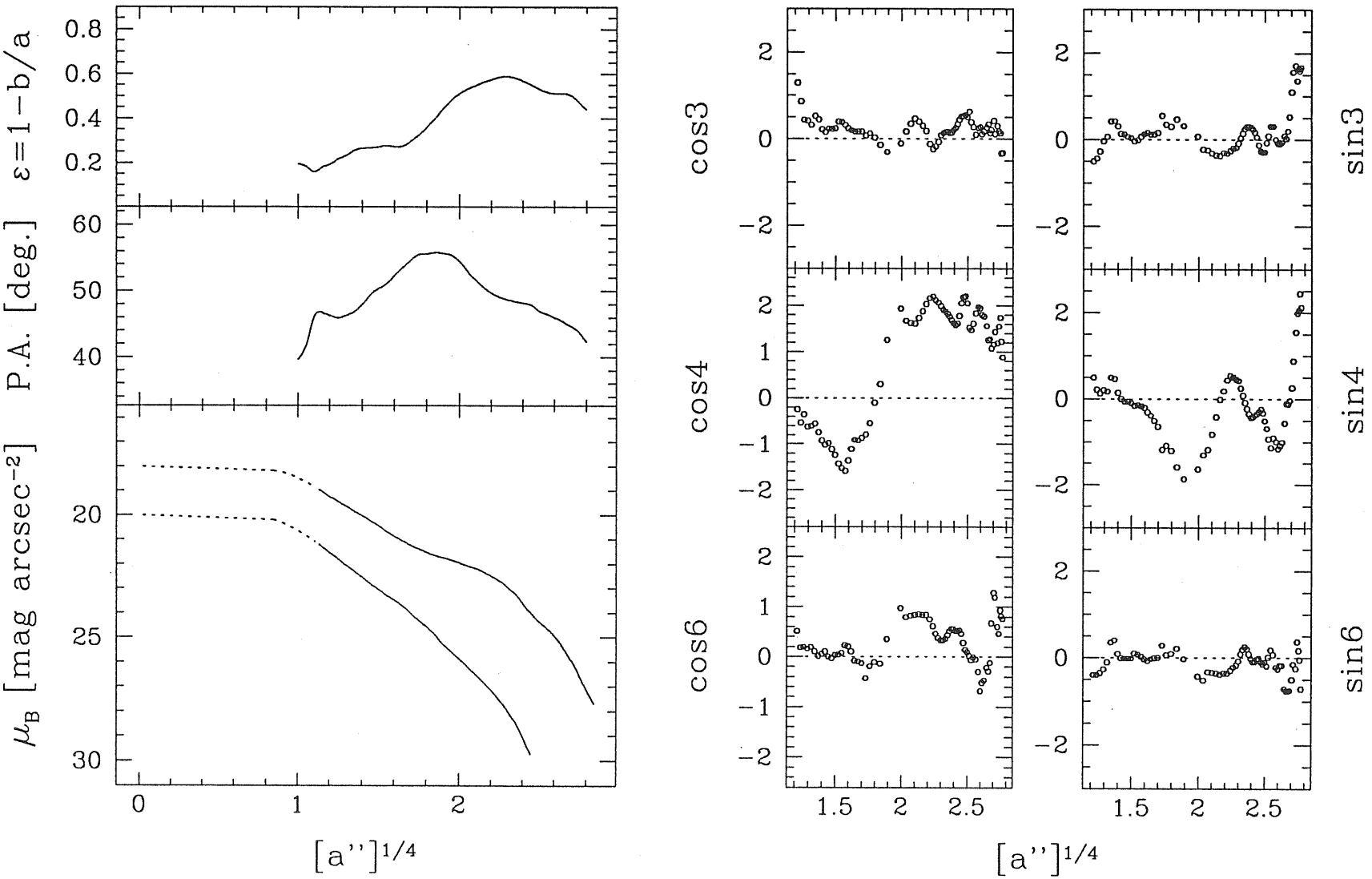
ε=1−b/a
P.A. [deg.]
μB [mag arcsec−2]
[a'']1/4
cos3
sin3
cos4
sin4
cos6
sin6
[a'']1/4

NGC 4269

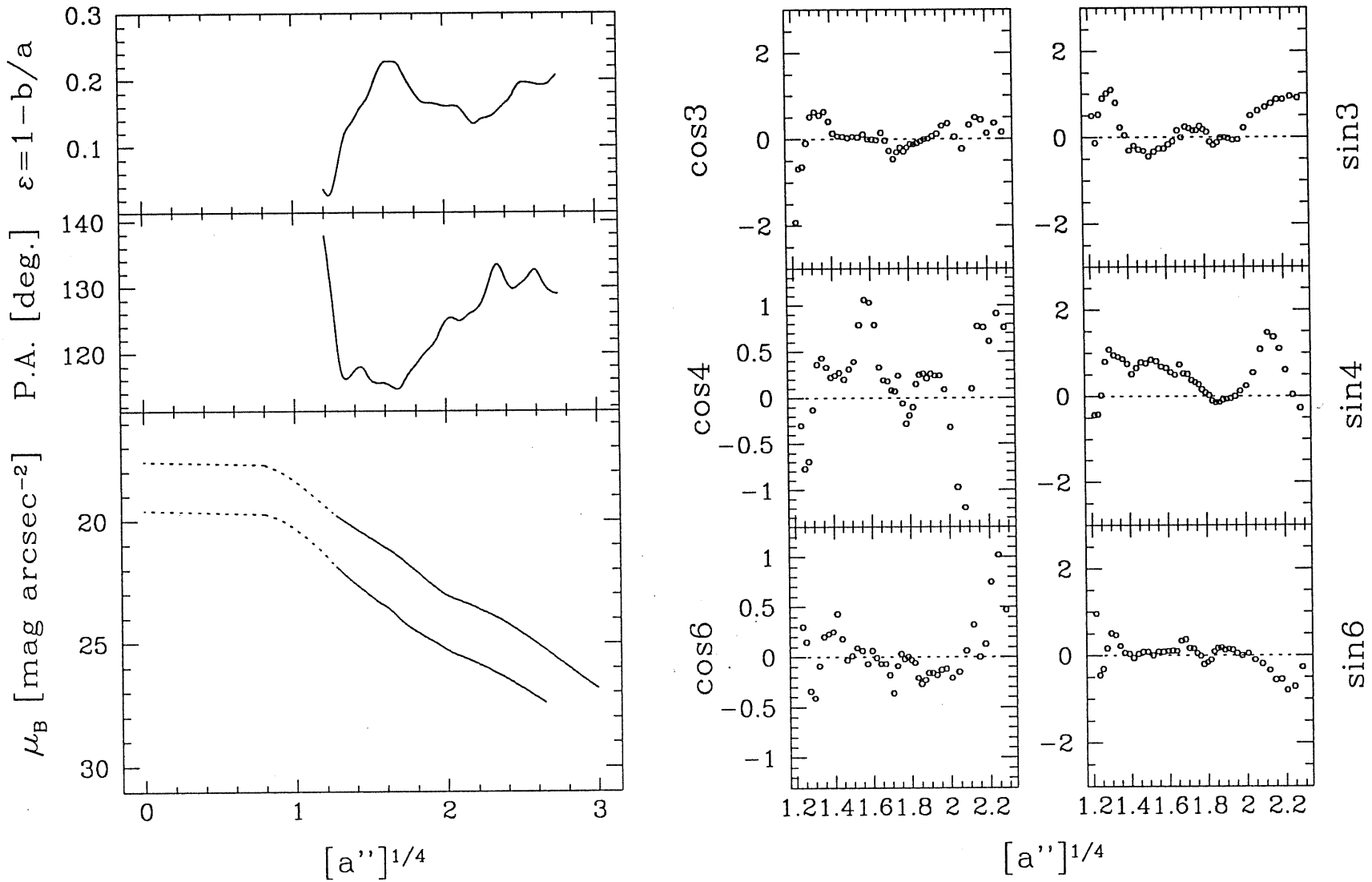
ε=1−b/a
P.A. [deg.]
μB [mag arcsec−2]
[a'']1/4
cos3
sin3
cos4
sin4
cos6
sin6
[a'']1/4

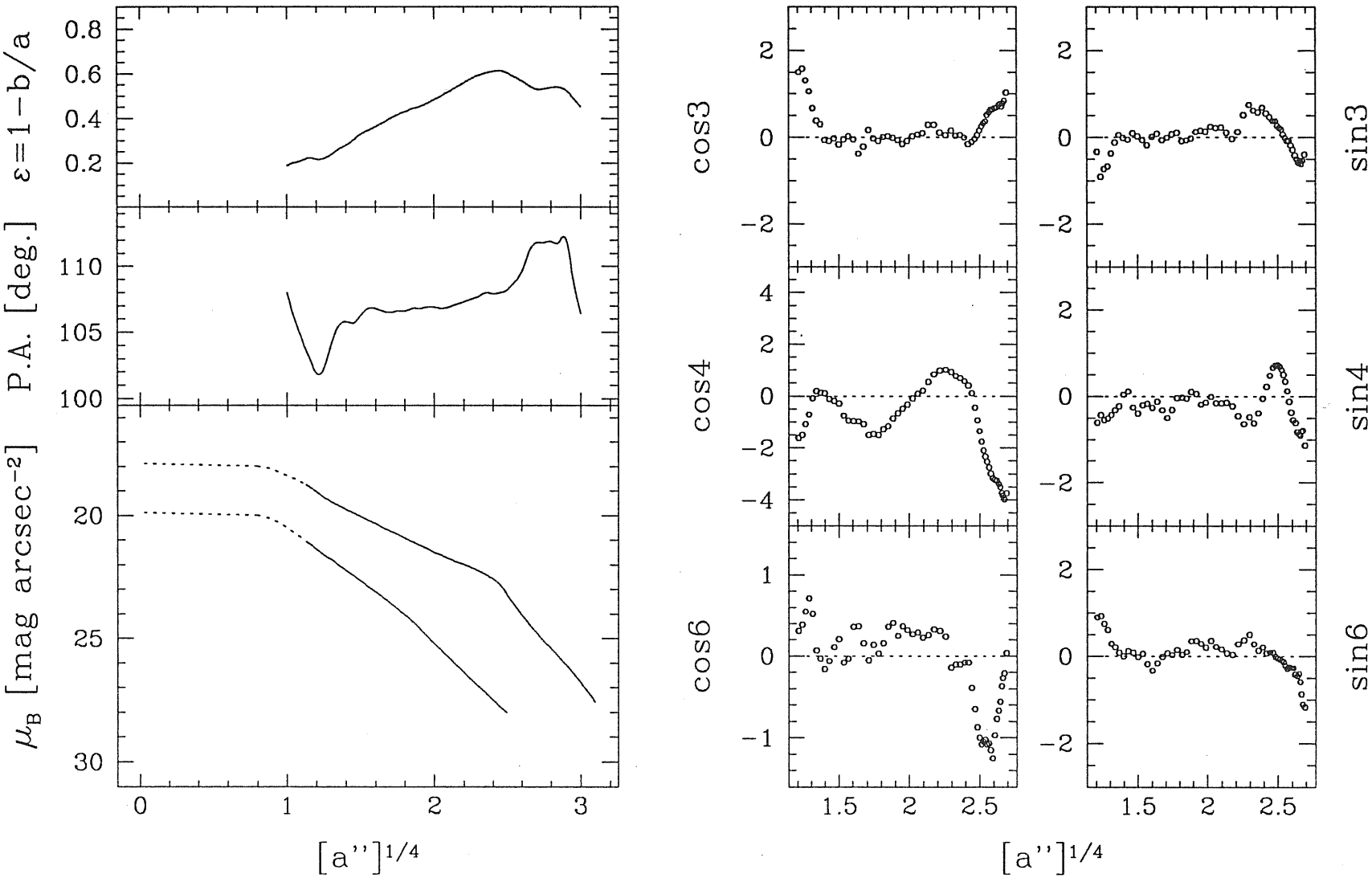
NGC 4270
μ_B [mag arcsec^{-2}]
P.A. [deg.]
$\varepsilon = 1 - b/a$
[a'']$^{1/4}$
cos3
sin3
cos4
sin4
cos6
sin6
[a'']$^{1/4}$

NGC 4281

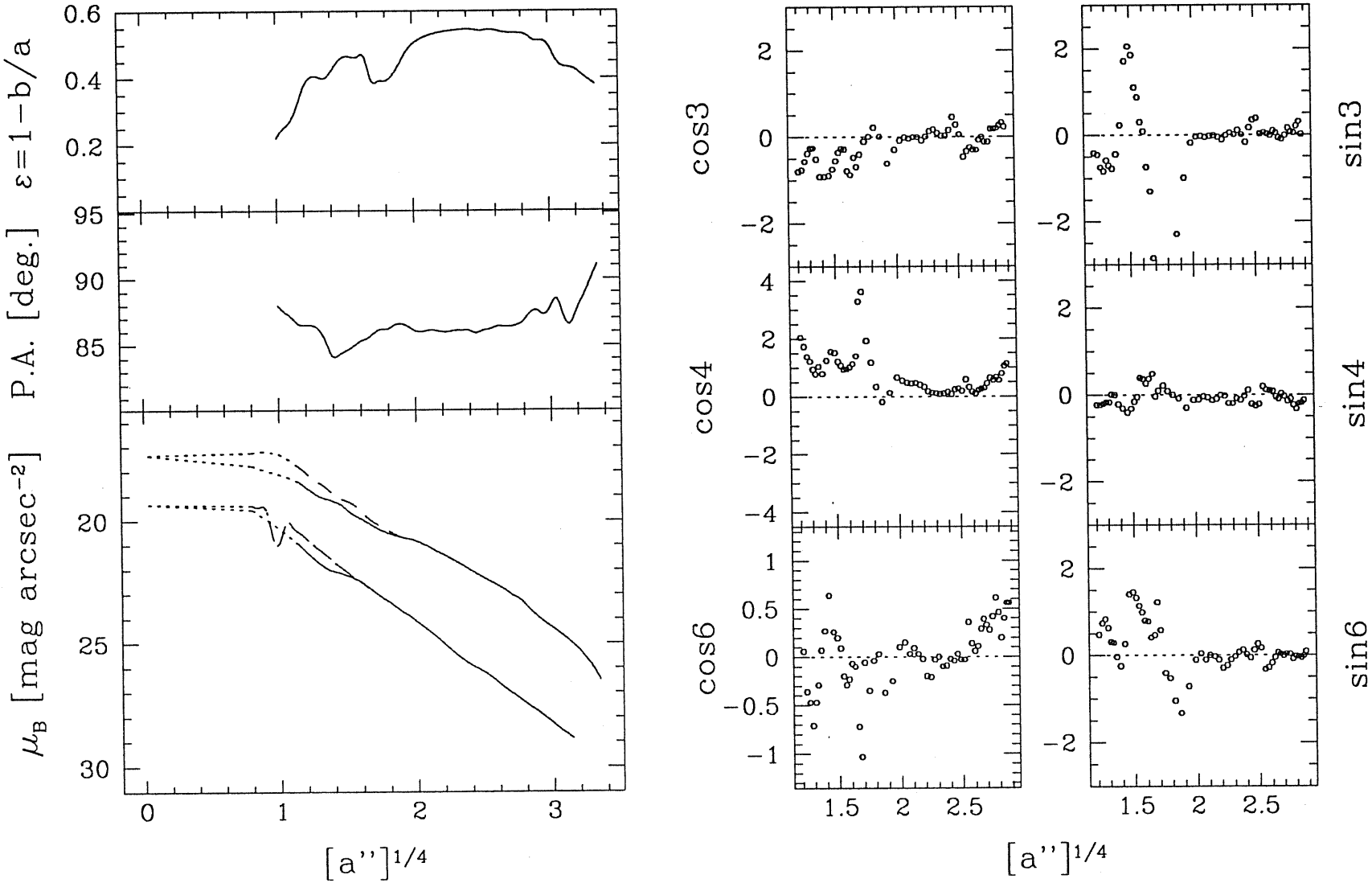
0.6
0.4
0.2
ε=1−b/a
95
90
85
P.A. [deg.]
20
25
30
μB [mag arcsec-2]
0
1
2
3
[a'']1/4
cos3
cos4
cos6
sin3
sin4
sin6
1.5
2
2.5
[a'']1/4

NGC 4339

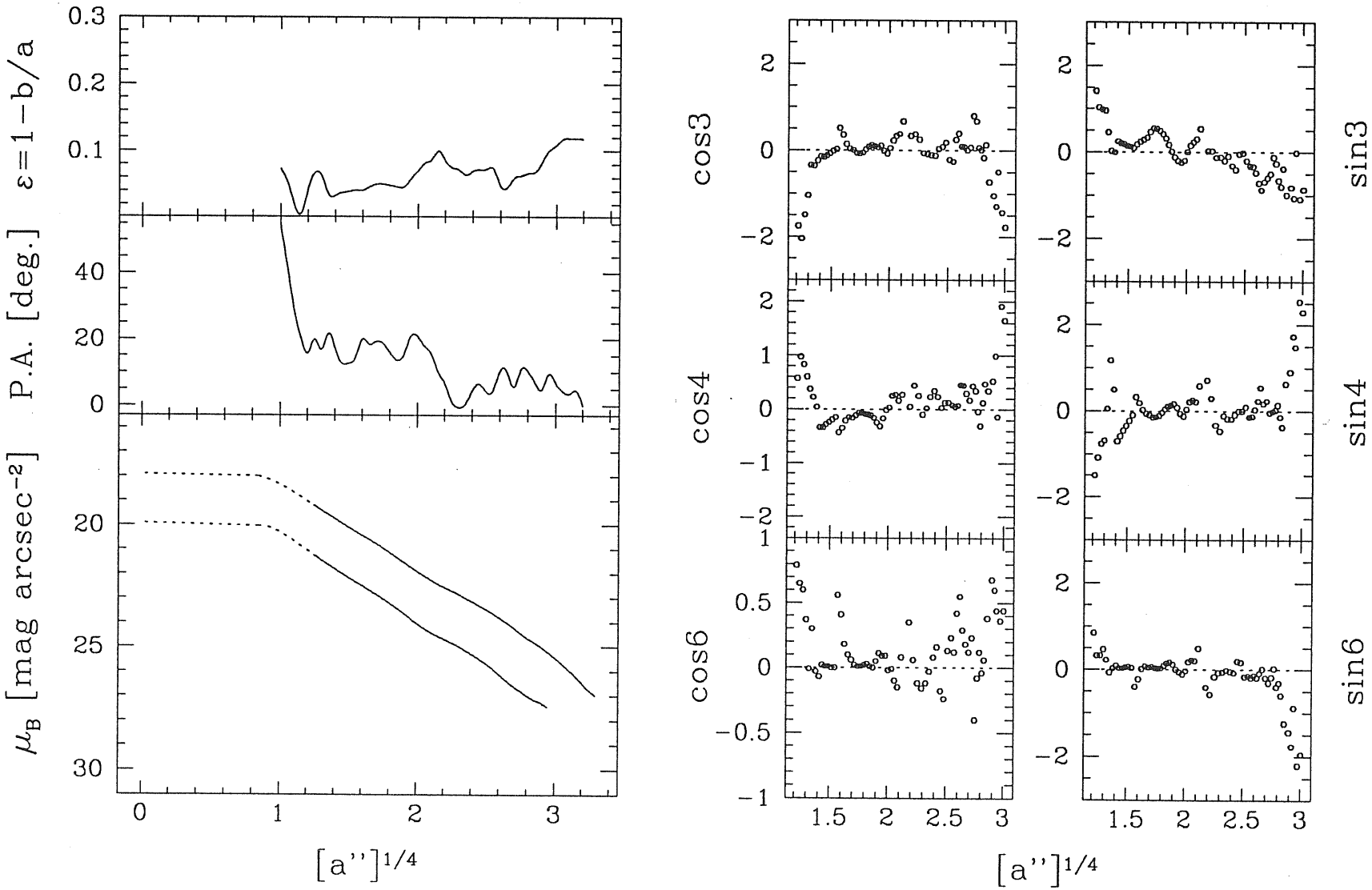
μ_B [mag arcsec^{-2}] P.A. [deg.] $\varepsilon = 1 - b/a$
0.3
0.2
0.1
40
20
0
20
25
30
0
1
2
3
[a'']$^{1/4}$
cos3
cos4
cos6
sin3
sin4
sin6
2
0
−2
1
−1
0.5
−0.5
1.5
2
2.5
3
[a'']$^{1/4}$

NGC 4342

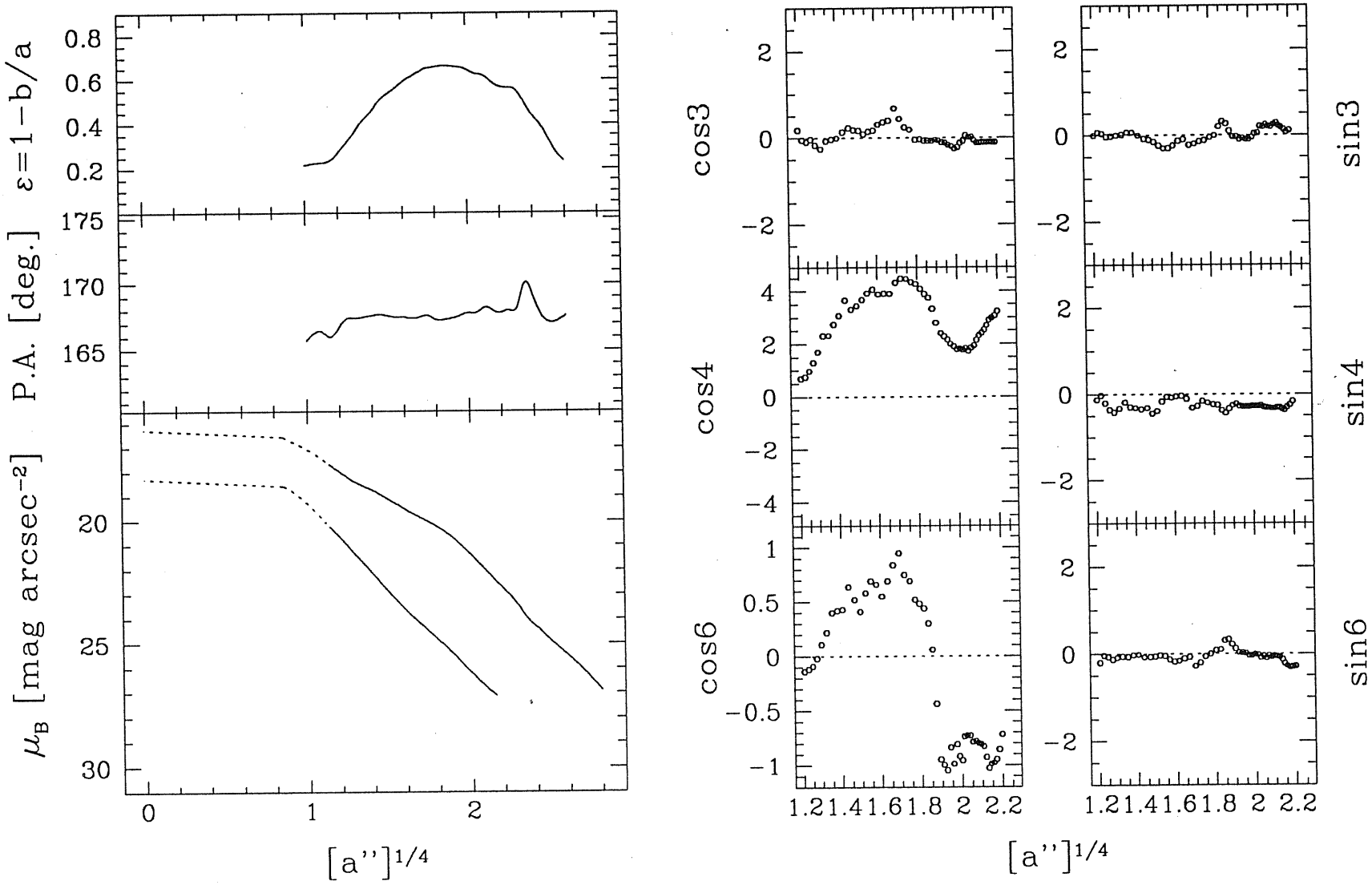
ε=1−b/a
P.A. [deg.]
μB [mag arcsec−2]
[a'']1/4
cos3
cos4
cos6
sin3
sin4
sin6
[a'']1/4

NGC 4360

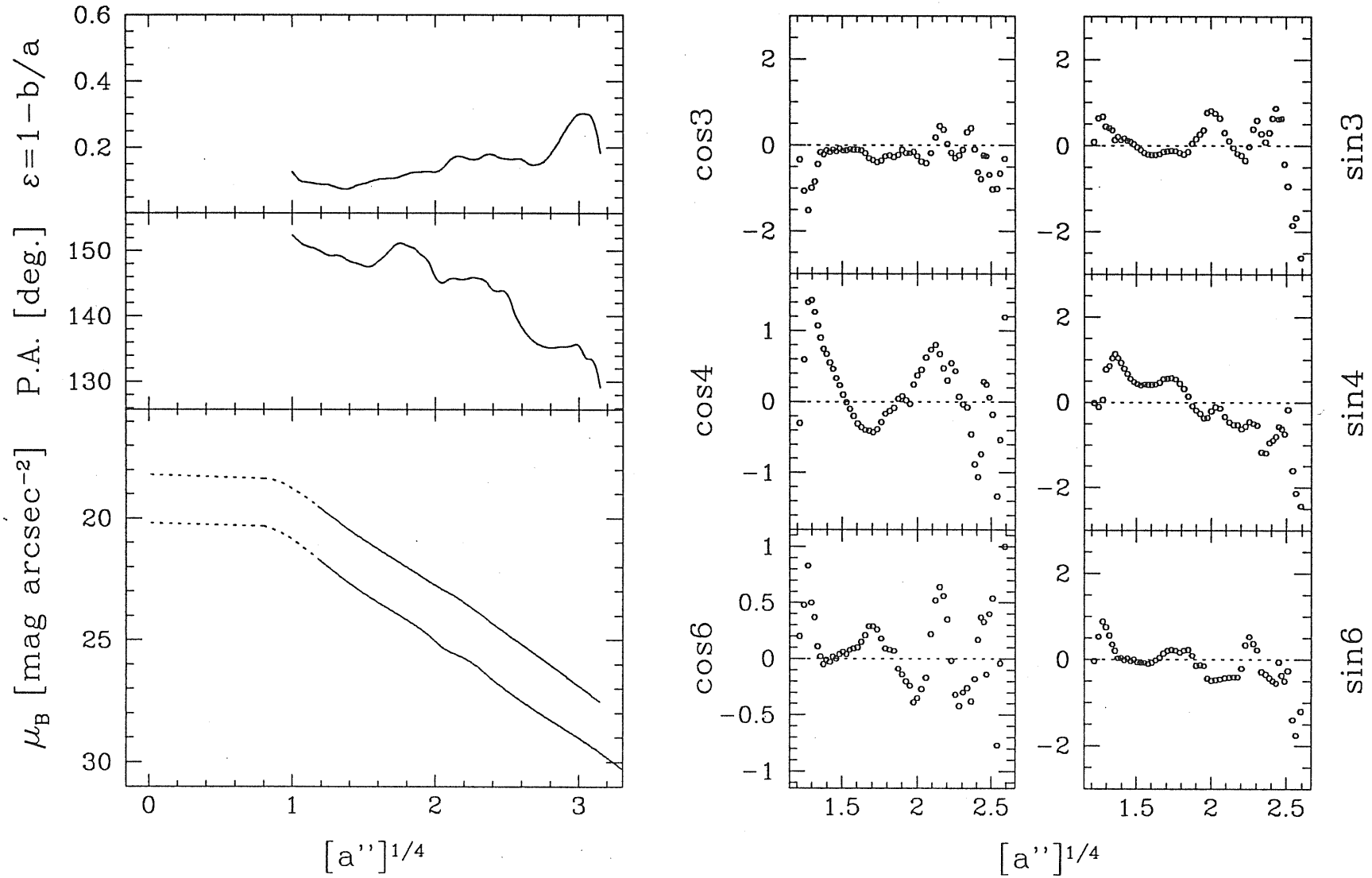
ε=1−b/a
P.A. [deg.]
μB [mag arcsec−2]
[a'']1/4
cos3
cos4
cos6
sin3
sin4
sin6
[a'']1/4

NGC 4365

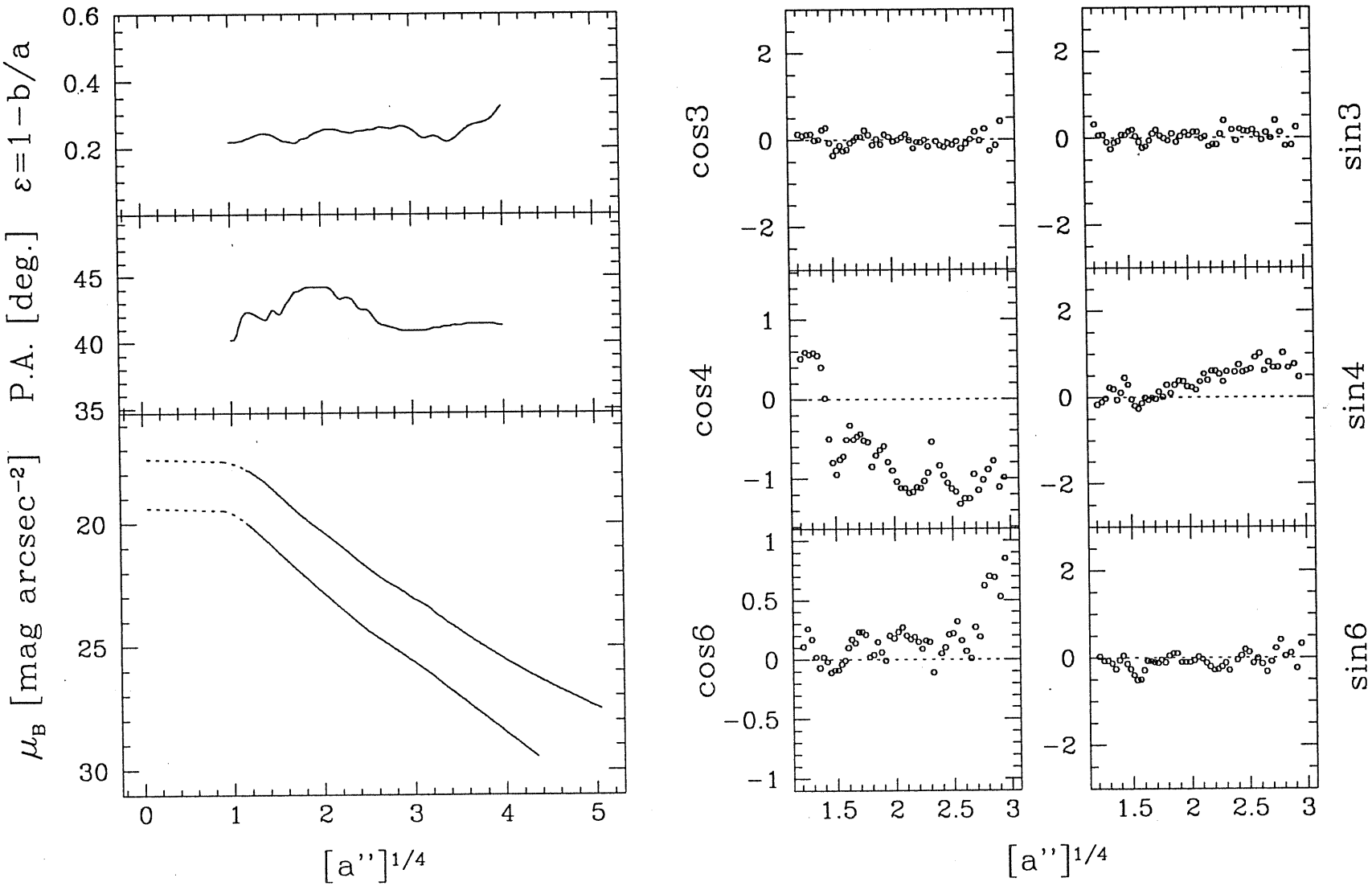
ε=1−b/a
P.A. [deg.]
μB [mag arcsec−2]
[a'']1/4
cos3
sin3
cos4
sin4
cos6
sin6
[a'']1/4

NGC 4370

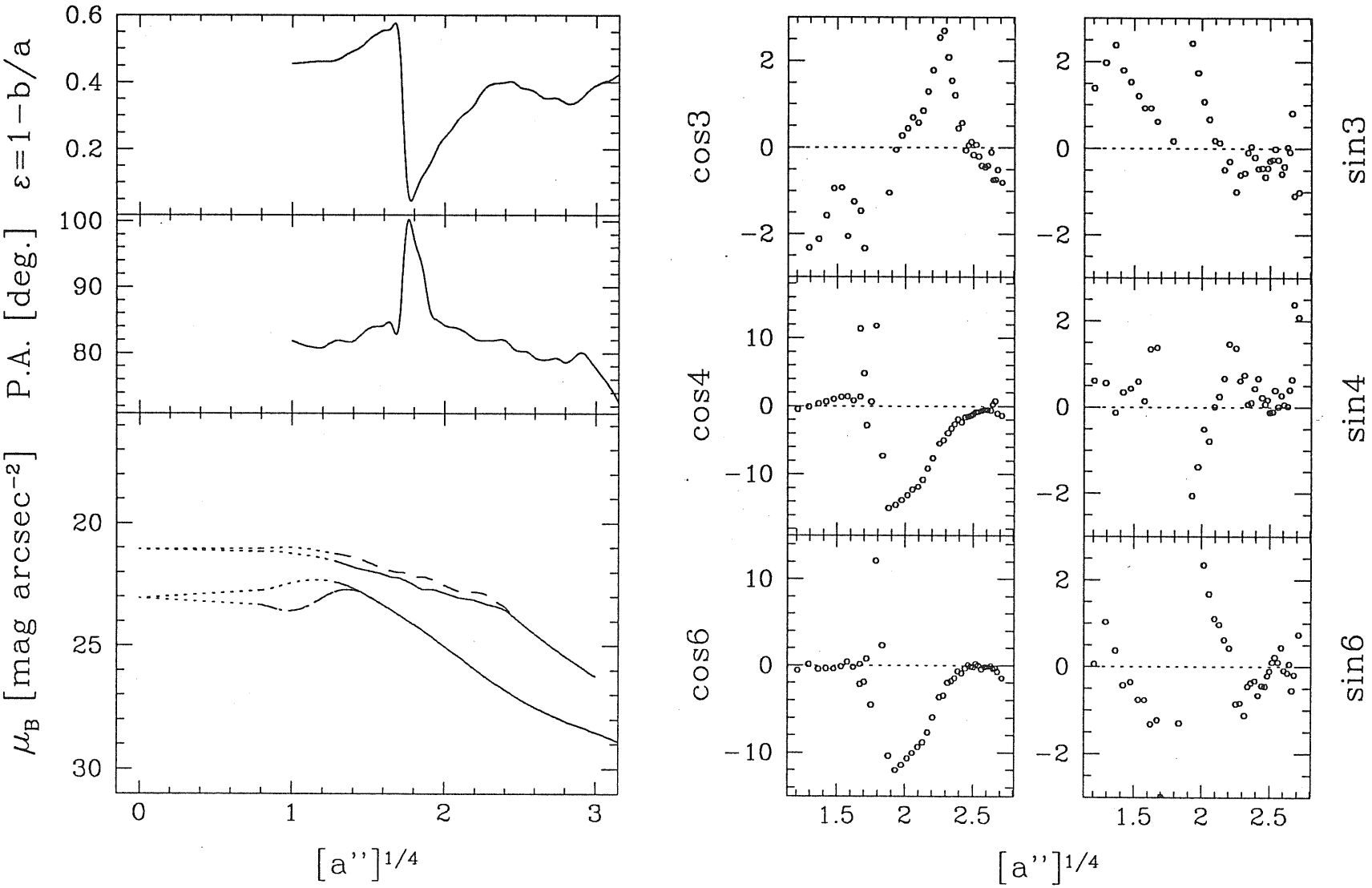
μ_B [mag arcsec^{-2}]
P.A. [deg.]
$\varepsilon = 1 - b/a$
0.6
0.4
0.2
100
90
80
20
25
30
0
1
2
3
[a'']$^{1/4}$
cos3
cos4
cos6
sin3
sin4
sin6
2
0
−2
10
−10
1.5
2
2.5
[a'']$^{1/4}$

NGC 4377

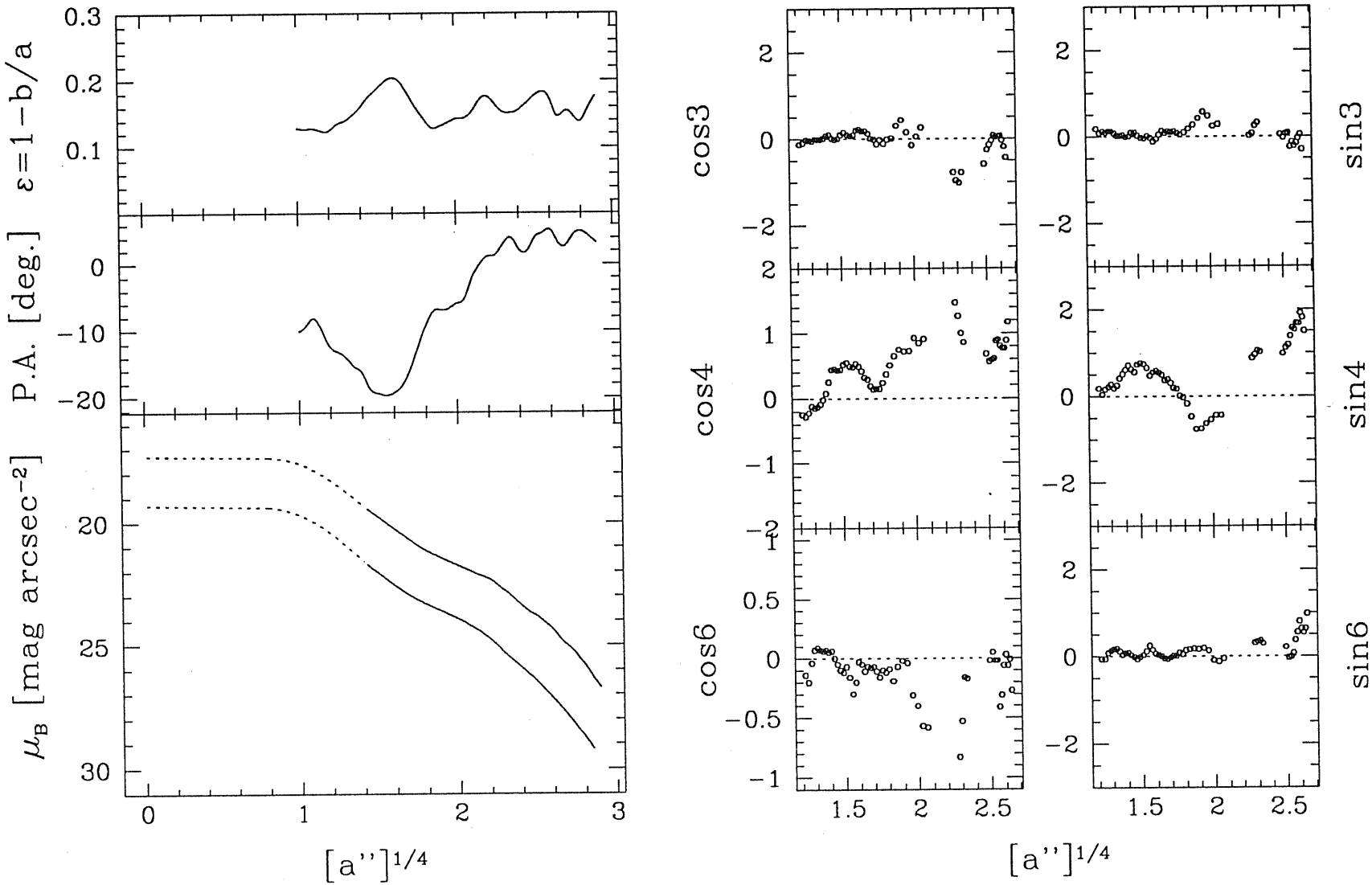
ε=1−b/a
P.A. [deg.]
μB [mag arcsec−2]
[a'']1/4
cos3
sin3
cos4
sin4
cos6
sin6
[a'']1/4

NGC 4472

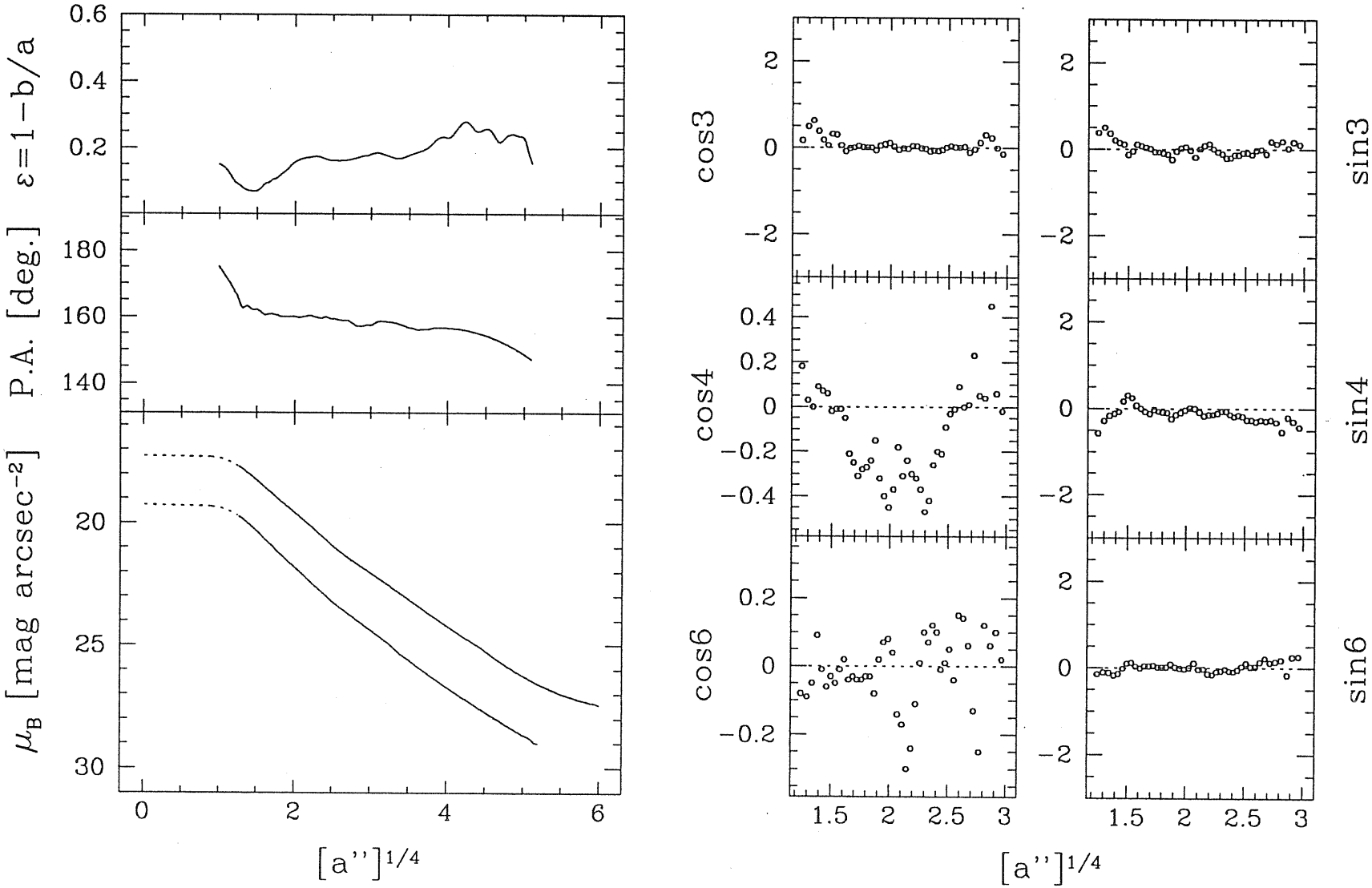
0.6
0.4
0.2
ε=1−b/a
180
160
140
P.A. [deg.]
20
25
30
μB [mag arcsec−2]
0
2
4
6
[a'']1/4
cos3
cos4
cos6
sin3
sin4
sin6
2
0
−2
0.4
0.2
−0.2
−0.4
1.5
2
2.5
3
[a'']1/4

NGC 4526

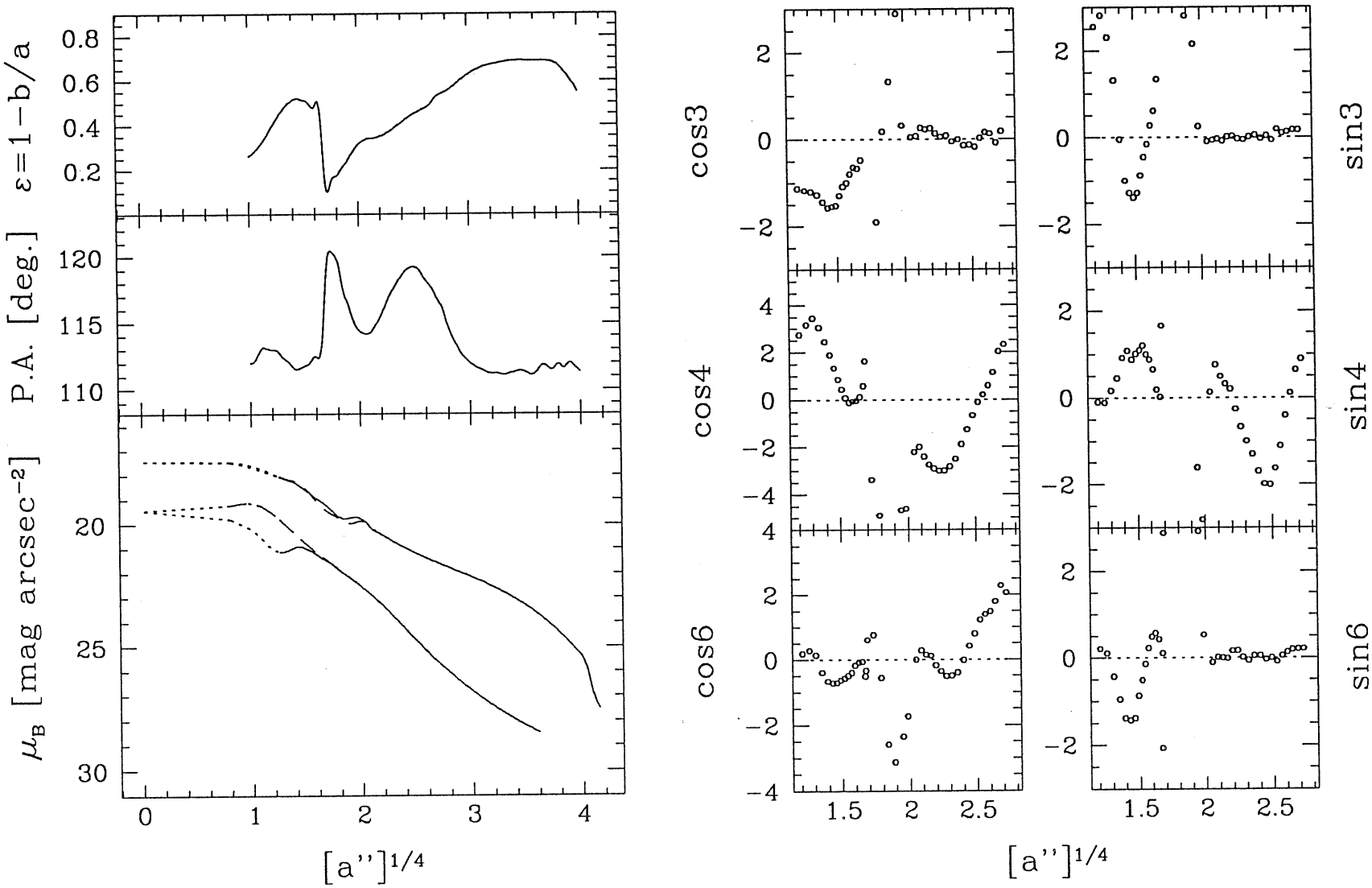
0.8
0.6
0.4
0.2
ε=1−b/a
120
115
110
P.A. [deg.]
20
25
30
μB [mag arcsec−2]
0
1
2
3
4
[a'']1/4
cos3
cos4
cos6
sin3
sin4
sin6
1.5
2
2.5
[a'']1/4

NGC 4570

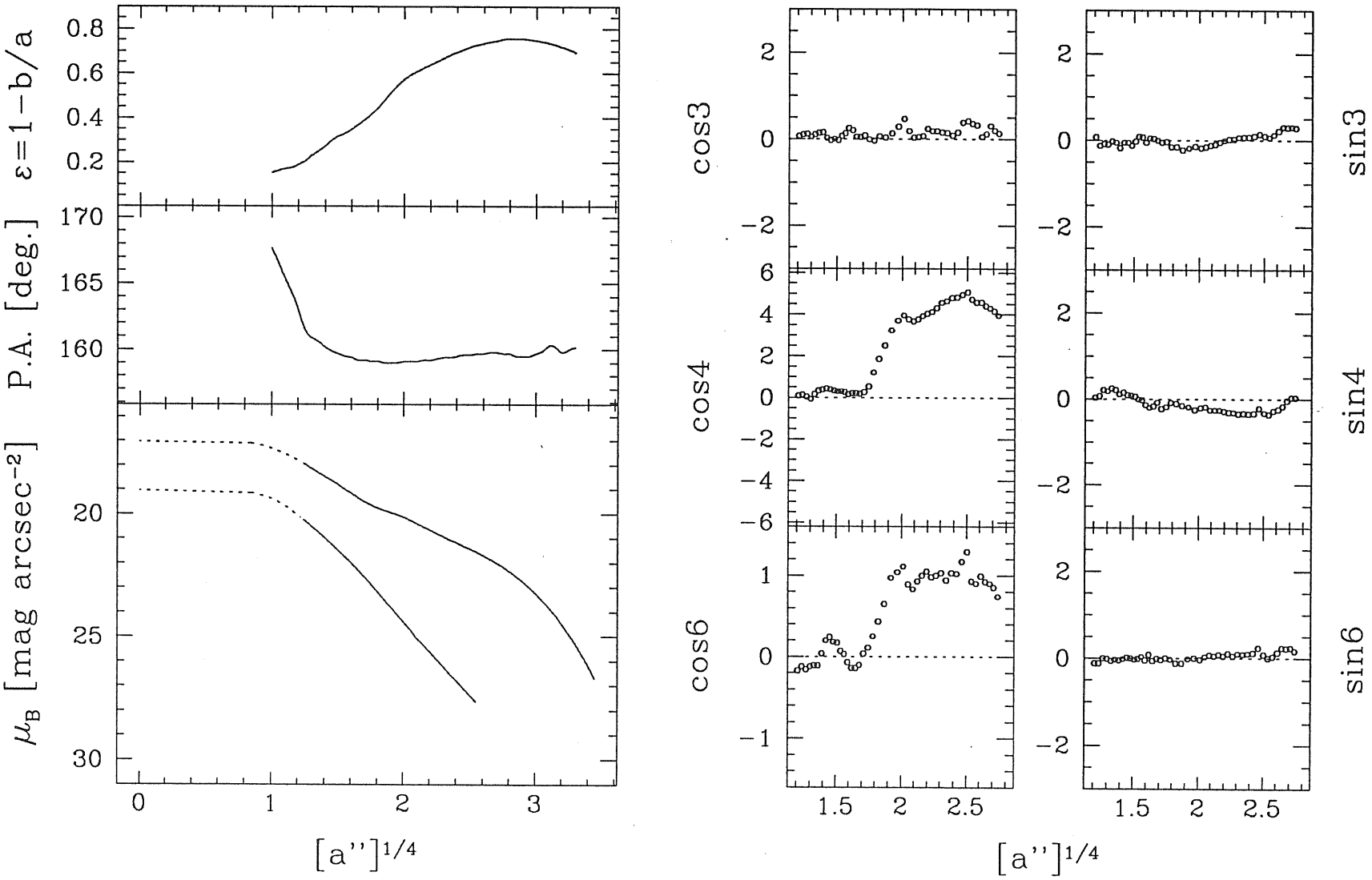
ε=1−b/a
P.A. [deg.]
μB [mag arcsec−2]
[a'']1/4
cos3
sin3
cos4
sin4
cos6
sin6
[a'']1/4

NGC 4600

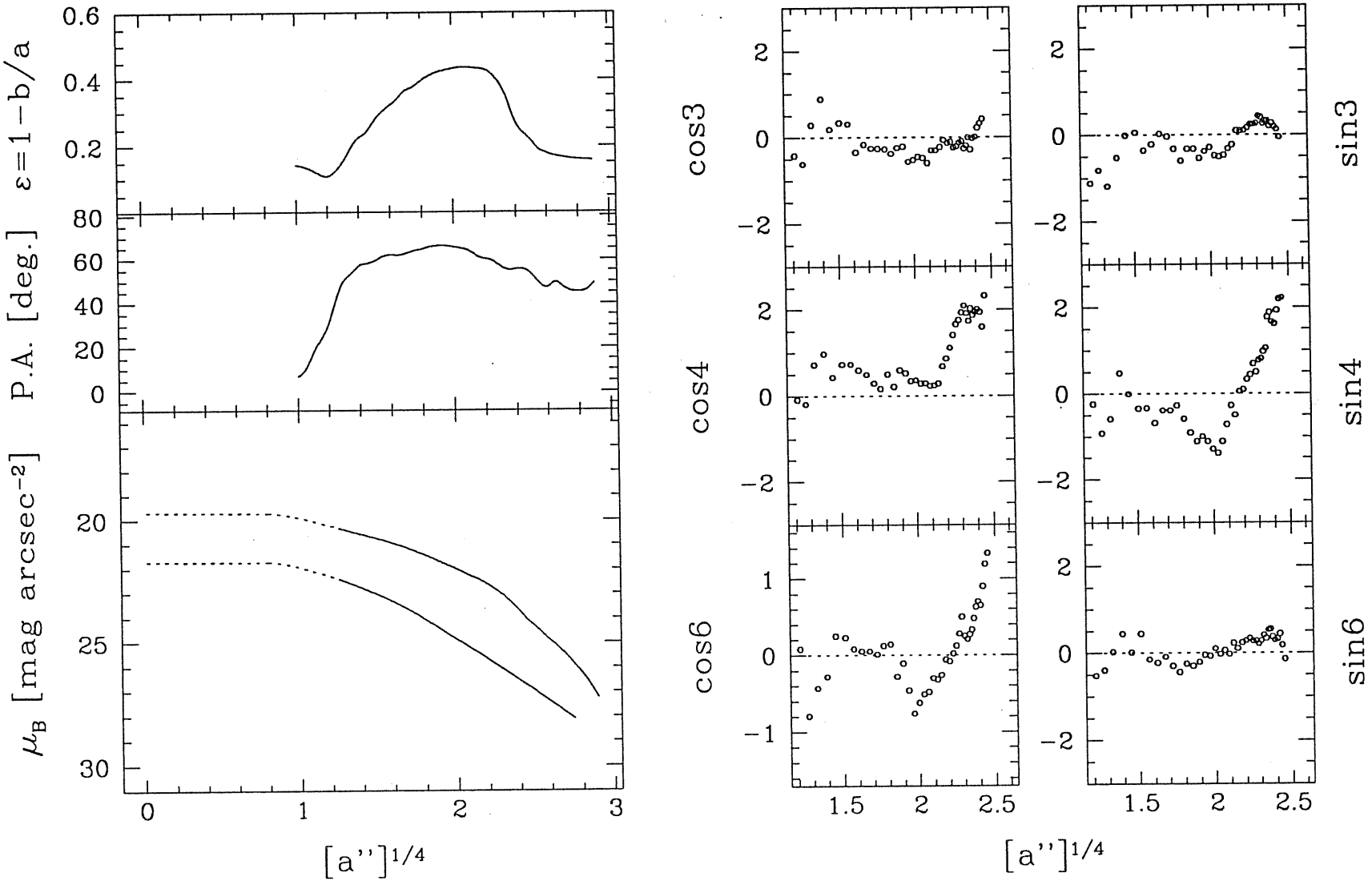
μ_B [mag arcsec^{-2}] P.A. [deg.] $\varepsilon = 1 - b/a$
0.6
0.4
0.2
80
60
40
20
0
20
25
30
0
1
2
3
[a'']$^{1/4}$
cos3
cos4
cos6
sin3
sin4
sin6
2
0
−2
1
−1
1.5
2
2.5
[a'']$^{1/4}$

NGC 4623

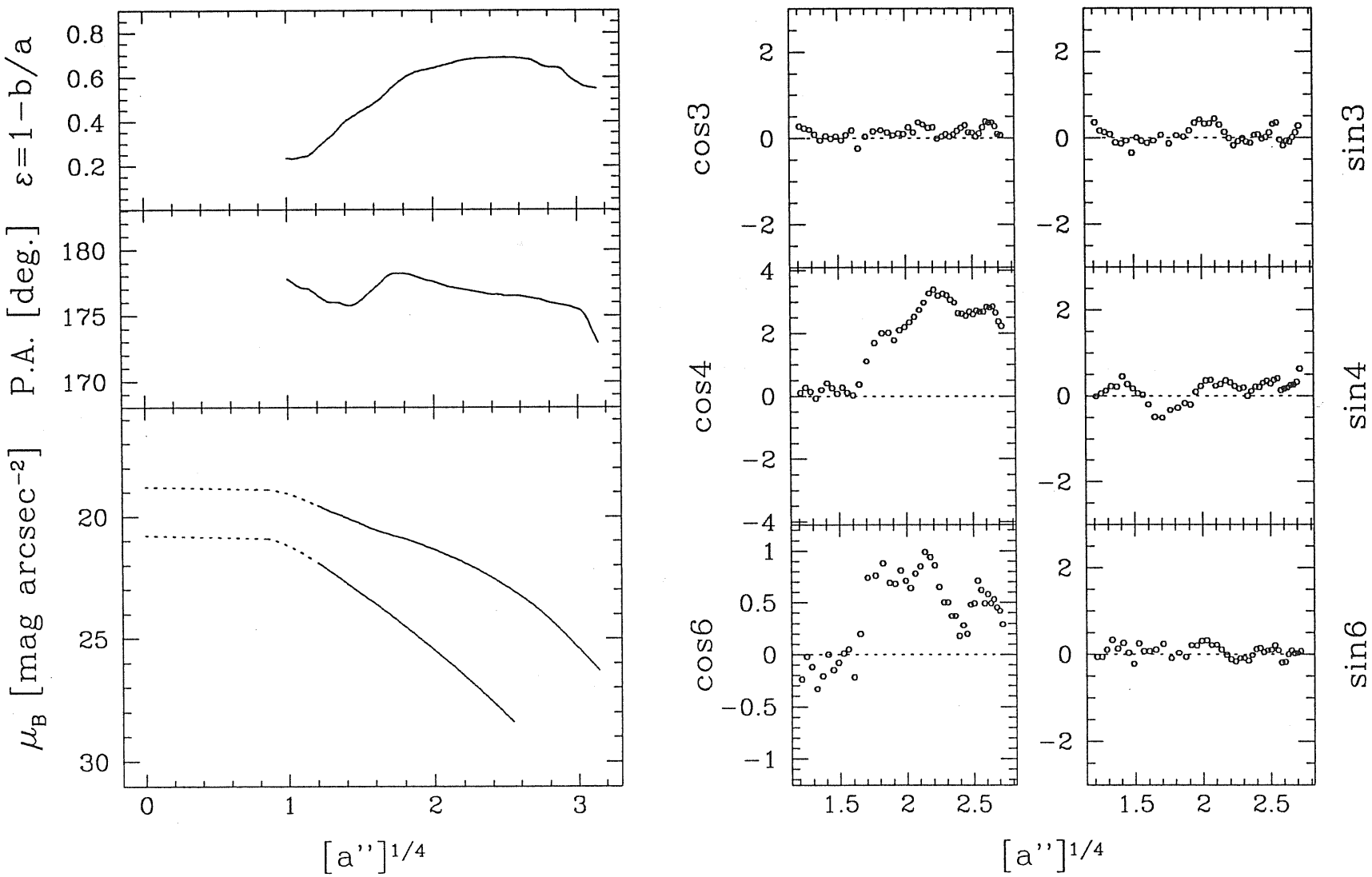
ε=1−b/a
P.A. [deg.]
μB [mag arcsec−2]
[a'']1/4
cos3
sin3
cos4
sin4
cos6
sin6
[a'']1/4

NGC 4636

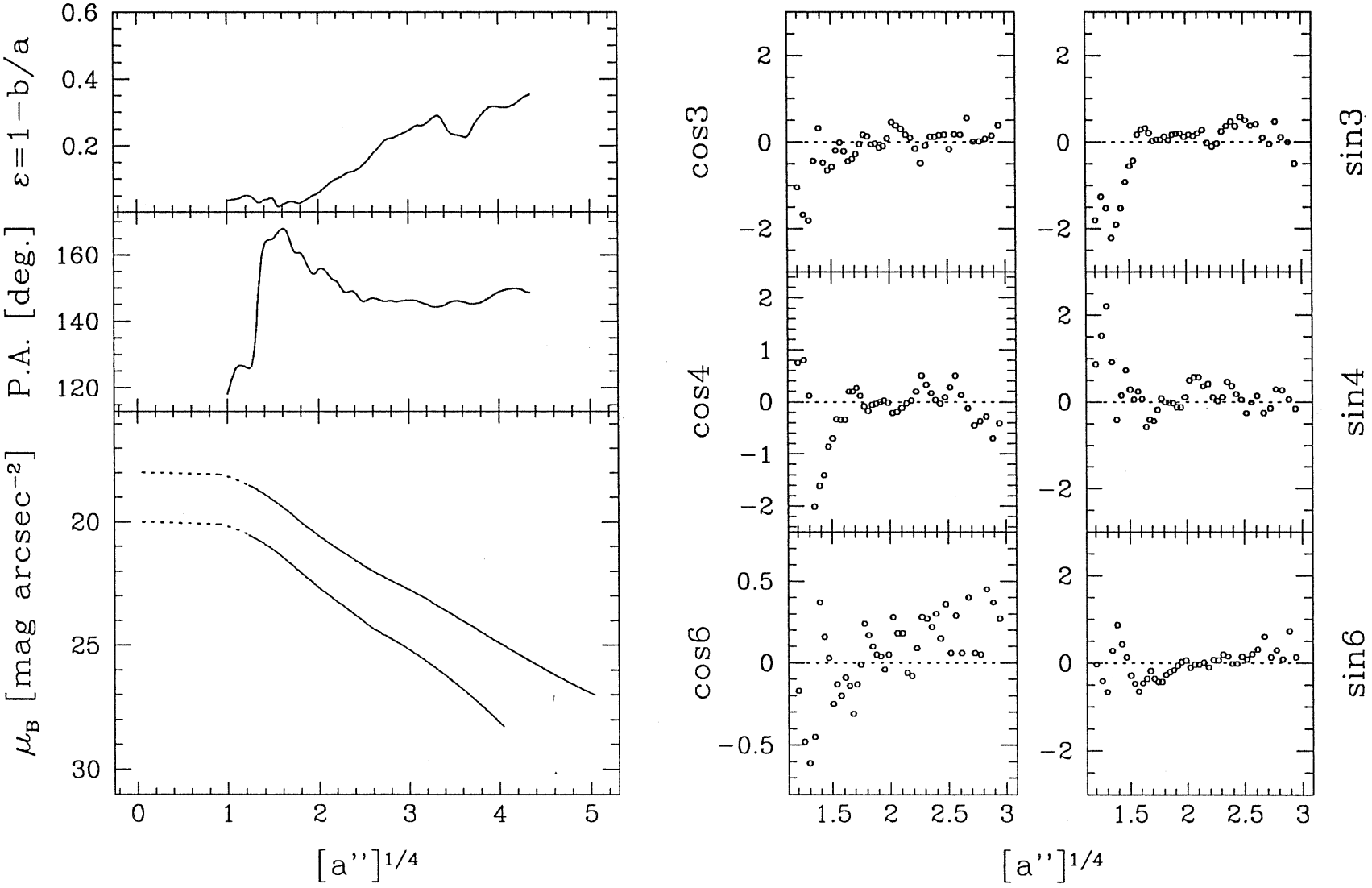
ε=1−b/a
P.A. [deg.]
μB [mag arcsec−2]
[a'']1/4
cos3
sin3
cos4
sin4
cos6
sin6
[a'']1/4

FCC 019

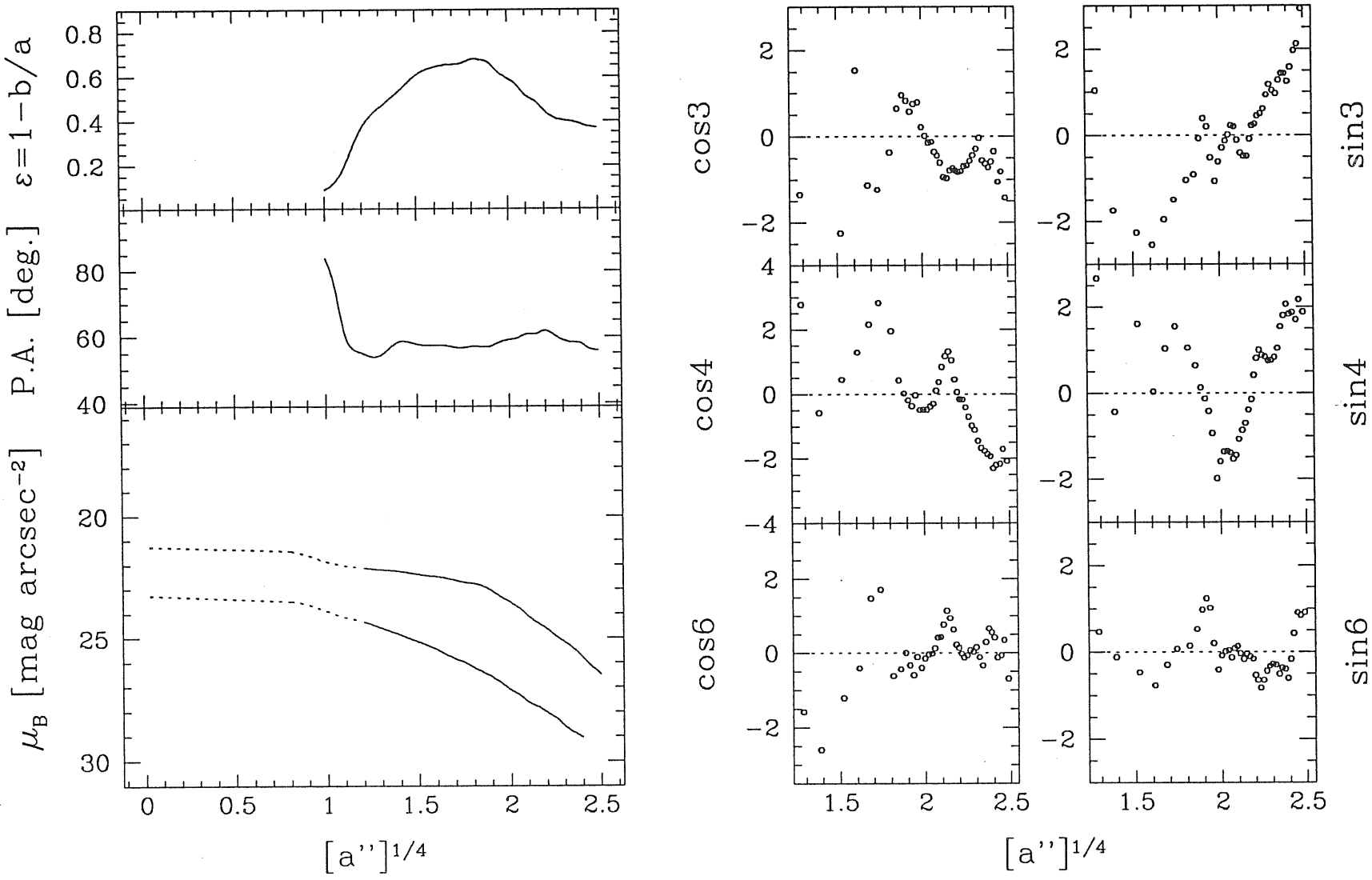
μ_B [mag arcsec^{-2}] P.A. [deg.] ε=1−b/a
0.8
0.6
0.4
0.2
80
60
40
20
25
30
0
0.5
1
1.5
2
2.5
[a'']$^{1/4}$
cos3
cos4
cos6
sin3
sin4
sin6
2
0
−2
4
−4
1.5
2
2.5
[a'']$^{1/4}$

FCC 055

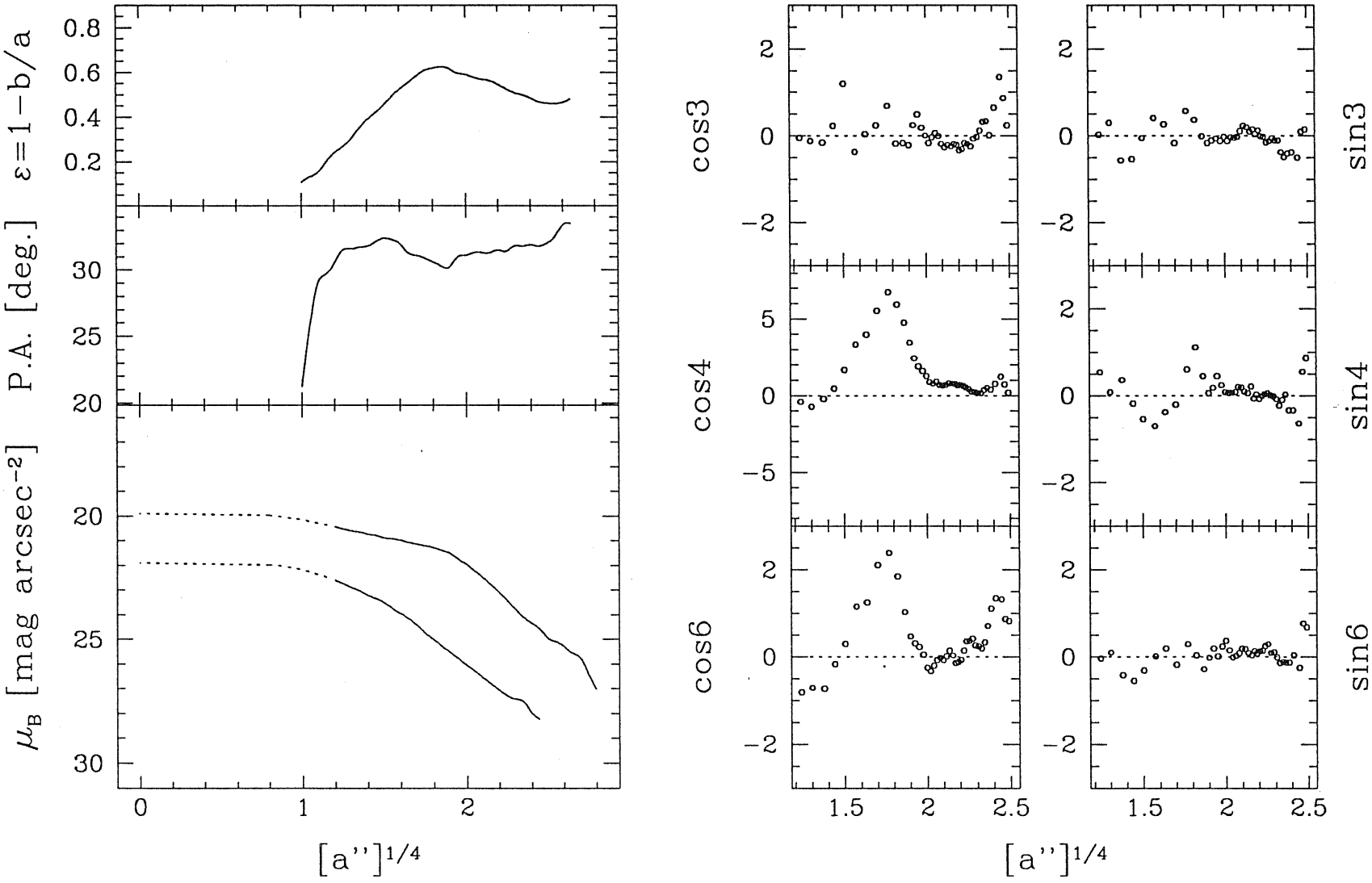
ε=1−b/a
P.A. [deg.]
μB [mag arcsec−2]
[a'']1/4
cos3
sin3
cos4
sin4
cos6
sin6
[a'']1/4

FCC 090

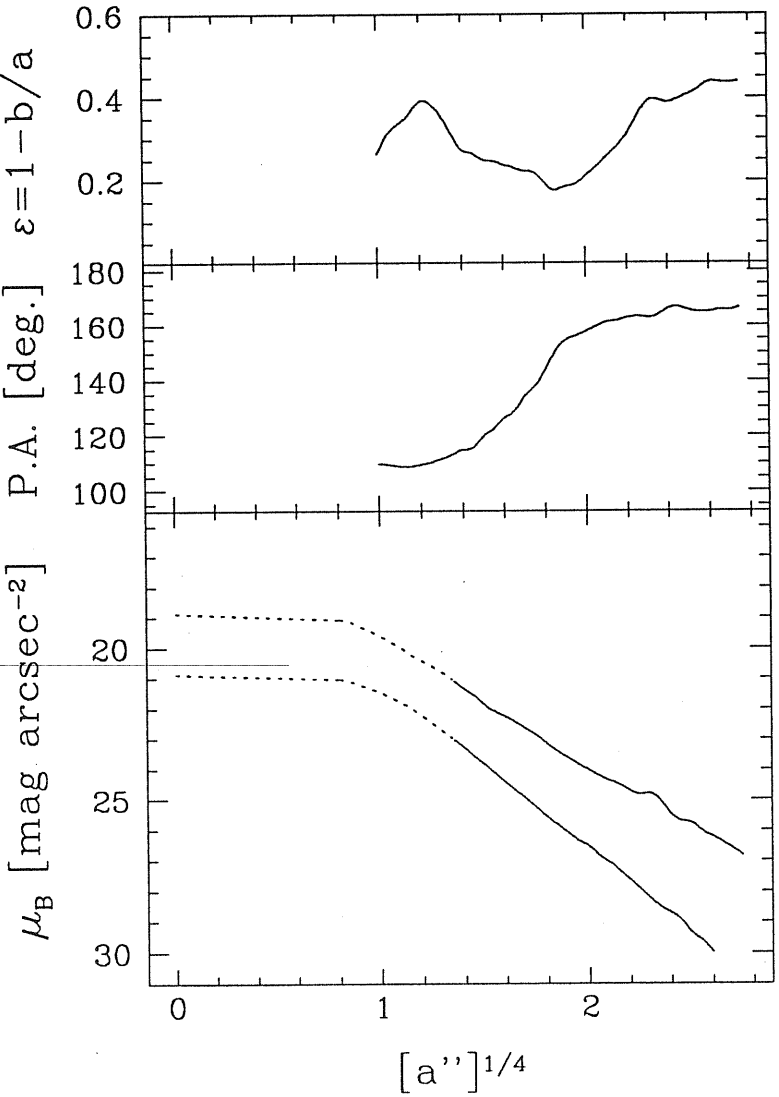
0.6
0.4
0.2
ε=1−b/a
180
160
140
120
100
P.A. [deg.]
20
25
30
μB [mag arcsec−2]
0
1
2
[a'']1/4

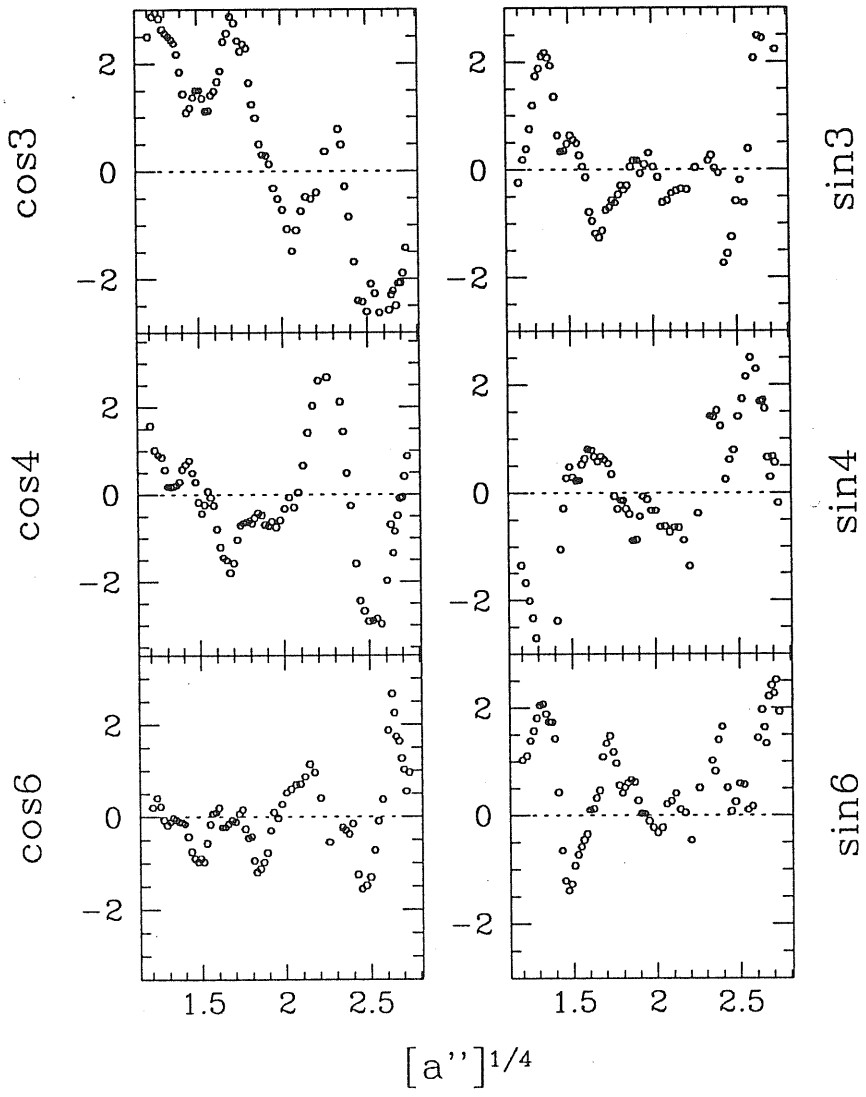
cos3
cos4
cos6
sin3
sin4
sin6
2
0
−2
1.5
2
2.5
[a'']1/4

FCC 119

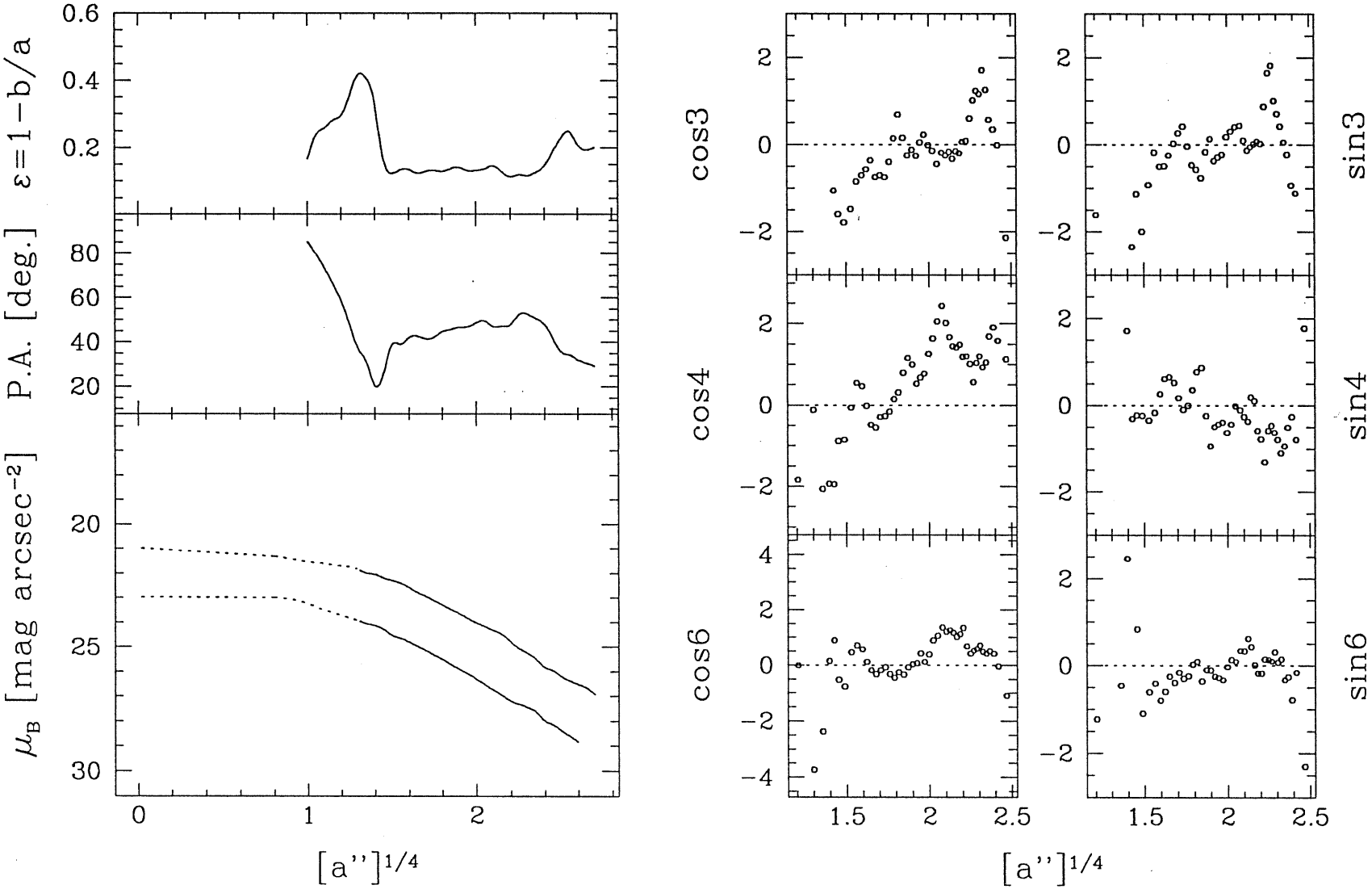
ε=1−b/a
P.A. [deg.]
μB [mag arcsec−2]
[a'']1/4
cos3
sin3
cos4
sin4
cos6
sin6
[a'']1/4

FCC 136

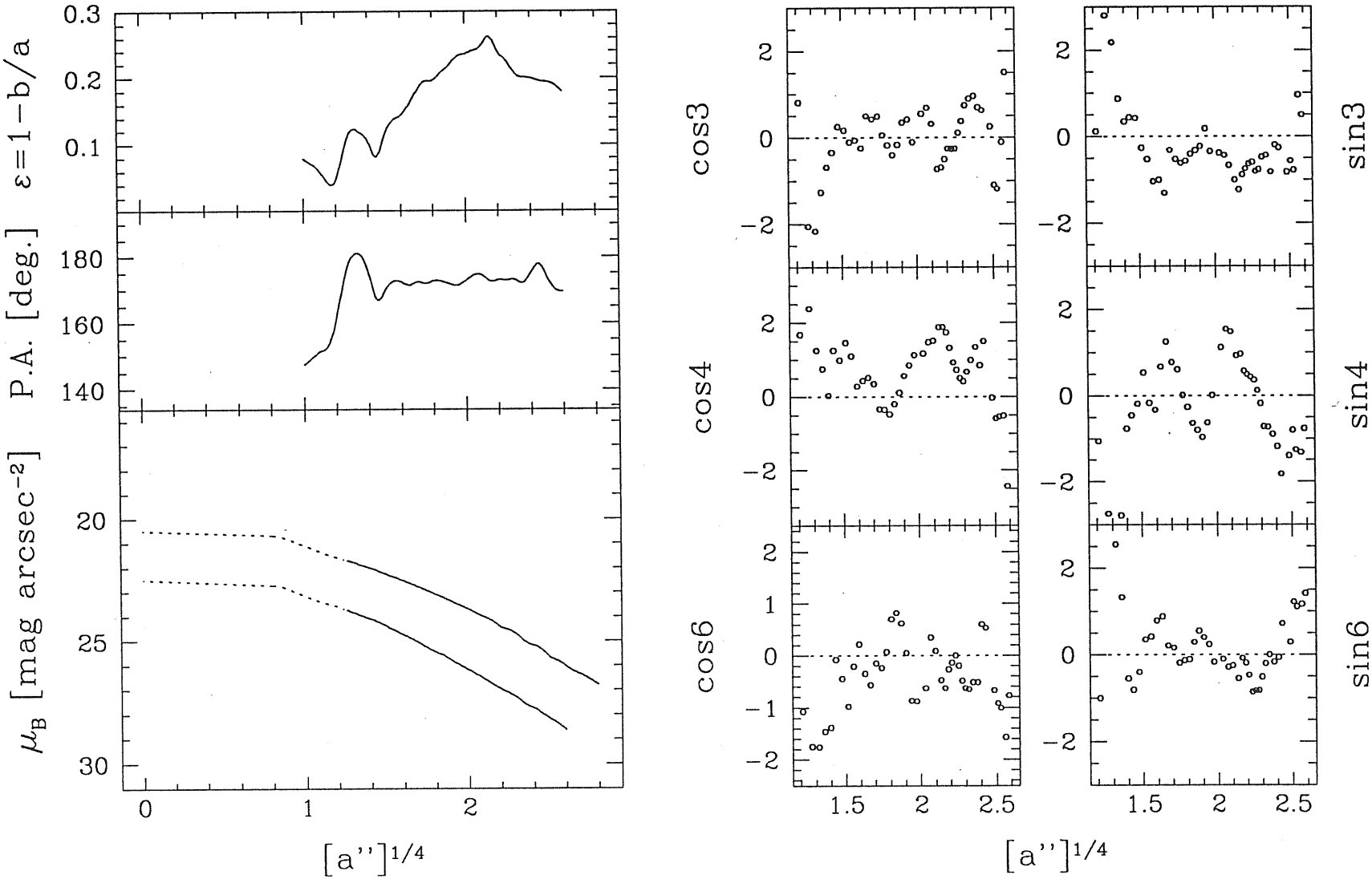
μ_B [mag arcsec^{-2}] P.A. [deg.] $\varepsilon=1-b/a$
0.3
0.2
0.1
180
160
140
20
25
30
0
1
2
[a'']$^{1/4}$
cos3
cos4
cos6
sin3
sin4
sin6
2
0
−2
1
−1
1.5
2
2.5
[a'']$^{1/4}$

FCC 152

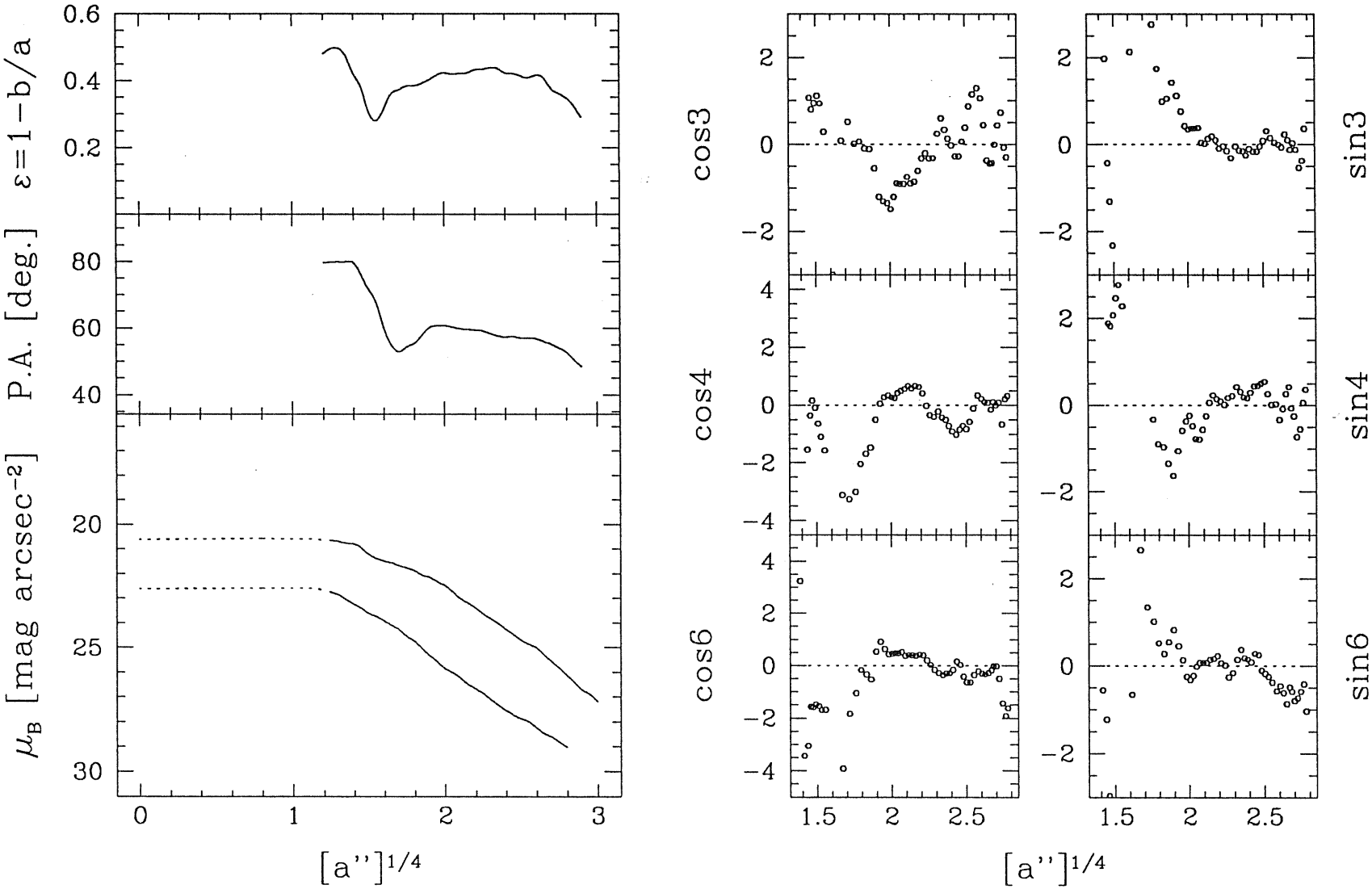
ε=1−b/a
P.A. [deg.]
μB [mag arcsec-2]
[a'']1/4
cos3
cos4
cos6
sin3
sin4
sin6
[a'']1/4

FCC 204

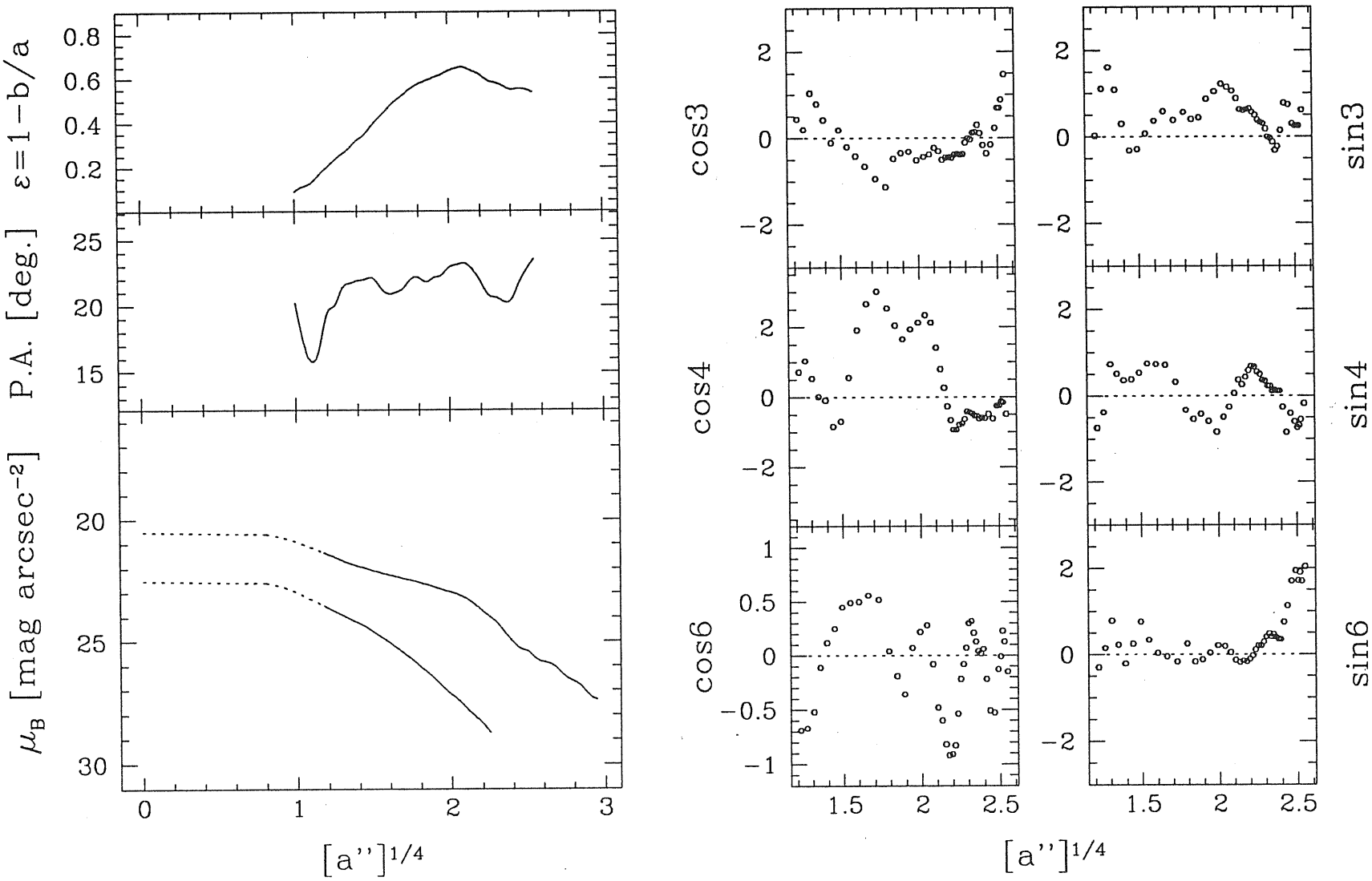
ε=1−b/a
P.A. [deg.]
μB [mag arcsec−2]
[a'']1/4
cos3
sin3
cos4
sin4
cos6
sin6
[a'']1/4

FCC 255

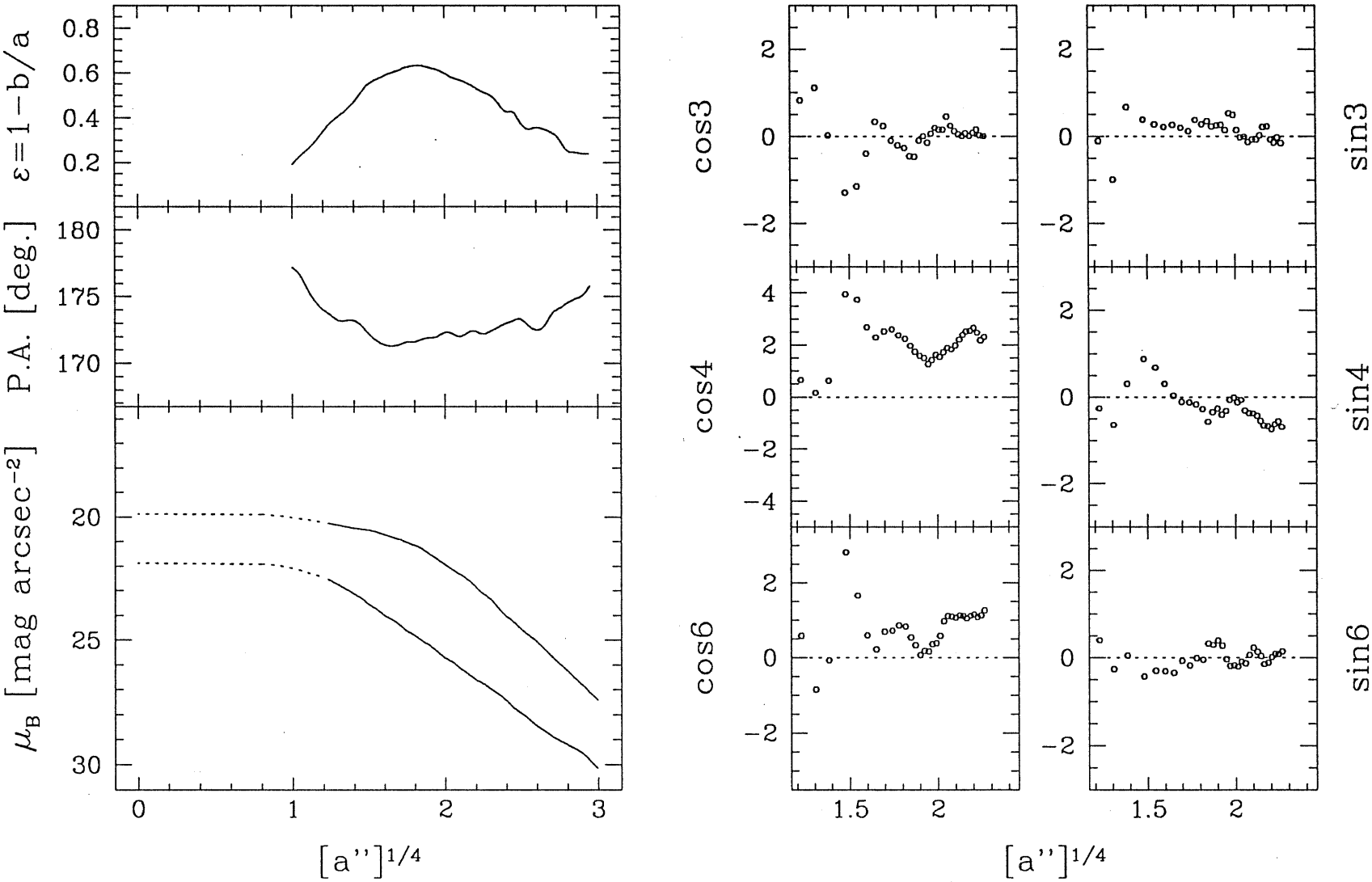
ε=1−b/a
P.A. [deg.]
μB [mag arcsec−2]
[a'']1/4
cos3
cos4
cos6
sin3
sin4
sin6
[a'']1/4

FCC 301

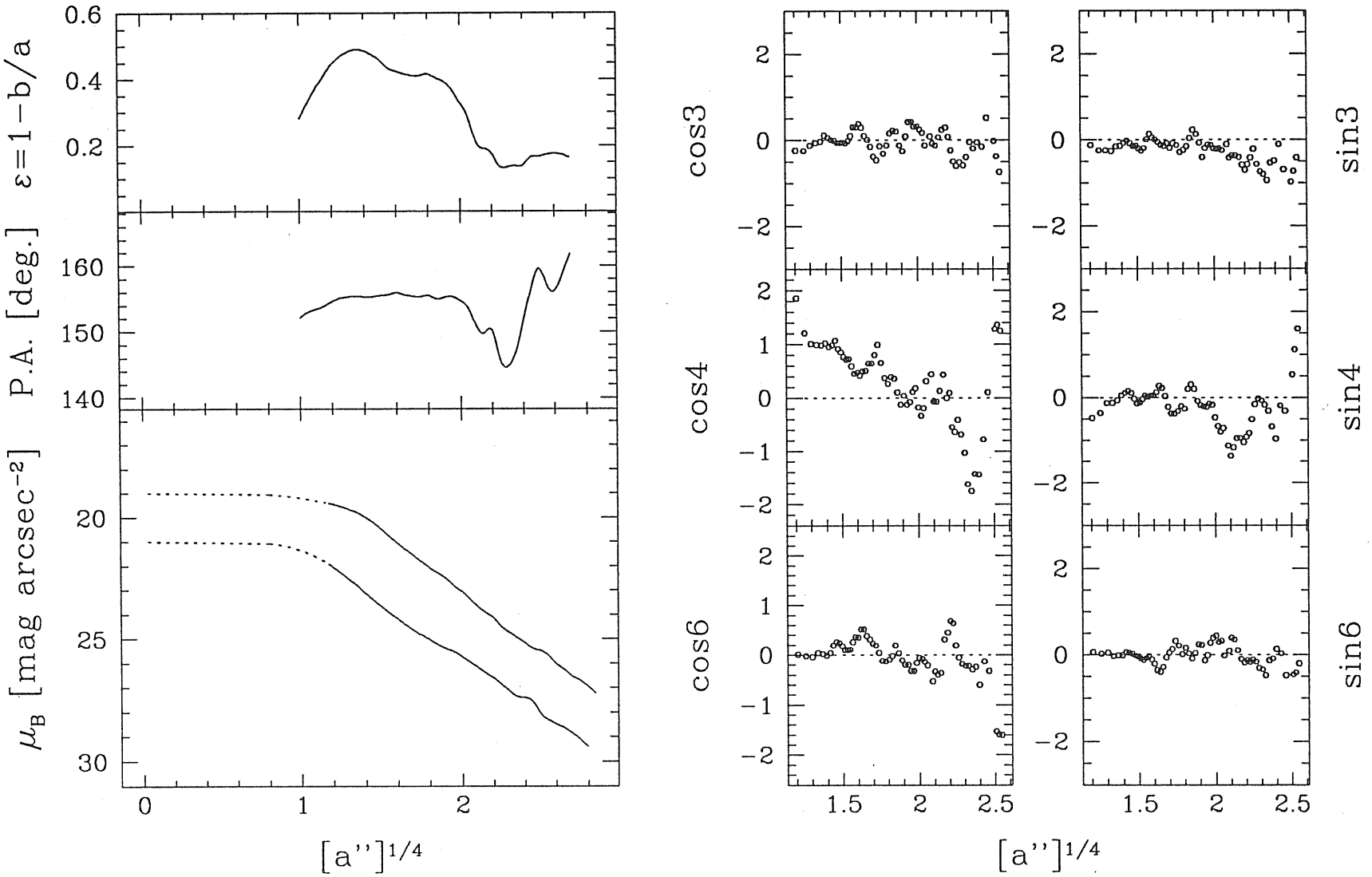
0.6
0.4
0.2
ε=1−b/a
160
150
140
P.A. [deg.]
20
25
30
μB [mag arcsec−2]
0
1
2
[a'']1/4
cos3
cos4
cos6
sin3
sin4
sin6
2
0
−2
1
−1
1.5
2
2.5
[a'']1/4

FCC 324

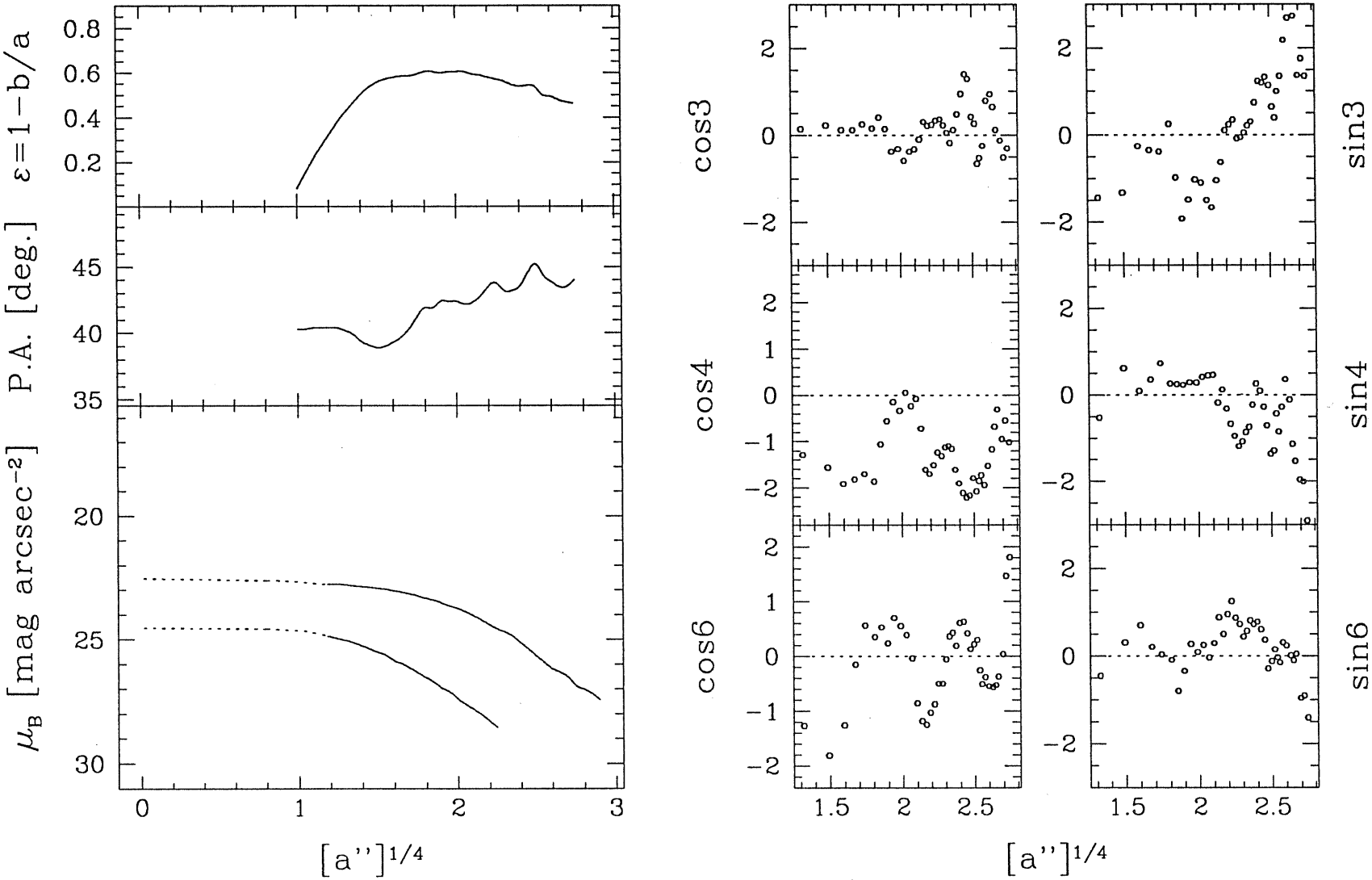
μ_B [mag arcsec^{-2}] P.A. [deg.] $\varepsilon = 1 - b/a$
0.8
0.6
0.4
0.2
45
40
35
20
25
30
0
1
2
3
[a'']$^{1/4}$
cos3
cos4
cos6
sin3
sin4
sin6
2
0
−2
1
−1
1.5
2
2.5
[a'']$^{1/4}$

FCC 335

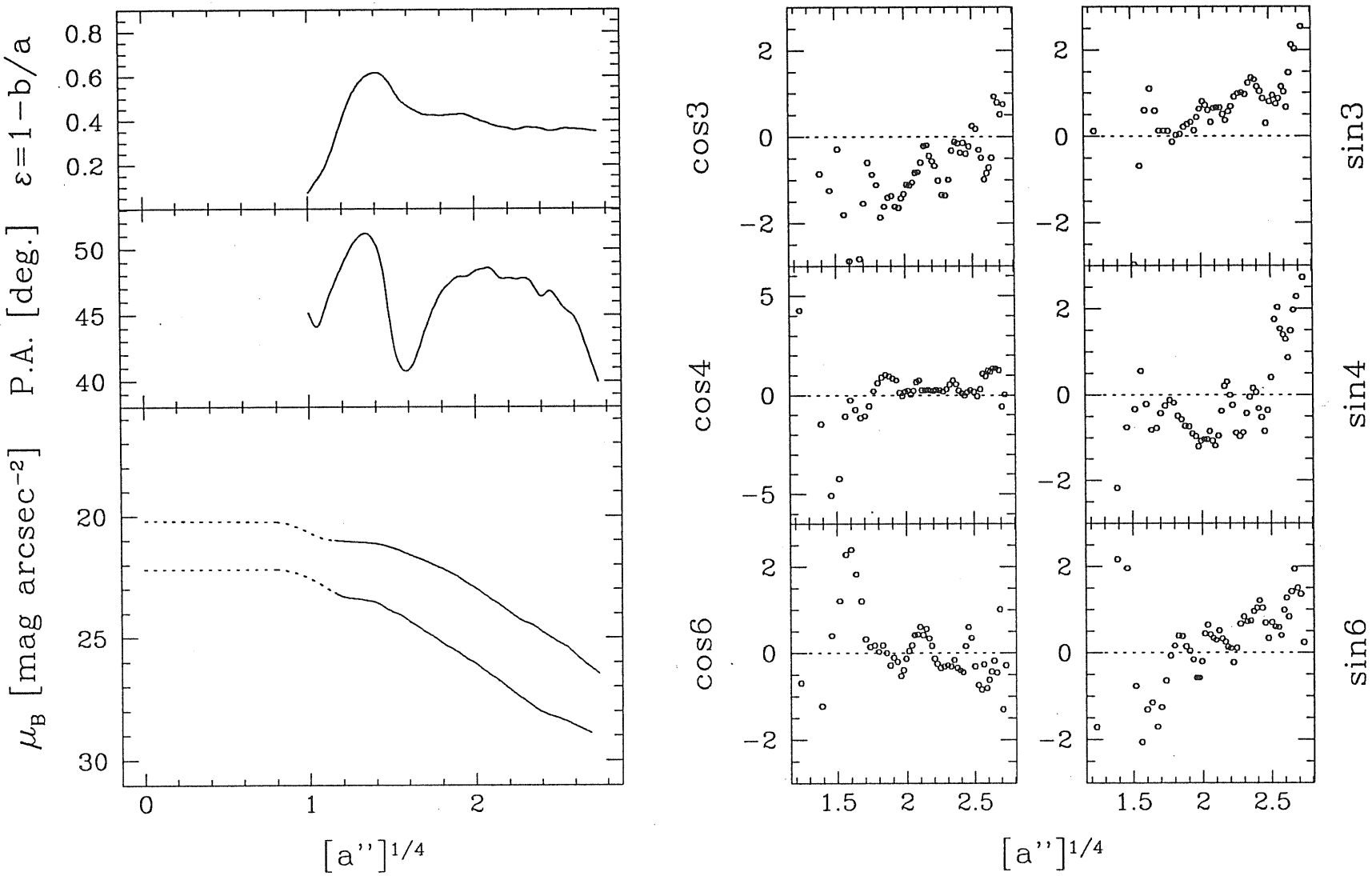
μ_B [mag arcsec^{-2}] P.A. [deg.] ε=1−b/a
0.8
0.6
0.4
0.2
50
45
40
20
25
30
0
1
2
[a'']$^{1/4}$
cos3
cos4
cos6
sin3
sin4
sin6
2
0
−2
5
−5
1.5
2
2.5
[a'']$^{1/4}$

NGC 1316

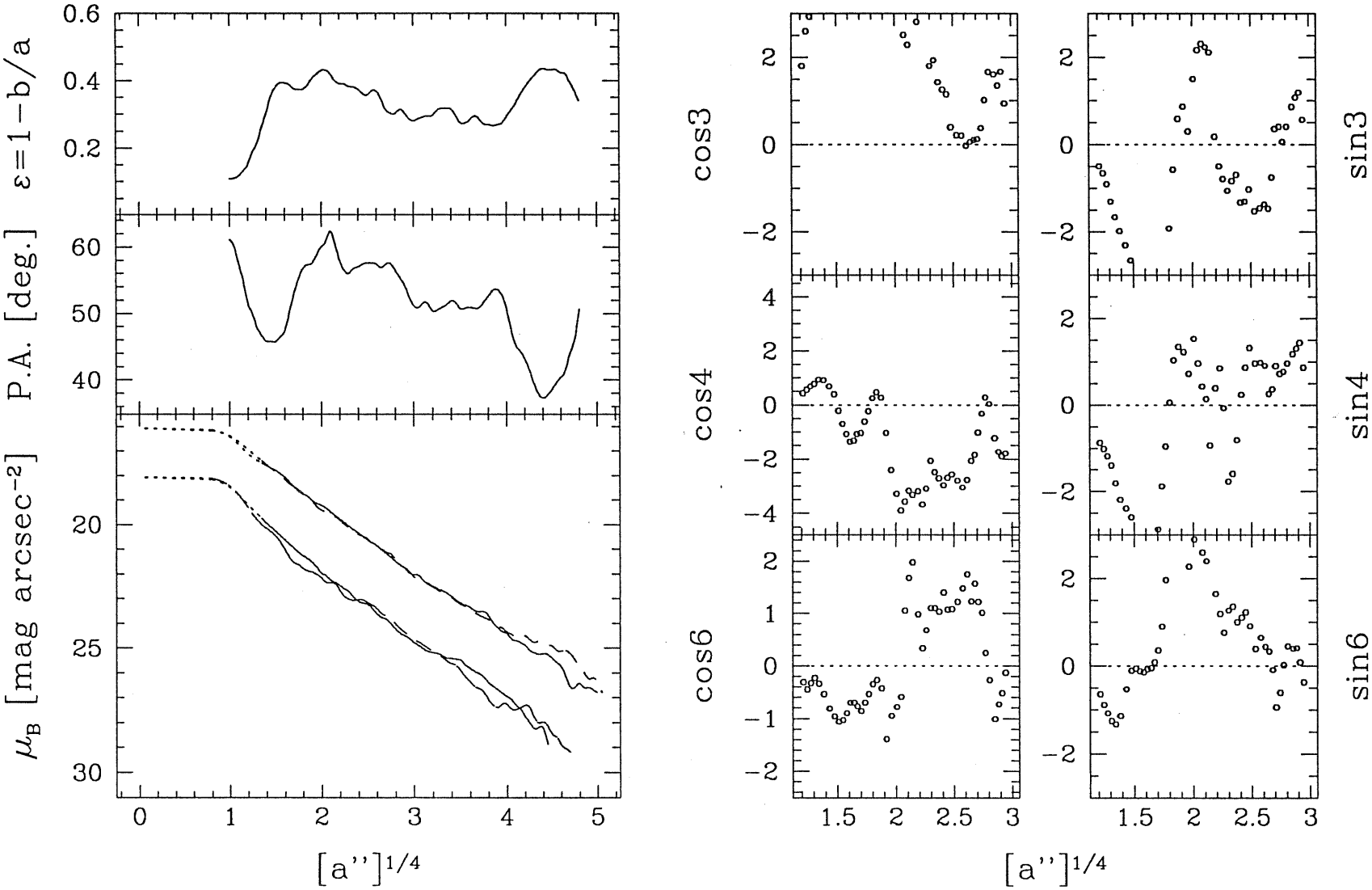
ε=1−b/a
P.A. [deg.]
μB [mag arcsec−2]
[a'']1/4
cos3
sin3
cos4
sin4
cos6
sin6
[a'']1/4

NGC 1336

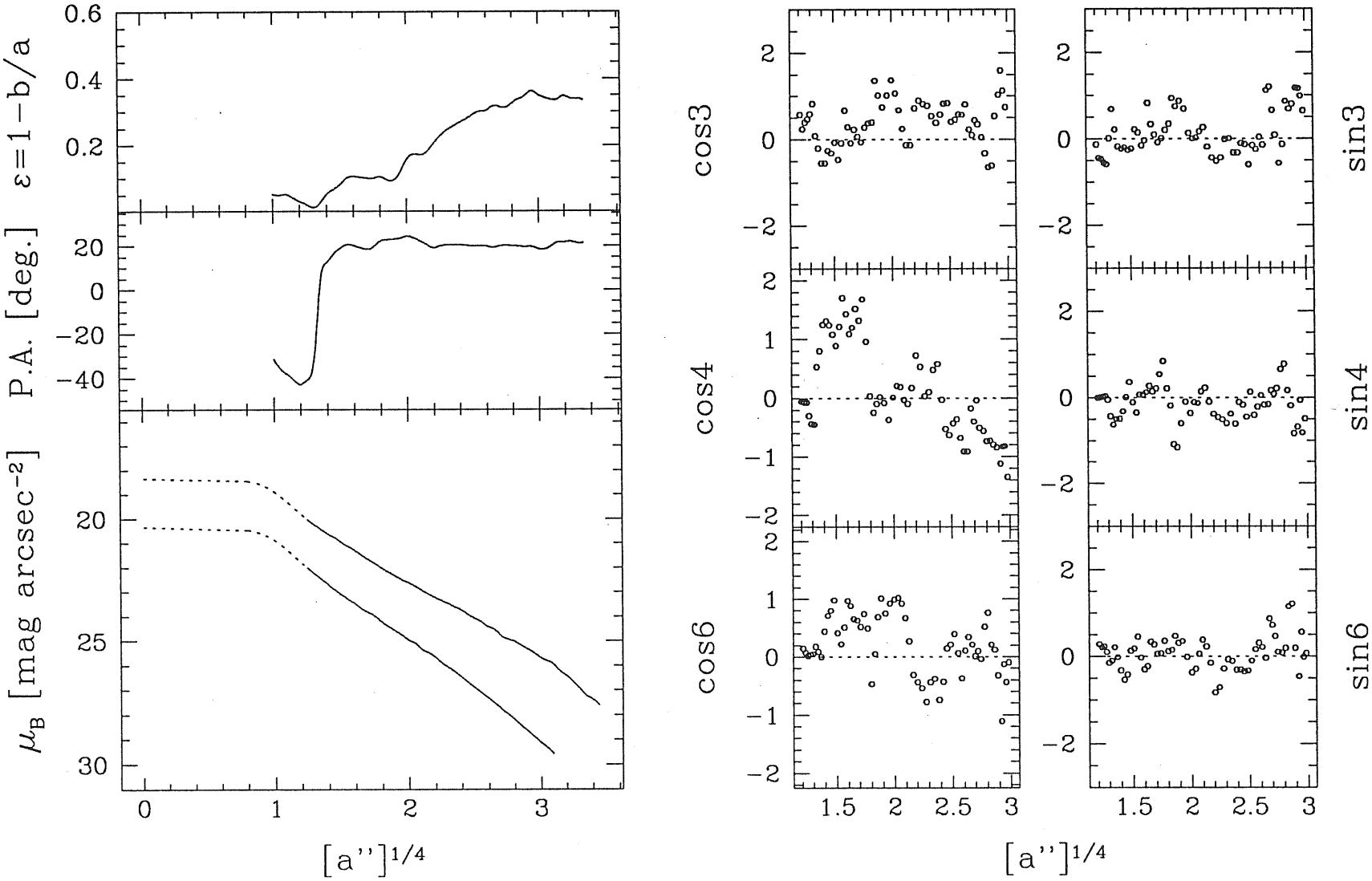
ε=1−b/a
P.A. [deg.]
μB [mag arcsec−2]
[a'']1/4
cos3
cos4
cos6
sin3
sin4
sin6
[a'']1/4

NGC 1339

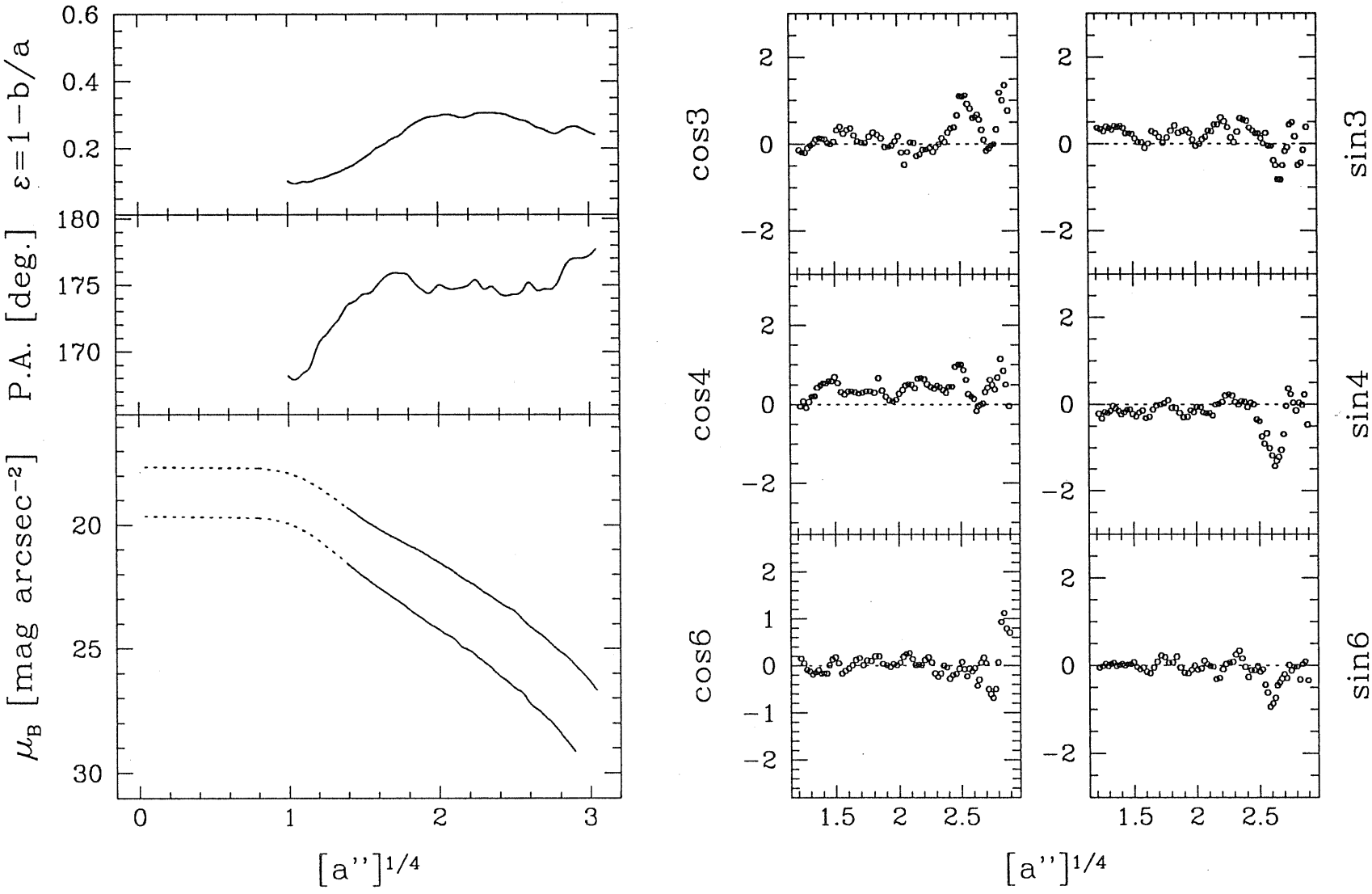
ε=1−b/a
P.A. [deg.]
μB [mag arcsec−2]
[a'']1/4
cos3
sin3
cos4
sin4
cos6
sin6
[a'']1/4

NGC 1351

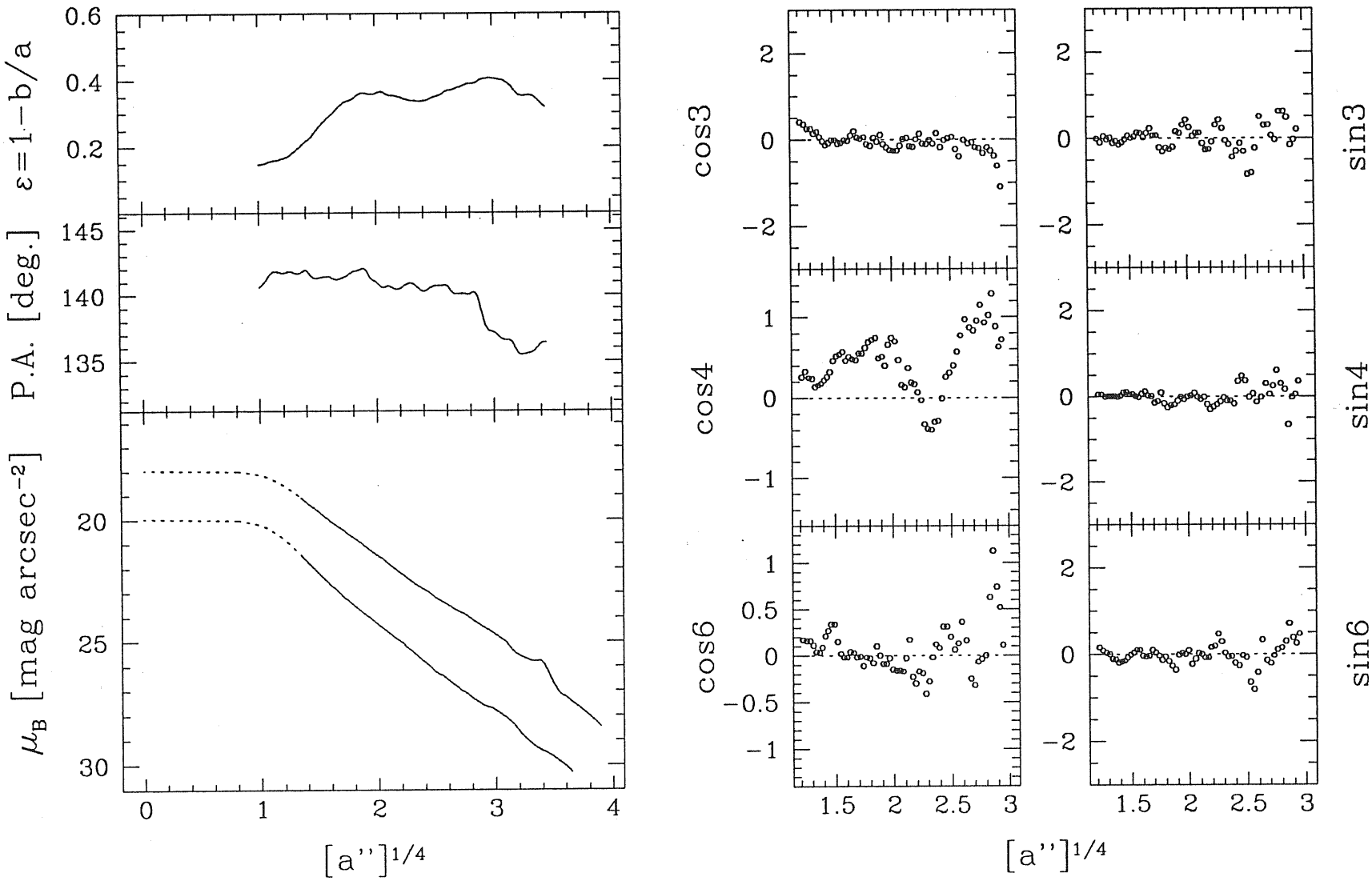
ε=1−b/a
P.A. [deg.]
μB [mag arcsec−2]
[a'']1/4
cos3
sin3
cos4
sin4
cos6
sin6
[a'']1/4

NGC 1373

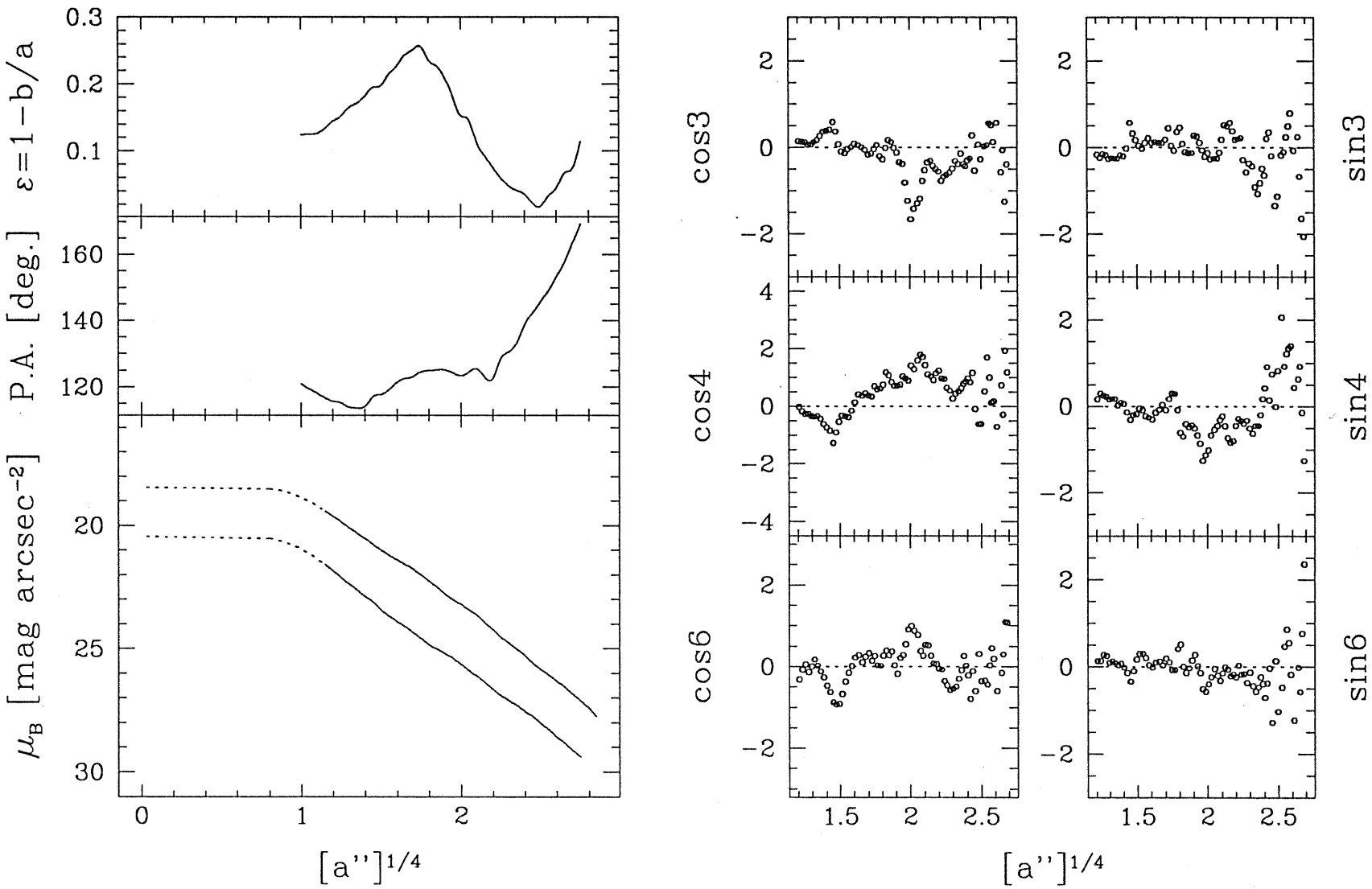
ε=1−b/a
P.A. [deg.]
μB [mag arcsec-2]
[a'']1/4
cos3
sin3
cos4
sin4
cos6
sin6
[a'']1/4

NGC 1374

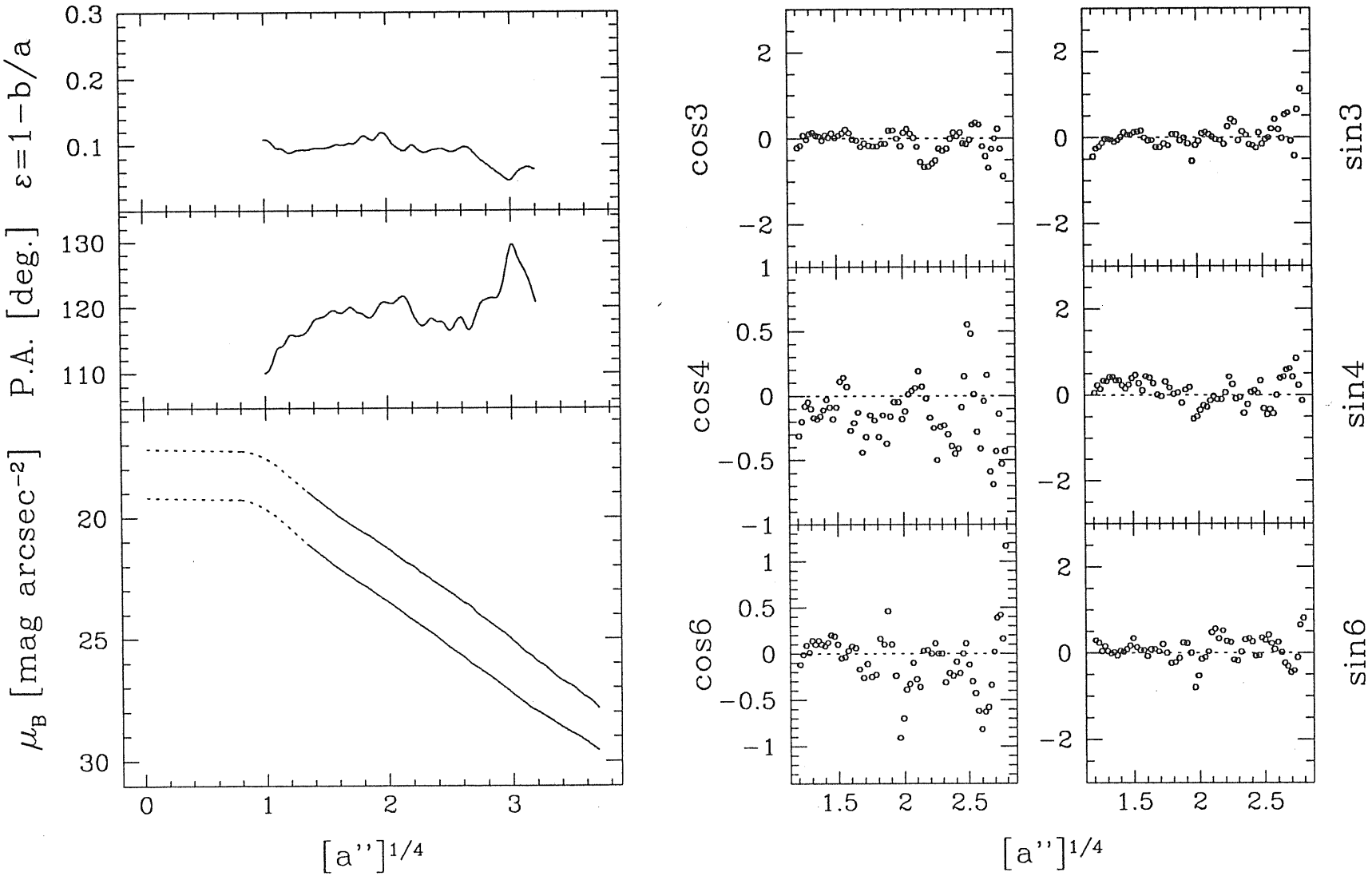
ε=1−b/a
P.A. [deg.]
μB [mag arcsec−2]
[a'']1/4
cos3
sin3
cos4
sin4
cos6
sin6
[a'']1/4

NGC 1375

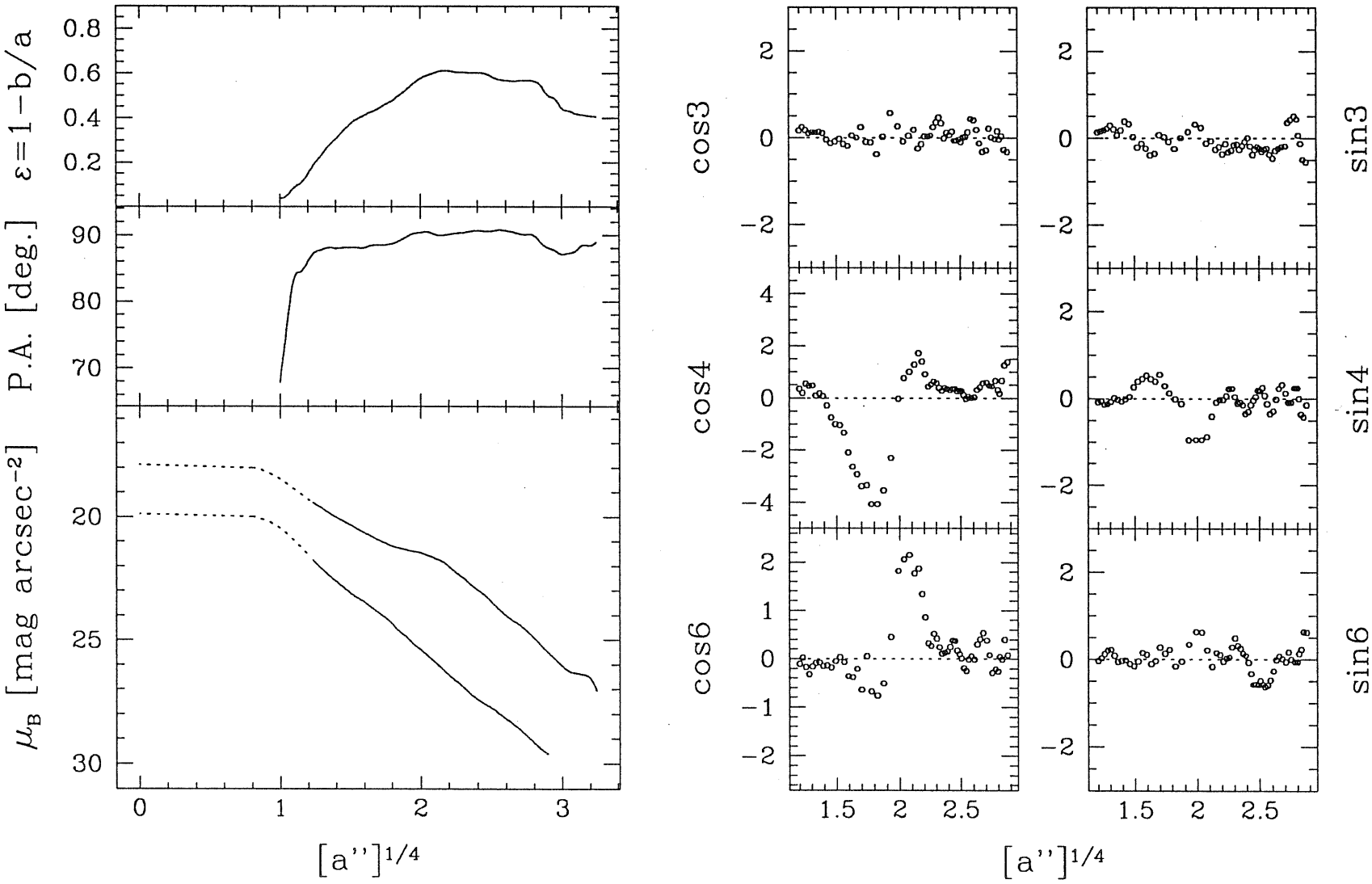
ε=1−b/a
P.A. [deg.]
μB [mag arcsec−2]
[a'']1/4
cos3
sin3
cos4
sin4
cos6
sin6
[a'']1/4

NGC 1379

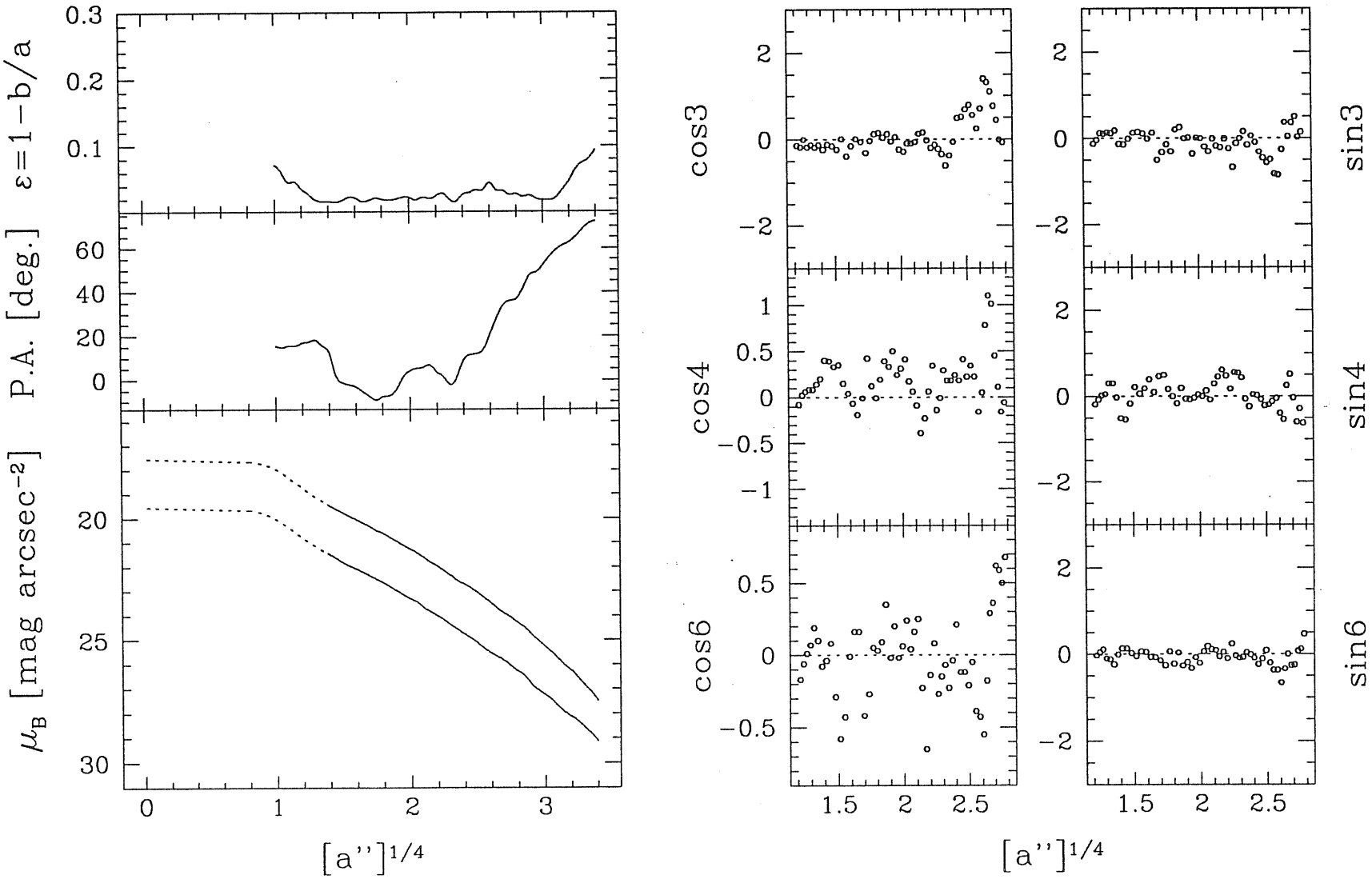
ε=1−b/a
P.A. [deg.]
μB [mag arcsec−2]
[a'']1/4
cos3
sin3
cos4
sin4
cos6
sin6
[a'']1/4

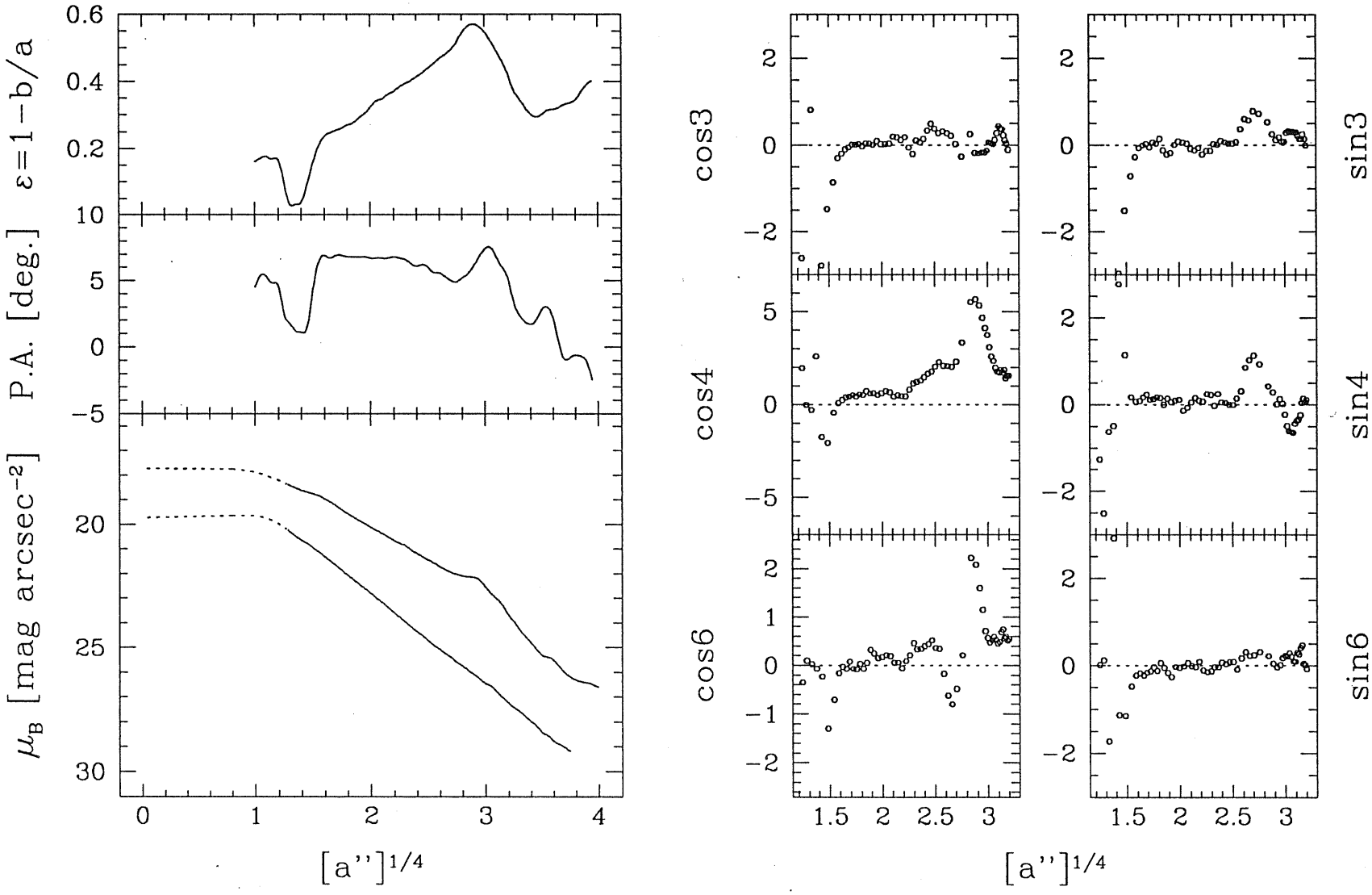
NGC 1380
μ_B [mag arcsec^{-2}] P.A. [deg.] $\varepsilon=1-b/a$
[a'']$^{1/4}$
cos3
cos4
cos6
sin3
sin4
sin6
[a'']$^{1/4}$

NGC 1380A

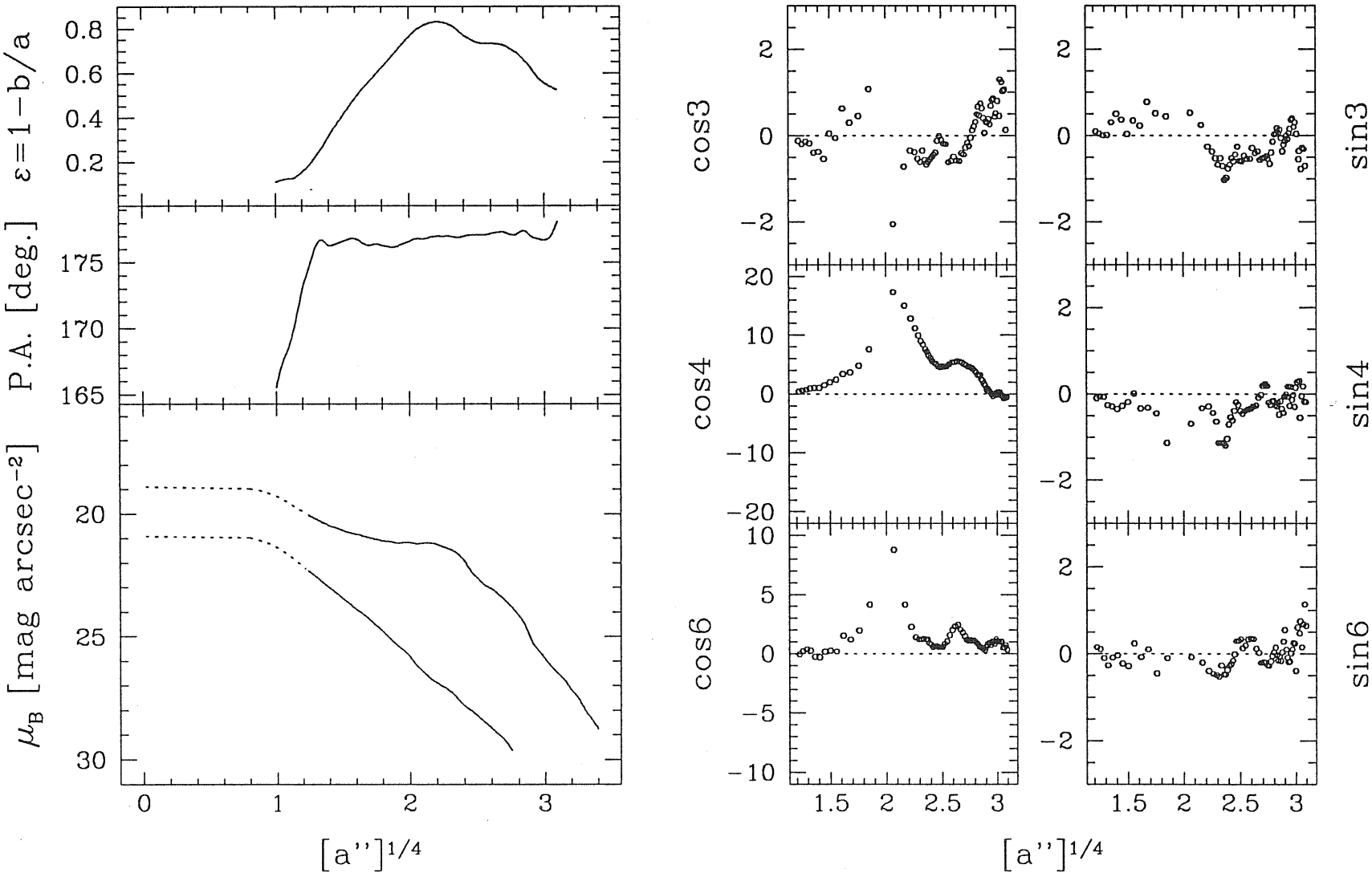
ε=1−b/a
P.A. [deg.]
μB [mag arcsec−2]
[a'']1/4
cos3
sin3
cos4
sin4
cos6
sin6
[a'']1/4

NGC 1381

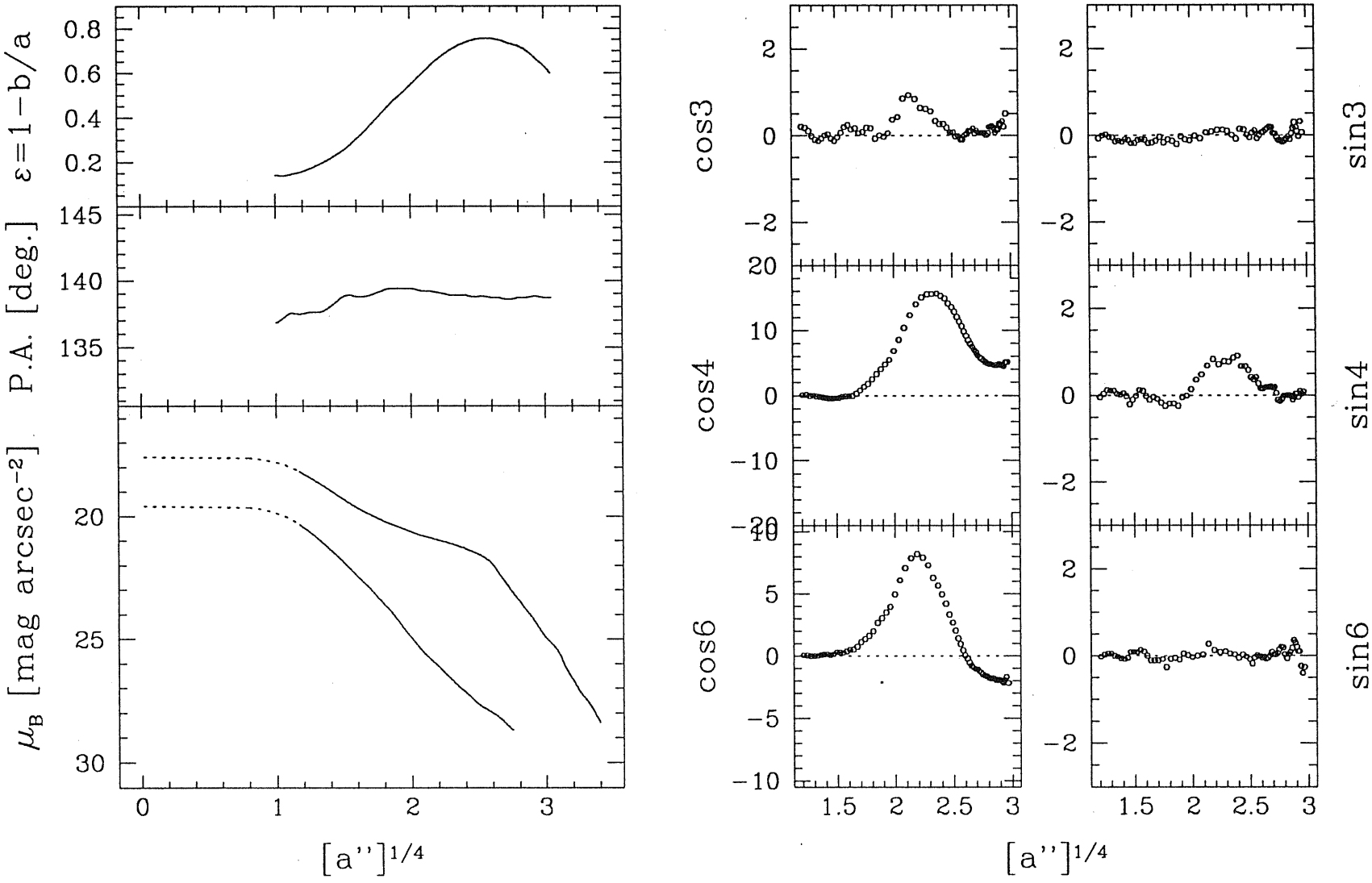
ε=1−b/a
P.A. [deg.]
μB [mag arcsec−2]
[a'']1/4
cos3
sin3
cos4
sin4
cos6
sin6
[a'']1/4

NGC 1396

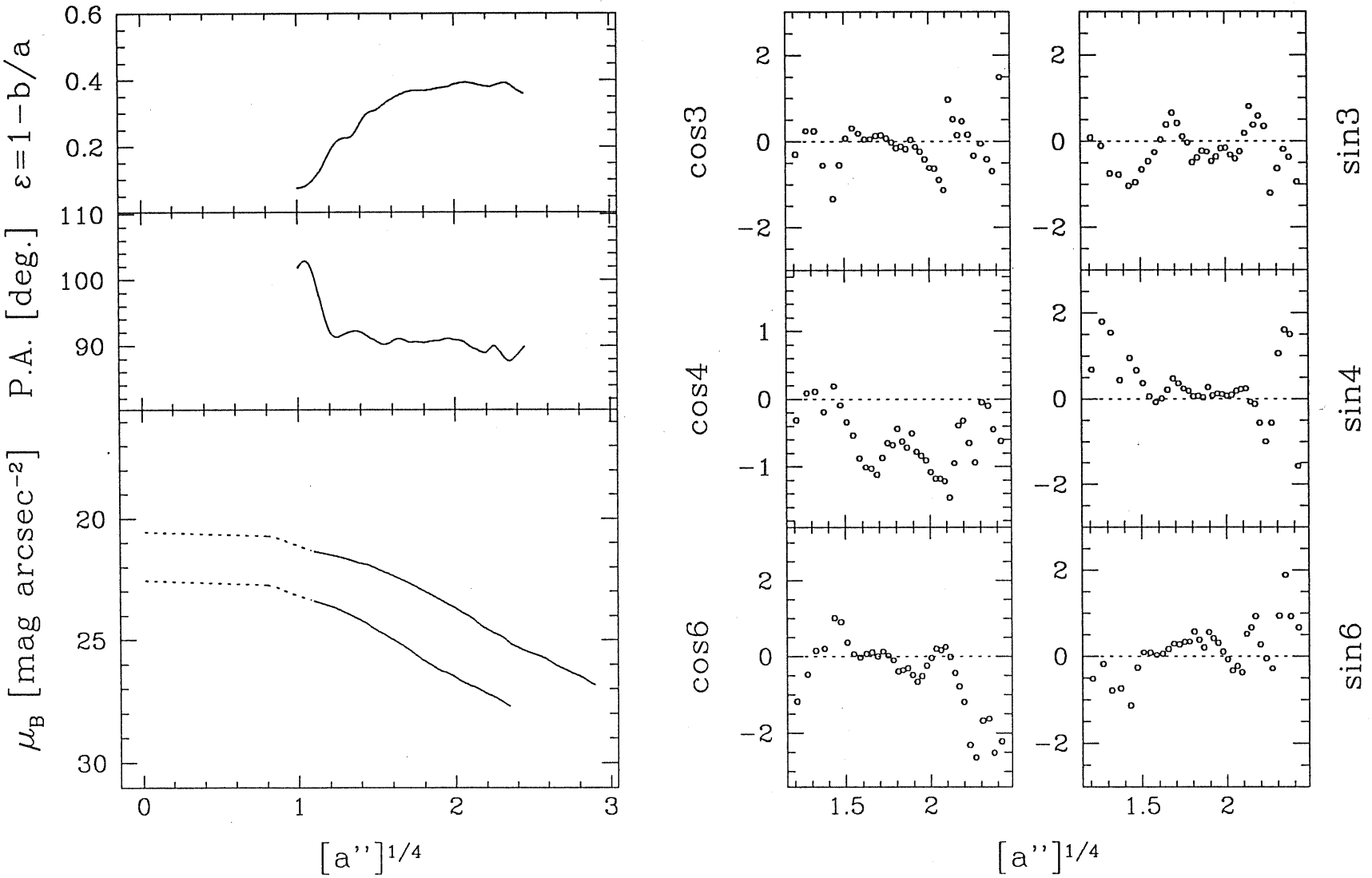
0.6
0.4
0.2
ε=1−b/a
110
100
90
P.A. [deg.]
20
25
30
μB [mag arcsec−2]
0
1
2
3
[a'']1/4
cos3
cos4
cos6
sin3
sin4
sin6
1.5
2
[a'']1/4

NGC 1399

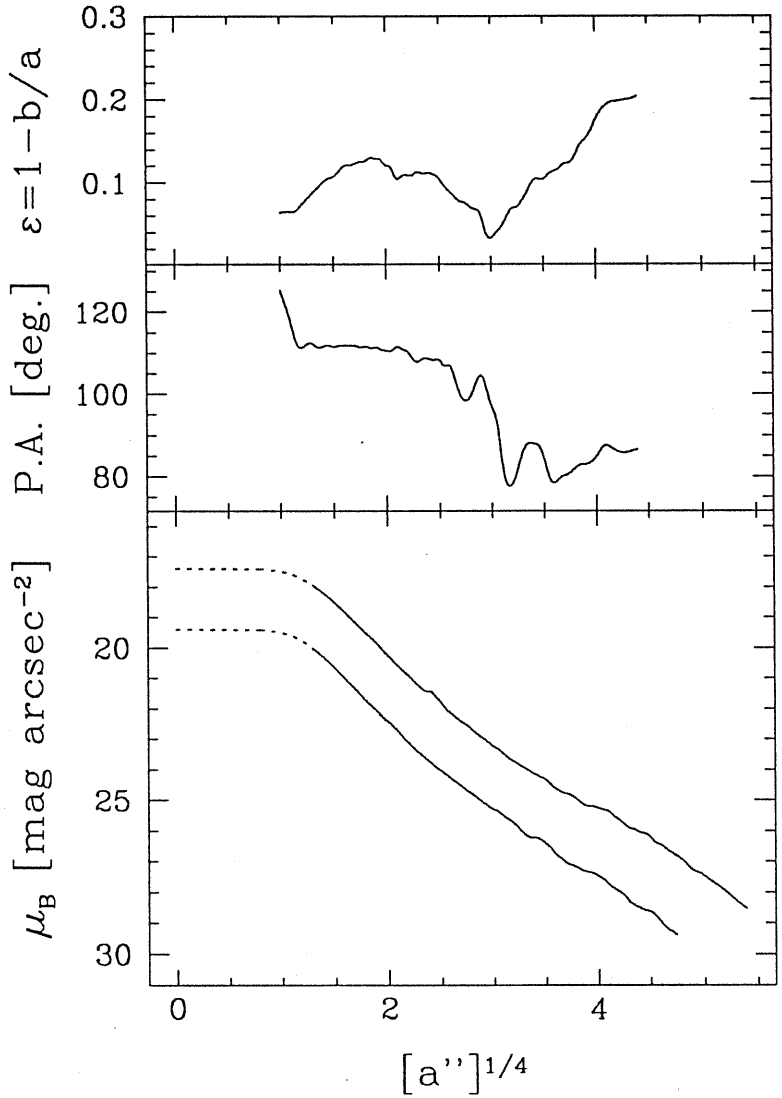
0.3
0.2
0.1
ε=1−b/a
120
100
80
P.A. [deg.]
20
25
30
μB [mag arcsec−2]
0
2
4
[a'']1/4

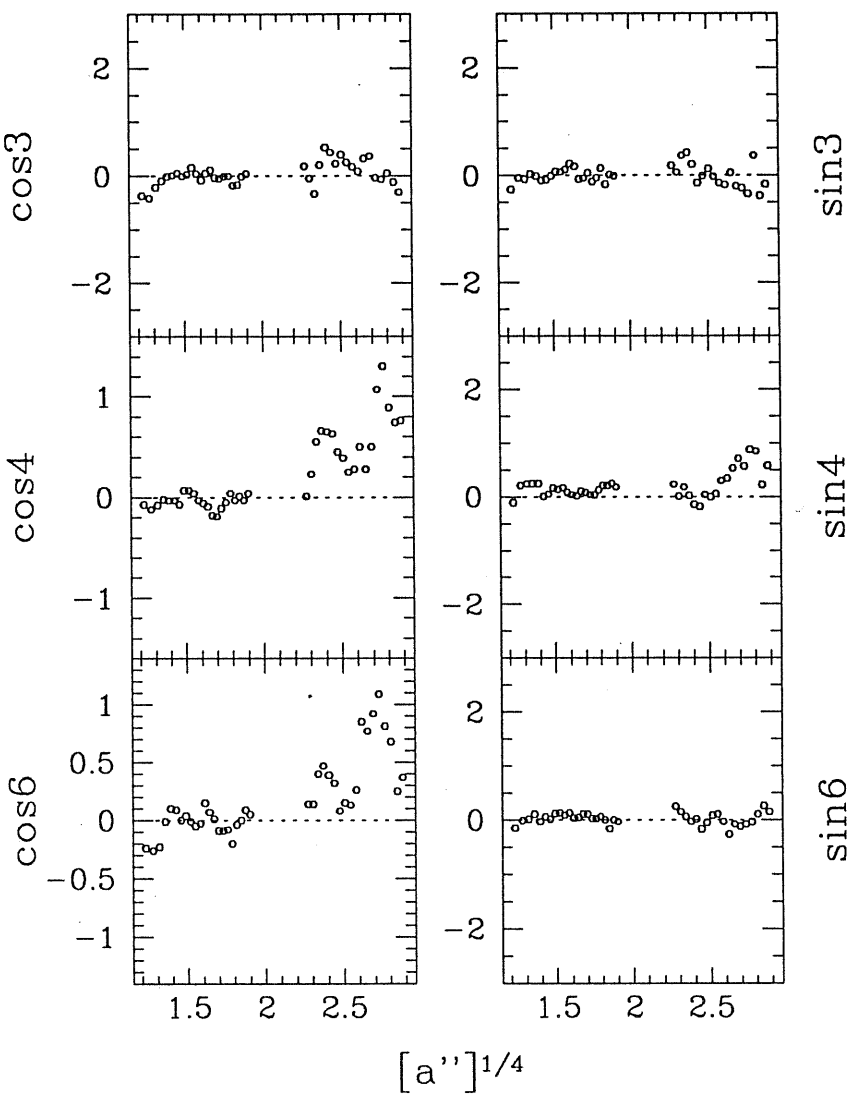
cos3
sin3
cos4
sin4
cos6
sin6
2
0
−2
1
−1
0.5
−0.5
1.5
2
2.5
[a'']1/4

NGC 1404

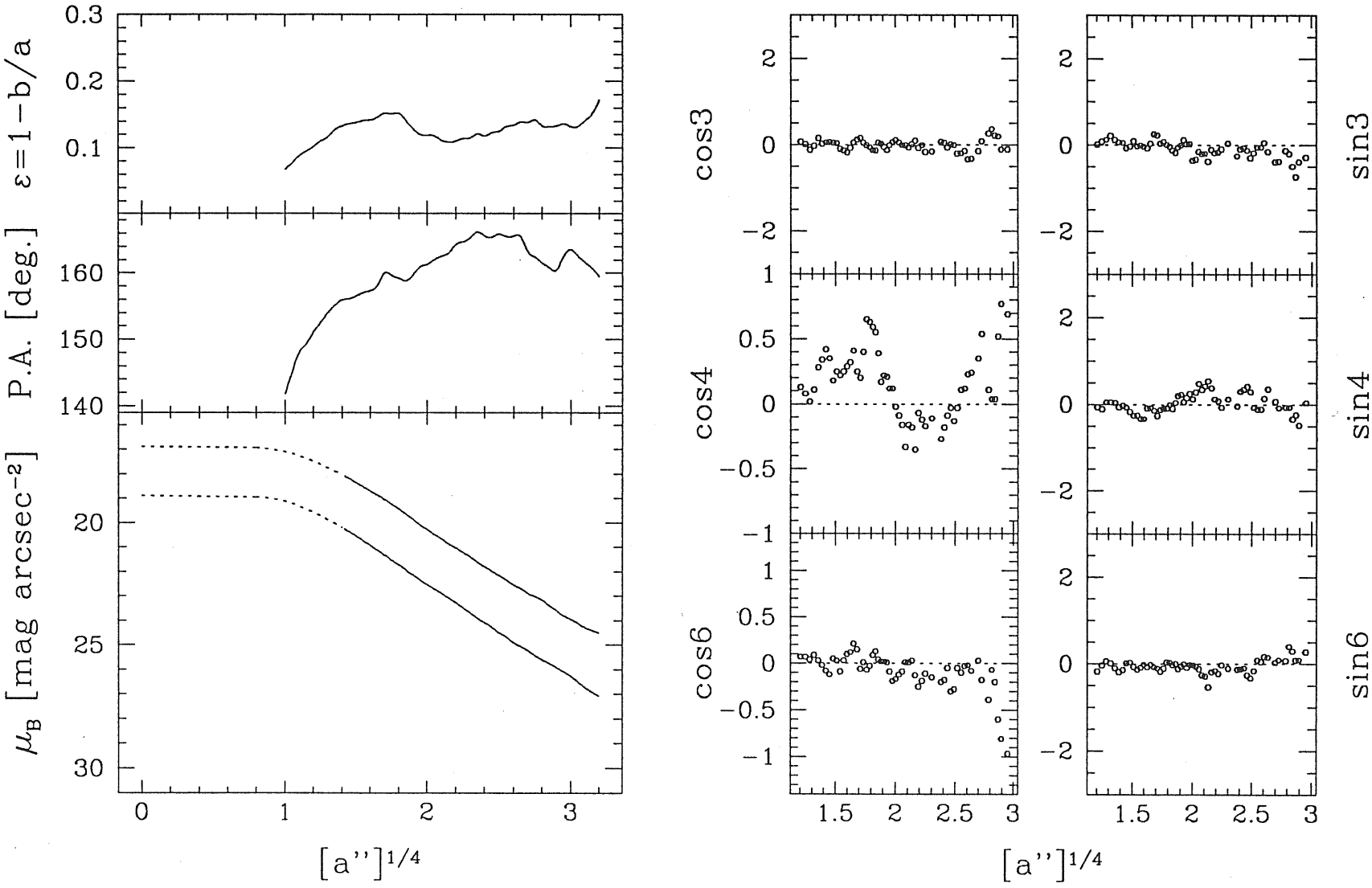
μ_B [mag arcsec^{-2}] P.A. [deg.] ε=1−b/a
0.3
0.2
0.1
160
150
140
20
25
30
0
1
2
3
[a'']$^{1/4}$
cos3
cos4
cos6
sin3
sin4
sin6
2
0
−2
1
0.5
−0.5
−1
1.5
2
2.5
3
[a'']$^{1/4}$

NGC 1419

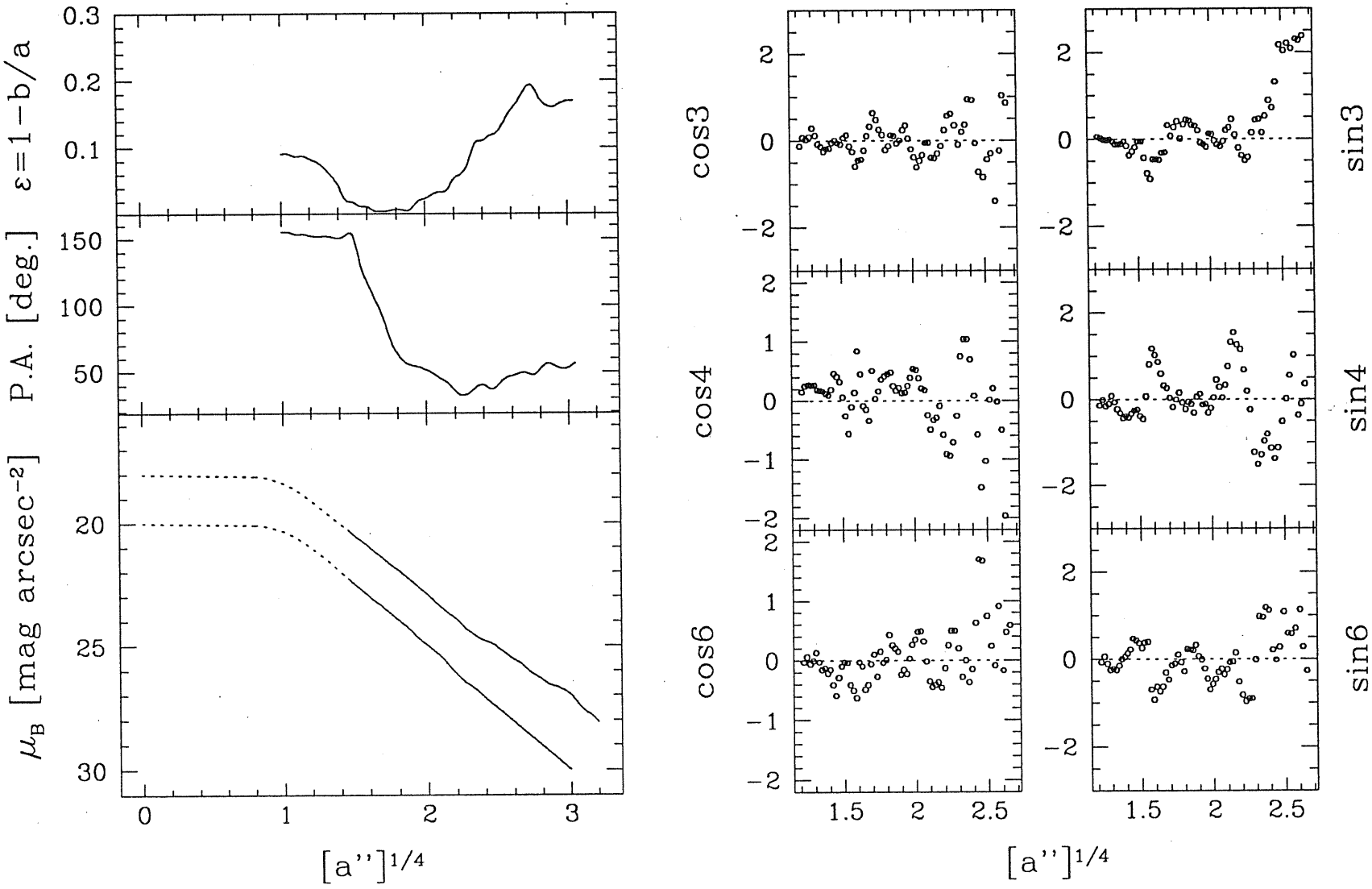
ε=1−b/a
P.A. [deg.]
μB [mag arcsec−2]
[a'']1/4
cos3
sin3
cos4
sin4
cos6
sin6
[a'']1/4

NGC 1427

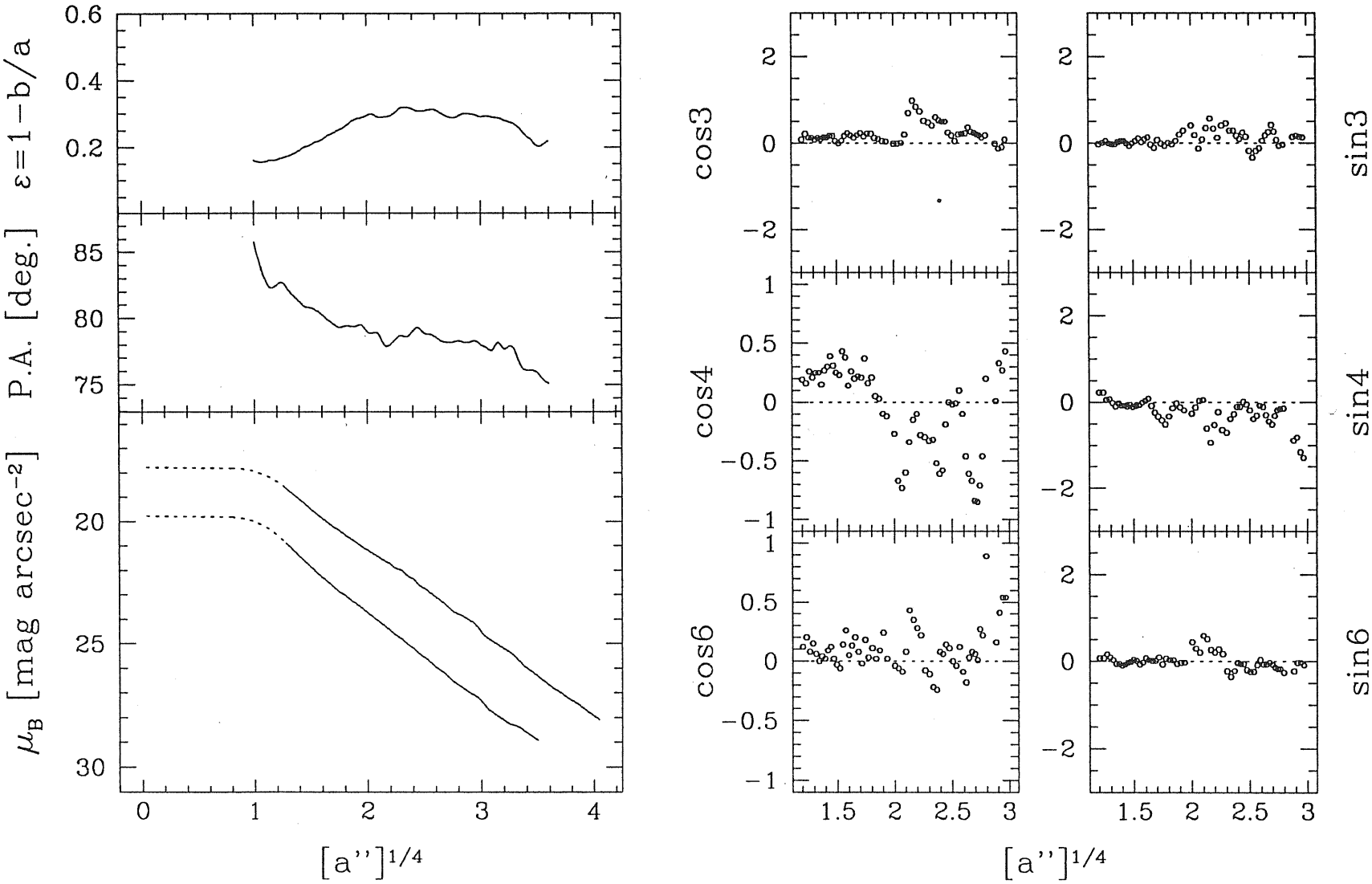
ε=1−b/a
P.A. [deg.]
μB [mag arcsec−2]
[a'']1/4
cos3
sin3
cos4
sin4
cos6
sin6
[a'']1/4

NGC 1428

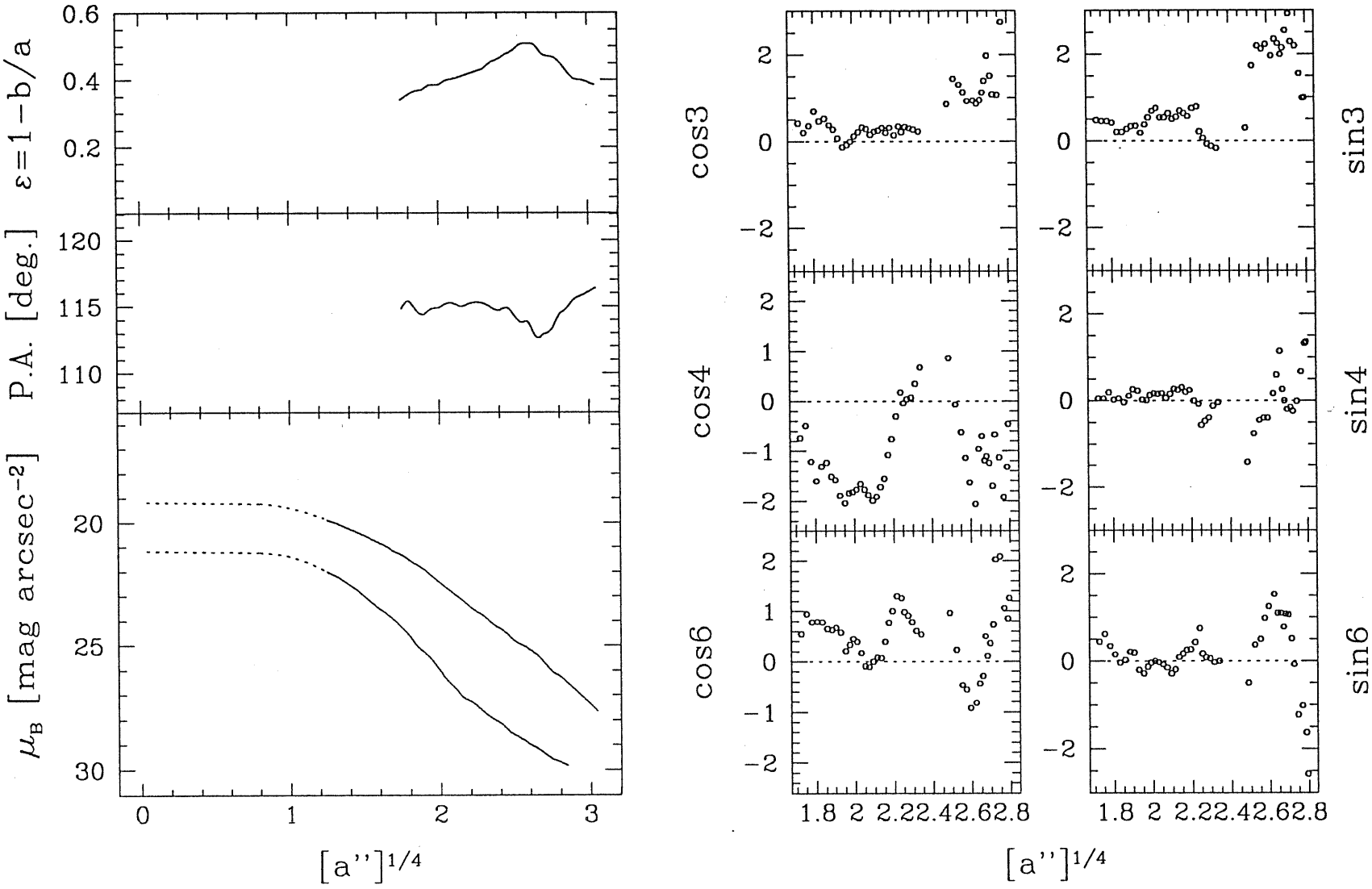
ε=1−b/a
P.A. [deg.]
μB [mag arcsec−2]
[a'']1/4
cos3
sin3
cos4
sin4
cos6
sin6
[a'']1/4

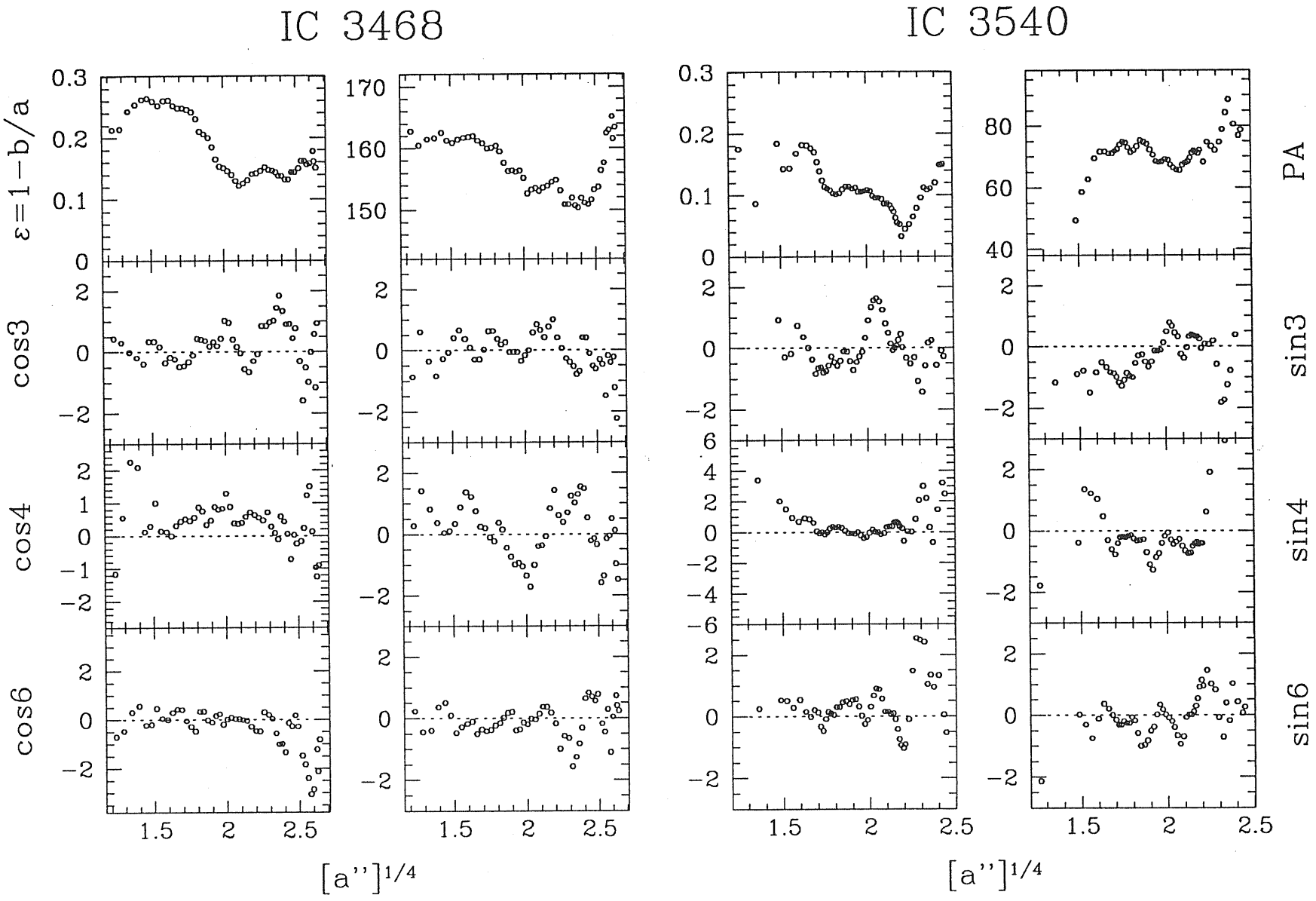
IC 3468
IC 3540
ε=1−b/a
cos3
cos4
cos6
PA
sin3
sin4
sin6
[a'']1/4
[a'']1/4

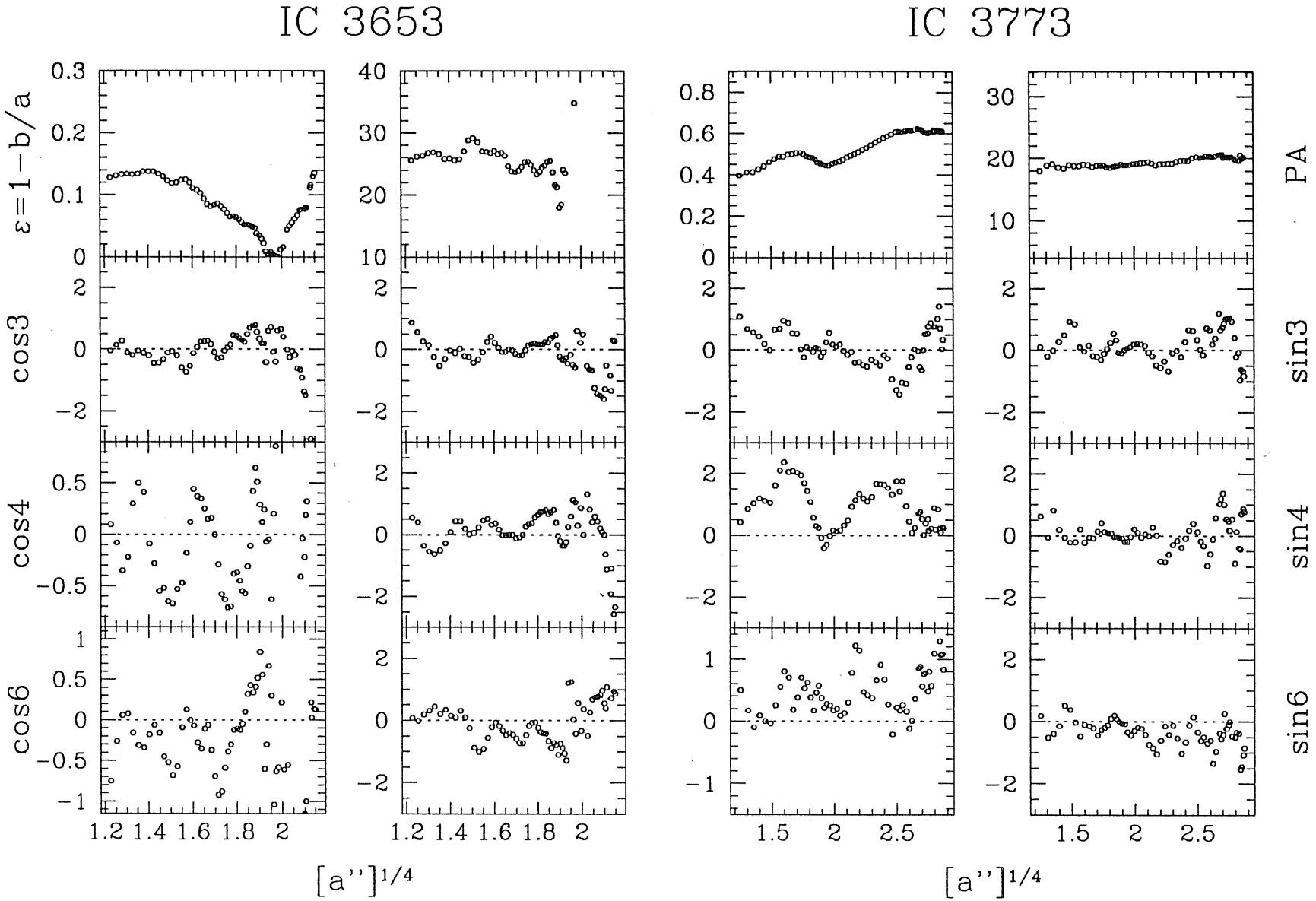
IC 3653
IC 3773
ε=1−b/a
PA
cos3
sin3
cos4
sin4
cos6
sin6
[a'']1/4
[a'']1/4

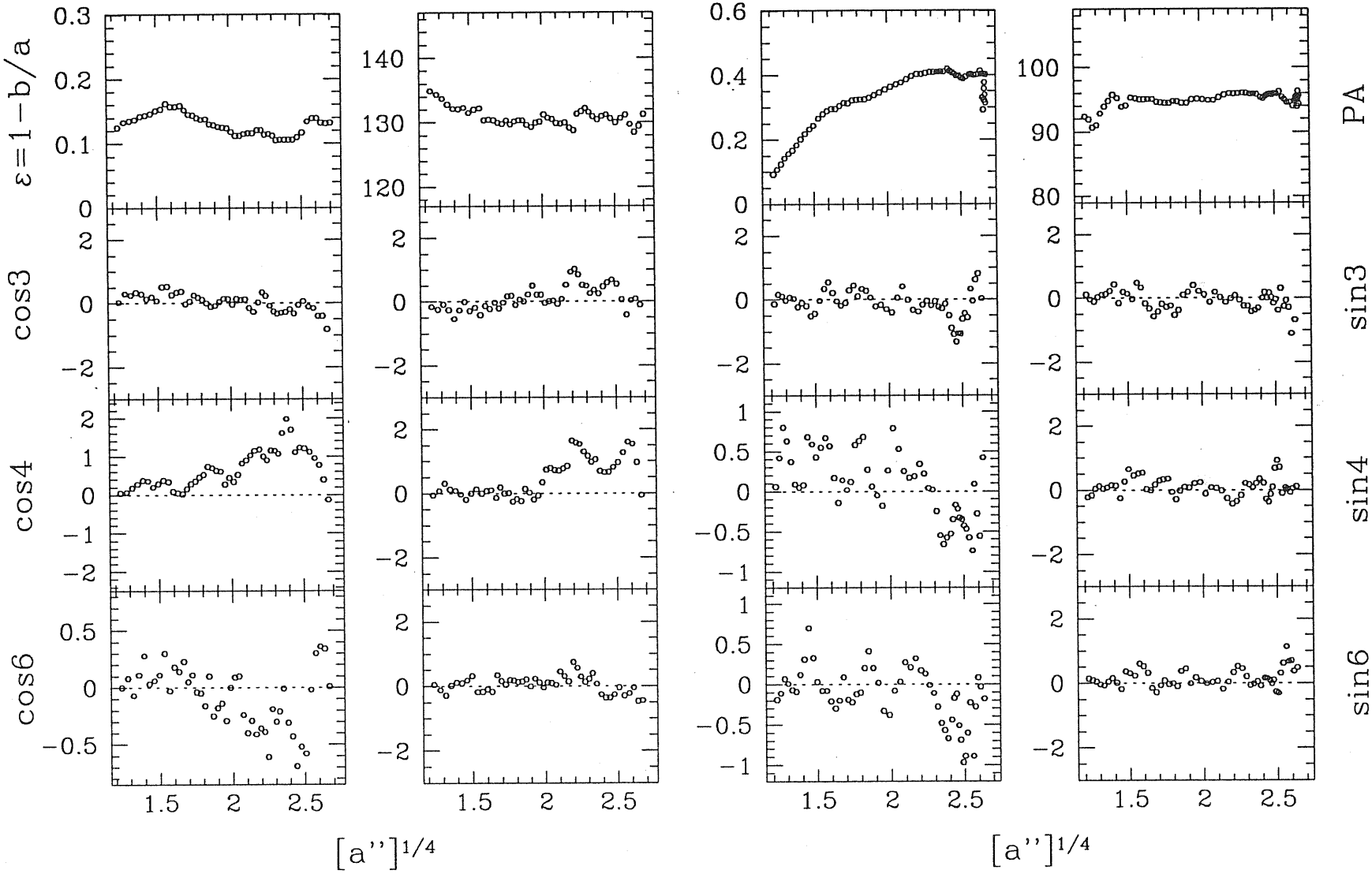
NGC 4168
NGC 4200
ε=1−b/a
cos3
cos4
cos6
PA
sin3
sin4
sin6
[a'']^1/4
[a'']^1/4

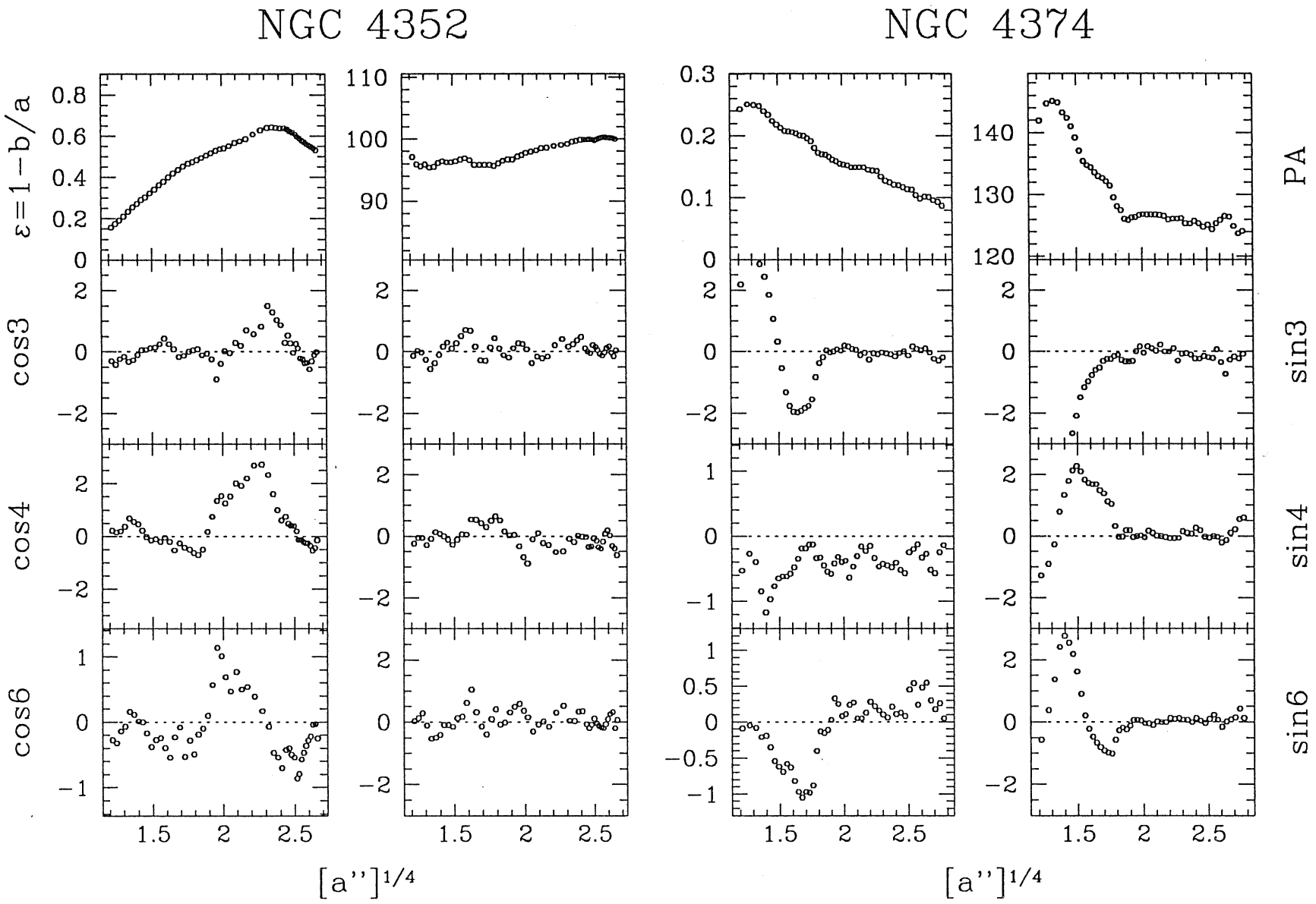
NGC 4352
NGC 4374
ε=1−b/a
cos3
cos4
cos6
PA
sin3
sin4
sin6
[a'']1/4
[a'']1/4

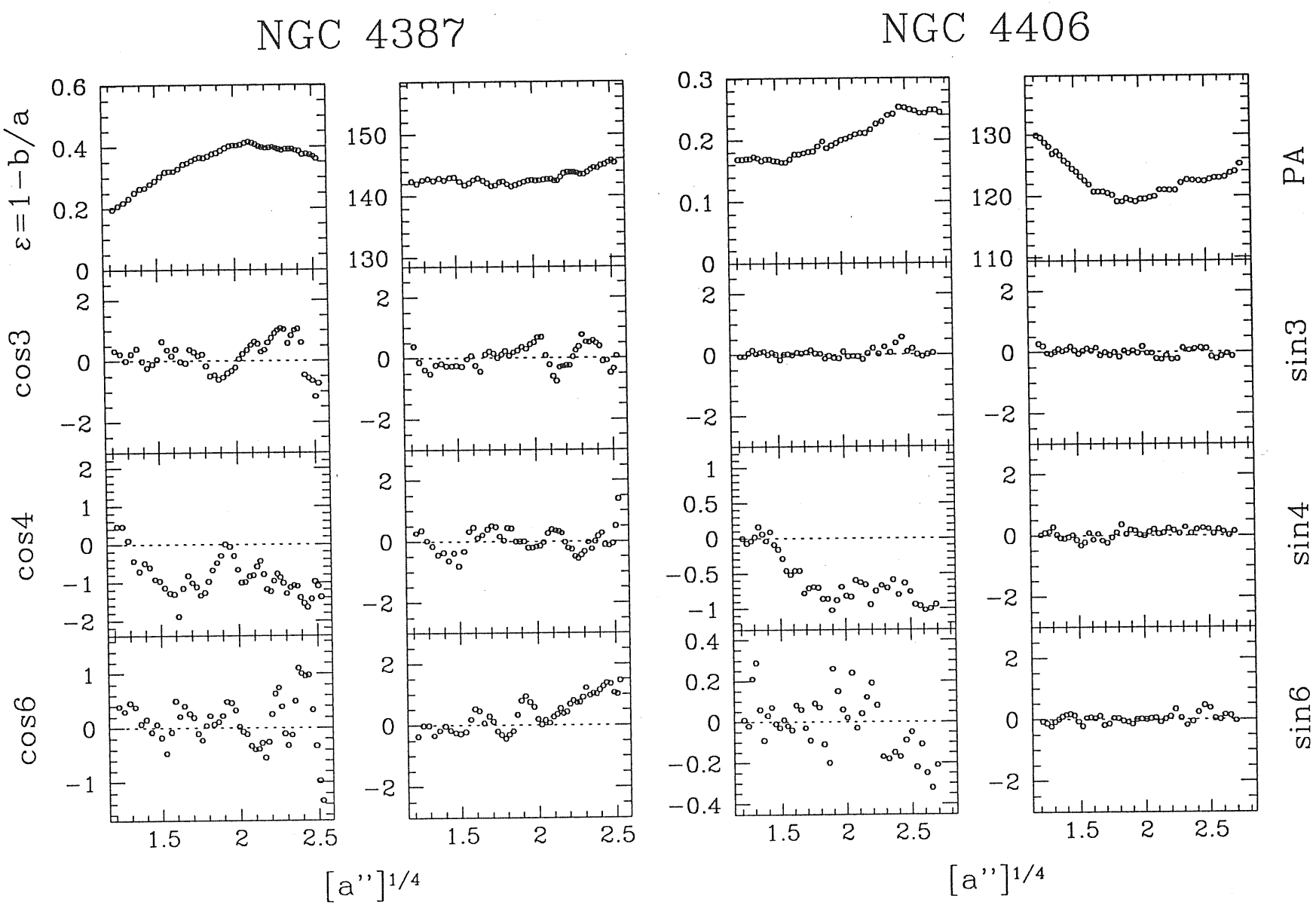
NGC 4387
NGC 4406
ε=1−b/a
cos3
cos4
cos6
PA
sin3
sin4
sin6
[a'']^1/4
[a'']^1/4

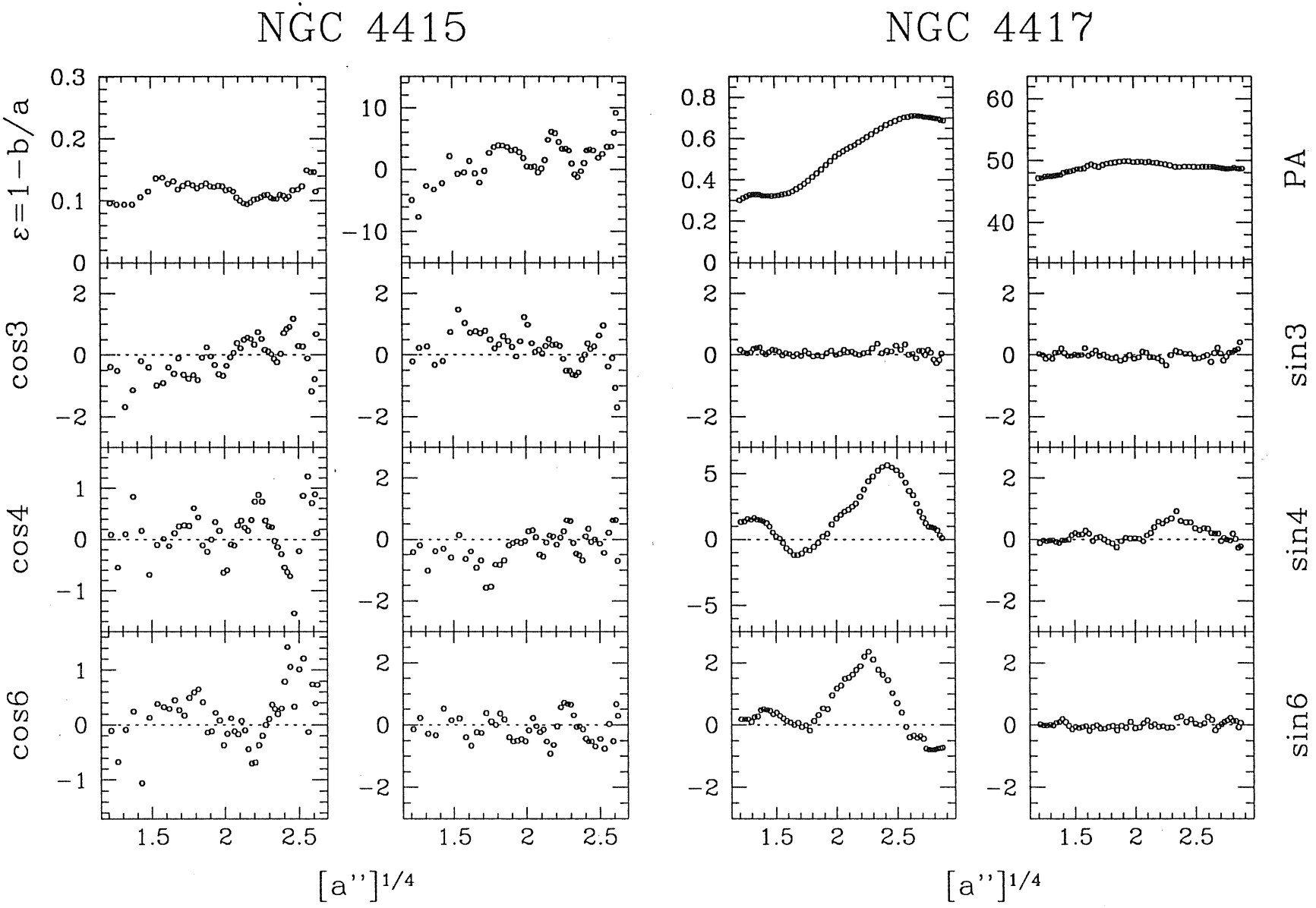
NGC 4415
NGC 4417
ε=1−b/a
cos3
cos4
cos6
PA
sin3
sin4
sin6
[a'']1/4
[a'']1/4

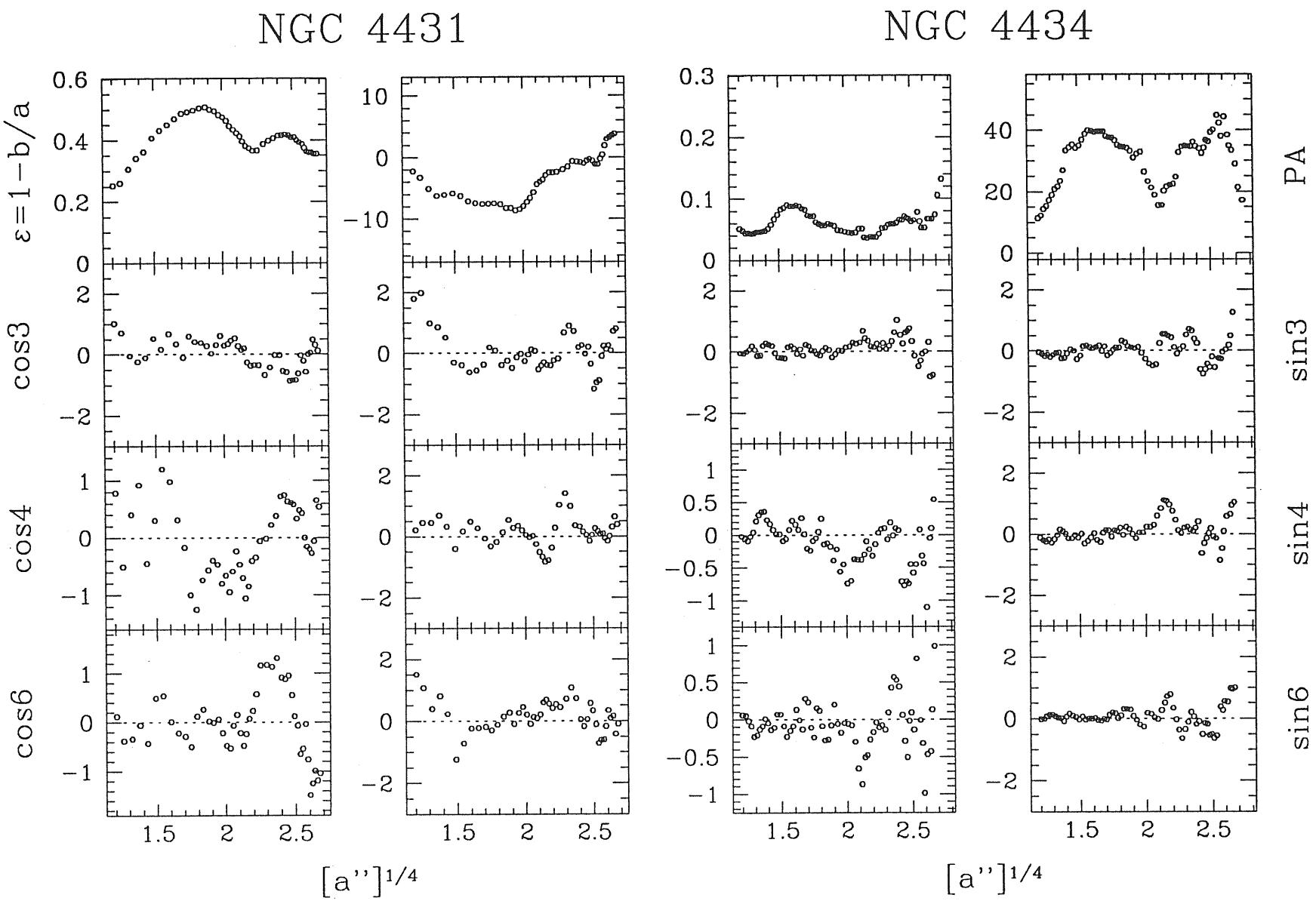
NGC 4431
NGC 4434
ε=1−b/a
PA
cos3
sin3
cos4
sin4
cos6
sin6
[a'']^1/4
[a'']^1/4

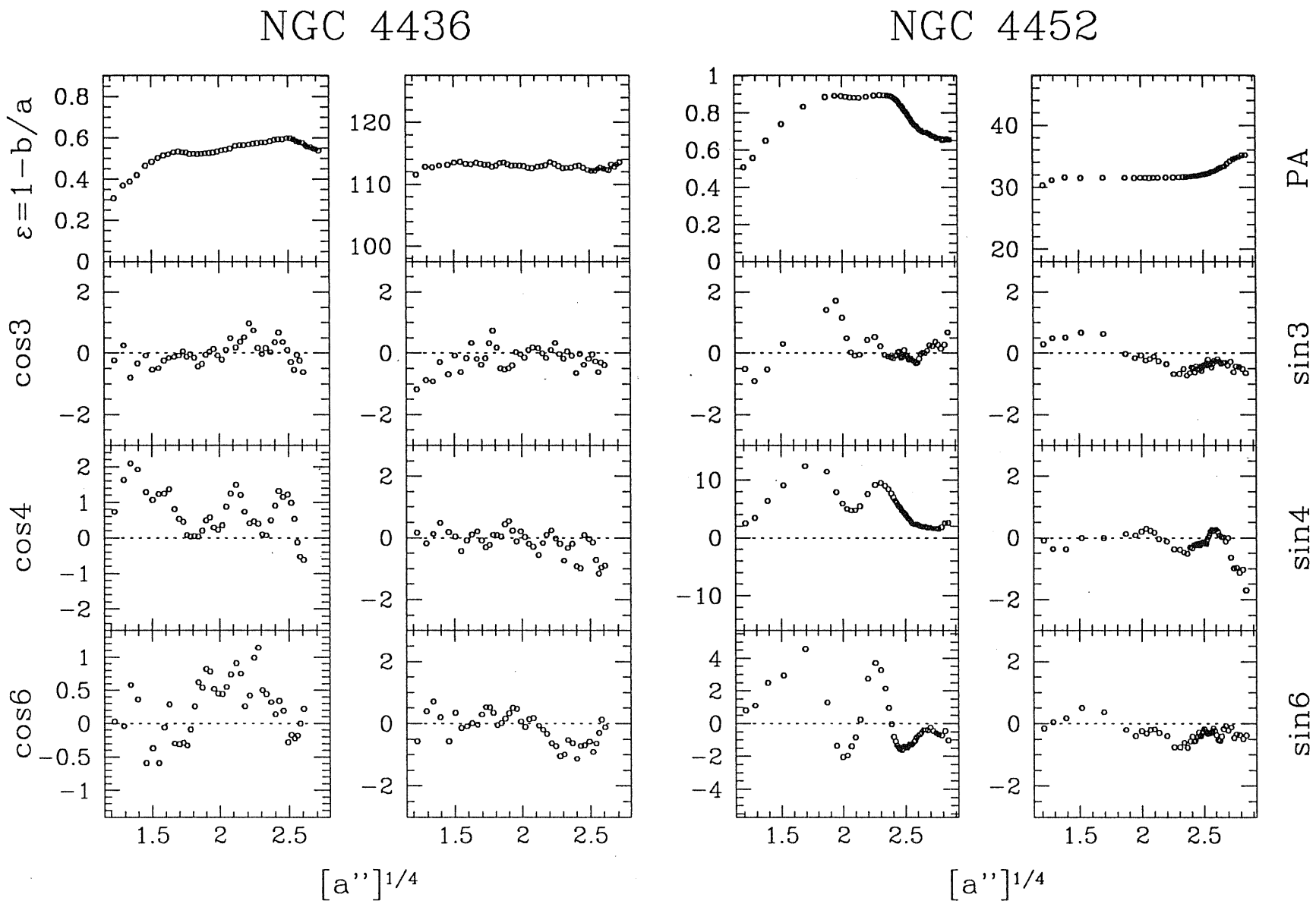
NGC 4436
NGC 4452
ε=1−b/a
PA
cos3
sin3
cos4
sin4
cos6
sin6
[a'']^1/4
[a'']^1/4

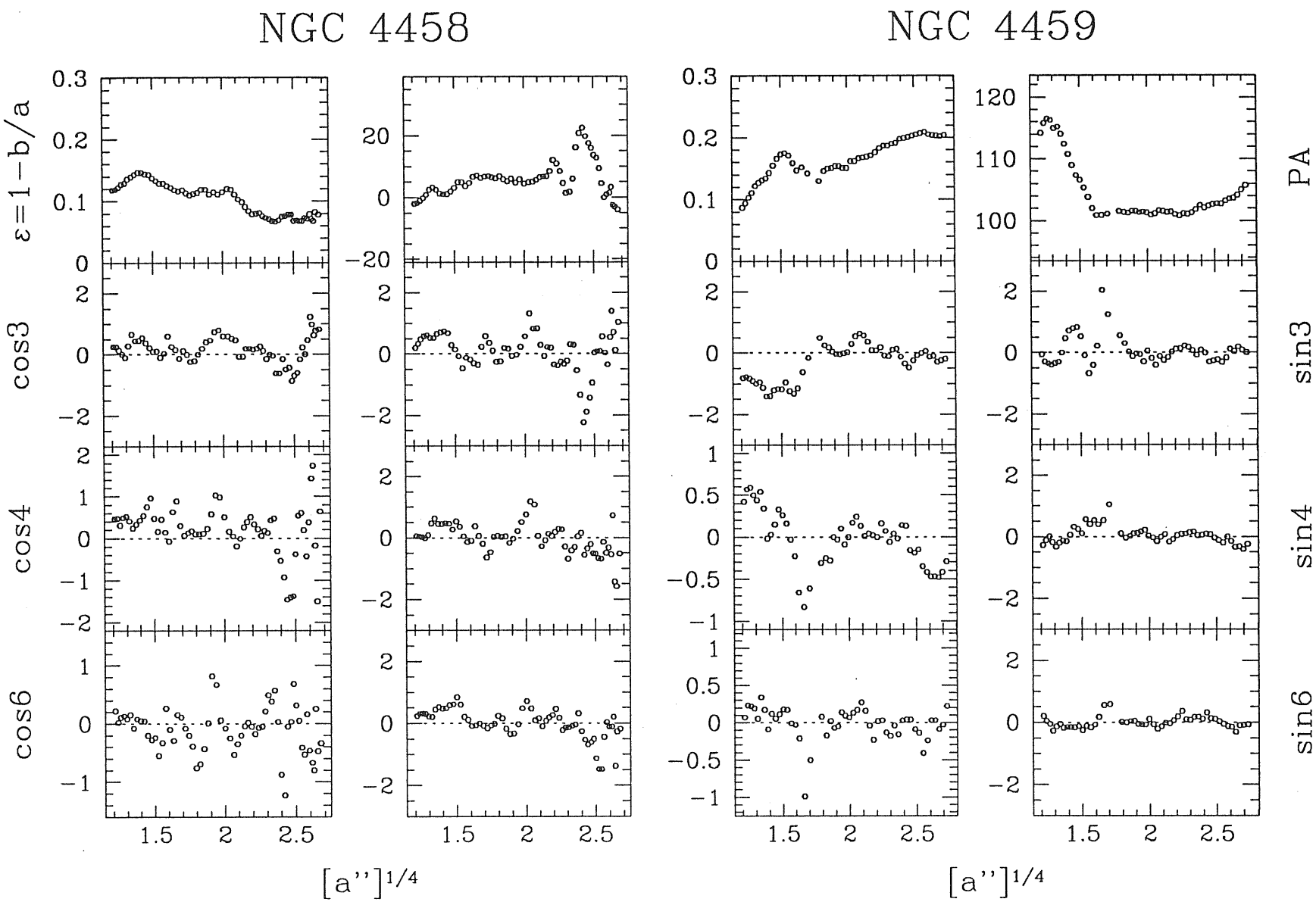
NGC 4458
NGC 4459
ε=1−b/a
cos3
cos4
cos6
sin3
sin4
sin6
PA
[a'']^1/4
[a'']^1/4

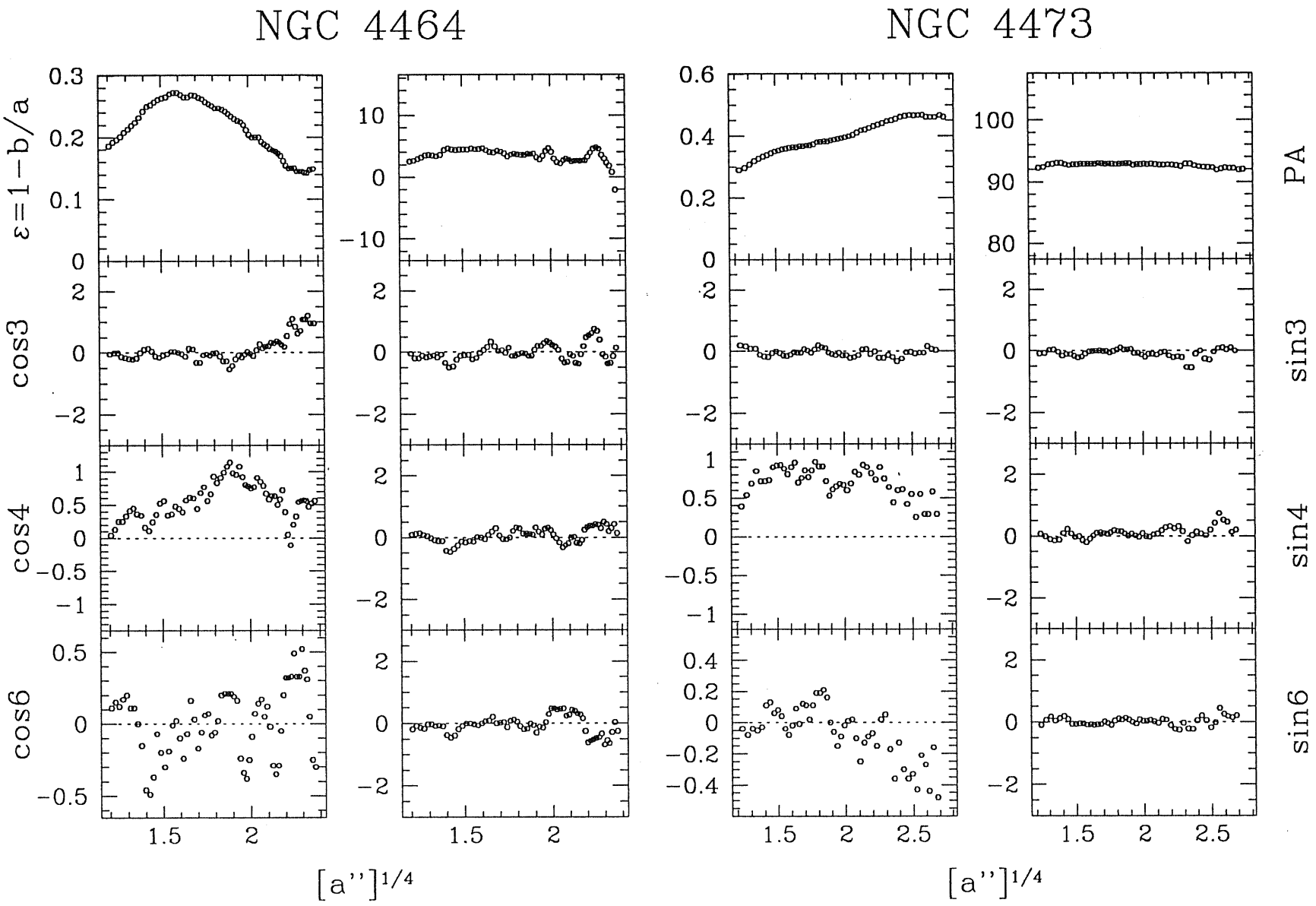
NGC 4464
NGC 4473
ε=1−b/a
cos3
cos4
cos6
PA
sin3
sin4
sin6
[a'']^1/4
[a'']^1/4

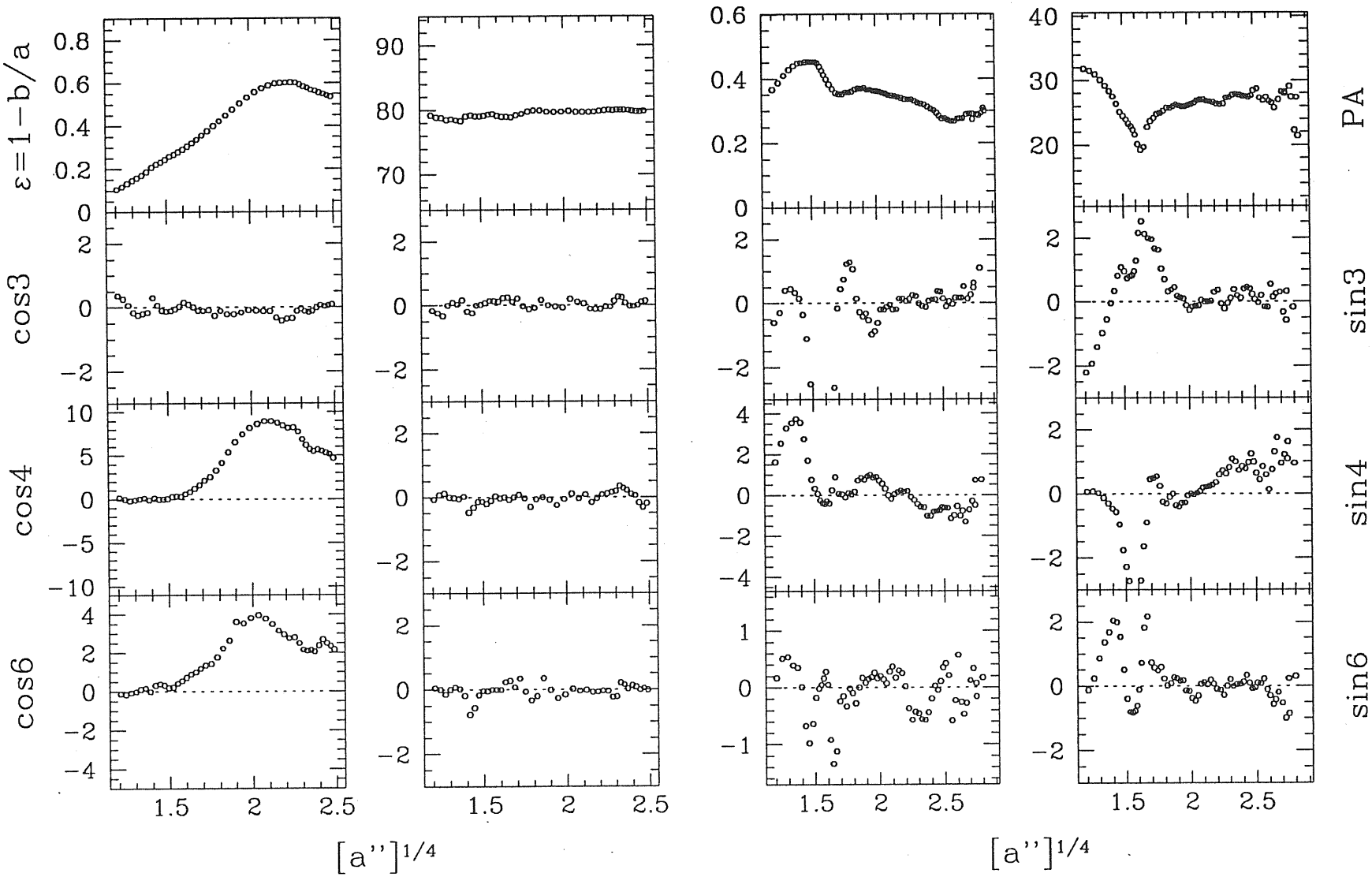
NGC 4474
NGC 4476
ε=1−b/a
cos3
cos4
cos6
PA
sin3
sin4
sin6
[a'']^1/4
[a'']^1/4

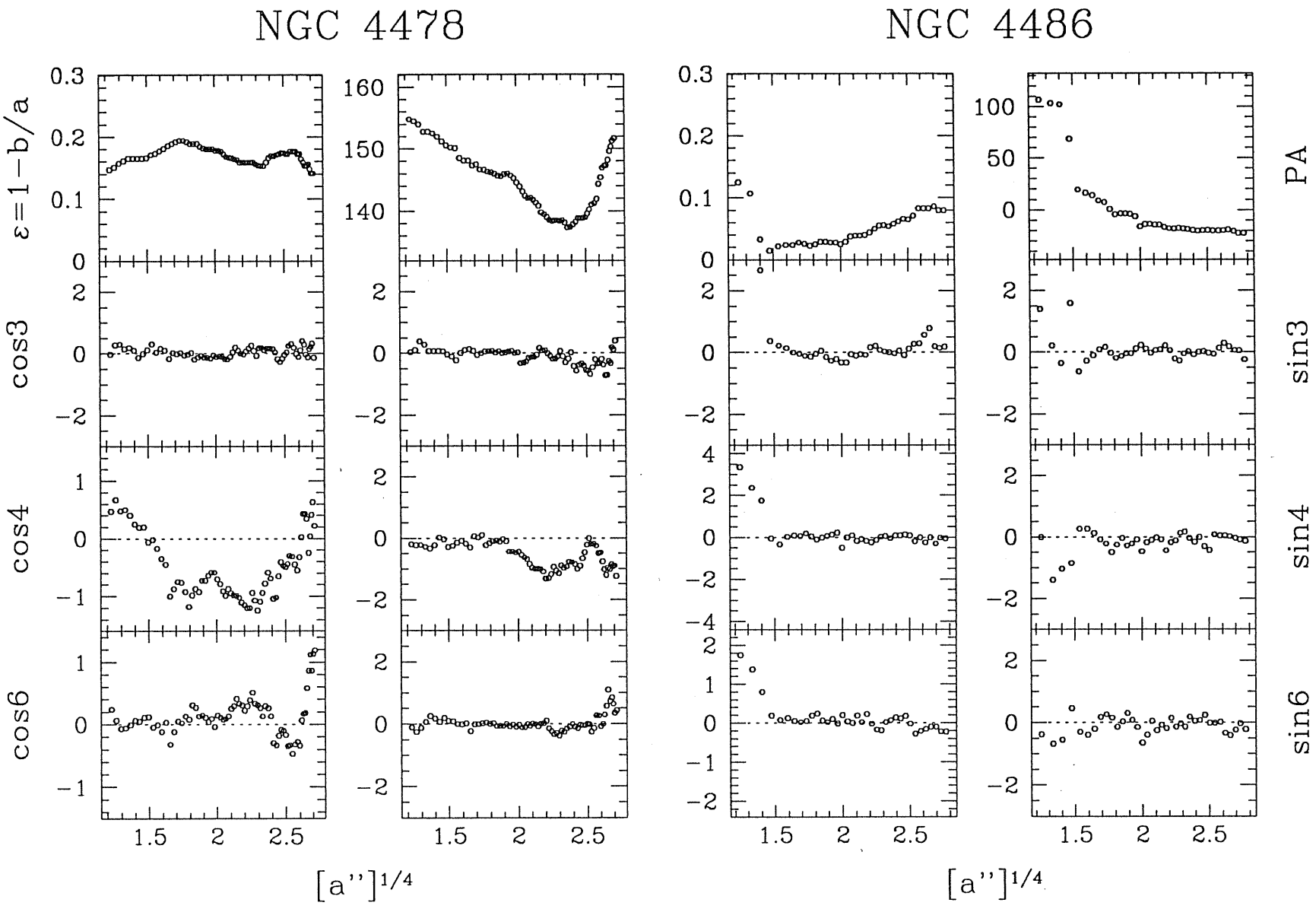
NGC 4478
NGC 4486
ε=1−b/a
cos3
cos4
cos6
PA
sin3
sin4
sin6
[a'']^1/4
[a'']^1/4

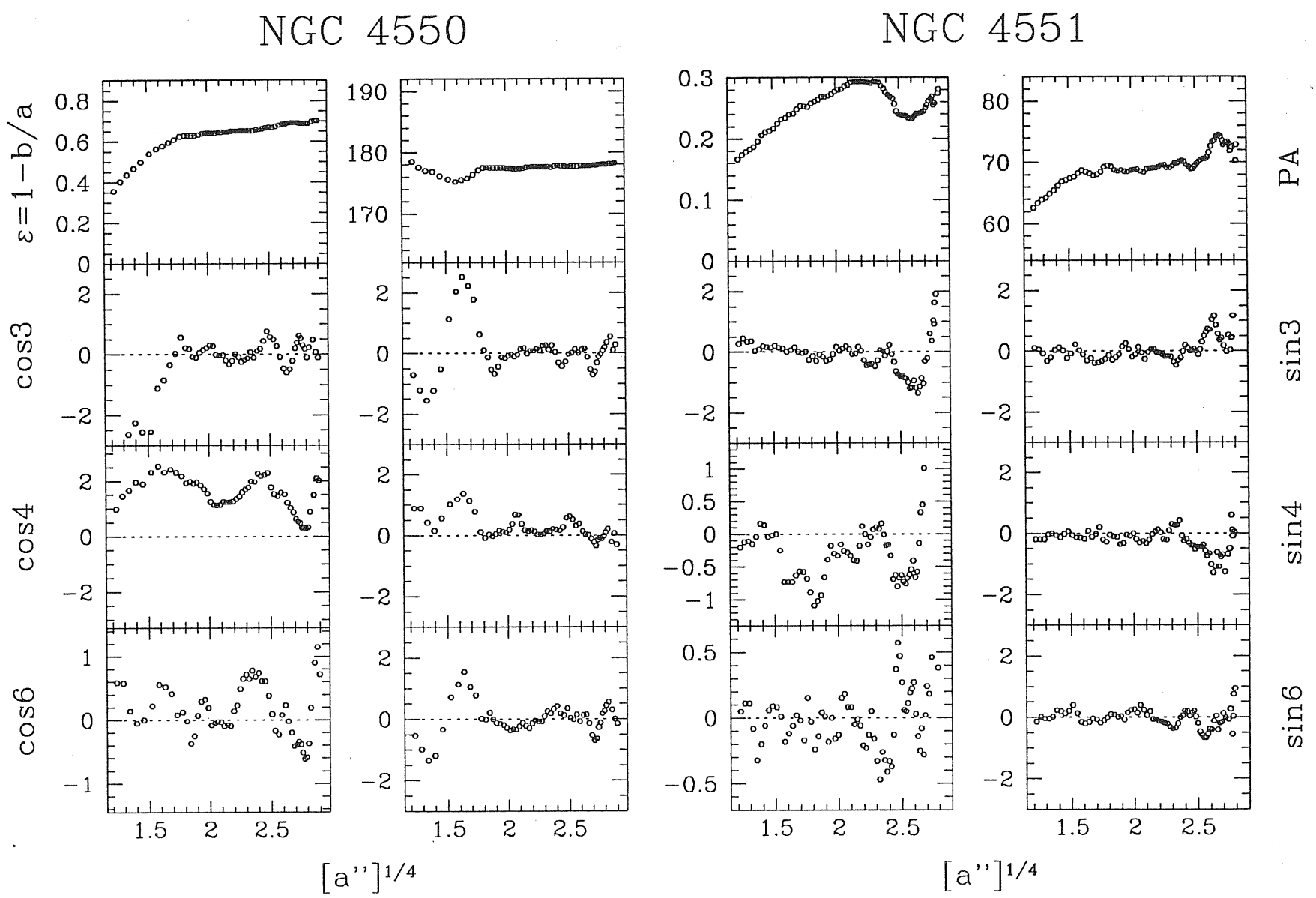
NGC 4550
NGC 4551
ε=1−b/a
cos3
cos4
cos6
PA
sin3
sin4
sin6
[a'']^1/4
[a'']^1/4

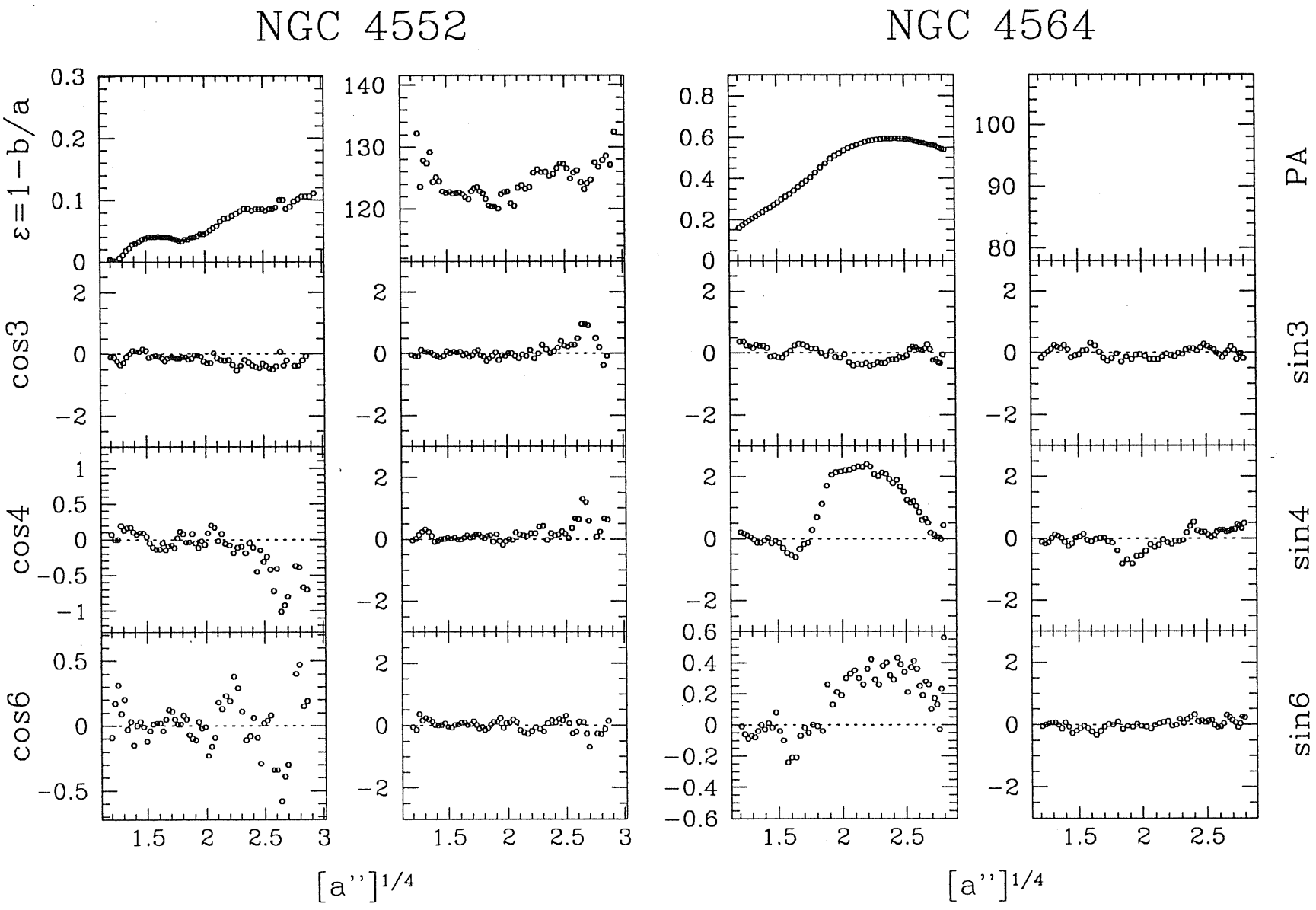
NGC 4552
NGC 4564
ε=1−b/a
cos3
cos4
cos6
PA
sin3
sin4
sin6
[a'']^1/4
[a'']^1/4

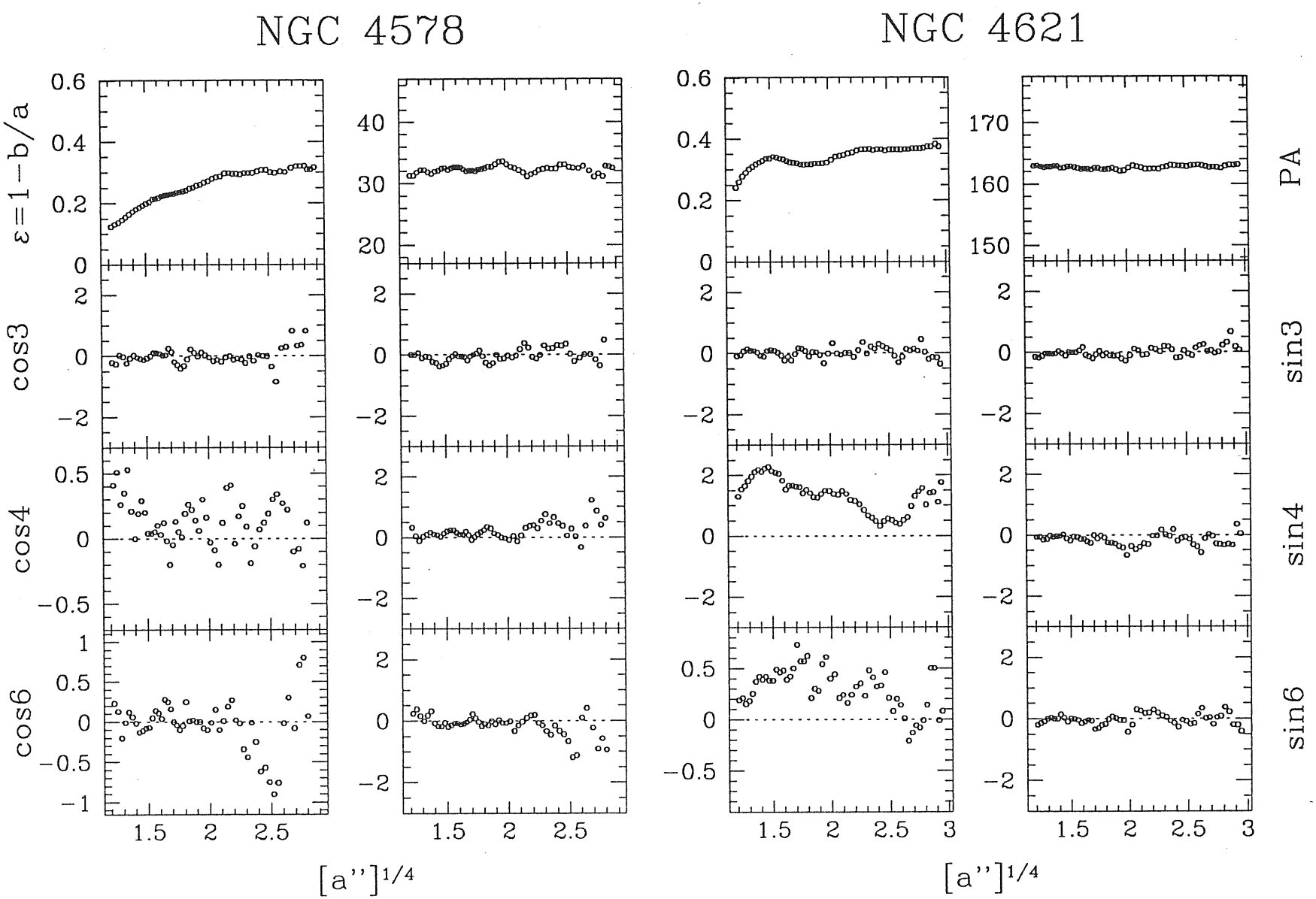
NGC 4578
NGC 4621
ε=1−b/a
cos3
cos4
cos6
sin3
sin4
sin6
PA
[a'']^1/4
[a'']^1/4

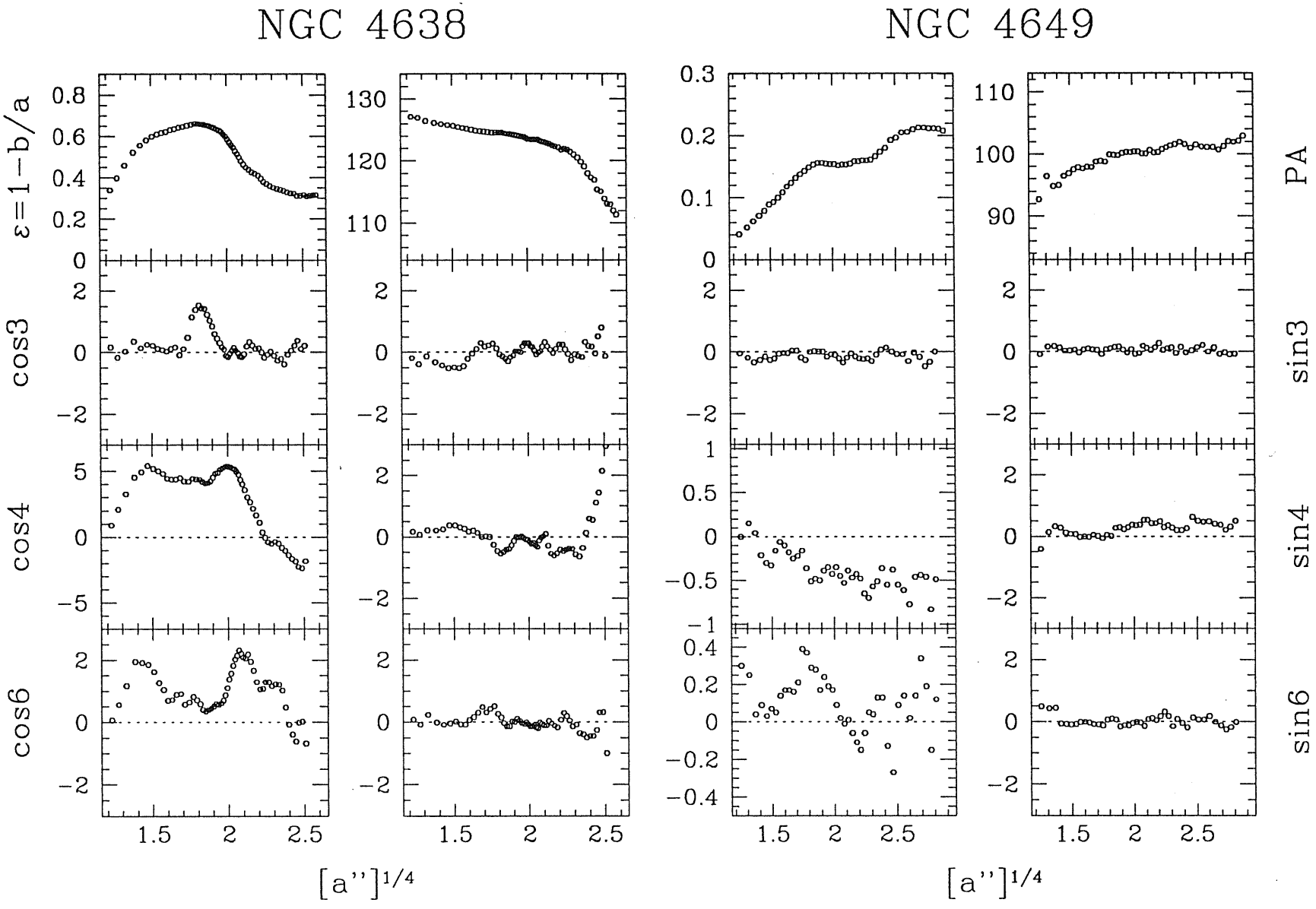
NGC 4638
NGC 4649
ε=1−b/a
cos3
cos4
cos6
PA
sin3
sin4
sin6
[a'']^1/4
[a'']^1/4

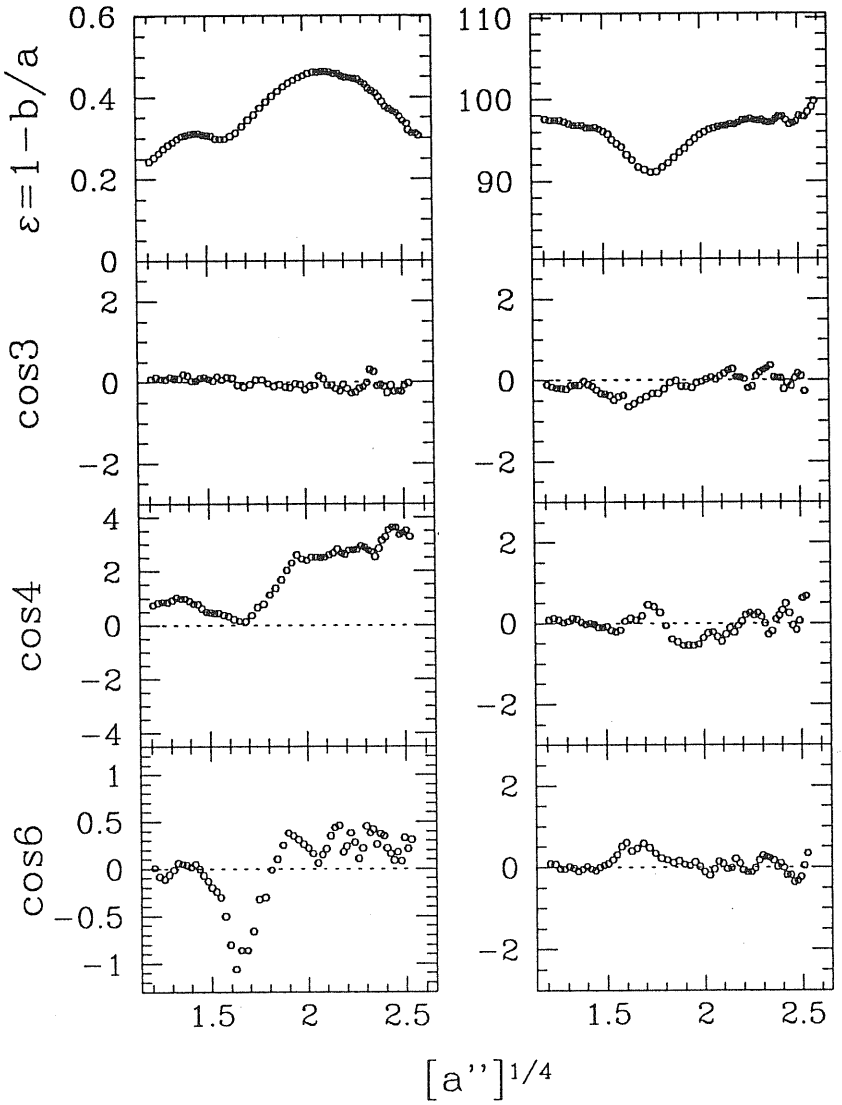
NGC 4660
ε=1−b/a
cos3
cos4
cos6
[a'']^1/4

Table B–1

NGC 4215

$(a'')^{1/4}$	μ_B [mag arcsec^{-2}]		$\epsilon = 1 - b/a$	P.A.
	maj	*min*		[deg]
0.00	17.29	17.29		
0.80	17.45	17.44		
0.85	17.49	17.50		
0.90	17.59	17.65		
0.95	17.72	17.86		
1.00	17.86	18.12	0.226	175.3
1.05	18.05	18.40	0.265	175.4
1.10	18.24	18.70	0.272	175.7
1.15	18.44	18.98	0.289	176.0
1.20	18.66	19.26	0.311	176.2
1.25	18.88	19.51	0.335	176.4
1.30	19.10	19.75	0.351	176.3
1.35	19.32	19.98	0.362	176.2
1.40	19.53	20.20	0.361	175.5
1.45	19.73	20.41	0.353	174.8
1.50	19.92	20.64	0.357	175.1
1.55	20.09	20.87	0.370	175.4
1.60	20.26	21.10	0.385	175.3
1.65	20.41	21.35	0.404	175.2
1.70	20.55	21.61	0.417	175.2
1.75	20.68	21.89	0.436	175.2
1.80	20.81	22.18	0.454	175.4
1.85	20.92	22.48	0.474	175.5
1.90	21.03	22.80	0.498	175.5
1.95	21.13	23.11	0.526	175.5
2.00	21.20	23.41	0.562	175.5
2.05	21.23	23.69	0.606	175.6
2.10	21.23	23.96	0.650	175.6
2.15	21.19	24.21	0.686	175.6
2.20	21.14	24.46	0.707	175.7
2.25	21.07	24.73	0.715	175.6
2.30	21.20	25.03	0.711	175.6
2.35	21.58	25.31	0.686	175.5
2.40	22.04	25.60	0.652	175.4
2.45	22.53	25.86	0.631	175.3
2.50	23.09	26.14	0.623	175.2
2.55	23.28	26.43	0.617	174.9
2.60	23.84	26.73	0.612	174.7
2.65	24.13	27.05	0.612	174.7
2.70	24.40		0.614	174.7
2.75	24.69		0.611	174.8
2.80	24.88		0.606	174.8
2.85	25.02		0.603	174.9
2.90	25.25		0.604	175.2
2.95	25.50		0.611	175.4
3.00	25.75		0.601	175.7
3.05	25.98		0.607	176.1
3.10	26.19			
3.15	26.40			
3.20	26.61			
3.25	26.83			
3.30	27.08			
3.35	27.38			

Table B–2

NGC 4255

$(a'')^{1/4}$	μ_B [mag arcsec^{-2}]		$\epsilon = 1 - b/a$	P.A.
	maj	*min*		[deg]
0.00	17.50	17.50		
0.80	17.69	17.67		
0.85	17.71	17.77		
0.90	17.81	17.91		
0.95	17.94	18.09		
1.00	18.10	18.30	0.202	112.7
1.05	18.28	18.52	0.235	110.2
1.10	18.48	18.75	0.209	108.0
1.15	18.73	18.99	0.199	107.9
1.20	19.00	19.24	0.170	109.5
1.25	19.28	19.48	0.139	112.0
1.30	19.55	19.70	0.115	112.7
1.35	19.82	19.94	0.089	111.1
1.40	20.09	20.21	0.059	107.9
1.45	20.36	20.46	0.055	105.6
1.50	20.61	20.75	0.064	102.8
1.55	20.82	21.07	0.089	106.0
1.60	21.00	21.35	0.142	108.8
1.65	21.15	21.75	0.184	110.1
1.70	21.28	22.04	0.232	110.2
1.75	21.41	22.27	0.286	110.3
1.80	21.52	22.56	0.338	110.5
1.85	21.63	22.86	0.383	110.3
1.90	21.74	23.16	0.424	110.3
1.95	21.85	23.45	0.461	110.6
2.00	21.97	23.77	0.490	111.0
2.05	22.10	24.12	0.509	111.3
2.10	22.26	24.47	0.519	111.7
2.15	22.49	24.79	0.525	111.8
2.20	22.77	25.09	0.526	111.8
2.25	23.05	25.36	0.524	111.9
2.30	23.30	25.62	0.520	111.8
2.35	23.61	25.90	0.512	111.9
2.40	23.92	26.19	0.504	112.1
2.45	24.29	26.47	0.491	111.9
2.50	24.64	26.73	0.478	111.8
2.55	24.99		0.462	112.2
2.60	25.35		0.449	113.4
2.65	25.70		0.414	113.2
2.70	26.05		0.396	112.8
2.75	26.39		0.382	112.9
2.80	26.72		0.381	113.7
2.85	27.03			
2.90	27.32			

Table B–3

NGC 4261

$(a'')^{1/4}$	μ_B [mag arcsec^{-2}]		$\epsilon = 1 - b/a$	P.A.
	maj	*min*		[deg]
0.00	17.75	17.75		
1.00	17.77	17.82	0.140	155.2
1.05	17.81	17.90	0.162	155.6
1.10	17.87	18.01	0.182	156.3
1.15	17.97	18.17	0.204	157.3
1.20	18.08	18.34	0.213	158.5
1.25	18.24	18.53	0.224	159.4
1.30	18.39	18.73	0.241	159.8
1.35	18.56	18.94	0.252	159.2
1.40	18.74	19.16	0.264	158.9
1.45	18.92	19.36	0.268	158.5
1.50	19.11	19.57	0.267	158.2
1.55	19.30	19.76	0.264	158.0
1.60	19.49	19.95	0.260	158.1
1.65	19.68	20.12	0.258	158.1
1.70	19.86	20.28	0.256	158.6
1.75	20.01	20.43	0.255	158.9
1.80	20.16	20.58	0.252	159.1
1.85	20.32	20.73	0.249	159.2
1.90	20.47	20.89	0.244	158.8
1.95	20.63	21.06	0.238	158.7
2.00	20.79	21.24	0.226	158.8
2.05	20.98	21.41	0.217	158.8
2.10	21.15	21.55	0.207	159.1
2.15	21.32	21.70	0.196	158.4
2.20	21.52	21.88	0.186	157.8
2.25	21.71	22.06	0.178	157.7
2.30	21.87	22.22	0.176	157.9
2.35	22.04	22.37	0.172	158.6
2.40	22.22	22.51	0.167	159.0
2.45	22.36	22.66	0.166	159.0
2.50	22.49	22.79	0.164	159.4
2.55	22.64	22.92	0.163	159.7
2.60	22.73	23.01	0.162	159.8
2.65	22.86	23.12	0.161	160.4
2.70	23.02	23.25	0.161	160.8
2.75	23.15	23.37	0.161	161.2
2.80	23.26	23.51	0.160	161.4
2.85	23.47	23.66	0.158	161.9
2.90	23.61	23.82	0.156	162.3
2.95	23.75	24.00	0.155	162.8
3.00	23.82	24.20	0.155	163.2
3.05	24.00	24.39	0.156	163.5
3.10	24.14	24.59	0.159	163.7
3.15	24.26	24.77	0.162	163.8
3.20	24.38	24.96	0.167	164.0
3.25	24.50	25.11	0.173	164.2
3.30	24.62	25.26	0.181	164.4
3.35	24.74	25.38	0.190	164.7
3.40	24.86	25.50	0.201	165.0
3.45	25.00	25.61	0.213	165.3
3.50	25.13	25.71	0.227	165.5
3.55	25.27	25.82	0.243	165.8
3.60	25.41	25.94	0.260	166.1
3.65	25.55	26.06	0.272	166.6

Table B–3 — *continued*

NGC 4261

$(a'')^{1/4}$	μ_B [mag arcsec^{-2}]		$\epsilon = 1 - b/a$	P.A.
	maj	*min*		[deg]
3.70	25.68	26.18	0.267	167.3
3.75	25.81	26.31	0.247	168.1
3.80	25.93	26.42		
3.85	26.05	26.52		
3.90	26.15			
3.95	26.24			
4.00	26.32			
4.05	26.40			
4.10	26.46			
4.15	26.51			
4.20	26.56			
4.25	26.60			
4.30	26.64			
4.35	26.67			
4.40	26.69			

Table B–4

NGC 4268

$(a'')^{1/4}$	μ_B [mag arcsec^{-2}]		$\epsilon = 1 - b/a$	P.A.
	maj	*min*		[deg]
0.00	18.01	18.01		
0.85	18.18	18.19		
0.90	18.24	18.32		
0.95	18.34	18.47		
1.00	18.49	18.64	0.195	39.6
1.05	18.65	18.84	0.183	41.8
1.10	18.84	19.05	0.159	46.1
1.15	19.04	19.30	0.181	46.7
1.20	19.24	19.54	0.193	46.3
1.25	19.44	19.79	0.217	45.9
1.30	19.63	20.05	0.232	46.3
1.35	19.83	20.28	0.255	46.8
1.40	20.02	20.54	0.265	47.9
1.45	20.22	20.79	0.267	49.3
1.50	20.43	21.03	0.271	50.3
1.55	20.65	21.26	0.277	51.0
1.60	20.86	21.47	0.272	52.3
1.65	21.05	21.71	0.275	53.5
1.70	21.23	22.00	0.296	54.6
1.75	21.38	22.30	0.325	55.5
1.80	21.52	22.56	0.359	55.6
1.85	21.65	22.87	0.399	55.8
1.90	21.74	23.27	0.442	55.7
1.95	21.83	23.57	0.481	55.4
2.00	21.95	23.87	0.510	54.5
2.05	22.06	24.17	0.531	53.0
2.10	22.17	24.48	0.547	51.7
2.15	22.31	24.80	0.562	50.6
2.20	22.49	25.14	0.575	49.7
2.25	22.67	25.51	0.585	49.1
2.30	22.93	25.94	0.588	48.7
2.35	23.21	26.43	0.581	48.4
2.40	23.60	27.03	0.568	48.2
2.45	24.00	27.75	0.551	47.9
2.50	24.33		0.532	47.0
2.55	24.61		0.518	46.5
2.60	24.92		0.512	46.0
2.65	25.37		0.512	45.4
2.70	25.88		0.503	44.7
2.75	26.45		0.473	43.9
2.80	27.12		0.438	42.3
2.85	27.71			

Table B–5

NGC 4269

$(a'')^{1/4}$	μ_B [mag arcsec^{-2}]		$\epsilon = 1 - b/a$	P.A.
	maj	*min*		[deg]
0.00	17.58	17.58		
0.80	17.72	17.73		
0.85	17.85	17.83		
0.90	18.00	17.97		
0.95	18.18	18.14		
1.00	18.39	18.35		
1.05	18.63	18.58		
1.10	18.90	18.85		
1.15	19.17	19.13		
1.20	19.44	19.43	0.037	137.8
1.25	19.69	19.75	0.029	129.1
1.30	19.92	20.05	0.072	118.5
1.35	20.14	20.34	0.120	116.2
1.40	20.34	20.60	0.138	117.4
1.45	20.54	20.85	0.158	117.9
1.50	20.73	21.08	0.173	116.2
1.55	20.93	21.33	0.202	115.5
1.60	21.13	21.52	0.225	115.5
1.65	21.34	21.80	0.228	114.9
1.70	21.57	22.10	0.224	114.8
1.75	21.83	22.33	0.203	116.7
1.80	22.09	22.54	0.183	118.2
1.85	22.37	22.73	0.168	119.7
1.90	22.63	22.91	0.165	120.9
1.95	22.87	23.09	0.164	122.6
2.00	23.06	23.28	0.161	124.8
2.05	23.20	23.44	0.161	125.3
2.10	23.32	23.57	0.159	124.9
2.15	23.44	23.70	0.145	125.8
2.20	23.59	23.84	0.134	126.5
2.25	23.73	23.98	0.141	128.1
2.30	23.87	24.14	0.144	131.5
2.35	24.03	24.30	0.151	133.4
2.40	24.22	24.47	0.163	131.1
2.45	24.41	24.65	0.174	129.7
2.50	24.61	24.83	0.193	130.4
2.55	24.82	25.03	0.196	131.5
2.60	25.04	25.23	0.194	132.6
2.65	25.27	25.44	0.192	130.6
2.70	25.50		0.195	129.3
2.75	25.73		0.207	128.9
2.80	25.96			
2.85	26.19			
2.90	26.42			
2.95	26.64			
3.00	26.85			

Table B–6

NGC 4270

$(a'')^{1/4}$	μ_B [mag arcsec^{-2}]		$\epsilon = 1 - b/a$	P.A.
	maj	*min*		[deg]
0.00	17.87	17.87		
0.80	17.99	17.99		
0.85	18.04	18.05		
0.90	18.11	18.16		
0.95	18.24	18.31		
1.00	18.37	18.49	0.188	108.0
1.05	18.50	18.70	0.201	106.1
1.10	18.65	18.91	0.210	104.5
1.15	18.82	19.14	0.223	103.1
1.20	19.04	19.37	0.217	101.9
1.25	19.26	19.60	0.221	102.3
1.30	19.45	19.80	0.239	104.2
1.35	19.60	20.02	0.263	105.5
1.40	19.76	20.24	0.280	105.8
1.45	19.90	20.45	0.304	105.7
1.50	20.04	20.66	0.330	106.3
1.55	20.19	20.88	0.346	106.8
1.60	20.33	21.09	0.363	106.8
1.65	20.49	21.32	0.380	106.6
1.70	20.63	21.55	0.399	106.5
1.75	20.76	21.79	0.416	106.6
1.80	20.92	22.04	0.430	106.6
1.85	21.06	22.29	0.443	106.8
1.90	21.20	22.59	0.453	106.8
1.95	21.34	22.90	0.467	106.9
2.00	21.49	23.21	0.484	106.9
2.05	21.61	23.50	0.501	106.8
2.10	21.75	23.79	0.520	106.9
2.15	21.87	24.08	0.539	107.1
2.20	21.99	24.37	0.558	107.3
2.25	22.10	24.66	0.577	107.5
2.30	22.24	24.94	0.593	107.7
2.35	22.40	25.22	0.603	108.0
2.40	22.57	25.50	0.611	107.9
2.45	22.81	25.77	0.614	108.0
2.50	23.22	26.03	0.604	108.2
2.55	23.64		0.586	108.8
2.60	24.04		0.569	109.6
2.65	24.41		0.547	111.1
2.70	24.77		0.531	111.8
2.75	25.11		0.532	111.8
2.80	25.42		0.538	111.9
2.85	25.74		0.540	111.8
2.90	26.07		0.527	112.1
2.95	26.41		0.492	109.0
3.00	26.79		0.451	106.4
3.05	27.18			
3.10	27.61			

Table B–7

NGC 4281

$(a'')^{1/4}$	μ_B [mag arcsec^{-2}]				$\epsilon = 1 - b/a$	P.A.
	*maj*1	*maj*2	*min*1	*min*2		[deg]
0.00	17.34	17.34	17.34	17.34		
0.80	17.77	17.24	17.56	17.40		
0.85	17.87	17.20	17.75	17.46		
0.90	17.97	17.20	17.94	17.57		
0.95	18.05	17.24	18.13	18.71		
1.00	18.13	17.32	18.34	18.89	0.218	88.0
1.05	18.22	17.46	18.56	18.09	0.247	87.5
1.10	18.33	17.65	18.79	18.30	0.266	87.1
1.15	18.47	17.86	19.03	18.52	0.310	86.6
1.20	18.67	18.08	19.29	18.76	0.369	86.5
1.25	18.87	18.30	19.54	19.00	0.400	86.5
1.30	19.04	18.50	19.78	19.23	0.404	86.2
1.35	19.13	18.71	19.97	19.46	0.398	85.3
1.40	19.22	18.93	20.07	19.70	0.416	84.2
1.45	19.36	19.12	20.15	19.92	0.446	84.3
1.50	19.60	19.23	20.25	20.14	0.463	84.6
1.55	19.80	19.40	20.38	20.35	0.463	84.9
1.60	19.95	19.66	20.53	20.55	0.464	85.3
1.65	20.12	19.93	20.75		0.462	85.5
1.70	20.28	20.12	20.95		0.392	85.9
1.75	20.43	20.29	21.16		0.390	86.2
1.80	20.54	20.44	21.34		0.391	86.2
1.85	20.63	20.58	21.55		0.406	86.5
1.90	20.70	20.69	21.74		0.438	86.6
1.95	20.76		21.92		0.474	86.4
2.00	20.84		22.13		0.500	86.1
2.05	20.97		22.33		0.514	86.0
2.10	21.10		22.55		0.524	86.1
2.15	21.27		22.78		0.531	86.1
2.20	21.40		23.03		0.536	86.0
2.25	21.56		23.28		0.539	86.0
2.30	21.71		23.52		0.542	86.1
2.35	21.88		23.73		0.544	86.1
2.40	22.05		23.91		0.545	86.1
2.45	22.22		24.06		0.544	85.9
2.50	22.38		24.22		0.541	86.1
2.55	22.53		24.42		0.544	86.2
2.60	22.68		24.65		0.543	86.4
2.65	22.85		24.87		0.538	86.4
2.70	23.05		25.06		0.535	86.4
2.75	23.20		25.26		0.534	86.5
2.80	23.46		25.46		0.533	86.8
2.85	23.74		25.65		0.526	87.4
2.90	23.98		25.83		0.512	87.6
2.95	24.19		26.04		0.512	87.3
3.00	24.39		26.26		0.500	87.8
3.05	24.59		26.48		0.462	88.5
3.10	24.80		26.68		0.437	87.2
3.15	25.04		26.88		0.432	86.6
3.20	25.31				0.426	87.7
3.25	25.64				0.411	88.7
3.30	26.03				0.395	89.9
3.35	26.50				0.379	91.1

Table B–8

NGC 4339

$(a'')^{1/4}$	μ_B [mag arcsec^{-2}]		$\epsilon = 1 - b/a$	P.A.
	maj	*min*		[deg]
0.00	17.92	17.92		
0.85	18.01	18.04		
0.90	18.10	18.07		
0.95	18.21	18.15		
1.00	18.34	18.29	0.073	54.7
1.05	18.49	18.46	0.053	42.1
1.10	18.66	18.64	0.019	29.1
1.15	18.83	18.84	0.006	20.4
1.20	19.02	19.04	0.043	15.7
1.25	19.20	19.24	0.067	20.0
1.30	19.38	19.43	0.062	16.7
1.35	19.56	19.62	0.034	21.7
1.40	19.73	19.80	0.033	17.2
1.45	19.91	19.98	0.037	12.7
1.50	20.08	20.15	0.039	12.7
1.55	20.25	20.32	0.041	14.3
1.60	20.42	20.48	0.041	20.0
1.65	20.58	20.66	0.046	18.4
1.70	20.75	20.83	0.050	19.3
1.75	20.93	21.01	0.050	18.7
1.80	21.12	21.20	0.048	16.0
1.85	21.31	21.40	0.046	13.7
1.90	21.51	21.61	0.046	15.2
1.95	21.70	21.82	0.058	20.7
2.00	21.90	22.05	0.070	20.9
2.05	22.08	22.24	0.082	17.9
2.10	22.25	22.41	0.087	15.6
2.15	22.42	22.56	0.100	10.2
2.20	22.56	22.69	0.085	6.6
2.25	22.69	22.82	0.075	1.3
2.30	22.83	22.96	0.071	−0.6
2.35	22.99	23.13	0.064	0.5
2.40	23.13	23.30	0.070	4.5
2.45	23.29	23.48	0.072	6.5
2.50	23.45	23.67	0.073	4.1
2.55	23.61	23.88	0.073	4.5
2.60	23.80	24.12	0.047	10.4
2.65	23.99	24.36	0.046	10.2
2.70	24.20	24.59	0.060	5.6
2.75	24.42	24.79	0.063	10.9
2.80	24.63	24.98	0.067	10.4
2.85	24.80	25.15	0.069	7.0
2.90	25.00	25.27	0.085	4.8
2.95	25.21	25.46	0.101	9.5
3.00	25.43		0.109	6.8
3.05	25.67		0.118	4.4
3.10	25.92		0.119	3.5
3.15	26.18		0.119	4.5
3.20	26.47		0.118	−0.1
3.25	26.75			
3.30	26.98			

Table B–9

NGC 4342

$(a'')^{1/4}$	μ_B [mag arcsec^{-2}]		$\epsilon = 1 - b/a$	P.A.
	maj	*min*		[deg]
0.00	16.27	16.27		
0.85	16.56	16.57		
0.90	16.74	16.75		
0.95	16.90	17.01		
1.00	17.09	17.31	0.216	165.7
1.05	17.30	17.65	0.223	166.3
1.10	17.53	18.01	0.227	166.4
1.15	17.78	18.37	0.234	166.0
1.20	18.02	18.72	0.267	166.7
1.25	18.25	19.09	0.312	167.4
1.30	18.45	19.46	0.356	167.4
1.35	18.61	19.82	0.409	167.5
1.40	18.76	20.20	0.447	167.6
1.45	18.94	20.57	0.494	167.7
1.50	19.14	20.95	0.529	167.6
1.55	19.34	21.32	0.556	167.5
1.60	19.54	21.66	0.586	167.5
1.65	19.73	21.98	0.610	167.4
1.70	19.91	22.28	0.631	167.5
1.75	20.08	22.58	0.650	167.6
1.80	20.27	22.88	0.657	167.3
1.85	20.50	23.19	0.663	167.3
1.90	20.77	23.52	0.661	167.4
1.95	21.07	23.88	0.657	167.6
2.00	21.40	24.22	0.647	167.8
2.05	21.75	24.54	0.628	167.8
2.10	22.10	24.86	0.620	168.2
2.15	22.46	25.12	0.593	168.0
2.20	22.79		0.569	167.8
2.25	23.14		0.563	168.0
2.30	23.57		0.555	168.2
2.35	24.03		0.506	170.1
2.40	24.33		0.446	169.1
2.45	24.65		0.401	167.6
2.50	24.96		0.340	167.1
2.55	25.25		0.276	167.2
2.60	25.55		0.234	167.6
2.65	25.86			
2.70	26.19			
2.75	26.55			
2.80	26.93			

Table B–10

NGC 4360

$(a'')^{1/4}$	μ_B [mag arcsec^{-2}]		$\varepsilon = 1 - b/a$	P.A.
	maj	*min*		[deg]
0.00	18.20	18.20		
0.80	18.36	18.33		
0.85	18.40	18.41		
0.90	18.49	18.54		
0.95	18.61	18.69		
1.00	18.78	18.87	0.127	152.4
1.05	18.96	19.09	0.101	151.4
1.10	19.17	19.30	0.095	150.7
1.15	19.38	19.53	0.092	150.4
1.20	19.61	19.77	0.089	149.9
1.25	19.83	20.00	0.088	149.3
1.30	20.05	20.24	0.081	149.3
1.35	20.27	20.46	0.075	149.1
1.40	20.48	20.68	0.076	148.4
1.45	20.69	20.89	0.085	148.1
1.50	20.89	21.09	0.091	147.7
1.55	21.08	21.28	0.097	147.6
1.60	21.27	21.47	0.104	148.4
1.65	21.46	21.64	0.106	149.3
1.70	21.64	21.82	0.107	150.5
1.75	21.82	21.99	0.111	151.2
1.80	22.01	22.18	0.119	150.8
1.85	22.19	22.36	0.125	150.4
1.90	22.38	22.56	0.126	149.4
1.95	22.57	22.79	0.127	148.4
2.00	22.75	23.05	0.126	146.0
2.05	22.92	23.30	0.137	145.1
2.10	23.08	23.48	0.161	145.7
2.15	23.25	23.61	0.173	145.7
2.20	23.45	23.74	0.170	145.6
2.25	23.66	23.92	0.164	145.9
2.30	23.88	24.12	0.166	145.8
2.35	24.10	24.39	0.178	145.3
2.40	24.34	24.64	0.178	144.0
2.45	24.54	24.87	0.169	143.9
2.50	24.77	25.09	0.165	143.3
2.55	24.98	25.31	0.165	140.4
2.60	25.18	25.52	0.164	138.3
2.65	25.39	25.71	0.150	136.8
2.70	25.60	25.91	0.148	135.9
2.75	25.81	26.10	0.157	135.4
2.80	26.02	26.28	0.180	135.2
2.85	26.24	26.46	0.213	135.3
2.90	26.45	26.65	0.250	135.4
2.95	26.67	26.83	0.281	135.5
3.00	26.88	27.01	0.301	135.5
3.05	27.10	27.21	0.301	133.6
3.10	27.32	27.40	0.281	133.2
3.15	27.54	27.61	0.183	129.1
3.20		27.82		
3.25		28.04		
3.30		28.28		

Table B–11

NGC 4365

$(a'')^{1/4}$	μ_B [mag arcsec^{-2}]		$\varepsilon = 1 - b/a$	P.A.
	maj	*min*		[deg]
0.00	17.37	17.37		
0.90	17.48	17.48		
0.95	17.52	17.52		
1.00	17.57	17.61	0.218	40.2
1.05	17.63	17.72	0.218	40.4
1.10	17.71	17.84	0.220	41.5
1.15	17.81	17.98	0.223	42.2
1.20	17.91	18.13	0.228	42.3
1.25	18.03	18.29	0.233	42.2
1.30	18.16	18.46	0.238	42.0
1.35	18.31	18.64	0.243	41.8
1.40	18.47	18.80	0.243	41.8
1.45	18.64	18.98	0.241	42.4
1.50	18.81	19.16	0.235	42.3
1.55	18.98	19.33	0.227	42.2
1.60	19.15	19.50	0.221	42.8
1.65	19.33	19.68	0.219	43.3
1.70	19.49	19.84	0.216	43.8
1.75	19.66	20.00	0.217	43.9
1.80	19.80	20.17	0.227	44.1
1.85	19.96	20.33	0.229	44.2
1.90	20.09	20.51	0.237	44.2
1.95	20.23	20.67	0.245	44.2
2.00	20.37	20.83	0.250	44.2
2.05	20.51	20.98	0.255	44.2
2.10	20.66	21.15	0.256	44.1
2.15	20.80	21.31	0.255	43.7
2.20	20.95	21.47	0.254	43.3
2.25	21.10	21.63	0.249	43.4
2.30	21.26	21.79	0.247	43.4
2.35	21.42	21.94	0.245	43.2
2.40	21.57	22.10	0.249	42.7
2.45	21.71	22.25	0.251	42.5
2.50	21.85	22.40	0.252	42.5
2.55	21.99	22.52	0.254	42.2
2.60	22.13	22.65	0.255	41.7
2.65	22.26	22.77	0.262	41.4
2.70	22.38	22.88	0.261	41.3
2.75	22.49	23.01	0.259	41.2
2.80	22.60	23.14	0.258	41.1
2.85	22.71	23.27	0.262	41.0
2.90	22.83	23.40	0.265	40.9
2.95	22.97	23.54	0.263	40.9
3.00	23.09	23.65	0.257	40.9
3.05	23.18	23.79	0.248	40.9
3.10	23.28	23.91	0.236	40.9
3.15	23.40	24.05	0.229	40.9
3.20	23.56	24.18	0.231	41.0
3.25	23.72	24.34	0.235	41.1
3.30	23.84	24.49	0.233	41.1
3.35	23.99	24.64	0.225	41.2
3.40	24.11	24.77	0.219	41.2
3.45	24.23	24.91	0.221	41.3
3.50	24.36	25.06	0.230	41.3
3.55	24.49	25.19	0.242	41.3

Table B–11 — *continued*

NGC 4365

$(a'')^{1/4}$	μ_B [mag arcsec^{-2}]		$\epsilon = 1 - b/a$	P.A.
	maj	*min*		[deg]
3.60	24.61	25.34	0.254	41.4
3.65	24.73	25.49	0.263	41.4
3.70	24.85	25.63	0.269	41.4
3.75	24.97	25.77	0.272	41.4
3.80	25.09	25.91	0.275	41.4
3.85	25.21	26.06	0.280	41.4
3.90	25.32	26.19	0.290	41.4
3.95	25.44	26.33	0.306	41.3
4.00	25.55	26.49	0.324	41.3
4.05	25.66	26.63		
4.10	25.76	26.77		
4.15	25.87	26.91		
4.20	25.98	27.06		
4.25	26.08	27.20		
4.30	26.18	27.34		
4.35	26.28	27.48		
4.40	26.38			
4.45	26.47			
4.50	26.57			
4.55	26.66			
4.60	26.75			
4.65	26.84			
4.70	26.93			
4.75	27.02			
4.80	27.11			
4.85	27.20			
4.90	27.29			
4.95	27.38			
5.00	27.46			
5.05	27.55			

Table B–12

NGC 4370

$(a'')^{1/4}$	μ_B [mag arcsec^{-2}]				$\epsilon = 1 - b/a$	P.A.
	maj1	*maj2*	*min1*	*min2*		[deg]
0.00	21.06	21.06	21.06	21.06		
0.80	21.17	21.03	20.75	21.34		
0.85	21.16	21.02	20.69	21.42		
0.90	21.16	21.01	20.60	21.51		
0.95	21.20	21.00	20.52	21.57		
1.00	21.24	21.00	20.44	21.57	0.455	81.8
1.05	21.28	21.02	20.37	21.51	0.457	81.4
1.10	21.32	21.05	20.33	21.39	0.459	81.0
1.15	21.37	21.10	20.31	21.23	0.461	80.8
1.20	21.43	21.16	20.32	21.04	0.462	80.8
1.25	21.50	21.21	20.36	20.88	0.462	81.5
1.30	21.58	21.26	20.43	20.76	0.468	81.9
1.35	21.68	21.32	20.53	20.72	0.482	81.7
1.40	21.79	21.38	20.66	20.74	0.494	81.8
1.45	21.88	21.48	20.81	20.82	0.506	82.8
1.50	21.94	21.60	20.99	20.97	0.527	83.7
1.55	22.01	21.73	21.16		0.543	84.0
1.60	22.08	21.86	21.35		0.554	84.2
1.65	22.20	21.95	21.54		0.564	84.3
1.70	22.23	22.00	21.74		0.510	84.5
1.75	22.35	22.04	21.94		0.109	99.2
1.80	22.51	22.17	22.14		0.063	97.1
1.85	22.69	22.19	22.35		0.117	93.2
1.90	22.69	22.25	22.57		0.155	86.6
1.95	22.74	22.39	22.80		0.202	85.0
2.00	22.84	22.53	23.03		0.236	84.2
2.05	22.95	22.67	23.27		0.264	83.9
2.10	23.04	22.77	23.47		0.295	83.6
2.15	23.09	22.81	23.73		0.313	82.9
2.20	23.14	22.81	23.96		0.339	82.1
2.25	23.24	22.85	24.18		0.374	81.9
2.30	23.34	23.00	24.40		0.392	81.9
2.35	23.41	23.23	24.60		0.397	82.0
2.40	23.55	23.42	24.80		0.399	81.9
2.45	23.77	23.76	24.99		0.401	80.8
2.50	24.02		25.18		0.385	80.3
2.55	24.28		25.35		0.379	80.2
2.60	24.52		25.51		0.370	79.3
2.65	24.76		25.66		0.354	79.0
2.70	24.99		25.80		0.352	79.1
2.75	25.21		25.93		0.351	79.2
2.80	25.43		26.07		0.338	78.6
2.85	25.65		26.19		0.337	79.3
2.90	25.86		26.29		0.352	80.1
2.95	26.06		26.41		0.374	79.3
3.00	26.26		26.52		0.391	77.7
3.05			26.64		0.401	76.2
3.10			26.76		0.409	74.6
3.15			26.89		0.426	72.6

Table B–13

NGC 4377

$(a'')^{1/4}$	μ_B [mag arcsec^{-2}]		$\epsilon = 1 - b/a$	P.A.
	maj	*min*		[deg]
0.00	17.29	17.29		
0.80	17.35	17.37		
0.85	17.39	17.42		
0.90	17.43	17.49		
0.95	17.51	17.58		
1.00	17.61	17.70	0.129	−10.1
1.05	17.75	17.85	0.127	−9.2
1.10	17.92	18.03	0.128	−8.1
1.15	18.12	18.24	0.125	−10.1
1.20	18.33	18.48	0.124	−12.4
1.25	18.56	18.74	0.134	−13.2
1.30	18.81	19.02	0.139	−14.0
1.35	19.08	19.30	0.148	−15.4
1.40	19.33	19.58	0.159	−16.3
1.45	19.58	19.85	0.174	−18.7
1.50	19.82	20.10	0.186	−19.4
1.55	20.06	20.35	0.197	−19.7
1.60	20.30	20.59	0.204	−19.3
1.65	20.54	20.82	0.198	−18.2
1.70	20.77	21.02	0.180	−15.9
1.75	20.99	21.20	0.160	−12.6
1.80	21.18	21.36	0.143	−9.4
1.85	21.34	21.51	0.129	−7.1
1.90	21.49	21.65	0.131	−6.9
1.95	21.63	21.80	0.136	−6.7
2.00	21.77	21.95	0.142	−5.9
2.05	21.91	22.13	0.143	−5.3
2.10	22.06	22.32	0.150	−2.1
2.15	22.20	22.54	0.168	0.0
2.20	22.34	22.79	0.176	1.2
2.25	22.59	23.08	0.166	1.4
2.30	22.84	23.41	0.153	3.1
2.35	23.12	23.68	0.151	4.0
2.40	23.41	23.95	0.154	2.3
2.45	23.66	24.24	0.164	1.9
2.50	23.86	24.55	0.175	4.0
2.55	24.11	24.88	0.182	4.7
2.60	24.41	25.22	0.175	5.2
2.65	24.81	25.58	0.147	3.3
2.70	25.08	25.95	0.153	2.8
2.75	25.41	26.35	0.150	4.4
2.80	25.84	26.77	0.138	5.0
2.85	26.31	27.22	0.157	4.2
2.90	26.74		0.176	3.2

Table B–14

NGC 4472

$(a'')^{1/4}$	μ_B [mag arcsec^{-2}]		$\epsilon = 1 - b/a$	P.A.
	maj	*min*		[deg]
0.00	17.27	17.27		
0.90	17.31	17.33		
0.95	17.33	17.36		
1.00	17.35	17.38	0.151	175.1
1.05	17.39	17.42	0.144	173.4
1.10	17.45	17.48	0.134	171.6
1.15	17.51	17.54	0.117	169.9
1.20	17.59	17.62	0.099	167.7
1.25	17.68	17.72	0.090	165.6
1.30	17.78	17.82	0.081	162.6
1.35	17.89	17.94	0.074	163.1
1.40	18.01	18.07	0.071	162.7
1.45	18.13	18.21	0.070	162.0
1.50	18.26	18.34	0.071	162.1
1.55	18.40	18.50	0.080	161.3
1.60	18.54	18.66	0.092	160.5
1.65	18.67	18.80	0.096	160.7
1.70	18.80	18.95	0.105	160.7
1.75	18.94	19.11	0.109	160.5
1.80	19.08	19.26	0.118	160.1
1.85	19.21	19.40	0.127	159.9
1.90	19.33	19.56	0.137	159.9
1.95	19.46	19.69	0.149	160.0
2.00	19.59	19.82	0.158	160.0
2.05	19.71	19.96	0.164	159.7
2.10	19.85	20.10	0.168	159.9
2.15	19.98	20.25	0.170	160.1
2.20	20.11	20.40	0.172	160.3
2.25	20.23	20.54	0.174	160.0
2.30	20.38	20.67	0.174	159.7
2.35	20.51	20.81	0.171	159.5
2.40	20.65	20.94	0.167	159.9
2.45	20.78	21.09	0.163	159.5
2.50	20.93	21.23	0.162	159.3
2.55	21.06	21.35	0.162	159.2
2.60	21.18	21.47	0.162	158.9
2.65	21.30	21.59	0.163	158.8
2.70	21.42	21.70	0.164	158.8
2.75	21.53	21.81	0.167	158.1
2.80	21.63	21.93	0.170	157.3
2.85	21.74	22.04	0.173	157.1
2.90	21.84	22.16	0.176	157.2
2.95	21.93	22.27	0.177	157.5
3.00	22.04	22.38	0.182	157.4
3.05	22.15	22.50	0.185	158.1
3.10	22.25	22.61	0.185	158.6
3.15	22.36	22.73	0.182	158.6
3.20	22.47	22.84	0.178	158.5
3.25	22.58	22.97	0.174	158.4
3.30	22.69	23.11	0.170	158.2
3.35	22.80	23.26	0.169	157.9
3.40	22.91	23.39	0.170	157.5
3.45	23.02	23.50	0.174	157.1
3.50	23.13	23.61	0.179	156.7
3.55	23.24	23.73	0.183	156.5

Table B–14 — *continued*

NGC 4472

$(a'')^{1/4}$	μ_B [mag arcsec^{-2}]		$\epsilon = 1 - b/a$	P.A.
	maj	*min*		[deg]
3.60	23.35	23.85	0.187	156.1
3.65	23.46	23.96	0.191	156.2
3.70	23.57	24.07	0.196	156.3
3.75	23.68	24.18	0.204	156.3
3.80	23.79	24.29	0.215	156.6
3.85	23.90	24.40	0.226	156.7
3.90	24.01	24.50	0.232	156.7
3.95	24.11	24.61	0.233	156.7
4.00	24.22	24.72	0.231	156.6
4.05	24.32	24.83	0.237	156.5
4.10	24.43	24.93	0.253	156.4
4.15	24.53	25.03	0.267	156.3
4.20	24.63	25.13	0.278	156.1
4.25	24.73	25.23	0.278	155.9
4.30	24.83	25.33	0.266	155.6
4.35	24.93	25.43	0.252	155.3
4.40	25.02	25.53	0.249	155.0
4.45	25.12	25.63	0.254	154.7
4.50	25.24	25.73	0.258	154.3
4.55	25.36	25.83	0.252	153.9
4.60	25.47	25.92	0.235	153.4
4.65	25.58	26.01	0.219	153.0
4.70	25.68	26.11	0.221	152.4
4.75	25.79	26.21	0.233	151.9
4.80	25.89	26.30	0.240	151.3
4.85	25.98	26.39	0.241	150.7
4.90	26.08	26.48	0.237	150.0
4.95	26.17	26.57	0.235	149.4
5.00	26.26	26.66	0.226	148.6
5.05	26.34	26.73	0.186	147.9
5.10	26.43	26.83	0.154	147.1
5.15	26.51	26.96		
5.20	26.59	27.00		
5.25	26.66			
5.30	26.72			
5.35	26.80			
5.40	26.86			
5.45	26.93			
5.50	26.99			
5.55	27.04			
5.60	27.09			
5.65	27.13			
5.70	27.19			
5.75	27.24			
5.80	27.27			
5.85	27.31			
5.90	27.35			
5.95	27.37			
6.00	27.45			

Table B–15

NGC 4526

$(a'')^{1/4}$	μ_B [mag arcsec^{-2}]				$\epsilon = 1 - b/a$	P.A. [deg]
	*maj*1	*maj*2	*min*1	*min*2		
0.00	17.43	17.43	17.43	17.43		
0.80	17.49	17.45	17.79	17.22		
0.85	17.53	17.48	17.90	17.18		
0.90	17.57	17.51	18.00	17.14		
0.95	17.63	17.56	18.11	17.13		
1.00	17.69	17.62	18.24	17.14	0.263	112.0
1.05	17.76	17.69	18.42	17.20	0.282	112.3
1.10	17.84	17.77	18.63	17.30	0.310	113.1
1.15	17.92	17.86	18.86	17.44	0.342	113.1
1.20	18.00	17.96	19.03	17.61	0.384	113.0
1.25	18.07	18.05	19.11	17.80	0.425	112.9
1.30	18.15	18.13	19.10	18.01	0.461	112.4
1.35	18.23	18.19	19.01	18.22	0.491	112.1
1.40	18.33	18.26	18.91	18.43	0.512	111.6
1.45	18.48	18.39	18.92	18.64	0.520	111.6
1.50	18.65	18.60	19.01	18.83	0.513	111.8
1.55	18.83	18.87	19.13	19.02	0.500	112.1
1.60	18.99	19.14	19.27	19.20	0.482	112.5
1.65	19.14	19.36	19.42	19.37	0.468	113.3
1.70	19.33	19.52	19.54	19.53	0.134	119.3
1.75	19.54	19.65	19.72	19.70	0.149	120.3
1.80	19.72	19.79	19.90	19.87	0.174	119.6
1.85	19.77	19.93	20.05	20.03	0.207	117.5
1.90	19.73	19.97	20.22	20.21	0.240	116.3
1.95	19.71	19.91	20.39	20.38	0.281	115.0
2.00	19.80	19.87	20.57	20.57	0.313	114.4
2.05	19.97		20.75	20.75	0.333	114.2
2.10	20.17		20.95	20.95	0.341	114.3
2.15	20.34		21.15	21.16	0.343	114.9
2.20	20.47		21.36	21.37	0.350	115.6
2.25	20.60		21.59	21.59	0.361	116.6
2.30	20.74		21.83	21.83	0.375	117.4
2.35	20.86		22.06	22.07	0.393	118.1
2.40	20.97		22.30	22.31	0.412	118.7
2.45	21.09		22.54	22.56	0.430	119.1
2.50	21.20		22.78	22.77	0.447	119.2
2.55	21.31		23.03	23.00	0.460	118.9
2.60	21.41		23.27	23.24	0.474	118.2
2.65	21.51		23.49	23.48	0.489	117.7
2.70	21.60		23.68		0.519	116.9
2.75	21.70		23.89		0.539	116.1
2.80	21.79		24.08		0.551	114.7
2.85	21.89		24.27		0.567	113.8
2.90	21.98		24.47		0.587	113.0
2.95	22.07		24.65		0.607	112.4
3.00	22.17		24.82		0.625	112.0
3.05	22.27		24.99		0.641	111.7
3.10	22.37		25.15		0.654	111.5
3.15	22.48		25.31		0.664	111.3
3.20	22.59		25.46		0.670	111.2
3.25	22.71		25.61		0.675	111.2
3.30	22.83		25.75		0.680	111.1
3.35	22.96		25.88		0.685	111.2
3.40	23.09		26.01		0.688	111.3
3.45	23.23		26.14		0.689	111.4

Table B–15 — *continued*

NGC 4526

$(a'')^{1/4}$	μ_B [mag arcsec^{-2}]				$\epsilon = 1 - b/a$	P.A. [deg]
	maj1	*maj2*	*min1*	*min2*		
3.50	23.38		26.26		0.689	111.3
3.55	23.54		26.37		0.688	111.1
3.60	23.71		26.48		0.687	111.3
3.65	23.89				0.687	111.8
3.70	24.08				0.687	111.7
3.75	24.28				0.685	111.5
3.80	24.50				0.676	111.9
3.85	24.72				0.656	111.6
3.90	24.96				0.624	112.0
3.95	25.21				0.591	111.7
4.00	25.49				0.549	111.3
4.05	26.15					
4.10	27.04					
4.15	27.53					
4.20	27.00					

Table B–16

NGC 4570

$(a'')^{1/4}$	μ_B [mag arcsec^{-2}]		$\epsilon = 1 - b/a$	P.A.
	maj	*min*		[deg]
0.00	17.03	17.03		
0.85	17.11	17.14		
0.90	17.15	17.20		
0.95	17.22	17.28		
1.00	17.31	17.38	0.152	167.7
1.05	17.41	17.51	0.163	166.6
1.10	17.53	17.67	0.171	165.4
1.15	17.66	17.85	0.177	164.3
1.20	17.81	18.06	0.190	163.0
1.25	17.96	18.27	0.207	161.5
1.30	18.14	18.50	0.231	160.9
1.35	18.30	18.73	0.251	160.6
1.40	18.47	18.97	0.274	160.2
1.45	18.62	19.22	0.299	159.9
1.50	18.79	19.47	0.318	159.7
1.55	18.98	19.73	0.331	159.5
1.60	19.15	19.99	0.349	159.4
1.65	19.33	20.27	0.370	159.2
1.70	19.49	20.56	0.392	159.2
1.75	19.63	20.85	0.417	159.1
1.80	19.75	21.16	0.444	159.1
1.85	19.85	21.47	0.479	159.0
1.90	19.94	21.78	0.514	159.0
1.95	20.03	22.09	0.545	159.0
2.00	20.14	22.41	0.573	159.1
2.05	20.25	22.70	0.593	159.1
2.10	20.39	23.05	0.609	159.1
2.15	20.52	23.32	0.624	159.2
2.20	20.65	23.61	0.638	159.2
2.25	20.79	23.91	0.653	159.3
2.30	20.92	24.20	0.667	159.4
2.35	21.05	24.50	0.682	159.4
2.40	21.17	24.79	0.695	159.5
2.45	21.30	25.07	0.706	159.6
2.50	21.42	25.36	0.719	159.6
2.55	21.55	25.65	0.727	159.7
2.60	21.69		0.734	159.7
2.65	21.83		0.741	159.8
2.70	21.99		0.746	159.8
2.75	22.15		0.754	159.7
2.80	22.33		0.755	159.7
2.85	22.53		0.756	159.5
2.90	22.74		0.755	159.5
2.95	22.97		0.751	159.5
3.00	23.22		0.748	159.7
3.05	23.50		0.742	159.9
3.10	23.79		0.735	160.3
3.15	24.11		0.727	160.2
3.20	24.47		0.717	159.8
3.25	24.85		0.706	160.0
3.30	25.27		0.693	160.2
3.35	25.71			
3.40	26.19			
3.45	26.71			

Table B–17

NGC 4600

$(a'')^{1/4}$	μ_B [mag arcsec^{-2}]		$\epsilon = 1 - b/a$	P.A.
	maj	*min*		[deg]
0.00	19.70	19.70		
0.80	19.73	19.73		
0.85	19.76	19.75		
0.90	19.80	19.80		
0.95	19.86	19.86		
1.00	19.92	19.94	0.143	6.9
1.05	20.00	20.03	0.138	10.1
1.10	20.08	20.12	0.129	17.0
1.15	20.17	20.22	0.116	23.7
1.20	20.25	20.32	0.109	30.5
1.25	20.34	20.43	0.122	41.7
1.30	20.43	20.54	0.150	50.2
1.35	20.52	20.66	0.190	53.6
1.40	20.60	20.79	0.223	57.1
1.45	20.69	20.92	0.239	58.1
1.50	20.78	21.06	0.273	59.4
1.55	20.87	21.21	0.301	61.3
1.60	20.98	21.36	0.320	62.0
1.65	21.08	21.53	0.341	61.9
1.70	21.20	21.70	0.365	62.8
1.75	21.32	21.88	0.376	63.9
1.80	21.45	22.09	0.394	64.6
1.85	21.59	22.28	0.409	65.7
1.90	21.74	22.49	0.420	66.1
1.95	21.88	22.70	0.426	66.1
2.00	22.03	22.90	0.432	65.6
2.05	22.19	23.10	0.435	64.9
2.10	22.34	23.30	0.435	63.7
2.15	22.50	23.51	0.433	61.2
2.20	22.68	23.72	0.429	60.1
2.25	22.89	23.93	0.416	59.1
2.30	23.14	24.14	0.386	56.5
2.35	23.44	24.35	0.338	55.1
2.40	23.75	24.57	0.274	55.4
2.45	24.11	24.78	0.240	55.3
2.50	24.38	25.00	0.217	52.7
2.55	24.67	25.22	0.191	49.0
2.60	24.95	25.44	0.179	47.1
2.65	25.24	25.67	0.171	49.5
2.70	25.55	25.89	0.166	47.4
2.75	25.90	26.11	0.162	45.6
2.80	26.29		0.160	45.2
2.85	26.75		0.158	46.0
2.90	27.27		0.157	49.3

Table B–18

NGC 4623

$(a'')^{1/4}$	μ_B [mag arcsec^{-2}]		$\epsilon = 1 - b/a$	P.A.
	maj	*min*		[deg]
0.00	18.79	18.79		
0.85	18.88	18.90		
0.90	18.93	18.98		
0.95	18.99	19.08		
1.00	19.06	19.21	0.235	177.8
1.05	19.16	19.35	0.233	177.4
1.10	19.28	19.52	0.240	177.1
1.15	19.42	19.70	0.247	177.0
1.20	19.54	19.89	0.273	176.6
1.25	19.68	20.09	0.304	176.2
1.30	19.81	20.30	0.330	176.0
1.35	19.92	20.51	0.363	176.0
1.40	20.05	20.73	0.398	175.8
1.45	20.17	20.94	0.420	175.8
1.50	20.29	21.16	0.441	176.1
1.55	20.43	21.37	0.460	176.6
1.60	20.56	21.58	0.481	177.1
1.65	20.65	21.81	0.505	177.6
1.70	20.74	22.03	0.537	178.1
1.75	20.83	22.27	0.567	178.2
1.80	20.91	22.51	0.592	178.2
1.85	21.01	22.74	0.613	178.1
1.90	21.12	22.99	0.626	177.9
1.95	21.24	23.23	0.634	177.7
2.00	21.35	23.48	0.641	177.6
2.05	21.48	23.73	0.649	177.4
2.10	21.61	23.98	0.658	177.2
2.15	21.74	24.24	0.667	177.1
2.20	21.88	24.50	0.676	177.0
2.25	22.03	24.76	0.681	176.9
2.30	22.18	25.03	0.685	176.8
2.35	22.35	25.30	0.686	176.7
2.40	22.52	25.58	0.687	176.6
2.45	22.70	25.85	0.688	176.6
2.50	22.88	26.13	0.689	176.5
2.55	23.07	26.41	0.688	176.5
2.60	23.27		0.686	176.5
2.65	23.48		0.682	176.4
2.70	23.70		0.675	176.3
2.75	23.95		0.656	176.2
2.80	24.22		0.645	176.0
2.85	24.50		0.644	175.9
2.90	24.79		0.634	175.8
2.95	25.10		0.602	175.7
3.00	25.40		0.579	175.5
3.05	25.71		0.561	175.1
3.10	26.01		0.553	174.0
3.15	26.31		0.548	172.9

Table B–19

NGC 4636

$(a'')^{1/4}$	μ_B [mag arcsec^{-2}]		$\epsilon = 1 - b/a$	P.A.
	maj	*min*		[deg]
0.00	17.99	17.99		
0.90	18.06	18.08		
0.95	18.10	18.12		
1.00	18.15	18.18	0.035	118.0
1.05	18.23	18.24	0.038	122.8
1.10	18.30	18.31	0.040	126.2
1.15	18.37	18.39	0.045	126.7
1.20	18.46	18.47	0.051	126.3
1.25	18.54	18.57	0.049	126.0
1.30	18.64	18.67	0.040	132.6
1.35	18.76	18.78	0.029	152.8
1.40	18.88	18.90	0.038	162.9
1.45	19.00	19.02	0.040	164.5
1.50	19.14	19.15	0.042	165.0
1.55	19.27	19.29	0.019	166.7
1.60	19.41	19.44	0.023	167.9
1.65	19.55	19.60	0.029	167.0
1.70	19.70	19.75	0.033	162.9
1.75	19.86	19.91	0.030	160.6
1.80	20.02	20.06	0.028	160.6
1.85	20.16	20.22	0.036	158.5
1.90	20.29	20.36	0.044	155.7
1.95	20.43	20.52	0.052	154.2
2.00	20.58	20.68	0.059	155.6
2.05	20.70	20.82	0.069	155.8
2.10	20.84	20.95	0.081	154.5
2.15	20.96	21.09	0.093	152.7
2.20	21.08	21.24	0.100	152.1
2.25	21.20	21.36	0.106	150.1
2.30	21.31	21.50	0.115	148.6
2.35	21.43	21.63	0.121	149.0
2.40	21.56	21.78	0.124	148.7
2.45	21.67	21.91	0.132	147.0
2.50	21.79	22.06	0.143	145.9
2.55	21.90	22.20	0.157	146.5
2.60	22.00	22.33	0.173	146.9
2.65	22.10	22.43	0.188	146.7
2.70	22.20	22.54	0.203	146.2
2.75	22.30	22.64	0.217	146.0
2.80	22.39	22.74	0.222	146.2
2.85	22.48	22.84	0.225	145.9
2.90	22.56	22.95	0.232	146.0
2.95	22.65	23.06	0.238	146.2
3.00	22.75	23.18	0.244	146.3
3.05	22.84	23.30	0.253	146.3
3.10	22.94	23.42	0.261	146.1
3.15	23.03	23.54	0.260	145.5
3.20	23.13	23.67	0.266	145.1
3.25	23.26	23.80	0.277	144.5
3.30	23.37	23.93	0.287	144.3
3.35	23.48	24.07	0.288	144.4
3.40	23.58	24.20	0.268	144.8
3.45	23.69	24.35	0.244	145.6
3.50	23.80	24.49	0.235	146.0
3.55	23.91	24.64	0.232	146.1

Table B–19 — *continued*

NGC 4636

$(a'')^{1/4}$	μ_B [mag arcsec^{-2}]		$\epsilon = 1 - b/a$	P.A.
	maj	*min*		[deg]
3.60	24.02	24.79	0.229	145.9
3.65	24.13	24.94	0.226	145.5
3.70	24.24	25.10	0.244	145.2
3.75	24.35	25.26	0.269	145.3
3.80	24.46	25.43	0.286	145.6
3.85	24.58	25.59	0.303	146.3
3.90	24.69	25.76	0.314	147.1
3.95	24.80	25.93	0.318	148.0
4.00	24.91	26.11	0.316	148.8
4.05	25.02	26.29	0.314	149.3
4.10	25.13		0.315	149.6
4.15	25.24		0.320	149.8
4.20	25.34		0.328	149.8
4.25	25.46		0.339	149.5
4.30	25.56		0.348	148.8
4.35	25.67		0.353	148.7
4.40	25.77			
4.45	25.88			
4.50	25.98			
4.55	26.08			
4.60	26.18			
4.65	26.29			
4.70	26.38			
4.75	26.48			
4.80	26.58			
4.85	26.67			
4.90	26.76			
4.95	26.85			
5.00	26.94			
5.05	27.02			

Table B–20

FCC 019

$(a'')^{1/4}$	μ_B [mag arcsec^{-2}]		$\epsilon = 1 - b/a$	P.A.
	maj	*min*		[deg]
0.00	21.25	21.25		
0.80	21.44	21.49		
0.85	21.52	21.55		
0.90	21.63	21.65		
0.95	21.76	21.77		
1.00	21.87	21.90	0.088	83.9
1.05	21.97	22.04	0.117	75.5
1.10	22.04	22.16	0.179	61.6
1.15	22.08	22.23	0.275	56.2
1.20	22.12	22.33	0.364	55.0
1.25	22.17	22.46	0.421	53.9
1.30	22.20	22.60	0.459	54.3
1.35	22.23	22.73	0.492	56.5
1.40	22.27	22.87	0.528	58.4
1.45	22.33	23.02	0.567	58.4
1.50	22.39	23.16	0.603	57.7
1.55	22.45	23.31	0.628	57.3
1.60	22.48	23.48	0.641	57.4
1.65	22.55	23.68	0.651	57.3
1.70	22.64	23.86	0.654	56.8
1.75	22.72	24.00	0.659	56.6
1.80	22.77	24.21	0.676	57.0
1.85	22.88	24.40	0.675	56.9
1.90	23.08	24.60	0.659	57.0
1.95	23.33	24.84	0.619	58.3
2.00	23.55	25.12	0.591	59.0
2.05	23.80	25.34	0.561	59.6
2.10	24.12	25.62	0.514	60.7
2.15	24.39	25.80	0.490	60.8
2.20	24.63	26.03	0.450	61.8
2.25	24.92	26.26	0.417	60.5
2.30	25.17	26.59	0.404	58.9
2.35	25.45	26.84	0.398	58.3
2.40	25.81	27.06	0.387	57.9
2.45	26.16		0.375	56.3
2.50	26.50		0.369	55.8

Table B–21

FCC 055

$(a'')^{1/4}$	μ_B [mag arcsec^{-2}]		$\epsilon = 1 - b/a$	P.A.
	maj	*min*		[deg]
0.00	19.89	19.89		9999.0
0.80	19.97	19.98		9999.0
0.85	20.00	20.00		9999.0
0.90	20.05	20.05		9999.0
0.95	20.10	20.11		9999.0
1.00	20.15	20.18	0.107	21.2
1.05	20.22	20.28	0.131	25.8
1.10	20.29	20.37	0.151	29.0
1.15	20.36	20.48	0.197	29.7
1.20	20.43	20.60	0.238	30.5
1.25	20.52	20.75	0.266	31.5
1.30	20.60	20.90	0.299	31.6
1.35	20.65	21.04	0.346	31.7
1.40	20.74	21.22	0.387	31.8
1.45	20.78	21.35	0.417	32.1
1.50	20.88	21.52	0.451	32.4
1.55	20.92	21.74	0.489	32.3
1.60	20.98	21.95	0.523	32.0
1.65	21.07	22.17	0.552	31.3
1.70	21.14	22.45	0.582	31.1
1.75	21.21	22.76	0.608	30.9
1.80	21.28	23.02	0.619	30.6
1.85	21.39	23.29	0.625	30.3
1.90	21.51	23.54	0.617	30.2
1.95	21.76	23.80	0.597	31.0
2.00	21.97	24.06	0.591	31.1
2.05	22.23	24.29	0.578	31.3
2.10	22.50	24.56	0.569	31.3
2.15	22.79	24.81	0.563	31.3
2.20	23.10	25.06	0.547	31.5
2.25	23.42	25.28	0.527	31.4
2.30	23.77	25.42	0.510	31.8
2.35	24.10	25.53	0.499	31.8
2.40	24.35	25.98	0.486	31.9
2.45	24.58	26.23	0.469	31.8
2.50	24.94		0.462	32.0
2.55	25.10		0.460	32.5
2.60	25.29		0.464	33.4
2.65	25.56		0.480	33.5
2.70	25.76			
2.75	26.40			
2.80	27.04			

Table B–22

FCC 090

$(a'')^{1/4}$	μ_B [mag arcsec^{-2}]		$\epsilon = 1 - b/a$	P.A.
	maj	*min*		[deg]
0.00	18.86	18.86		
0.80	19.07	19.03		
0.85	19.15	19.11		
0.90	19.29	19.22		
0.95	19.45	19.34		
1.00	19.62	19.47	0.263	109.7
1.05	19.82	19.63	0.311	109.4
1.10	20.03	19.81	0.336	108.7
1.15	20.25	20.01	0.358	108.7
1.20	20.45	20.25	0.389	109.4
1.25	20.64	20.50	0.386	110.2
1.30	20.85	20.77	0.358	111.5
1.35	21.10	21.03	0.315	113.0
1.40	21.36	21.29	0.275	114.7
1.45	21.59	21.60	0.266	115.5
1.50	21.90	21.86	0.251	119.6
1.55	22.11	22.16	0.247	122.3
1.60	22.27	22.45	0.239	126.1
1.65	22.46	22.72	0.232	128.6
1.70	22.67	22.99	0.223	134.0
1.75	22.89	23.29	0.220	137.5
1.80	23.16	23.58	0.197	143.3
1.85	23.41	23.84	0.177	150.1
1.90	23.62	24.10	0.185	154.4
1.95	23.83	24.35	0.190	156.0
2.00	24.03	24.54	0.209	157.7
2.05	24.22	24.85	0.231	159.5
2.10	24.38	25.07	0.255	161.1
2.15	24.52	25.36	0.279	161.6
2.20	24.72	25.65	0.309	162.6
2.25	24.82	25.96	0.351	163.1
2.30	24.80	26.26	0.388	162.8
2.35	25.06	26.53	0.395	163.6
2.40	25.49	26.72	0.388	165.9
2.45	25.70	26.97	0.395	166.6
2.50	25.77	27.37	0.406	165.4
2.55	26.03	27.61	0.418	164.8
2.60	26.22	28.01	0.436	164.8
2.65	26.40		0.437	165.5
2.70	26.61		0.435	165.4
2.75	26.84		0.438	166.4

Table B–23

FCC 119

$(a'')^{1/4}$	μ_B [mag arcsec^{-2}]		$\epsilon = 1 - b/a$	P.A.
	maj	*min*		[deg]
0.00	20.97	20.97		
0.80	21.31	20.99		
0.85	21.36	21.02		
0.90	21.42	21.07		
0.95	21.48	21.14		
1.00	21.53	21.25	0.165	85.1
1.05	21.57	21.39	0.238	79.5
1.10	21.61	21.52	0.258	73.4
1.15	21.66	21.62	0.281	66.2
1.20	21.70	21.72	0.295	58.5
1.25	21.73	21.83	0.353	47.7
1.30	21.84	21.94	0.416	37.2
1.35	22.00	22.06	0.408	31.0
1.40	22.05	22.14	0.333	20.3
1.45	22.20	22.30	0.171	25.4
1.50	22.30	22.53	0.123	38.6
1.55	22.41	22.65	0.133	38.9
1.60	22.59	22.81	0.135	41.8
1.65	22.79	22.98	0.124	42.6
1.70	22.95	23.15	0.129	41.4
1.75	23.13	23.34	0.132	42.1
1.80	23.31	23.52	0.129	44.7
1.85	23.49	23.72	0.137	45.6
1.90	23.66	23.92	0.141	46.6
1.95	23.86	24.10	0.131	46.8
2.00	24.03	24.31	0.132	48.6
2.05	24.19	24.54	0.136	49.4
2.10	24.34	24.75	0.146	46.9
2.15	24.51	24.97	0.128	47.1
2.20	24.80	25.20	0.113	47.8
2.25	25.08	25.32	0.119	52.3
2.30	25.26	25.45	0.116	52.5
2.35	25.51	25.64	0.126	50.6
2.40	25.84	25.99	0.145	48.0
2.45	25.97	26.15	0.187	41.6
2.50	26.21	26.39	0.229	35.5
2.55	26.38	26.61	0.248	34.2
2.60	26.52	26.84	0.209	32.0
2.65	26.68		0.193	30.6
2.70	26.93		0.201	29.1

Table B–24

FCC 136

$(a'')^{1/4}$	μ_B [mag arcsec^{-2}]		$\epsilon = 1 - b/a$	P.A.
	maj	*min*		[deg]
0.00	20.49	20.49		
0.80	20.68	20.71		
0.85	20.74	20.77		
0.90	20.85	20.89		
0.95	20.98	21.03		
1.00	21.11	21.17	0.079	147.4
1.05	21.25	21.30	0.072	149.4
1.10	21.38	21.41	0.061	151.4
1.15	21.50	21.51	0.044	153.3
1.20	21.60	21.61	0.047	161.5
1.25	21.70	21.73	0.094	174.0
1.30	21.80	21.86	0.123	180.4
1.35	21.92	21.99	0.118	180.5
1.40	22.03	22.11	0.105	174.9
1.45	22.15	22.24	0.082	167.1
1.50	22.29	22.42	0.114	169.9
1.55	22.41	22.59	0.136	172.6
1.60	22.54	22.75	0.144	172.4
1.65	22.67	22.91	0.159	171.4
1.70	22.81	23.10	0.180	172.4
1.75	22.95	23.29	0.195	171.9
1.80	23.10	23.46	0.196	172.7
1.85	23.24	23.60	0.208	172.6
1.90	23.40	23.81	0.218	171.8
1.95	23.55	24.00	0.232	171.4
2.00	23.70	24.18	0.236	172.8
2.05	23.88	24.37	0.241	174.4
2.10	24.03	24.57	0.248	174.4
2.15	24.20	24.79	0.262	172.6
2.20	24.44	24.97	0.240	173.0
2.25	24.55	25.14	0.227	172.9
2.30	24.75	25.33	0.209	173.1
2.35	25.04	25.59	0.201	172.1
2.40	25.18	25.74	0.200	175.1
2.45	25.35	25.96	0.196	177.9
2.50	25.66	26.17	0.194	173.8
2.55	25.82	26.38	0.190	170.1
2.60	26.04	26.64	0.179	169.5
2.65	26.25			
2.70	26.40			
2.75	26.60			
2.80	26.81			

Table B–25

FCC 152

$(a'')^{1/4}$	μ_B [mag arcsec^{-2}]		$\epsilon = 1 - b/a$	P.A.
	maj	*min*		[deg]
0.00	20.61	20.61		
0.80	20.57	20.60		
0.85	20.58	20.59		
0.90	20.59	20.59		
0.95	20.60	20.59		
1.00	20.60	20.59		
1.05	20.59	20.59		
1.10	20.60	20.60		
1.15	20.61	20.61		
1.20	20.64	20.68	0.480	79.6
1.25	20.66	20.76	0.495	79.8
1.30	20.70	20.87	0.497	79.9
1.35	20.77	21.07	0.475	79.9
1.40	20.80	21.26	0.422	79.6
1.45	20.99	21.44	0.380	75.8
1.50	21.23	21.63	0.311	71.7
1.55	21.39	21.76	0.280	67.6
1.60	21.50	21.94	0.312	60.0
1.65	21.57	22.11	0.360	54.9
1.70	21.69	22.31	0.372	52.9
1.75	21.77	22.56	0.383	54.3
1.80	21.89	22.77	0.385	55.4
1.85	22.06	23.06	0.391	57.8
1.90	22.16	23.34	0.402	60.1
1.95	22.34	23.60	0.416	60.7
2.00	22.49	23.85	0.423	60.7
2.05	22.75	24.03	0.420	60.3
2.10	23.02	24.25	0.421	59.8
2.15	23.20	24.50	0.423	59.6
2.20	23.41	24.68	0.432	59.4
2.25	23.64	24.87	0.434	59.2
2.30	23.84	25.11	0.438	58.4
2.35	24.04	25.35	0.437	57.7
2.40	24.27	25.55	0.423	57.3
2.45	24.48	25.74	0.421	57.5
2.50	24.70	25.87	0.415	57.0
2.55	24.87	26.01	0.408	57.0
2.60	25.02	26.25	0.415	56.9
2.65	25.31	26.47	0.410	56.0
2.70	25.59	26.62	0.378	55.2
2.75	25.84	26.83	0.362	54.1
2.80	26.14	27.03	0.349	52.8
2.85	26.45		0.325	50.4
2.90	26.74		0.289	48.5
2.95	26.90			
3.00	27.21			

Table B–26

FCC 204

$(a'')^{1/4}$	μ_B [mag arcsec^{-2}]		$\epsilon = 1 - b/a$	P.A.
	maj	*min*		[deg]
0.00	20.50	20.50		
0.80	20.60	20.60		
0.85	20.66	20.66		
0.90	20.73	20.74		
0.95	20.81	20.85		
1.00	20.92	20.99	0.091	20.2
1.05	21.04	21.14	0.114	17.3
1.10	21.17	21.30	0.128	15.8
1.15	21.30	21.46	0.163	16.7
1.20	21.43	21.63	0.198	19.4
1.25	21.56	21.79	0.230	20.0
1.30	21.70	21.94	0.260	21.3
1.35	21.81	22.10	0.286	21.7
1.40	21.91	22.25	0.323	21.9
1.45	22.01	22.42	0.348	22.0
1.50	22.10	22.63	0.390	22.1
1.55	22.19	22.84	0.427	21.4
1.60	22.27	23.06	0.463	20.9
1.65	22.35	23.29	0.498	21.0
1.70	22.43	23.53	0.524	21.3
1.75	22.50	23.77	0.553	22.0
1.80	22.59	24.05	0.575	22.1
1.85	22.68	24.30	0.589	21.8
1.90	22.79	24.59	0.603	22.1
1.95	22.88	24.90	0.616	22.3
2.00	22.98	25.17	0.634	22.9
2.05	23.09	25.44	0.647	23.1
2.10	23.25	25.76	0.651	23.2
2.15	23.48	26.06	0.635	22.7
2.20	23.76	26.36	0.618	21.8
2.25	24.00	26.74	0.592	20.8
2.30	24.28		0.581	20.6
2.35	24.67		0.568	20.3
2.40	25.03		0.550	20.4
2.45	25.30		0.553	21.6
2.50	25.42		0.550	22.7
2.55	25.71		0.537	23.5
2.60	25.84			
2.65	25.94			
2.70	26.19			
2.75	26.48			
2.80	26.65			
2.85	26.87			
2.90	27.23			
2.95	27.40			

Table B–27

FCC 255

$(a'')^{1/4}$	μ_B [mag arcsec^{-2}]		$\epsilon = 1 - b/a$	P.A.
	maj	*min*		[deg]
0.00	19.87	19.87		
0.80	19.90	19.91		
0.85	19.92	19.94		
0.90	19.95	19.97		
0.95	19.99	20.03		
1.00	20.03	20.09	0.190	177.2
1.05	20.07	20.18	0.228	176.6
1.10	20.12	20.27	0.258	175.5
1.15	20.17	20.36	0.294	174.6
1.20	20.22	20.46	0.337	174.0
1.25	20.28	20.60	0.376	173.6
1.30	20.34	20.77	0.405	173.2
1.35	20.40	20.94	0.432	173.2
1.40	20.46	21.14	0.468	173.2
1.45	20.50	21.33	0.513	172.8
1.50	20.54	21.56	0.549	172.2
1.55	20.61	21.76	0.569	171.7
1.60	20.72	22.00	0.585	171.4
1.65	20.83	22.17	0.600	171.3
1.70	20.92	22.40	0.612	171.4
1.75	21.04	22.63	0.624	171.6
1.80	21.16	22.82	0.631	171.6
1.85	21.31	23.03	0.631	171.8
1.90	21.53	23.23	0.623	171.9
1.95	21.73	23.48	0.613	172.0
2.00	21.94	23.72	0.598	172.3
2.05	22.16	23.90	0.578	172.2
2.10	22.35	24.15	0.568	172.0
2.15	22.57	24.37	0.552	172.3
2.20	22.85	24.59	0.534	172.4
2.25	23.12	24.75	0.515	172.2
2.30	23.36	24.97	0.500	172.4
2.35	23.71	25.17	0.466	172.7
2.40	24.04	25.44	0.427	173.0
2.45	24.27	25.73	0.425	173.2
2.50	24.55	25.93	0.379	173.3
2.55	24.81	26.18	0.349	172.8
2.60	25.05	26.44	0.356	172.5
2.65	25.38	26.65	0.349	172.8
2.70	25.67	26.86	0.334	173.7
2.75	25.95	27.03	0.307	174.1
2.80	26.24	27.20	0.255	174.5
2.85	26.54	27.36	0.245	174.8
2.90	26.83	27.56	0.240	175.1
2.95	27.13	27.85	0.238	175.8
3.00	27.43	28.17		

Table B–28

FCC 301

$(a'')^{1/4}$	μ_B [mag arcsec^{-2}]		$\epsilon = 1 - b/a$	P.A.
	maj	*min*		[deg]
0.00	18.99	18.99		
0.80	19.06	19.08		
0.85	19.09	19.12		
0.90	19.12	19.18		
0.95	19.16	19.26		
1.00	19.21	19.37	0.280	152.1
1.05	19.27	19.50	0.328	153.0
1.10	19.33	19.66	0.371	153.4
1.15	19.39	19.84	0.409	153.9
1.20	19.46	20.06	0.444	154.6
1.25	19.56	20.31	0.467	155.1
1.30	19.68	20.58	0.482	155.3
1.35	19.81	20.83	0.490	155.4
1.40	20.00	21.13	0.487	155.3
1.45	20.22	21.41	0.475	155.3
1.50	20.50	21.68	0.459	155.5
1.55	20.79	21.94	0.436	155.6
1.60	21.07	22.18	0.424	155.9
1.65	21.33	22.42	0.417	155.6
1.70	21.58	22.66	0.411	155.4
1.75	21.84	22.85	0.411	155.3
1.80	22.08	23.04	0.416	155.5
1.85	22.30	23.24	0.404	155.0
1.90	22.51	23.40	0.393	155.2
1.95	22.83	23.53	0.368	155.3
2.00	23.06	23.74	0.329	154.7
2.05	23.37	23.95	0.285	153.5
2.10	23.69	24.18	0.212	150.8
2.15	23.92	24.41	0.191	149.8
2.20	24.15	24.61	0.177	150.2
2.25	24.50	24.87	0.138	145.8
2.30	24.73	25.13	0.135	144.7
2.35	24.94	25.35	0.139	146.9
2.40	25.16	25.40	0.140	151.7
2.45	25.39	25.57	0.165	156.7
2.50	25.48	26.05	0.167	159.6
2.55	25.69	26.31	0.173	157.1
2.60	26.02	26.48	0.176	156.2
2.65	26.25	26.63	0.173	158.8
2.70	26.52	26.85	0.164	161.9
2.75	26.70	27.10		
2.80	26.95	27.40		
2.85	27.23			

Table B–29

FCC 324

$(a'')^{1/4}$	μ_B [mag arcsec^{-2}]		$\epsilon = 1 - b/a$	P.A.
	maj	*min*		[deg]
0.00	22.53	22.53		
0.80	22.62	22.57		
0.85	22.62	22.58		
0.90	22.63	22.60		
0.95	22.65	22.62		
1.00	22.67	22.64	0.081	40.3
1.05	22.70	22.67	0.145	40.3
1.10	22.73	22.73	0.207	40.4
1.15	22.76	22.81	0.266	40.4
1.20	22.76	22.89	0.320	40.4
1.25	22.76	22.96	0.371	40.4
1.30	22.79	23.04	0.418	40.2
1.35	22.83	23.14	0.461	39.9
1.40	22.86	23.26	0.499	39.4
1.45	22.89	23.39	0.532	39.1
1.50	22.93	23.52	0.555	38.9
1.55	22.97	23.64	0.570	39.0
1.60	23.03	23.86	0.578	39.3
1.65	23.09	23.99	0.584	39.7
1.70	23.16	24.16	0.586	40.3
1.75	23.24	24.35	0.592	41.2
1.80	23.34	24.54	0.604	41.9
1.85	23.42	24.73	0.606	41.9
1.90	23.53	24.96	0.599	42.4
1.95	23.64	25.12	0.603	42.4
2.00	23.75	25.40	0.604	42.4
2.05	23.88	25.62	0.606	42.2
2.10	24.04	25.82	0.594	42.3
2.15	24.23	26.05	0.589	42.8
2.20	24.41	26.30	0.580	43.5
2.25	24.58	26.55	0.572	43.8
2.30	24.71		0.562	43.2
2.35	24.89		0.547	43.2
2.40	25.14		0.539	43.5
2.45	25.41		0.542	44.5
2.50	25.69		0.538	45.2
2.55	25.94		0.502	44.4
2.60	26.18		0.494	43.9
2.65	26.33		0.480	43.5
2.70	26.53		0.469	43.5
2.75	26.86		0.463	44.0
2.80	27.02			
2.85	27.19			
2.90	27.45			

Table B–30

FCC 335

$(a'')^{1/4}$	μ_B [mag arcsec^{-2}]		$\epsilon = 1 - b/a$	P.A.
	maj	*min*		[deg]
0.00	20.19	20.19		
0.80	20.24	20.20		
0.85	20.29	20.22		
0.90	20.40	20.31		
0.95	20.53	20.41		
1.00	20.69	20.56	0.073	45.2
1.05	20.85	20.74	0.128	44.1
1.10	20.96	20.95	0.188	45.6
1.15	21.00	21.15	0.284	47.3
1.20	21.02	21.30	0.395	48.7
1.25	21.05	21.37	0.493	50.0
1.30	21.07	21.41	0.561	50.9
1.35	21.09	21.47	0.600	51.2
1.40	21.13	21.54	0.616	50.5
1.45	21.20	21.74	0.607	48.2
1.50	21.31	21.93	0.560	43.6
1.55	21.43	22.07	0.500	41.2
1.60	21.58	22.31	0.467	40.8
1.65	21.71	22.53	0.445	41.9
1.70	21.85	22.76	0.428	43.8
1.75	22.01	22.96	0.425	45.4
1.80	22.16	23.22	0.423	46.7
1.85	22.33	23.42	0.426	47.4
1.90	22.52	23.62	0.428	47.9
1.95	22.77	23.87	0.428	47.9
2.00	22.97	24.06	0.412	48.3
2.05	23.22	24.34	0.398	48.5
2.10	23.45	24.57	0.384	48.5
2.15	23.68	24.81	0.372	47.8
2.20	23.93	25.08	0.366	47.8
2.25	24.18	25.34	0.358	47.7
2.30	24.36	25.57	0.367	47.8
2.35	24.50	25.82	0.368	47.3
2.40	24.75	26.03	0.364	46.4
2.45	24.96	26.17	0.354	46.8
2.50	25.18	26.28	0.356	46.2
2.55	25.36	26.41	0.364	45.4
2.60	25.66	26.57	0.362	44.9
2.65	25.96	26.73	0.360	43.5
2.70	26.22	26.90	0.355	41.7
2.75	26.48		0.351	39.9

Table B–31

NGC 1316

$(a'')^{1/4}$	μ_B [mag arcsec^{-2}]				$\epsilon = 1 - b/a$	P.A.
	*maj*1	*maj*2	*min*1	*min*2		[deg]
0.00	16.08	16.08	16.07	16.07		
0.80	16.17	16.14	16.18	16.12		
0.85	16.20	16.17	16.22	16.17		
0.90	16.25	16.23	16.29	16.23		
0.95	16.32	16.30	16.38	16.32		
1.00	16.43	16.39	16.50	16.44	0.108	61.1
1.05	16.58	16.50	16.64	16.61	0.110	60.1
1.10	16.75	16.63	16.81	16.81	0.117	57.4
1.15	16.94	16.78	16.99	17.05	0.132	55.0
1.20	17.12	16.93	17.19	17.32	0.150	51.6
1.25	17.27	17.10	17.39	17.59	0.186	50.0
1.30	17.39	17.26	17.57	17.82	0.212	47.9
1.35	17.51	17.40	17.76	18.02	0.259	46.7
1.40	17.60	17.56	17.95	18.16	0.302	45.8
1.45	17.71	17.71	18.11	18.30	0.351	45.8
1.50	17.80	17.86	18.27	18.47	0.378	45.7
1.55	17.93	18.02	18.45	18.70	0.393	46.4
1.60	18.07	18.17	18.62	19.01	0.393	47.3
1.65	18.25	18.34	18.80	19.33	0.389	49.9
1.70	18.46	18.46	18.96	19.54	0.376	52.8
1.75	18.65	18.58	19.13	19.63	0.373	55.0
1.80	18.76	18.72	19.26	19.78	0.374	56.7
1.85	18.86	18.86	19.39	19.88	0.385	57.3
1.90	19.03	19.03	19.53	19.93	0.405	57.5
1.95	19.14	19.28	19.73	20.02	0.418	58.7
2.00	19.22	19.41	19.98	20.17	0.430	60.0
2.05	19.33	19.51	20.07	20.35	0.431	60.8
2.10	19.49	19.60	20.26	20.36	0.422	62.4
2.15	19.64	19.69	20.35	20.41	0.401	60.6
2.20	19.79	19.83	20.48	20.69	0.391	58.0
2.25	19.92	20.00	20.61	20.92	0.390	56.5
2.30	20.07	20.16	20.74	21.03	0.383	56.0
2.35	20.22	20.30	20.95	21.07	0.381	56.7
2.40	20.34	20.40	21.11	21.03	0.375	57.0
2.45	20.50	20.49	21.19	21.06	0.362	57.4
2.50	20.63	20.58	21.24	21.16	0.356	57.6
2.55	20.74	20.78	21.41	21.27	0.369	57.6
2.60	20.86	20.91	21.62	21.41	0.369	57.4
2.65	21.02	20.99	21.77	21.61	0.346	56.9
2.70	21.18	21.12	21.84	21.71	0.314	57.4
2.75	21.34	21.19	22.03	21.85	0.304	57.5
2.80	21.49	21.40	22.23	22.03	0.301	56.6
2.85	21.64	21.59	22.41	22.22	0.314	55.4
2.90	21.78	21.75	22.51	22.37	0.306	54.3
2.95	21.97	21.90	22.62	22.50	0.288	52.6
3.00	22.02	22.12	22.78	22.65	0.280	51.2
3.05	22.06	22.18	22.90	22.77	0.286	50.9
3.10	22.28	22.29	23.04	22.88	0.292	51.6
3.15	22.39	22.42	23.14	23.01	0.295	51.5
3.20	22.50	22.53	23.18	23.11	0.296	50.4
3.25	22.59	22.65	23.22	23.23	0.311	50.5
3.30	22.68	22.76	23.31	23.38	0.318	50.9
3.35	22.79	22.88	23.41	23.53	0.318	51.3
3.40	22.91	22.97	23.42	23.63	0.316	51.9
3.45	23.06	23.12	23.45	23.72	0.297	51.6

Table B–31 — *continued*

NGC 1316

$(a'')^{1/4}$	μ_B [mag arcsec^{-2}]				$\epsilon = 1 - b/a$	P.A.
	*maj*1	*maj*2	*min*1	*min*2		[deg]
3.50	23.19	23.24	23.50	23.94	0.275	50.7
3.55	23.27	23.33	23.70	24.18	0.274	50.8
3.60	23.36	23.42	23.82	24.36	0.282	50.9
3.65	23.49	23.57	23.95	24.56	0.295	50.8
3.70	23.53	23.69	24.04	24.64	0.288	50.9
3.75	23.53	23.77	24.20	24.80	0.272	51.7
3.80	23.71	23.86	24.40	25.10	0.270	52.6
3.85	24.00	23.97	24.55	25.31	0.266	53.5
3.90	24.18	24.10	24.68	25.38	0.269	53.6
3.95	24.34	24.19	24.82	25.25	0.273	52.8
4.00	24.41	24.35	24.95	25.26	0.291	50.8
4.05	24.64	24.44	25.08	25.46	0.311	47.6
4.10	24.70	24.57	25.32	25.47	0.332	45.2
4.15	24.78	24.51	25.47	25.39	0.357	44.3
4.20	24.89	24.51	25.76	25.30	0.378	43.2
4.25	25.09	24.65	26.00	25.39	0.396	41.6
4.30	25.19	24.76	26.24	25.78	0.412	39.6
4.35	25.25	24.72	26.19	26.01	0.428	38.0
4.40	25.22	24.78	26.23	25.97	0.436	37.3
4.45	25.26	24.87	26.89	26.15	0.433	37.7
4.50	25.43	24.93		26.48	0.432	38.6
4.55	25.59	25.10		26.59	0.433	39.6
4.60	25.76	25.12		26.90	0.424	40.4
4.65	26.19	25.10		27.05	0.421	41.5
4.70	26.60	25.25		27.20	0.396	44.1
4.75	26.55	25.52			0.370	46.2
4.80	26.42	25.82			0.339	50.7
4.85	26.59	25.98				
4.90	26.59	26.24				
4.95	26.68	26.19				
5.00	26.81	26.41				
5.05		26.80				

Table B–32

NGC 1336

$(a'')^{1/4}$	μ_B [mag arcsec^{-2}]		$\epsilon = 1 - b/a$	P.A.
	maj	*min*		[deg]
0.00	18.35	18.35		
0.80	18.45	18.46		
0.85	18.51	18.52		
0.90	18.60	18.61		
0.95	18.73	18.73		
1.00	18.91	18.89	0.052	−31.4
1.05	19.13	19.09	0.050	−35.8
1.10	19.36	19.32	0.052	−38.2
1.15	19.59	19.57	0.042	−40.7
1.20	19.83	19.81	0.031	−42.8
1.25	20.06	20.05	0.022	−40.6
1.30	20.27	20.27	0.013	−31.3
1.35	20.46	20.49	0.024	3.5
1.40	20.64	20.71	0.052	12.7
1.45	20.79	20.92	0.067	16.5
1.50	21.00	21.13	0.082	19.2
1.55	21.15	21.32	0.102	20.7
1.60	21.32	21.49	0.107	20.3
1.65	21.51	21.70	0.104	19.3
1.70	21.69	21.85	0.102	18.6
1.75	21.85	22.01	0.101	19.8
1.80	22.03	22.23	0.106	22.3
1.85	22.19	22.42	0.097	23.0
1.90	22.35	22.59	0.095	23.2
1.95	22.50	22.77	0.118	23.7
2.00	22.62	22.96	0.157	24.5
2.05	22.77	23.10	0.173	23.9
2.10	22.93	23.34	0.172	22.4
2.15	23.09	23.48	0.179	20.7
2.20	23.23	23.67	0.203	19.2
2.25	23.36	23.90	0.225	20.0
2.30	23.48	24.08	0.243	20.5
2.35	23.62	24.27	0.256	20.6
2.40	23.75	24.48	0.268	20.6
2.45	23.93	24.69	0.278	20.3
2.50	24.08	24.90	0.291	20.1
2.55	24.24	25.11	0.301	20.1
2.60	24.43	25.33	0.304	20.0
2.65	24.54	25.54	0.316	19.4
2.70	24.80	25.76	0.316	20.0
2.75	24.93	25.98	0.313	20.3
2.80	25.02	26.20	0.326	20.1
2.85	25.18	26.43	0.338	19.9
2.90	25.33	26.65	0.348	19.7
2.95	25.49	26.88	0.362	19.7
3.00	25.68	27.11	0.352	18.7
3.05	25.81	27.33	0.342	18.6
3.10	25.95	27.57	0.337	20.0
3.15	26.23		0.337	21.7
3.20	26.42		0.348	21.8
3.25	26.67		0.340	22.1
3.30	26.95		0.340	21.3
3.35	27.22		0.335	21.6
3.40	27.38			
3.45	27.63			

Table B–33

NGC 1339

$(a'')^{1/4}$	μ_B [mag arcsec^{-2}]		$\epsilon = 1 - b/a$	P.A.
	maj	*min*		[deg]
0.00	17.65	17.65		
0.80	17.69	17.72		
0.85	17.73	17.74		
0.90	17.77	17.79		
0.95	17.82	17.86		
1.00	17.90	17.95	0.103	168.2
1.05	18.01	18.07	0.094	167.9
1.10	18.14	18.23	0.100	168.4
1.15	18.29	18.41	0.100	168.9
1.20	18.47	18.62	0.108	170.5
1.25	18.68	18.86	0.113	171.2
1.30	18.90	19.09	0.122	171.9
1.35	19.11	19.34	0.130	172.6
1.40	19.34	19.60	0.141	173.5
1.45	19.55	19.85	0.152	173.8
1.50	19.77	20.09	0.168	174.3
1.55	19.97	20.31	0.183	174.4
1.60	20.15	20.53	0.201	175.0
1.65	20.34	20.74	0.213	175.6
1.70	20.49	20.95	0.228	175.9
1.75	20.66	21.16	0.238	175.9
1.80	20.82	21.39	0.258	175.8
1.85	20.97	21.63	0.274	175.1
1.90	21.14	21.84	0.286	174.6
1.95	21.33	22.04	0.293	174.4
2.00	21.52	22.23	0.296	175.0
2.05	21.70	22.43	0.301	174.8
2.10	21.91	22.62	0.298	174.7
2.15	22.13	22.92	0.292	174.8
2.20	22.32	23.08	0.294	175.0
2.25	22.51	23.32	0.303	175.4
2.30	22.73	23.55	0.305	174.7
2.35	22.93	23.81	0.305	174.9
2.40	23.15	24.10	0.304	174.4
2.45	23.33	24.32	0.300	174.2
2.50	23.50	24.59	0.291	174.3
2.55	23.83	24.80	0.284	174.5
2.60	24.10	25.20	0.278	175.2
2.65	24.34	25.45	0.264	174.6
2.70	24.56	25.71	0.257	174.7
2.75	24.86	26.01	0.246	174.7
2.80	25.13	26.38	0.246	175.4
2.85	25.34	26.75	0.259	176.6
2.90	25.69	27.15	0.265	177.0
2.95	25.97		0.260	177.0
3.00	26.34		0.248	177.2
3.05	26.70		0.240	177.7

Table B–34

NGC 1351

$(a'')^{1/4}$	μ_B [mag arcsec^{-2}]		$\epsilon = 1 - b/a$	P.A.
	maj	*min*		[deg]
0.00	17.97	17.97		
0.80	18.01	18.03		
0.85	18.03	18.05		
0.90	18.07	18.10		
0.95	18.11	18.15		
1.00	18.16	18.23	0.147	140.6
1.05	18.24	18.33	0.151	141.1
1.10	18.34	18.46	0.157	141.7
1.15	18.46	18.62	0.160	141.8
1.20	18.61	18.81	0.165	141.7
1.25	18.77	19.02	0.172	141.8
1.30	18.94	19.25	0.185	141.7
1.35	19.13	19.48	0.199	141.7
1.40	19.33	19.74	0.215	141.9
1.45	19.51	19.98	0.230	141.4
1.50	19.69	20.22	0.252	141.3
1.55	19.89	20.46	0.272	141.4
1.60	20.08	20.69	0.290	141.4
1.65	20.25	20.89	0.306	141.2
1.70	20.41	21.13	0.324	141.3
1.75	20.61	21.33	0.336	141.5
1.80	20.77	21.53	0.342	141.8
1.85	20.94	21.73	0.356	141.9
1.90	21.13	21.91	0.361	142.0
1.95	21.31	22.08	0.358	141.3
2.00	21.48	22.29	0.359	141.0
2.05	21.64	22.48	0.365	140.6
2.10	21.85	22.67	0.356	140.7
2.15	22.03	22.85	0.353	140.5
2.20	22.22	23.02	0.349	140.5
2.25	22.40	23.24	0.343	140.8
2.30	22.58	23.43	0.338	140.9
2.35	22.74	23.65	0.337	140.6
2.40	22.88	23.84	0.337	140.3
2.45	23.04	24.05	0.340	140.5
2.50	23.23	24.26	0.349	140.7
2.55	23.37	24.39	0.354	140.7
2.60	23.51	24.58	0.366	140.7
2.65	23.66	24.75	0.370	140.2
2.70	23.79	24.95	0.376	140.1
2.75	23.91	25.09	0.383	140.1
2.80	24.09	25.28	0.389	140.1
2.85	24.25	25.44	0.391	140.1
2.90	24.40	25.59	0.401	138.6
2.95	24.54	25.67	0.405	137.4
3.00	24.71	25.79	0.405	137.2
3.05	24.88	25.96	0.402	136.8
3.10	25.07	26.13	0.396	136.6
3.15	25.38	26.35	0.382	136.5
3.20	25.55	26.64	0.361	135.7
3.25	25.67	26.90	0.352	135.5
3.30	25.77	27.11	0.354	135.6
3.35	25.79	27.30	0.350	135.8
3.40	25.83	27.43	0.334	136.3
3.45	26.26	27.55	0.318	136.4

Table B–34 — *continued*

NGC 1351

$(a'')^{1/4}$	μ_B [mag arcsec^{-2}]		$\epsilon = 1 - b/a$	P.A.
	maj	*min*		[deg]
3.50	26.76	27.70		
3.55	27.11	27.88		
3.60	27.25	28.05		
3.65	27.45	28.31		
3.70	27.63			
3.75	27.82			
3.80	28.02			
3.85	28.23			
3.90	28.47			

Table B–35

NGC 1373

$(a'')^{1/4}$	μ_B [mag arcsec^{-2}]		$\epsilon = 1 - b/a$	P.A.
	maj	*min*		[deg]
0.00	18.44	18.44		
0.80	18.51	18.53		
0.85	18.55	18.59		
0.90	18.63	18.69		
0.95	18.73	18.81		
1.00	18.86	18.96	0.124	120.9
1.05	19.02	19.15	0.125	119.4
1.10	19.20	19.36	0.126	118.1
1.15	19.41	19.59	0.133	116.7
1.20	19.62	19.84	0.144	115.7
1.25	19.85	20.11	0.151	115.2
1.30	20.08	20.37	0.164	113.9
1.35	20.31	20.62	0.171	113.6
1.40	20.53	20.88	0.181	114.0
1.45	20.77	21.11	0.195	117.0
1.50	20.99	21.43	0.197	117.7
1.55	21.21	21.68	0.214	119.1
1.60	21.40	21.91	0.227	121.4
1.65	21.58	22.11	0.243	122.5
1.70	21.78	22.36	0.251	123.1
1.75	22.01	22.59	0.256	124.5
1.80	22.26	22.84	0.236	124.9
1.85	22.50	23.02	0.227	125.1
1.90	22.78	23.20	0.210	125.1
1.95	23.02	23.40	0.182	124.2
2.00	23.21	23.64	0.153	123.4
2.05	23.44	23.90	0.147	124.4
2.10	23.66	24.13	0.113	125.4
2.15	23.96	24.38	0.093	122.9
2.20	24.24	24.66	0.076	122.5
2.25	24.54	24.91	0.060	128.4
2.30	24.78	25.12	0.048	130.6
2.35	25.03	25.31	0.041	133.2
2.40	25.28	25.55	0.035	138.8
2.45	25.60	25.76	0.022	142.3
2.50	25.85	26.04	0.017	145.7
2.55	26.08	26.30	0.033	149.2
2.60	26.32	26.58	0.044	153.2
2.65	26.58	26.85	0.067	157.9
2.70	26.85	27.13	0.073	163.4
2.75	27.13	27.41	0.114	169.3
2.80	27.42			
2.85	27.77			

Table B–36

NGC 1374

$(a'')^{1/4}$	μ_B [mag arcsec^{-2}]		$\epsilon = 1 - b/a$	P.A.
	maj	*min*		[deg]
0.00	17.18	17.18		
0.80	17.26	17.26		
0.85	17.30	17.32		
0.90	17.37	17.41		
0.95	17.46	17.52		
1.00	17.58	17.66	0.109	110.0
1.05	17.73	17.83	0.106	111.1
1.10	17.92	18.03	0.096	113.7
1.15	18.13	18.24	0.095	114.2
1.20	18.34	18.46	0.089	115.7
1.25	18.56	18.69	0.091	115.7
1.30	18.77	18.92	0.093	115.8
1.35	18.98	19.13	0.093	116.4
1.40	19.18	19.34	0.095	117.9
1.45	19.38	19.53	0.096	118.4
1.50	19.58	19.72	0.096	118.8
1.55	19.77	19.94	0.098	119.5
1.60	19.97	20.11	0.101	119.2
1.65	20.14	20.30	0.100	119.3
1.70	20.32	20.46	0.103	120.0
1.75	20.47	20.64	0.103	119.3
1.80	20.63	20.79	0.113	119.0
1.85	20.77	20.96	0.111	118.4
1.90	20.95	21.14	0.108	119.1
1.95	21.13	21.32	0.118	120.6
2.00	21.30	21.49	0.115	120.7
2.05	21.50	21.67	0.102	120.6
2.10	21.69	21.86	0.095	121.4
2.15	21.88	22.07	0.092	121.4
2.20	22.01	22.24	0.100	119.3
2.25	22.23	22.42	0.094	117.6
2.30	22.40	22.60	0.089	117.3
2.35	22.59	22.77	0.092	118.3
2.40	22.76	22.98	0.094	117.8
2.45	22.93	23.18	0.095	117.7
2.50	23.10	23.38	0.091	116.5
2.55	23.29	23.56	0.091	117.6
2.60	23.49	23.73	0.096	118.4
2.65	23.62	23.96	0.097	116.6
2.70	23.89	24.13	0.089	118.0
2.75	24.10	24.31	0.079	120.5
2.80	24.28	24.48	0.072	121.2
2.85	24.46	24.66	0.065	121.4
2.90	24.65	24.86	0.058	121.8
2.95	24.84	25.06	0.051	125.5
3.00	25.07	25.26	0.047	129.5
3.05	25.30	25.46	0.058	127.8
3.10	25.54	25.65	0.065	125.9
3.15	25.69	25.84	0.067	123.8
3.20	25.93	25.97	0.063	120.7
3.25	26.08	26.12		
3.30	26.30	26.28		
3.35	26.53	26.45		
3.40	26.71	26.61		
3.45	26.84	26.76		

Table B–36 — *continued*

NGC 1374

$(a'')^{1/4}$	μ_B [mag arcsec^{-2}]		$\epsilon = 1 - b/a$	P.A.
	maj	*min*		[deg]
3.50	26.99	26.89		
3.55	27.23	27.04		
3.60	27.40	27.21		
3.65	27.58	27.39		
3.70	27.85	27.56		

Table B–37

NGC 1375

$(a'')^{1/4}$	μ_B [mag arcsec^{-2}]		$\epsilon = 1 - b/a$	P.A.
	maj	*min*		[deg]
0.00	17.87	17.87		
0.80	18.00	17.98		
0.85	18.06	18.05		
0.90	18.17	18.15		
0.95	18.30	18.28		
1.00	18.46	18.46	0.038	67.8
1.05	18.66	18.69	0.050	76.2
1.10	18.87	18.96	0.085	83.3
1.15	19.08	19.25	0.108	84.5
1.20	19.29	19.56	0.149	86.1
1.25	19.48	19.86	0.196	87.4
1.30	19.65	20.13	0.234	87.8
1.35	19.84	20.38	0.275	88.1
1.40	20.01	20.62	0.305	88.0
1.45	20.17	20.85	0.339	88.1
1.50	20.32	21.09	0.370	88.1
1.55	20.48	21.28	0.393	88.1
1.60	20.64	21.46	0.410	88.1
1.65	20.78	21.66	0.425	88.4
1.70	20.93	21.88	0.439	88.5
1.75	21.06	22.09	0.459	88.5
1.80	21.19	22.34	0.475	88.7
1.85	21.27	22.64	0.500	89.1
1.90	21.34	22.87	0.524	89.7
1.95	21.40	23.16	0.551	90.2
2.00	21.46	23.40	0.576	90.4
2.05	21.56	23.64	0.590	90.5
2.10	21.68	23.90	0.602	90.1
2.15	21.81	24.17	0.611	90.0
2.20	22.02	24.43	0.611	90.1
2.25	22.27	24.67	0.605	90.3
2.30	22.49	24.92	0.604	90.4
2.35	22.74	25.19	0.602	90.6
2.40	22.98	25.42	0.602	90.7
2.45	23.19	25.59	0.599	90.6
2.50	23.47	25.76	0.585	90.6
2.55	23.76	25.97	0.572	90.8
2.60	24.00	26.18	0.567	90.7
2.65	24.21	26.39	0.565	90.5
2.70	24.39	26.62	0.566	90.2
2.75	24.64	26.88	0.566	90.1
2.80	24.92	27.15	0.565	90.0
2.85	25.23	27.41	0.545	88.9
2.90	25.51	27.61	0.501	88.1
2.95	25.78		0.487	87.7
3.00	26.05		0.444	87.1
3.05	26.27		0.431	87.3
3.10	26.34		0.419	87.6
3.15	26.40		0.413	88.5
3.20	26.53		0.409	88.4
3.25	27.07		0.405	89.0

Table B–38

NGC 1379

$(a'')^{1/4}$	μ_B [mag arcsec^{-2}]		$\epsilon = 1 - b/a$	P.A.
	maj	*min*		[deg]
0.00	17.54	17.54		
0.80	17.66	17.66		
0.85	17.70	17.71		
0.90	17.77	17.80		
0.95	17.86	17.91		
1.00	17.99	18.05	0.072	15.6
1.05	18.16	18.22	0.062	14.8
1.10	18.36	18.41	0.046	15.5
1.15	18.56	18.61	0.047	15.5
1.20	18.77	18.81	0.036	16.8
1.25	18.97	19.00	0.029	17.4
1.30	19.16	19.18	0.020	18.1
1.35	19.32	19.35	0.017	15.5
1.40	19.49	19.49	0.017	12.5
1.45	19.64	19.65	0.016	2.1
1.50	19.79	19.83	0.018	−1.3
1.55	19.93	19.96	0.023	−2.2
1.60	20.07	20.09	0.022	−3.2
1.65	20.20	20.22	0.017	−5.2
1.70	20.35	20.37	0.018	−7.4
1.75	20.51	20.51	0.022	−9.1
1.80	20.63	20.65	0.020	−7.6
1.85	20.80	20.82	0.019	−7.2
1.90	20.96	20.99	0.020	−4.3
1.95	21.13	21.16	0.023	1.2
2.00	21.28	21.31	0.023	4.1
2.05	21.44	21.46	0.019	5.2
2.10	21.63	21.69	0.023	5.7
2.15	21.82	21.85	0.021	6.7
2.20	21.98	22.02	0.025	3.5
2.25	22.18	22.19	0.029	1.4
2.30	22.37	22.40	0.020	−2.2
2.35	22.58	22.58	0.017	1.5
2.40	22.71	22.77	0.027	9.0
2.45	22.89	22.94	0.030	11.4
2.50	23.07	23.15	0.034	11.9
2.55	23.28	23.37	0.034	14.0
2.60	23.49	23.54	0.045	21.0
2.65	23.73	23.70	0.034	28.4
2.70	23.91	23.86	0.033	34.0
2.75	24.09	24.09	0.027	36.0
2.80	24.30	24.28	0.028	36.9
2.85	24.49	24.48	0.024	41.9
2.90	24.78	24.82	0.026	47.9
2.95	25.01	25.04	0.021	49.0
3.00	25.26	25.23	0.019	52.4
3.05	25.50	25.44	0.019	56.2
3.10	25.76	25.71	0.022	59.3
3.15	26.04	25.95	0.034	61.3
3.20	26.25	26.13	0.047	62.8
3.25	26.55	26.32	0.065	65.4
3.30	26.87	26.58	0.075	68.8
3.35	27.14	26.83	0.081	71.3
3.40	27.49	27.13	0.094	72.4

Table B–39

NGC 1380

$(a'')^{1/4}$	μ_B [mag arcsec^{-2}]		$\epsilon = 1 - b/a$	P.A.
	maj	*min*		[deg]
0.00	17.74	17.74		
0.80	17.76	17.65		
0.85	17.78	17.64		
0.90	17.81	17.64		
0.95	17.84	17.64		
1.00	17.89	17.66	0.161	4.5
1.05	17.95	17.70	0.171	5.4
1.10	18.03	17.77	0.176	5.3
1.15	18.12	17.86	0.169	4.8
1.20	18.22	17.99	0.166	4.6
1.25	18.33	18.14	0.100	2.5
1.30	18.43	18.31	0.034	1.8
1.35	18.53	18.50	0.032	1.2
1.40	18.63	18.66	0.038	1.1
1.45	18.70	18.79	0.091	1.5
1.50	18.77	18.97	0.156	4.3
1.55	18.85	19.14	0.207	6.4
1.60	18.97	19.32	0.235	6.9
1.65	19.10	19.50	0.247	6.7
1.70	19.26	19.69	0.254	6.9
1.75	19.42	19.88	0.260	6.9
1.80	19.57	20.07	0.269	6.8
1.85	19.72	20.25	0.276	6.8
1.90	19.86	20.45	0.290	6.8
1.95	19.99	20.63	0.304	6.8
2.00	20.13	20.81	0.322	6.7
2.05	20.26	21.01	0.341	6.7
2.10	20.38	21.19	0.347	6.7
2.15	20.52	21.40	0.360	6.7
2.20	20.67	21.60	0.369	6.8
2.25	20.78	21.80	0.383	6.7
2.30	20.88	21.99	0.393	6.6
2.35	21.05	22.18	0.402	6.3
2.40	21.19	22.37	0.413	6.1
2.45	21.33	22.53	0.425	6.2
2.50	21.46	22.73	0.439	6.0
2.55	21.58	22.93	0.453	5.6
2.60	21.72	23.08	0.468	5.6
2.65	21.85	23.26	0.479	5.3
2.70	21.97	23.42	0.494	5.0
2.75	22.03	23.61	0.515	4.9
2.80	22.10	23.75	0.544	5.2
2.85	22.13	23.94	0.564	5.5
2.90	22.16	24.10	0.570	6.1
2.95	22.27	24.28	0.564	6.8
3.00	22.56	24.46	0.547	7.4
3.05	22.82	24.58	0.521	7.5
3.10	23.03	24.80	0.493	6.8
3.15	23.31	25.03	0.461	6.0
3.20	23.68	25.24	0.424	5.2
3.25	23.97	25.44	0.375	3.4
3.30	24.29	25.59	0.349	2.4
3.35	24.56	25.79	0.325	1.9
3.40	24.82	26.00	0.303	1.7
3.45	25.08	26.17	0.294	2.0

Table B–39 — *continued*

NGC 1380

$(a'')^{1/4}$	μ_B [mag arcsec^{-2}]		$\epsilon = 1 - b/a$	P.A.
	maj	*min*		[deg]
3.50	25.32	26.44	0.300	2.8
3.55	25.39	26.56	0.313	3.0
3.60	25.51	26.77	0.316	2.2
3.65	25.77	26.90	0.321	0.4
3.70	26.02	27.03	0.330	−0.9
3.75	26.20	27.20	0.335	−0.8
3.80	26.32		0.344	−0.6
3.85	26.39		0.367	−0.7
3.90	26.43		0.389	−1.1
3.95	26.50		0.402	−2.5
4.00	26.62			

Table B–40

NGC 1380A

$(a'')^{1/4}$	μ_B [mag arcsec^{-2}]		$\epsilon = 1 - b/a$	P.A.
	maj	*min*		[deg]
0.00	18.90	18.90		
0.80	18.98	18.98		
0.85	19.02	19.04		
0.90	19.09	19.13		
0.95	19.18	19.23		
1.00	19.29	19.37	0.109	165.5
1.05	19.43	19.53	0.119	167.4
1.10	19.58	19.72	0.124	168.6
1.15	19.75	19.92	0.130	170.5
1.20	19.92	20.15	0.154	172.9
1.25	20.08	20.36	0.182	174.6
1.30	20.22	20.57	0.223	176.2
1.35	20.36	20.81	0.265	176.7
1.40	20.48	21.02	0.314	176.3
1.45	20.58	21.23	0.361	176.4
1.50	20.68	21.45	0.404	176.6
1.55	20.77	21.67	0.449	176.8
1.60	20.83	21.90	0.490	176.8
1.65	20.90	22.08	0.527	176.5
1.70	20.97	22.31	0.560	176.3
1.75	21.04	22.55	0.593	176.4
1.80	21.10	22.79	0.626	176.3
1.85	21.13	23.07	0.659	176.2
1.90	21.18	23.32	0.694	176.2
1.95	21.17	23.54	0.730	176.4
2.00	21.17	23.82	0.763	176.6
2.05	21.22	24.17	0.792	176.8
2.10	21.19	24.44	0.812	176.8
2.15	21.19	24.70	0.825	176.9
2.20	21.24	24.88	0.831	177.0
2.25	21.35	25.05	0.829	177.0
2.30	21.46	25.24	0.819	177.0
2.35	21.63	25.51	0.800	176.9
2.40	21.93	25.82	0.772	177.0
2.45	22.36	26.01	0.754	177.1
2.50	22.64	26.24	0.739	177.1
2.55	22.91	26.48	0.734	177.1
2.60	23.06	26.73	0.734	177.2
2.65	23.28	26.97	0.732	177.3
2.70	23.53	27.24	0.726	177.3
2.75	23.82	27.64	0.708	177.1
2.80	24.13		0.690	177.2
2.85	24.53		0.660	177.4
2.90	25.18		0.627	177.0
2.95	25.56		0.584	176.8
3.00	25.90		0.558	176.7
3.05	26.24		0.539	177.0
3.10	26.51		0.525	178.1
3.15	26.79			
3.20	27.17			
3.25	27.49			
3.30	27.98			
3.35	28.35			

Table B–41

NGC 1381

$(a'')^{1/4}$	μ_B [mag arcsec^{-2}]		$\epsilon = 1 - b/a$	P.A.
	maj	*min*		[deg]
0.00	17.59	17.59		
0.80	17.63	17.65		
0.85	17.66	17.68		
0.90	17.70	17.73		
0.95	17.75	17.79		
1.00	17.81	17.87	0.142	136.8
1.05	17.89	17.98	0.139	137.1
1.10	18.00	18.11	0.143	137.5
1.15	18.12	18.27	0.150	137.5
1.20	18.27	18.46	0.158	137.5
1.25	18.43	18.66	0.169	137.6
1.30	18.60	18.88	0.182	137.6
1.35	18.77	19.12	0.197	137.7
1.40	18.95	19.37	0.213	138.0
1.45	19.14	19.62	0.232	138.4
1.50	19.32	19.89	0.252	138.8
1.55	19.50	20.17	0.276	138.9
1.60	19.66	20.45	0.304	138.8
1.65	19.82	20.72	0.332	138.8
1.70	19.95	20.99	0.364	138.9
1.75	20.08	21.30	0.396	139.1
1.80	20.21	21.60	0.428	139.3
1.85	20.32	21.90	0.460	139.4
1.90	20.42	22.26	0.489	139.4
1.95	20.54	22.63	0.516	139.4
2.00	20.64	22.95	0.544	139.4
2.05	20.74	23.29	0.574	139.3
2.10	20.82	23.61	0.603	139.2
2.15	20.89	23.86	0.633	139.2
2.20	20.97	24.11	0.660	139.1
2.25	21.04	24.40	0.683	139.0
2.30	21.13	24.66	0.703	138.9
2.35	21.22	24.94	0.721	138.9
2.40	21.32	25.17	0.734	138.9
2.45	21.44	25.42	0.745	138.8
2.50	21.56	25.67	0.753	138.8
2.55	21.73	25.84	0.756	138.8
2.60	21.97	26.01	0.755	138.7
2.65	22.36	26.18	0.750	138.7
2.70	22.72	26.45	0.742	138.6
2.75	23.12	26.70	0.731	138.6
2.80	23.46		0.722	138.7
2.85	23.81		0.708	138.7
2.90	24.16		0.686	138.8
2.95	24.56		0.658	138.8
3.00	24.94		0.633	138.7
3.05	25.22		0.597	138.7
3.10	25.60			
3.15	26.19			
3.20	26.66			
3.25	27.14			
3.30	27.47			
3.35	27.90			
3.40	28.40			

Table B–42

NGC 1396

$(a'')^{1/4}$	μ_B [mag arcsec^{-2}]		$\epsilon = 1 - b/a$	P.A.
	maj	*min*		[deg]
0.00	20.55	20.55		
0.80	20.72	20.75		
0.85	20.78	20.82		
0.90	20.89	20.94		
0.95	21.01	21.07		
1.00	21.13	21.18	0.075	101.8
1.05	21.25	21.29	0.081	102.9
1.10	21.35	21.39	0.100	100.6
1.15	21.42	21.50	0.134	95.9
1.20	21.49	21.60	0.182	92.2
1.25	21.56	21.72	0.215	91.3
1.30	21.65	21.87	0.226	91.8
1.35	21.75	22.03	0.233	92.2
1.40	21.84	22.19	0.269	92.1
1.45	21.92	22.39	0.301	91.4
1.50	22.07	22.61	0.310	90.7
1.55	22.21	22.78	0.327	90.2
1.60	22.35	22.98	0.343	90.7
1.65	22.50	23.17	0.356	91.1
1.70	22.65	23.39	0.365	90.6
1.75	22.81	23.62	0.369	90.6
1.80	22.99	23.85	0.369	90.5
1.85	23.16	24.05	0.371	90.7
1.90	23.34	24.24	0.376	90.8
1.95	23.52	24.35	0.379	91.1
2.00	23.69	24.53	0.387	90.9
2.05	23.89	24.72	0.392	90.7
2.10	24.06	24.86	0.392	89.9
2.15	24.35	25.01	0.386	89.3
2.20	24.55	25.19	0.381	89.0
2.25	24.72	25.32	0.382	90.0
2.30	24.88	25.52	0.391	88.7
2.35	25.13	25.71	0.388	87.7
2.40	25.29		0.371	88.6
2.45	25.44		0.360	89.9
2.50	25.56			
2.55	25.67			
2.60	25.83			
2.65	26.04			
2.70	26.18			
2.75	26.33			
2.80	26.47			
2.85	26.65			
2.90	26.85			

Table B–43

NGC 1399

$(a'')^{1/4}$	μ_B [mag arcsec^{-2}]		$\epsilon = 1 - b/a$	P.A.
	maj	*min*		[deg]
0.00	17.40	17.40		
0.80	17.42	17.41		
0.85	17.43	17.43		
0.90	17.45	17.45		
0.95	17.47	17.47		
1.00	17.50	17.51	0.064	125.3
1.05	17.54	17.56	0.065	121.5
1.10	17.60	17.62	0.065	117.0
1.15	17.67	17.70	0.066	112.4
1.20	17.75	17.79	0.073	111.3
1.25	17.85	17.91	0.080	112.2
1.30	17.97	18.04	0.087	112.3
1.35	18.09	18.19	0.093	111.4
1.40	18.23	18.34	0.100	111.6
1.45	18.38	18.51	0.105	111.9
1.50	18.54	18.68	0.107	111.5
1.55	18.70	18.86	0.113	111.8
1.60	18.86	19.04	0.120	111.9
1.65	19.04	19.22	0.121	111.9
1.70	19.22	19.40	0.123	111.8
1.75	19.39	19.59	0.125	111.4
1.80	19.56	19.77	0.126	111.6
1.85	19.72	19.94	0.130	111.2
1.90	19.90	20.11	0.129	111.4
1.95	20.09	20.29	0.128	110.8
2.00	20.27	20.44	0.121	110.6
2.05	20.45	20.59	0.118	110.6
2.10	20.63	20.78	0.105	111.5
2.15	20.80	20.99	0.108	110.9
2.20	20.95	21.16	0.109	110.3
2.25	21.13	21.33	0.109	108.5
2.30	21.29	21.48	0.113	107.9
2.35	21.42	21.64	0.111	108.7
2.40	21.44	21.78	0.112	108.5
2.45	21.62	21.93	0.110	108.3
2.50	21.81	22.05	0.106	108.2
2.55	22.03	22.17	0.097	106.8
2.60	22.17	22.31	0.090	106.9
2.65	22.32	22.43	0.084	103.6
2.70	22.44	22.56	0.078	99.8
2.75	22.56	22.69	0.076	98.4
2.80	22.71	22.81	0.071	99.5
2.85	22.85	22.94	0.068	102.8
2.90	22.97	23.07	0.062	104.5
2.95	23.10	23.19	0.041	101.6
3.00	23.24	23.30	0.033	96.9
3.05	23.36	23.40	0.040	92.9
3.10	23.50	23.53	0.047	83.2
3.15	23.64	23.65	0.059	78.0
3.20	23.74	23.77	0.069	78.4
3.25	23.85	23.96	0.071	82.0
3.30	23.96	24.12	0.079	86.3
3.35	24.07	24.22	0.090	88.1
3.40	24.16	24.22	0.102	88.0
3.45	24.25	24.30	0.105	87.4

Table B–43 — *continued*

NGC 1399

$(a'')^{1/4}$	μ_B [mag arcsec^{-2}]		$\epsilon = 1 - b/a$	P.A.
	maj	*min*		[deg]
3.50	24.34	24.42	0.104	84.2
3.55	24.50	24.58	0.110	79.8
3.60	24.64	24.79	0.114	78.5
3.65	24.74	24.92	0.117	79.6
3.70	24.79	25.06	0.123	80.3
3.75	24.86	25.12	0.124	80.9
3.80	24.99	25.21	0.132	82.2
3.85	25.12	25.29	0.145	82.9
3.90	25.19	25.34	0.152	83.0
3.95	25.21	25.38	0.161	83.6
4.00	25.26	25.47	0.175	84.9
4.05	25.31	25.58	0.186	86.8
4.10	25.37	25.74	0.193	87.6
4.15	25.53	25.88	0.197	86.8
4.20	25.65	25.98	0.198	86.1
4.25	25.79	26.11	0.199	85.8
4.30	25.91	26.31	0.200	85.9
4.35	25.96	26.42	0.201	86.3
4.40	26.05	26.51	0.204	86.6
4.45	26.09	26.58		
4.50	26.22	26.63		
4.55	26.39	26.77		
4.60	26.46	26.96		
4.65	26.60	27.16		
4.70	26.72	27.27		
4.75	26.83	27.39		
4.80	26.96			
4.85	27.15			
4.90	27.29			
4.95	27.36			
5.00	27.47			
5.05	27.60			
5.10	27.72			
5.15	27.84			
5.20	27.97			
5.25	28.12			
5.30	28.27			
5.35	28.41			
5.40	28.54			

Table B–44

NGC 1404

$(a'')^{1/4}$	μ_B [mag arcsec^{-2}]		$\epsilon = 1 - b/a$	P.A.
	maj	*min*		[deg]
0.00	16.90	16.90		
0.80	16.94	16.95		
0.85	16.96	16.97		
0.90	16.99	17.00		
0.95	17.04	17.05		
1.00	17.10	17.12	0.068	141.8
1.05	17.17	17.21	0.077	145.0
1.10	17.27	17.32	0.088	148.0
1.15	17.37	17.44	0.095	149.3
1.20	17.50	17.57	0.102	151.1
1.25	17.62	17.72	0.110	152.5
1.30	17.75	17.87	0.116	153.9
1.35	17.89	18.03	0.127	155.1
1.40	18.04	18.19	0.133	155.9
1.45	18.19	18.37	0.136	156.1
1.50	18.37	18.55	0.138	156.5
1.55	18.53	18.74	0.141	157.0
1.60	18.71	18.93	0.142	157.3
1.65	18.87	19.13	0.146	158.1
1.70	19.05	19.32	0.152	160.0
1.75	19.24	19.53	0.151	159.6
1.80	19.44	19.72	0.152	159.2
1.85	19.65	19.93	0.141	158.8
1.90	19.86	20.14	0.129	159.7
1.95	20.09	20.34	0.120	160.9
2.00	20.28	20.54	0.119	161.3
2.05	20.48	20.71	0.118	162.0
2.10	20.66	20.89	0.111	162.5
2.15	20.87	21.08	0.109	163.0
2.20	21.03	21.27	0.110	164.3
2.25	21.21	21.47	0.114	164.7
2.30	21.39	21.69	0.115	165.3
2.35	21.61	21.89	0.121	166.2
2.40	21.80	22.09	0.118	165.6
2.45	21.98	22.27	0.123	165.4
2.50	22.16	22.50	0.125	165.9
2.55	22.34	22.67	0.132	165.5
2.60	22.55	22.91	0.134	165.6
2.65	22.69	23.06	0.139	165.5
2.70	22.89	23.23	0.138	163.2
2.75	23.02	23.43	0.142	162.4
2.80	23.17	23.61	0.133	161.5
2.85	23.39	23.75	0.132	160.8
2.90	23.59	23.92	0.133	160.4
2.95	23.81	24.09	0.136	162.5
3.00	23.95	24.28	0.132	163.5
3.05	24.11	24.50	0.132	162.6
3.10	24.29	24.73	0.141	161.6
3.15	24.40	24.91	0.151	160.7
3.20	24.52	25.10	0.172	159.4

Table B–45

NGC 1419

$(a'')^{1/4}$	μ_B [mag arcsec^{-2}]		$\epsilon = 1 - b/a$	P.A.
	maj	*min*		[deg]
0.00	18.01	18.01		
0.80	18.09	18.08		
0.85	18.12	18.11		
0.90	18.18	18.17		
0.95	18.27	18.25		
1.00	18.38	18.35	0.091	155.5
1.05	18.53	18.48	0.091	155.3
1.10	18.70	18.64	0.087	153.5
1.15	18.90	18.83	0.088	153.8
1.20	19.12	19.04	0.084	152.6
1.25	19.36	19.27	0.079	151.9
1.30	19.60	19.50	0.071	152.2
1.35	19.83	19.74	0.059	151.6
1.40	20.06	20.01	0.045	150.6
1.45	20.28	20.26	0.023	153.1
1.50	20.55	20.52	0.019	152.3
1.55	20.76	20.76	0.013	130.8
1.60	21.01	21.02	0.012	116.1
1.65	21.25	21.24	0.006	104.4
1.70	21.49	21.49	0.005	91.4
1.75	21.73	21.72	0.006	75.5
1.80	21.94	21.97	0.008	64.1
1.85	22.19	22.20	0.007	57.7
1.90	22.43	22.49	0.008	54.9
1.95	22.70	22.77	0.020	53.6
2.00	22.93	22.99	0.024	51.5
2.05	23.23	23.24	0.030	48.8
2.10	23.48	23.49	0.034	45.0
2.15	23.72	23.83	0.036	41.6
2.20	23.93	24.14	0.053	35.8
2.25	24.24	24.43	0.060	32.3
2.30	24.47	24.63	0.076	34.1
2.35	24.67	24.86	0.106	38.5
2.40	24.81	25.12	0.110	40.4
2.45	24.92	25.37	0.117	37.0
2.50	25.14	25.60	0.122	39.8
2.55	25.35	25.84	0.137	45.0
2.60	25.56	26.08	0.155	46.9
2.65	25.72	26.33	0.168	48.7
2.70	26.00	26.57	0.186	49.3
2.75	26.20	26.81	0.192	47.7
2.80	26.38	27.05	0.174	52.1
2.85	26.57	27.29	0.163	56.1
2.90	26.66	27.53	0.160	54.4
2.95	26.79	27.77	0.165	52.2
3.00	26.97	28.00	0.169	52.9
3.05	27.32		0.169	56.5
3.10	27.62			
3.15	27.81			
3.20	28.10			

Table B–46

NGC 1427

$(a'')^{1/4}$	μ_B [mag arcsec^{-2}]		$\epsilon = 1 - b/a$	P.A.
	maj	*min*		[deg]
0.00	17.78	17.78		
0.80	17.81	17.82		
0.85	17.82	17.84		
0.90	17.85	17.88		
0.95	17.89	17.93		
1.00	17.94	18.00	0.161	85.8
1.05	18.02	18.10	0.156	84.2
1.10	18.11	18.22	0.157	82.9
1.15	18.23	18.37	0.161	82.3
1.20	18.37	18.55	0.162	82.5
1.25	18.54	18.76	0.168	82.7
1.30	18.72	18.97	0.173	82.2
1.35	18.91	19.20	0.180	81.7
1.40	19.10	19.43	0.189	81.3
1.45	19.29	19.65	0.200	80.9
1.50	19.50	19.86	0.206	80.8
1.55	19.69	20.08	0.215	80.6
1.60	19.88	20.29	0.221	80.3
1.65	20.05	20.48	0.234	79.9
1.70	20.23	20.68	0.242	79.6
1.75	20.37	20.88	0.251	79.3
1.80	20.55	21.02	0.260	79.4
1.85	20.71	21.21	0.273	79.4
1.90	20.86	21.37	0.284	79.4
1.95	21.03	21.55	0.288	79.5
2.00	21.17	21.73	0.295	79.0
2.05	21.32	21.92	0.299	78.9
2.10	21.47	22.10	0.290	78.8
2.15	21.62	22.28	0.291	78.0
2.20	21.75	22.46	0.293	78.0
2.25	21.92	22.65	0.304	78.4
2.30	22.01	22.81	0.318	78.7
2.35	22.22	23.01	0.319	78.6
2.40	22.35	23.18	0.315	79.0
2.45	22.59	23.39	0.308	79.3
2.50	22.75	23.57	0.309	78.9
2.55	22.92	23.74	0.312	78.8
2.60	23.10	23.96	0.312	78.6
2.65	23.28	24.12	0.302	78.3
2.70	23.48	24.31	0.293	78.2
2.75	23.67	24.52	0.288	78.2
2.80	23.80	24.68	0.292	78.3
2.85	23.91	24.84	0.300	78.2
2.90	24.06	25.00	0.300	78.2
2.95	24.23	25.13	0.297	78.3
3.00	24.53	25.33	0.291	78.0
3.05	24.75	25,61	0.293	77.8
3.10	24.91	25.80	0.290	77.6
3.15	25.06	25.96	0.288	78.2
3.20	25.20	26.10	0.282	77.7
3.25	25.34	26.25	0.276	77.9
3.30	25.54	26.32	0.269	77.6
3.35	25.78	26.44	0.255	76.5
3.40	25.99	26.61	0.236	76.1
3.45	26.15	26.76	0.221	76.1

Table B–46 — *continued*

NGC 1427

$(a'')^{1/4}$	μ_B [mag arcsec^{-2}]		$\epsilon = 1 - b/a$	P.A.
	maj	*min*		[deg]
3.50	26.34	26.92	0.204	75.9
3.55	26.51		0.207	75.4
3.60	26.69		0.219	75.1
3.65	26.86			
3.70	26.99			
3.75	27.16			
3.80	27.30			
3.85	27.44			
3.90	27.61			
3.95	27.78			
4.00	27.93			
4.05	28.10			

Table B–47

NGC 1428

$(a'')^{1/4}$	μ_B [mag arcsec^{-2}]		$\epsilon = 1 - b/a$	P.A.
	maj	*min*		[deg]
0.00	19.16	19.16		
0.80	19.22	19.23		
0.85	19.25	19.25		
0.90	19.29	19.28		
0.95	19.34	19.32		
1.00	19.40	19.39		
1.05	19.47	19.47		
1.10	19.56	19.58		
1.15	19.66	19.71		
1.20	19.78	19.85		
1.25	19.89	20.01		
1.30	20.01	20.16		
1.35	20.13	20.33		
1.40	20.27	20.55		
1.45	20.40	20.76		
1.50	20.54	21.02		
1.55	20.70	21.29		
1.60	20.84	21.52		
1.65	21.00	21.74		
1.70	21.19	21.99		
1.75	21.34	22.30	0.339	114.8
1.80	21.55	22.62	0.354	115.4
1.85	21.73	23.04	0.366	114.7
1.90	21.94	23.30	0.371	114.4
1.95	22.20	23.60	0.384	114.8
2.00	22.46	24.02	0.384	114.9
2.05	22.70	24.42	0.396	115.2
2.10	22.95	24.74	0.403	115.2
2.15	23.17	25.07	0.409	115.0
2.20	23.45	25.25	0.417	115.2
2.25	23.66	25.47	0.425	115.3
2.30	23.87	25.74	0.433	115.2
2.35	24.14	25.96	0.451	114.9
2.40	24.32	26.12	0.461	114.7
2.45	24.56	26.41	0.475	114.9
2.50	24.82	26.60	0.486	114.4
2.55	25.00	26.79	0.505	113.8
2.60	25.17	26.98	0.509	113.8
2.65	25.41	27.15	0.503	112.7
2.70	25.73	27.37	0.477	112.9
2.75	26.06	27.57	0.470	113.2
2.80	26.25	27.69	0.460	114.3
2.85	26.52	27.84	0.434	114.8
2.90	26.80		0.406	115.5
2.95	27.08		0.400	115.8
3.00	27.37		0.393	116.1
3.05	27.66		0.384	116.4

References

Aguilar L.A. & White S.D.M. 1986, ApJ, 307, 97

Bally J. & Thronson H.A. 1989, AJ, 97, 69

Barbon R., Benacchio L. & Capaccioli M. 1976, Mem. Soc. Astron. It., 47 ,263

Barbon R., Cappellaro E. & Turatto M. 1989, A&AS, 81, 421

Barnes J. 1988, ApJ, 331, 699

Bender R. & Möllenhoff C. 1987, A&A, 177, 71

Bender R. & Nieto J.-L. 1990, A&A, 239, 97

Bender R., Burstein D. & Faber S.M. 1992, ApJ, 399, 462

Bender R., Döbereiner S., Möllenhoff C. 1988, A&AS, 74, 385 (= BDM88)

Bender R., Surma P., Döbereiner S., Möllenhoff C. & Madejsky R. 1989a, A&A, 217, 35 (= BSDMM)

Bender R., Capaccioli M., Macchetto D. & Nieto J.-L. 1989b, The Messenger, 55, 6

Bendinelli O. 1991, ApJ, 366, 599

Bertola F. 1985, in J.-L. Nieto ed., New Aspects of Galaxy Photometry. Springer–Verlag, Berlin), p. 131

Bertola F. & Capaccioli M. 1975, ApJ, 200, 439

Bertola F. & Capaccioli M. 1978, ApJ, 219, L95

Bertola F., Vietri M. & Zeilinger W.W. 1990, in B. Jarvis & D.M. Terndrup, eds, Bulges of Galaxies. ESO, Garching, p. 275

Bettoni D. & Fasano G. AJ, 1993, submitted

Binggeli B. & Cameron L.M. 1991, A&A, 252, 27 (= BC91)

Binggeli B. & Cameron L.M. 1993, preprint (= BC93)

Binggeli B., Sandage A. & Tammann G. 1985, AJ, 90, 1681 (BST)

Binggeli B., Sandage A. & Tammann G. 1988, ARA&A, 26, 509

Binggeli B., Tammann G. & Sandage A. 1987, AJ, 94, 251

Binney J.J. 1976, MNRAS, 177, 19

Boroson T. 1981, ApJS, 46, 177 (=Bor81)

Brosche P. 1973, A&A, 23, 259

Burstein D., Bender R. & Faber S.M. 1993, in I.J. Danziger, W.W. Zeilinger & K. Kjär, eds, Proc. ESO/EIPC Workshop on: Structure, Dynamics and Chemical Evolution of Elliptical Galaxies. ESO, Garching, p. 31 (= BBF)

Caon N., Capaccioli M. & Rampazzo R. 1990, A&AS, 86, 429 (= CCR)

Capaccioli M. 1985, in J.-L. Nieto ed., New Aspects of Galaxy Photometry. Springer–Verlag, Berlin), p. 53

Capaccioli M. 1987, in de Zeeuw T., ed., Proc. IAU Symp. 127, Structure and Dynamics of Elliptical Galaxies. Reidel, Dordrecht, p. 47

Capaccioli M. 1989a, in Second Extragalactic Astronomy Regional Meeting. Academia de Ciencias, Cordoba, p. 317

Capaccioli M. 1989b, in H.G. Corwin Jr. & L. Bottinelli, eds, Le Monde des Galaxies. Springer–Verlag, Berlin, p. 208

Capaccioli M. & Caon N. 1989, in Grosbøl P.J., Murtagh F. & Warmels R.H., eds, First ESO/ST–ECF Data Analysis Workshop. ESO, Garching, p. 107

Capaccioli M. & Caon N. 1991, MNRAS, 248, 523

Capaccioli M. & Caon N. 1992, in Busarello G., Capaccioli M., Longo G., eds, Morphological and Physical Classification of Galaxies. Kluwer, Dordrecht, p. 99

Capaccioli M. & de Vaucouleurs G. 1983, ApJS, 52, 465

Capaccioli M., Caon N. & Rampazzo R. 1990, MNRAS, 242, 24p

Capaccioli M., Held E.V. & Nieto J.-L. 1987, AJ, 94, 1519

Capaccioli M., Piotto G. & Rampazzo R. 1988, AJ, 96, 497 (= CPR88)

Capaccioli M., Cappellaro E., Della Valle M., D'Onofrio M., Rosino L., & Turatto M. 1990a, ApJ, 350, 110

Capaccioli M., Held E.V., Lorenz H. & Vietri M. 1990b, AJ, 99, 1813

Capaccioli M., Vietri M., Held E.V. & Lorenz H. 1990c, ApJ, 371, 535

Carlberg R.G. 1984, ApJ, 286, 403

Ciotti L. 1991, A&A, 249, 99

Danziger I.J., Carollo C.M., Buson L., Matteucci F. & Brocato E. 1993, in I.J. Danziger, W.W. Zeilinger & K. Kjär, eds, Proc. ESO/EIPC Workshop on: Structure, Dynamics and Chemical Evolution of Elliptical Galaxies. ESO, Garching, p. 399

Davies R.L. & Birkinshaw M. 1986, ApJ, 303, L45

Davies R.L., Efstathiou G., Fall S.M., Illingworth G. & Schechter P.L. 1983, ApJ, 266, 41

Davies R.L., Burstein D., Dressler A., Faber S.M., Lynden-Bell D., Terlevich R.J. & Wegner G. 1987, ApJS, 64, 581

Davies J.I., Phillipps S., Cawson M.G.M., Disney M.J. & Kibblewhite E.J. 1988, MNRAS, 232, 239 (= DPCDK)

de Carvalho R.R. & Djorgovski S. 1992, ApJ, 389, L49

de Vaucouleurs G. 1948, Ann. Astrophys., 11, 247

de Vaucouleurs G. 1958, ApJ, 128, 465

de Vaucouleurs G. 1959, Hand. Phys., Vol. 53, p. 311

de Vaucouleurs G. 1961, in Proc. IAU Symp. N. 15, Problems of Extragalactic Research. MacMillan, New York, p. 3

de Vaucouleurs G. 1968, Applied Optics, 7, 1513

de Vaucouleurs G. & Capaccioli M. 1979, ApJS, 40, 699

de Vaucouleurs G. & Olson D.W. 1982, ApJ, 230, 697

de Vaucouleurs G., de Vaucouleurs A., Corwin H.G. Jr., Buta R.J., Paturel G. & Fouqué P. 1991, Third Reference Catalogue of Bright Galaxies. Springer–Verlag, New York (RC3)
Djorgovski S. 1992, in R.R. de Carvalho ed., Cosmology and Large–Scale Structure in the Universe. ASP Conf. Ser. 24, p. 19
Djorgovski S. & Davis M. 1987, ApJ, 313, 59 (= DD87)
Djorgovski S., de Carvalho R. & Han M.-S. 1989, in van den Bergh S. & Pritchet C.J., eds, The Extragalactic Distance Scale, ASP Conf. Ser., Vol. 4. ASP, San Francisco, p. 329
D'Onofrio M. 1991, Ph.D. Thesis, I.S.A.S., Trieste
Dressler A. 1980, ApJ, 236, 351
Dressler A. 1984, ApJ, 281, 511
Dressler A., Lynden–Bell D., Burstein D., Davies R.L., Faber S.M., Terlevich R.J. & Wegner G. 1987, ApJ, 313, 42
Einasto M. 1991, MNRAS, 250, 802
Einasto M. 1992, MNRAS, 258, 571
Fabbiano G., Kim D.-W. & Trinchieri G. 1992, ApJS, 80, 531
Faber S.M. & Jackson R.E. 1976, ApJ, 204, 668
Faber S.M., Dressler A., Davies R.L., Burstein D., Linden–Bell D., Terlevich R. & Wegner G. 1987, in Faber S.M., ed., Nearly Normal Galaxies. Springer–Verlag, Berlin, p. 175
Fasano G. 1990, Internal Report of the Padova Astronomical Observatory
Ferguson H.C. 1989, AJ, 98, 367
Ferguson H.C. & Sandage A. 1988, AJ, 96, 1520
Forman W., Jones C. & Tucker W. 1985, ApJ, 293, 102
Franx M., Illingworth G.D. & Heckman T. 1989, ApJ, 344, 613
Freeman K.C. 1970, ApJ, 160, 811
Galletta G. 1980, A&A, 81, 179
Governato F., Reduzzi L. & Rampazzo R. 1993, MNRAS, in press
Gregg M.D. 1992, ApJ, 384, 43
Hamabe M. & Kormendy J. 1987, in de Zeeuw T., ed., Proc. IAU Symp. 127, Structure and Dynamics of Elliptical Galaxies. Reidel, Dordrecht, p. 379 (= HK)
Hamilton A.J.S. 1988, MNRAS, 331, L50
Hoessel J.G. 1980, ApJ, 241, 493
Hoessel J.G. & Schneider D.P. 1985, AJ, 90, 1468 (= HS85)
Hubble E. & Humason M.L. 1931, ApJ, 74, 43
Illingworth G. 1977, ApJ, 218, L43
Irwin M.J., Davies J.I., Disney M.J. & Phillipps S. 1990, MNRAS, 245, 289 (= IDDP)
Jacoby G.H., Branch D., Ciardullo R., Davies R.L., Harris W.E., Pierce M.J., Pritchet C.J., Tonry J.L. & Welch D.L. 1992, PASP, 104, 599
Jerjen H., Tammann G. & Binggeli B. 1992, in Busarello G., Capaccioli M., Longo G., eds, Morphological and Physical Classification of Galaxies. Kluwer, Dordrecht, p. 17
Jørgensen I., Franx M. & Kjærgaard P. 1992, A&AS, 95, 489 (= JFK92)
Kent S.M. 1985, ApJS, 59, 115 (= Ken85)

Knapp G.R., Turner E.L. & Cunnifee P.E. 1985, AJ, 90, 454
Knapp G.R., Guhathakurta P., Kim D.-W. & Jura M. 1989, ApJS, 70, 329
Kodaira K., Watanabe M. & Okamura S. 1986, ApJS, 60, 475 (= KWO86)
Kormendy J. 1977b, ApJ, 217, 406
Kormendy J. 1977a, ApJ, 218, 333 (= Kor77)
Kormendy J. 1980, in P. Crane & K. Kjar eds., ESO Workshop on Two Dimensional Photometry. ESO, Geneva, p. 191
Kormendy J. 1985, ApJ, 292, L9
Kormendy J. & Djorgovski S. 1989, ARA&A, 27, 235
Lauer T.R. 1985, ApJS, 57, 473 (= Lau85)
Longo G. & de Vaucouleurs A. 1983, The Univ. of Texas Monographs in Astron., 3
Longo G. & de Vaucouleurs A. 1985, The Univ. of Texas Monographs in Astron., 3A
Longo G., Capaccioli M., Bender R. & Busarello G. 1989, A&A, 225, L17
Longo G., Capaccioli M. & Ceriello A. 1991, A&AS, 90, 370
Lucey J.R., Guzman R., Carter D. & Terlevich R.J. 1991, MNRAS, 253, 584
Makino J., Akiyama K. & Sugimoto D. 1990, PASP, 42, 205
Malkan M.A. 1984, ApJ, 287, 555 (= Mal84)
Malkan M.A., Margon B. & Chanan G.A. 1984, ApJ, 280, 66
Malumuth E.M. & Kirshner R.P. 1985, ApJ, 291, 8 (= MK85)
Mamon G.A. 1989, A&A, 219, 98
Mellier Y. & Mathez G. 1987, A&A, 175, 1
Meurs E.A.J. 1987, in The Optimization of the Use of CCD Detectors in Astronomy. ESO, Garching, p. 105
Michard R. 1985, A&AS, 59, 205 (= Mic85)
Michard R. & Marchal J. 1990, A&A, 232, L9
Møller P., Stiavelli M. & Zeilinger W.W. 1993, MNRAS, in press
Nieto J.-L. 1992, in Busarello G., Capaccioli M., Longo G., eds, Morphological and Physical Classification of Galaxies. Kluwer, Dordrecht, p. 69
Nieto J.-L. & Bender R. 1989, A&A, 215, 266
Peletier R., Davies R.L., Illingworth G.D., Davis L.E. & Cawson M. 1990, AJ, 100, 1091 (= PDIDC)
Poulain P. 1988, A&AS, 72, 215
Poulain P. & Nieto J.-L. 1993, preprint
Poveda A., Iturriaga R. & Orozoco I. 1960, in Bol. Obs. Tonantzintla, N. 20, p. 3
Prugniel P., Nieto J.-L. & Simien F. 1987, A&A, 173, 49
Richter G., Lorenz H. & Capaccioli M. 1993, A&A, in press
Rix H.-W. & White S.D.M. 1990, ApJ, 362, 52
Roberts M.S., Hogg D.E., Bregman J.N., Forman W.R. & Jones C. 1991, ApJS, 75, 751
Ryden B.S. 1991, MNRAS, 253, 743
Ryden B.S. 1992, ApJ, 386, 42

Saglia R.P., Bertin G., Bertola F., Danziger J., Dejonghe H., Sadler E.M., Stiavelli M., de Zeeuw P.T. & Zeilinger W.W. 1993, ApJ, 403, 567
Schneider D.P., Gunn J.E. & Hoessel J.G. 1983, ApJ, 268, 476 (= SGH83)
Schombert J.M. 1986, ApJ, 60, 603
Schombert J.M. 1987, ApJS, 64, 643 (= Sch87)
Schombert J.M. & Bothun G.D. 1987, AJ, 92, 60
Scorza C. 1993, Ph.D. Thesis, Univ. of Heidelberg
Sersic J.-L., 1968, Atlas de Galaxias Australes. Observatorio Astronomico, Cordoba
Sparks W.B., Wall J.V., Jorden P.R., Thorne D.J. & van Breda I. 1991, ApJS, 76, 471
Stiavelli M., Londrillo P. & Messina A. 1991, MNRAS, 251, 57p
Stiavelli M., Møller P. & Zeilinger W.W. 1993, preprint
Terlevich R., Davies R.L., Faber S.M. & Burstein D. 1981, MNRAS, 196, 381
Thomsen B. & Frandsen S. 1983, AJ, 88, 789 (= TF83)
Tonry J.L., Ajhar E.A. & Luppino G.A. 1990, AJ, 100, 1416
Tully R.B. & Shaya E.J. 1984, ApJ, 281, 31
Vader J.P., Vigroux L., Lachieze-Rey M. & Souviron J. 1988, A&A, 203, 217
van Albada T.S. 1982, MNRAS, 201, 939
van der Bergh S. & Pierce M. 1990, ApJ, 364, 444
van der Marel R.P. & Franx M. 1993, preprint
Wardle M. & Knapp G.R. 1986, AJ, 91, 23
White S. 1979, MNRAS, 189, 831
Whitmore B.C. 1984, ApJ, 278, 61
Whitmore B.C. 1991, in Giuricin G., Mardirossian F., Mezzetti M., eds, Galaxy Environments and the Large Scale Structure of the Universe. SISSA Ref. 146/91/A, Trieste, p. 5
Young P.J. 1976, AJ, 81, 807
Zepf S.E. & Whitmore B.C. 1993, ApJ, preprint

The Manifold of Hot Galaxian Components: related papers (by N. Caon)

[1] *Surface photometry of early-type galaxies.* 1989, in ESO Conference and Workshop Proceedings No 31, eds. P.J.Grosbøl, F.Murtagh e R.H.Warmels, p. 107 — in coll. with M. Capaccioli

[2] *Wide field telescopes as essential tools in surface photometry of galaxies.* 1989, in Workshop on the utilization of the Asiago Schmidt telescopes, C. Barbieri and E. Cappellaro eds, p. 31 — in coll. with M. Capaccioli

[3] *Further evidence of continuity between elliptical and disk galaxies.* 1990, in Dynamics and Interactions of Galaxies, Wielen ed., p. 219 — in coll. with M. Capaccioli and R. Rampazzo

[4] *Further evidence of continuity between elliptical and S0 galaxies.* 1990, MNRAS, 242, 24p — in coll. with M. Capaccioli and R. Rampazzo

[5] *Photographic and CCD surface photometry of 33 early-type galaxies in the Virgo cluster.* 1990, A&AS, 86, 429 — in coll. with M. Capaccioli and R. Rampazzo

[6] *On the lack of a simple relation between R_e and μ_e for early-type galaxies.* 1991, MNRAS, 248, 523 — in coll. with M. Capaccioli

[7] *Integrated properties of the early-type Galaxies of the Virgo cluster.* 1991, in Galaxy Environments and the Large Scale Structure of the Universe, G. Giuricin, F. Mardirossian, and M. Mezzetti eds. — in coll. with M. Capaccioli and S. Trevisani

[8] *Families of Galaxies in the μ_e-R_e Plane.* 1992, MNRAS, 259, 323 — in coll. with M. Capaccioli and M. D'Onofrio

[9] *On the photometric scaling laws for early-type galaxies.* 1992, in Morphological and physical classification of galaxies, G. Longo, M. Capaccioli, and G. Busarello eds., p. 425 — in coll. with M. Capaccioli

[10] *Stellar disks in early-type galaxies.* 1992, in Morphological and physical classification of galaxies, G. Longo, M. Capaccioli, and G. Busarello, eds., p. 99 — in coll. with M. Capaccioli

[11] *Families of galaxies in the μ_e-R_e plane.* 1992, in Standard Candles, Mem. Soc. Astron. It., 63, 509 — in coll. with M. Capaccioli, M. D'Onofrio and S. Trevisani

[12] *The dichotomy in the physical properties of Hot Galaxian Components.* In Proceedings of the Workshop on Observational Cosmology (Milano, Italy, September 1992) — in coll. with M. Capaccioli and M. D'Onofrio

[13] *The two families of Hot Galaxian Components.* Talk presented at the Primo Congresso Nazionale di Cosmologia (Rome, Italy, November 1992)

[14] *The (R_e, μ_e) plane of Hot Stellar Systems.* 1993, in ESO/EIPC Workshop on Structure, Dynamics and Chemical Evolution of Early-type Galaxies, J. Danziger, W.W. Zeilinger and K. Kjár eds, p. 43 — in coll. with M. Capaccioli and M. D'Onofrio

[15] *Elliptical Galaxies and the continuity of the Hubble sequence.* 1993, in ESO/EIPC Workshop on Structure, Dynamics and Chemical Evolution of Early-type Galaxies, J. Danziger, W.W. Zeilinger and K. Kjár eds., p. 3 — in coll. with R. Bender, M. Capaccioli, F. Macchetto, J.L. Nieto, E. Davoust, G. Piotto, P. Poulain, J.L. Prieur, P. Prugniel, R. Rampazzo, C. Scorza, W.M. Sparks, P. Surma, and S. Wagner.

[16] *A step further in the identification of two families of Hot Galaxian Components.* Poster presented at the meeting: Panchromatic View of Galaxies (Kiel, Germany, March 1993) — in coll. with M. D'Onofrio

[17] *On the shape of the light profiles of early-type galaxies.* 1993, MNRAS, in press — in coll. with M. Capaccioli and M. D'Onofrio

[18] *Environmental properties of early-type galaxies in the Virgo cluster.* 1993, MNRAS, submitted — in coll. with M. Einasto

[19] *B-band 'global mapping' photometry of 47 galaxies in the Fornax and in the Virgo clusters.* 1993, A&AS, submitted — in coll. with M. D'Onofrio and M. Capaccioli

[20] *A new method to remove column offsets in CCD images.* 1993, PASP, submitted — in coll. with G. Piotto and C. Pellegrini

[21] *Global properties of a complete sample of early-type galaxies.* 1993, A&A, in preparation — in coll. with M. D'Onofrio and M. Capaccioli

[22] *Major axis kinematics of 15 early-type galaxies in the Fornax cluster.* 1993, in preparation — in coll. with S. Zaggia, M. D'Onofrio and M. Capaccioli